IDŐJÁRÁS

QUARTERLY JOURNAL
OF THE HUNGARIAN METEOROLOGICAL SERVICE

CONTENTS

Special issue: 3*0-year anniversary of ALADIN cooperation*

Guest Editors: Gabriella Szépszó and András Horányi

Editorial

Special Issue: 30-year anniversary of ALADIN cooperation

The ALADIN international cooperation had been initiated by Météo-France in 1990, and the Hungarian Meteorological Service (HMS) decided to join right at the beginning. The first milestone of the cooperation was a short visit in Paris in March, 1991, which was followed by the initial development phase of the ALADIN numerical weather prediction (NWP) model in Toulouse. At that time, nobody had an idea of the magnitude of the impact what this cooperation and model will have on the participating meteorological services. ALADIN is not a single model, but a modeling system, which encompasses various components like powerful data assimilation, computationally efficient model dynamics, physical parameterization packages tailored to different resolutions in mesoscale, a surface model, which can be used online and offline, components of an ensemble prediction system, and a regional climate model. Recently, two non-hydrostatic configurations of the ALADIN model are used: AROME is developed specifically to run on convective-permitting resolutions, while ALARO can also be used in intermediate resolutions between the mesoscale and the convection-permitting scales. For the last 15 years or so, the HIRLAM cooperation has been also using the ALADIN model (called HARMONIE by them). The ALADIN, RC-LACE, and HIRLAM consortia decided to develop AROME, ALARO, and HARMONIE on the same basis and principles in the framework of the ACCORD consortium established in 2020. The ALADIN model became the most commonly used NWP system in Europe. This Special Issue pays tribute to the 30 years of the ALADIN cooperation with special emphasis on the role of the Hungarian Meteorological Service.

Originally, the ALADIN model was developed only for dynamical adaptation, i.e., no separate data assimilation system was foreseen, the model initial conditions (also the surface physiographic datasets) were taken from the global model by sophisticated interpolation methods. Soon it was realized that a state-of-the-art limited area model cannot live without an independent data assimilation system, and therefore, data assimilation developments had been started. Now the 3D-Var (three-dimensional variational data assimilation) scheme is widely used by the participating institutes. *Tóth et al.* gives an overview of the data assimilation work in general and the latest developments in AROME at the Hungarian Meteorological Service in particular. The article of *Randriamampianina et al.* summarizes some of the data assimilation impact studies, which were performed by the ALADIN model for the EUMETNET/EUCOS cooperation.

The use of the ALADIN model for ensemble prediction was emerged in the early 2000s. While *Simon et al.* presents some results of ALARO via testing its performance with different settings at 1–2 km resolution over Slovakia in some convective cases, they also prove the added value of the so-called A-LAEF ensemble

system with respect to the single model runs. A-LAEF (operated and maintained by the RC-LACE consortium) is based on the ALARO model and represents both the initial condition and model uncertainties. The first Hungarian limited area ensemble prediction system (LAMEPS) called HUNEPS became operational in 2008. One of the complementary tasks needed to be completed was the statistical calibration of the probabilistic forecasts. Different ensemble model output statistics (EMOS) were intensively tested and optimized with special focus on surface wind. In the paper of *Baran* and *Baran* in this Special Issue, EMOS is further tuned to improve higher level wind forecasts of the convection-permitting AROME-EPS system. AROME-EPS replaced its predecessor, ALARO-EPS in 2020 in Hungary. Its operational forecasts are provided for wind farms to support their energy production estimates, and the raw predictions will be completed with calibrated ensemble forecasts from 2022 onwards. Ensemble methods can be applied also in environmental impact modeling as shown by *Ferenczi et al.* In their study, AROME-EPS forecasts served the meteorological inputs for the CHIMERE air chemistry model to quantify the impact of the uncertainty coming from weather predictions compared to that of the inaccuracies of emission input data on air quality forecasts.

The mature NWP team and the availability of high-performance computer system made it possible to start climate dynamics research in Hungary to provide proper tools to explore regional climate change. The work started with adaptation of regional climate models (RCM) in 2004: REMO developed by the Max Planck Institute in Hamburg and ALADIN-Climate in cooperation with Météo-France and the entire ALADIN project. Gradual establishment of the climate modeling activity at OMSZ was exciting from the first RCM simulations (using ERA40 reanalysis as lateral boundary conditions at the beginning!) via future projections and data provision for climate impact studies in Hungary up to educating the users and stakeholders to use probabilistic (climate) information. The paper of *Bán et al.* is dedicated to recent results of ALADIN-Climate and their evaluation in context of the European results (from EURO-CORDEX).

RCM outputs are provided not only for research and stakeholder partners of the Hungarian Meteorological Service, but also further meteorological studies are carried out based on these RCM data. Investigation of urban climate change started in 2010 with coupling the SURFEX/TEB surface model to ALADIN-Climate. Direct description of processes over specific surfaces (like lakes, cities) requires at least a km-scale grid distance, which is still beyond the current resolution of RCMs. SURFEX (used in offline mode) is focusing on the relevant processes and widely applied both in NWP and climate modeling in the ACCORD community. The model was carefully validated in the last 10 years, and now it is ready for refinement of climate projections as demonstrated by the paper of *Gabriella Allaga-Zsebeházi*.

Last but not least, although formally the ALADIN cooperation might come to an end and reincarnates into its new life with the introduction of the ACCORD consortium, the modeling system will remain and evolve with us for long-long time.

Finally, we would like to express our gratitude to all authors contributing to this special edition of Időjárás as well as to the reviewers helping to improve the scientific content of the papers.

Gabriella Szépszó and András Horányi
Guest Editors

IDŐJÁRÁS

Recent developments in the data assimilation of AROME/HU numerical weather prediction model

Helga Tóth[1,*], **Viktória Homonnai**[1], **Máté Mile**[2], **Anikó Várkonyi**[1], **Zsófia Kocsis**[1], **Kristóf Szanyi**[1], **Gabriella Tóth**[1], **Balázs Szintai**[1], and **Gabriella Szépszó**[1]

[1]*Hungarian Meteorological Service*
P.O. Box 38, H-1525 Budapest, Hungary

[2]*Norwegian Meteorological Institute*
P.O. Box 43, Blindern, N-0313 Oslo, Norway

[*]*Corresponding authors E-mail: toth.h@met.hu*

Abstract— A local three-dimensional variational data assimilation (DA) system was implemented operationally in AROME/HU (Application of Research to Operations at Mesoscale) non-hydrostatic mesoscale model at the Hungarian Meteorological Service (OMSZ) in 2013. In the first version, rapid update cycling (RUC) approach was employed with 3-hour frequency in local upper-air DA using conventional observations only. Optimal interpolation method was adopted for the surface data assimilation later in 2016. This paper describes the current developments showing the impact of more conventional and remote-sensing observations assimilated in this system, which reveals the benefit of additional local high-resolution observations. Furthermore, it is shown that an hourly assimilation-forecast cycle outperforms the 3-hourly updated system in our DA. Besides the upper-air assimilation developments, a simplified extended Kalman filter (SEKF) was also tested for surface data assimilation, showing promising performance on both the analyses and the forecasts of AROME/HU system.

Key-words: data assimilation, simplified extended Kalman filter, rapid update cycle, aircraft observations, atmospheric motion vectors

1. Introduction

Accurate estimation of the atmospheric initial state is an essential prerequisite for high-quality weather forecasts. Global numerical weather prediction (NWP) models use all information available about the Earth system to determine the initial condition: different kinds of observations, previous weather forecasts (called as background or first guess), and a priori physical information. They are combined in a statistically optimal way based on their reliability using data assimilation (DA) techniques. In the recent operational practice, three algorithms are widely applied in global models: the optimal interpolation (OI) minimizes the quadratic difference between the analysis and the truth; the variational method is based on minimization of a cost function measuring the analysis departures from the observations and the first guess; the Kalman filter method takes into account the flow-dependency of background errors. Variational methods are mostly utilized for upper-air data assimilation (*Fischer et al.,* 2005; *Courtier et al.,* 1994): in the 3-dimensional and 4-dimensional (3D-Var and 4D-Var) versions, the procedure looks for the best fit to background and observations at the analysis time and along a trajectory, respectively. OI is employed in surface data assimilation (*Mahfouf et al.,* 2000), as it is the simplified extended version of the Kalman filter (SEKF) (*de Rosnay et al.*, 2013; *Mahfouf*, 2009) which allows involving also satellite measurements in exchange for its higher computational cost.

For limited area models (LAMs), dynamical adaptation is a plausible way to prepare initial conditions without complex and computationally expensive methods. In this simple technique, the coarser-resolution driving model fields are interpolated onto the higher resolution target grid in the initial time step. The first limited area model of the ALADIN (Aire Limitée Adaptation dynamique Développement InterNational) consortium was originally developed without data assimilation, and in its earliest version at the Hungarian Meteorological Service (OMSZ) the initial conditions were created by dynamical adaptation (*Horányi et al.,* 1996), i.e., interpolating the fields of the global NWP model of Météo-France, ARPEGE (Action de Recherche Petite Echelle Grande Echelle) to the ALADIN grid. Nevertheless, only local and dense observations ensure to have access to those small-scale atmospheric features which are crucial for high-resolution mesoscale weather forecasts. The incremental 3D-Var algorithm was implemented to ALADIN, which looks for the minimum of departure between the analysis and the background field assuming that the background is a good estimation of the analysis and the linearized version of the observation operator can be used during the computation of the minimization. This is the standard or regularized linear least squares problem (*Fischer*, 2007). The method was introduced into the operational ALADIN version of OMSZ in 2005 (referred as ALADIN/HU; *Bölöni,* 2006). In the beginning, it assimilated only conventional observations (SYNOP, TEMP, temperature, and horizontal wind components

measured by aircrafts) 4 times a day at 0, 6, 12, and 18 UTC, and it was gradually extended with a variety of satellite data and wind profiler measurements (*Randriamampianina,* 2006).

The AROME (Application of Research to Operations at Mesoscale) model consists of the non-hydrostatic dynamical core of ALADIN, the atmospheric physical parameterization of the Meso-NH research model, and the SURFEX surface model (*Seity et al.,* 2011). It has been running operationally at OMSZ over a domain covering the Carpathian Basin with 2.5 km horizontal resolution and 60 vertical levels since 2010 (*Szintai et al.,* 2015). The initial and lateral boundary conditions (LBCs) were first taken from ALADIN/HU, benefiting from the already existing coarser resolution LAM analyses. However, it was proven later that the interpolated analysis does not contain reliable physical information on the smallest scales resolved by AROME/HU and in addition, more observations can be used at higher resolution. Therefore, the implementation of the local AROME DA system was started and the upper-air 3D-Var system became operational in 2013, assimilating conventional data (*Mile et al.,* 2015).

The 3D-Var approach assumes that all observations inside the assimilation window are measured exactly at the analysis time generating increased representation error in time. In order to be able to use more observations with reduced temporal representation error, experiments have been started with hourly analysis updates (i.e., rapid update cycle, RUC) in 2018 (*Jávorné Radnóczi et al.,* 2020).

The raw analysis often exhibits some imbalances which primarily originate from inconsistencies between the observed mass and wind fields inducing high-frequency oscillations in the first hours of the forecasts. In ALADIN/HU, a digital filter initialization (*Lynch et al.,* 1997) is applied to the analysis, which removes the high-frequency waves from the initial condition during a forward and backward model integration. This filtering technique is assumed to be detrimental for the mesoscale spectrum of AROME model, thus not employed in AROME/HU. Instead, a space consistent coupling is used, i.e., the LBC at the initial time is provided by the AROME/HU analysis, which efficiently exempts from high amplitude oscillating noises (*Mile et al.,* 2015).

Representation of background error statistics has key importance in variational methods, as the background error covariance matrix (the so-called B matrix) controls the propagation of the information coming from observations to the model grid and variables (*Berre,* 2000). The B matrix in ALADIN/HU was originally estimated with the NMC method (NMC stands for National Meteorological Center) that samples the forecast errors from a set of differences between two forecasts valid at the same time, but at different ranges (*Parish* and *Derber,* 1992). Later the ensemble technique was introduced, where the background errors are approximated by subtracting the members of an ensemble forecast generated with a set of data assimilation cycles (EDA) using perturbed observations that induce a spread also among the first guess fields through the

cycling (*Bölöni et al.,* 2014). The ensemble was first created by downscaling an ensemble of ARPEGE lateral boundary conditions using ALADIN (*Bölöni,* 2006), but later it was originating from the ALADIN ensemble prediction system (EPS) of OMSZ (*Hágel,* 2009). EDA method was applied to compute the background errors also in the case of AROME/HU: initially with downscaling the ensemble of ALADIN LBCs and recently with a 5-member ensemble provided by the convection-permitting AROME-EPS system (*Jávorné Radnóczi et al.,* 2020).

The initial conditions for the soil scheme in the early version of ALADIN/HU were interpolated from the ARPEGE analysis fields. In 2008, the CANARI optimal interpolation (*Taillefer,* 2002; *Tóth,* 2004) was implemented, in which the soil temperature and moisture analyses are calculated based on the relationship between soil and near-surface variables. In AROME/HU, the surface analysis of ALADIN/HU was interpolated to the 2.5 km resolution grid initially, while an improved version of the optimal interpolation was adopted in 2016. At the same time, experiments were started with simplified extended Kalman filter to exploit the advantage of the new observation techniques (like remote sensing data).

An obvious way to develop a data assimilation system is to involve new observations. Hourly analysis update requires to supply the assimilation with frequently and reliably available data. The DFS (degrees of freedom for signal) diagnostic tool (*Cardinali et al.,* 2004) indicates the relative contribution of given observations to the analysis. In a previous study (*Mile et al.,* 2015), DFS scores showed the large contribution of wind measurements and suggested the importance of humidity-related observations. In the last few years, sensitivity studies have been started in ALADIN/HU and more intensively in AROME/HU to estimate the impact of atmospheric motion vectors derived from satellite images, radial wind measured by meteorological radars, temperature, and wind information registered by the radars of air traffic controllers (i.e., Mode-S observations); radar reflectivity, zenith total delay (ZTD) observations of GNSS (global navigation satellite systems), and humidity observed by aircrafts (*Mile et al.,* 2015, 2019; *Fischer et al.,* 2017, 2018).

This paper aims to provide a comprehensive overview of current DA developments. In Section 2, the operational DA system is described. In Section 3, the local, experimental DA studies are represented applying conventional and non-conventional observations, as additional Mode-S MRAR (Meteorological Routine Air Report) data and satellite atmospheric motion vectors. Besides this, the surface data assimilation and RUC related developments are also presented in this Section. Finally, a summary of the recent results and further potential research are provided.

2. The operational data assimilation system of AROME/HU model

The data assimilation system of the operational AROME/HU model consists of an incremental 3D-Var and an OI technique for the upper-air and surface analysis, respectively. Furthermore, this system composes a three-hourly updated forward intermittent cycle called RUC (*Benjamin et al.,* 2004; *Mile et al.*, 2015, *Szintai et al.*, 2015). The LBCs are provided by the ECMWF/IFS (European Centre for Medium-Range Weather Forecasts / Integrated Forecasting System) model at hourly time intervals. The current operational AROME/HU version has been based on the cy43t2 model cycle since March 2021, and it has run at 2.5 km horizontal resolution, with 60 hybrid pressure terrain-following vertical levels. Most of the developments (except for SEKF) shown in this paper were carried out with the previous operational model version, cy40t1 (the 'cy' refers to the model 'cycle'; cycle number 40 is derived from the corresponding IFS cycle, i.e., cy40, on which AROME is based; IFS is jointly developed by ECMWF and Météo-France; and 't' refers to the model release specific to Météo-France, i.e., Toulouse; finally 1 refers to the release number).

The analyses of AROME/HU forecasts are updated three hourly at 0, 3, 6, 9, 12, 15, 18, and 21 UTC. The AROME/HU 3D-Var system uses only conventional observations from ground-based synoptic stations (SYNOP), radiosondes (TEMP), zenith total delays (GNSS ZTD), and aircraft data (AMDAR and MRAR). The assimilated observations, meteorological parameters, and the date of their operational implementations are summarized in *Table 1*. Most of the observations (except for GNSS ZTD) are routinely received and preprocessed in OPLACE (Observation Preprocessing system of RC LACE) hosted by the Hungarian Meteorological Service (*Trojáková et al.*, 2019).

Table 1: Assimilated observation types and parameters in AROME/HU operational system

Observation type	Parameter	Date of Operational implementation
SYNOP	u, v, T2M, HU2M, z	March 2013
TEMP	u, v, T, q, z	March 2013
AMDAR	u, v, T, q	March 2013 (u, v, T) November 2016 (q)
Slovenian / Czech Mode-S MRAR	u, v, T	November 2016 / March 2021
GNSS	ZTD	September 2018

In our local data assimilation system, two kinds of analyses are prepared and distinguished based on the length of cut-off time: short cut-off and long cut-off (*Bölöni*, 2006). This is the time interval of observations collection for data

assimilation. The aim of using short cut-off analysis is to provide initial conditions for operational model prediction as quickly as possible. The long cut-off analysis is prepared later for the same network time with longer waiting time for the observations, this analysis is used as an initial condition for the next first guess. In the recent AROME/HU version, this short cut-off time is set to +/- 90 minutes.

The operational AROME/HU version runs 8 times a day and provides forecasts up to 48 hours for main terms (0, 6, 12, and 18 UTC) and 36 hours for additional terms (3, 9, 15, and 21 UTC).

3. Surface data assimilation developments in AROME/HU model

3.1. Optimal interpolation

In the IFS/ARPEGE/ALADIN model family, the optimal interpolation method has been used for data assimilation purposes for a long time. Meanwhile, the variational assimilation scheme became paramount for upper-air DA allowing the use of remote-sensing observations, however, the OI approach is still employed for surface analysis by many operational centers. The land surface assimilation based on OI consists of the quality control of conventional observations, the 2 m analysis of temperature and relative humidity, and the corresponding correction of surface parameters using 2 m increments (*Giard* and *Bazile*, 2000). For the 2 m analysis, the OI method solves the analysis equation for each grid point individually assuming that only a limited number of observations influences one grid-point. The correction of surface parameters is done differently in ALADIN and AROME models because of the applied different surface parametrization schemes. In ALADIN model, the so-called ISBA (Interaction Soil Biosphere Atmosphere) scheme (*Noilhan* and *Planton,* 1989; *Noilhan* and *Mahfouf,* 1996) is used, while in AROME model, a more advanced, i.e., an externalized surface scheme is utilized, which is called SURFEX (*Masson et al.,* 2013).

The first local DA system in AROME was introduced operationally with variational upper-air data assimilation replacing the former downscaled ALADIN initial conditions (*Bölöni*, 2006; *Mile et al.,* 2015). Although the downscaling procedure remained for the AROME surface initialization, the use of ALADIN surface analyses continued. Such a dependence on the ALADIN system was not optimal in an operational AROME system, therefore, the experimentation of AROME surface DA using the OI method (OI-main) was started as well. Various observing system experiments have been carried out for the summer and winter seasons and different weather situations. Verification results revealed that the operational configuration with downscaled ALADIN surface has usually wet and cold bias in AROME near-surface forecast parameters, while with OI-main, AROME shifted towards the dry and warm bias changing slightly the diurnal cycle of surface parameters during the first 24 h of the model forecast (not shown). Moreover, the verification of precipitation forecasts with AROME OI-main

surface analysis showed mostly positive impact in particular case studies (summer and winter) and a short summer period as well (*Fig. 1*). After six months of surface spin-up, the AROME surface assimilation with OI-main became operational in 2016.
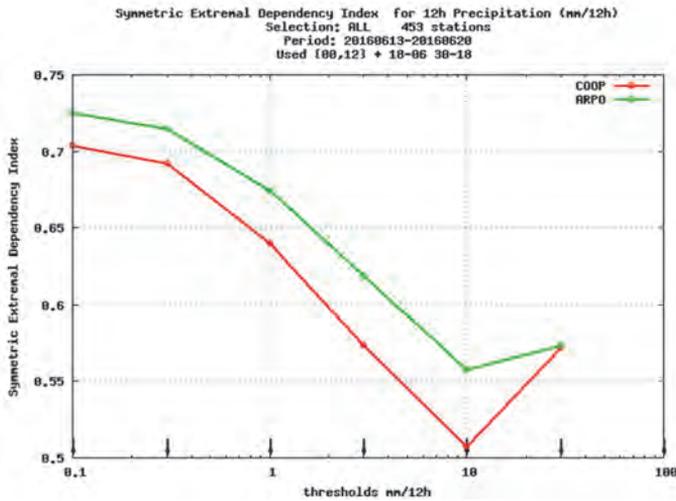
Fig. 1. Symmetric extremal dependency index (SEDI) verification skill score for 12 h accumulated precipitation forecast comparing AROME operational (COOP) system without surface data assimilation and with AROME experiment using OI-main surface data assimilation (ARPO). Verification against conventional SYNOP observations (period June 13 to 20, 2016).

3.2. Simplified extended Kalman filter

The exact initialization of the soil variables is a very crucial point to provide precise numerical weather prediction (NWP) forecasts. Inaccurate soil moisture content and soil temperature can lead to significant forecast errors of the screen-level atmospheric variables, 2 m air temperature (T2M), and 2 m relative humidity (HU2M) (*Hess*, 2001). Several methods have been developed to minimize errors in soil parameters. In this study, SEKF proposed by *Mahfouf et al.* (2009) is tested using AROME/HU cy43t2. SEKF allows assimilation of both conventional (screen-level) and non-conventional (satellite) observations to produce surface analysis. ASCAT soil moisture and SPOT/VGT leaf area index (LAI) non-conventional satellite observations were assimilated by several authors (*Barbu et al.*, 2014; *Albergel et al.*, 2017; *Rüdiger et al.*, 2010). These studies demonstrated the benefit of joint assimilation of soil moisture and LAI by using the multi-patch

version of SURFEX. It was shown, that the assimilation worked effectively, but the impact of the assimilation on the vegetation phenology and the water and carbon fluxes varied from season to season.

In EKF, dynamically changing coefficients are used, and the analysis is obtained as:

$$x_a = x_b + \mathbf{K}\,(y - \mathcal{H}x_b),\tag{1}$$

$$\mathbf{K} = \mathbf{B}\mathbf{H}^\mathbf{T}(\mathbf{H}\mathbf{B}\mathbf{H}^\mathbf{T} + \mathbf{R}),\tag{2}$$

where x_a is the analysis (so-called control variables: TG1, TG2, WG1, WG2), x_b is the result of a previous model run, y is the observation (T2M, HU2M), $\mathcal{H}$ is the non-linear observation operator, which transforms control variables from model space into observation space. $\mathbf{H}$ matrix is the linearized observation operator, $\mathbf{K}$ is the Kalman-gain matrix that represents the relative importance of the error of the observation concerning the prior estimate. $\mathbf{B}$ and $\mathbf{R}$ are the covariance matrices of the background errors and the observation errors, respectively. In this study, the simplified version of the EKF, namely SEKF is used, meaning the background covariance matrix $\mathbf{B}$ does not evolve with time. The elements of $\mathbf{H}$ (called Jacobian matrix), are calculated by finite differences. Perturbing each component (x_j) of the control vector $\mathbf{x}$, the elements of matrix $\mathbf{H}$ are composed for each integration i:

$$\mathbf{H}_{ij} = \frac{\partial y_i}{\partial x_j}\,.\tag{3}$$

In this study, SEKF is used as control vectors of the water contents and temperatures of two soil layers (superficial (WG1, TG1) and root-zone (WG2, TG2)) propagated by SURFEX three-layer soil scheme (superficial 0-1 cm, root zone 0-2 m, and deep soil 2-3 m). The observation terms are screen-level T2M and HU2M. The Jacobian matrix is the following:

$$\mathbf{H} = \begin{matrix} \frac{\partial T2M}{\partial TG1} & \frac{\partial T2M}{\partial TG2} & \frac{\partial T2M}{\partial WG1} & \frac{\partial T2M}{\partial WG2} \\[2ex] \frac{\partial HU2M}{\partial TG1} & \frac{\partial HU2M}{\partial TG2} & \frac{\partial HU2M}{\partial WG1} & \frac{\partial HU2M}{\partial WG2} \end{matrix}\,.\tag{4}$$

The small perturbations (with magnitude 10^{-3} or less) lead to a good approximation of the linear behavior (*Mahfouf*, 2009), and the Jacobian perturbations are assigned 10^{-4} for the soil water content and 10^{-5} for the soil temperature in our configurations. The assimilation window is set to 3 hours. In the analysis cycle, SURFEX is run several times, firstly to get the reference forecast, then the perturbed runs of the control variables.

In this study, a test run was performed and validated. The experiment lasted from July 9 to 31, 2020 (starting with a 2-week spin up period from June 25, 2020). Forcing files were required for offline SURFEX runs (i.e., radiation, precipitation, wind, humidity, temperature, and pressure), which were coming from AROME/HU inline forecasts. The wind, humidity, temperature, and pressure values correspond to the lowest model level of AROME/HU, which is currently 9 m.

Pointwise verification was executed for both periods against SYNOP and TEMP observations. The verification of 2 m temperature forecasts shows a large improvement for the nighttime hours with SEKF, and the large warm bias during the nights was reduced considerably (*Fig. 2*). SEKF was able to improve the 2 m temperature analysis throughout the whole period (*Fig. 3,* left). However, its daytime forecasts over Hungary do not differ significantly from the OI-main ones (*Fig. 3*, right).
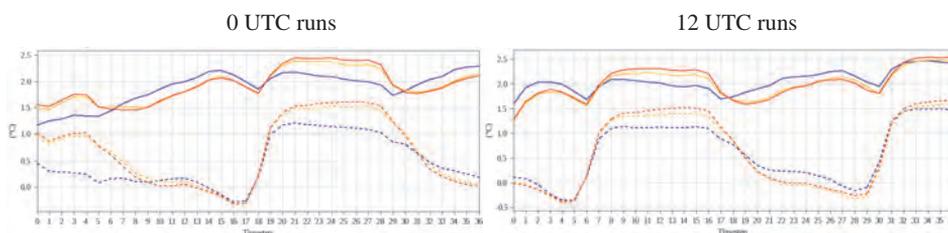
Fig 2. Bias (dashed line) and RMSE (solid line) of 2 m temperature forecasts in the 0 and 12 UTC runs from July 9 to 31, 2020. Blue: cy43 with SEKF, orange: cy43 with OI-main, red: cy40 with OI-main.
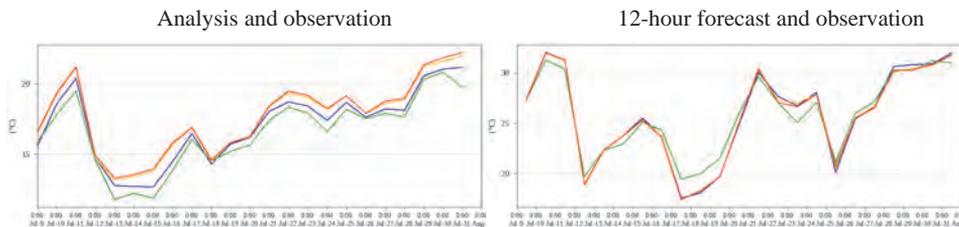
Fig. 3. Evolution of 2 m temperature analysis and 12-hour forecast in the 0 UTC runs and observations (green) from July 9 to 31, 2020. Blue: cy43 with SEKF, orange: cy43 with OI-main, red: cy40 with OI-main.

July 2020 had warm and overall rainy weather in the Carpathian Basin, where spatiotemporal distribution of precipitation was extreme. It is a typical problem in AROME/HU that the minimum temperature is usually overestimated and the maximum temperature is underestimated in the dry and warm anticyclonic periods. The case study of July 15, 2020 indicates that the 2 m temperature analysis was inaccurate using OI-main (*Fig. 4,* right). More accurate analysis was provided by SEKF, especially in the central part of the country (*Fig. 4,* middle). At the same time, the 12-hour forecast of SEKF resulted in an unrealistic warm pattern over the south part of the domain (*Fig. 5*, middle).
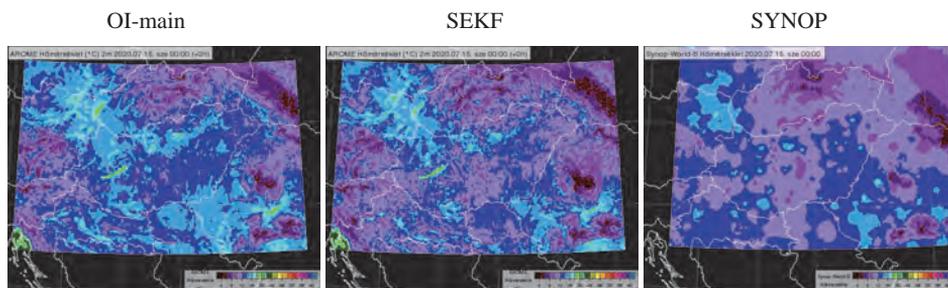
Fig. 4. 2 m temperature analysis in AROME/HU cy43 with OI-main and SEKF, observations at 0 UTC on July 15, 2020.
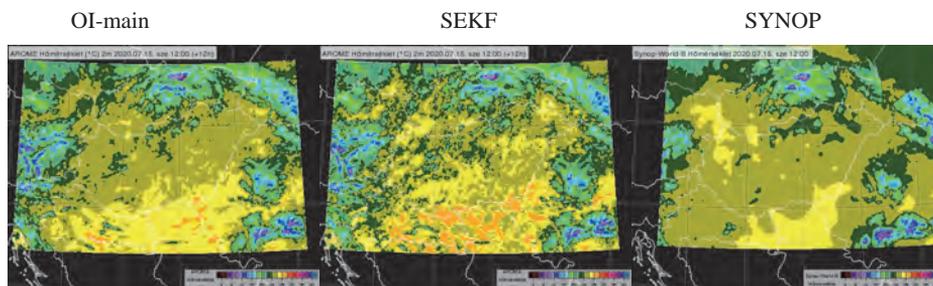
Fig. 5. 12-hour forecast of 2 m temperature in AROME/HU cy43 with OI-main and SEKF, observations at 12 UTC on July 15, 2020.

SEKF produced very dry soil in comparison with OI-main (*Fig. 6*). This issue is able to generate the above mentioned 2 m temperature overestimation in the south during the day.

OI-main   SEKF
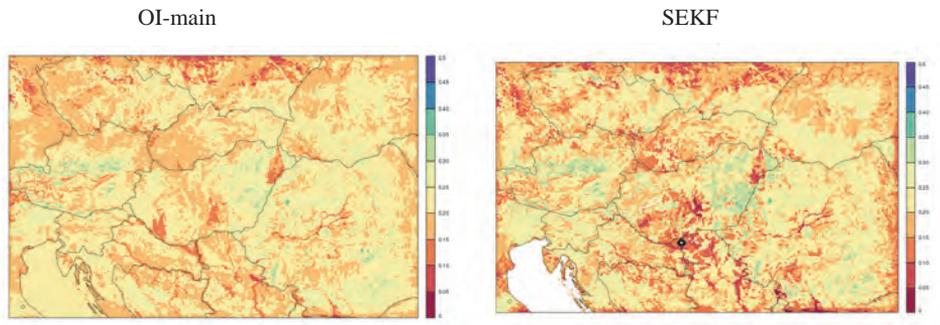
Fig. 6. Root-zone soil moisture (WG2) analysis at 0 UTC on 15 July, 2020 for OI-main and SEKF.

The evolution of WG2 analysis can be seen in *Fig. 7* for a given point marked with a black circle in *Fig. 6*. The soil moisture content decreased very rapidly by using SEKF, however, OI-main did not change drastically the soil moisture values. The main soil texture is sand (73%) in this area, so the soil moisture reflects immediately on the variability of the precipitation.
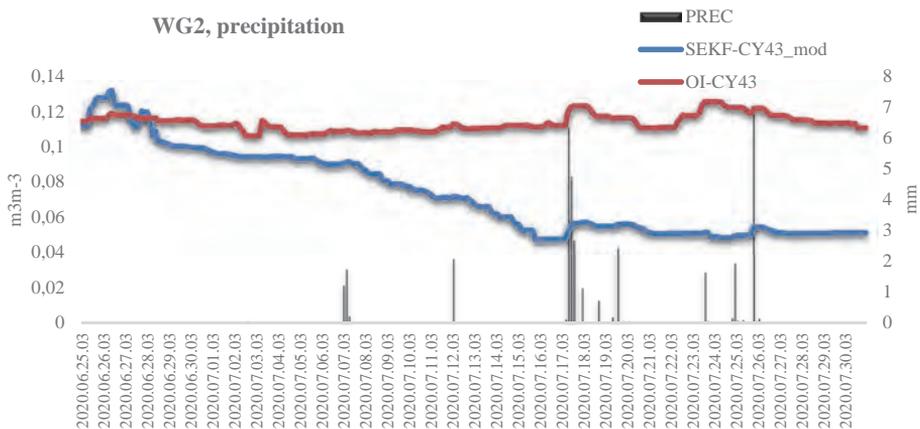
Fig. 7. Evolution of soil moisture (WG2) and precipitation (black) for SEKF (blue) and OI-main (red).

Fig. 8 shows analysis minus guess (A-G) increments for soil temperature and soil moisture in different analysis times summed for the whole period and all grid points over the domain. The TG2 increment is bigger for the nighttime and smaller for the daytime periods in the case of SEKF. For OI-main the TG2 increments are small and consistent. In contrast, the WG2 increments are large for daytime and smaller for nighttime for both methods. The WG2 increments are similar and comparable with each other.
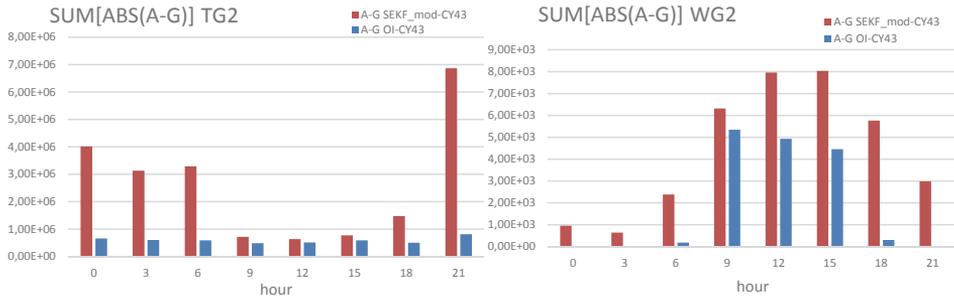
Fig. 8. Soil temperature (TG2) and soil moisture (WG2) increments for all of the grid points over the domain from July 9 to 31, 2020 for SEKF (blue) and OI-main (red).

To conclude, SEKF provides a positive impact on the analyses and the short-range forecasts as well. However, further investigations are still needed to find the best possible combination of the assimilation parameters, like observation, background errors, and the perturbation size of the Jacobians.

4. Upper-air data assimilation developments in AROME/HU model

4.1. Investigation of rapid update cycle

The main goal of the rapid update cycling (RUC) approach is to employ more observations with reduced representation error in time, which would serve as a basis for the enhancement of data assimilation by including radar data assimilation soon (*Mile et al.*, 2015). This study was carried out with AROME/HU cy40t1 with different assimilation window lengths. The cut-off time in the case of RUC was reduced to 30 minutes instead of 90 minutes, which is used in the operational 3-hourly updated DA cycle.

In this study, two 30-day test periods had been chosen. The first was a winter period covering all days between January 8 and February 6, 2017. The second period was a spring period from May 4 to June 2, 2019, including numerous

convective events inside the model domain. Each model run had started at 0, 6, 12, and 18 UTC analyses and performed 12-hour forecasts. The assimilation cycle was started six days earlier than the first long forecast to provide an appropriate first guess field for the beginning of the experiments. Some modifications were made in the configuration settings, e.g., the assimilation cycle frequency was set to 1 hour and the cut-off time was shrunk to +/-30 minutes accordingly. Meanwhile, the surface assimilation cycle frequency was set to be adjustable, i.e., in these experiments 1-, 3-, and 6-hourly updated surface data assimilation were applied. In the last two experimental setups, (called *AROME_combo_1hourly_surf3,* and *AROME_combo_1hourly_surf6* hereafter), the asynoptic surface analyses were initialized from previous model forecasts without taking into account surface observations. The following four configurations were tested for both periods:

- *AROME_3hourly* represents the original settings of operational AROME/HU;

- *AROME_1hourly* represents 1-hourly DA cycle for 3D-Var and surface data;

- *AROME_combo_1hourly_surf3* consists of a combination of 1-hourly updated upper-air assimilation cycle with 3D-Var and 3-hourly updated surface assimilation cycles with surface data;

- *AROME_combo_1hourly_surf6* is the same as *AROME_combo_1hourly_surf3* but the surface assimilation is updated every 6 hours.

To evaluate the results provided by four configurations, two different verification approaches were applied. Standard verification methods (RMSE, bias) were used for 2 m temperature forecasts (*Figs. 9–10*), and SAL verification method was used for precipitation in the spring case. SAL verification method provides an objective quality measure for forecasted precipitation fields compared to radar observations as three distinct components are used, namely structure, amplitude, and location (*Wernli et al.,* 2008). In order to get a comprehensive picture of all three components, the central statistic approach was applied (*Table 2*). Better performing cases are closer to the center, therefore, a given percentage of cases (5%, 10%, 20%, and 50%) can be covered by a shorter radius.

The results suggest that *AROME_1hourly* performs better than *AROME_3hourly* in the case of 2 m temperature and dew point temperature. Higher accuracy was provided by reduction of surface assimilation cycle frequency (*AROME_combo_1hourly_surf3, AROME_combo_1hourly_surf6*).

Meanwhile, considering precipitation, there is no significant difference between the configurations as SAL verification shows balanced performance for each setting (*Table 2*).
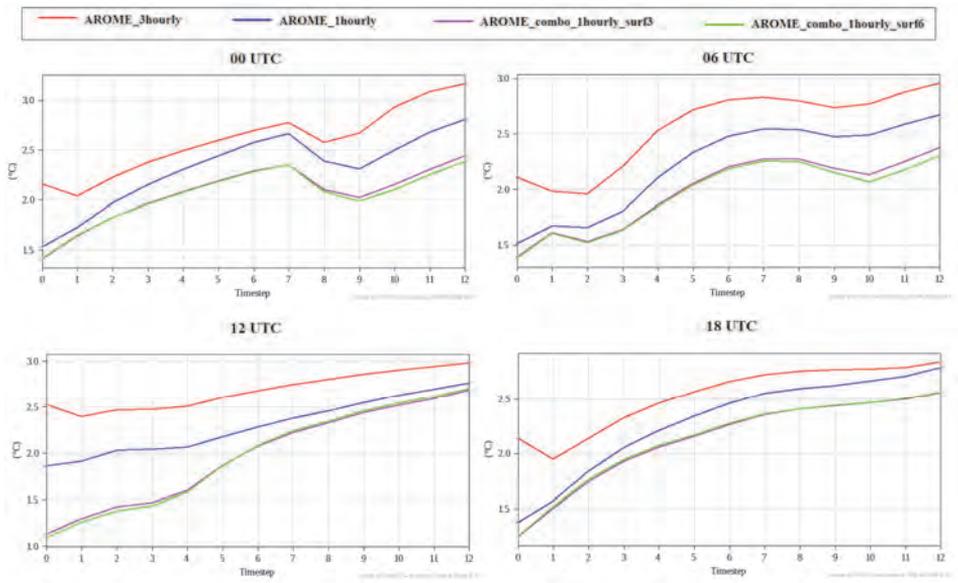
Fig. 9. RMSE of 2 m temperature for each configuration in the function of lead-time in the winter period.
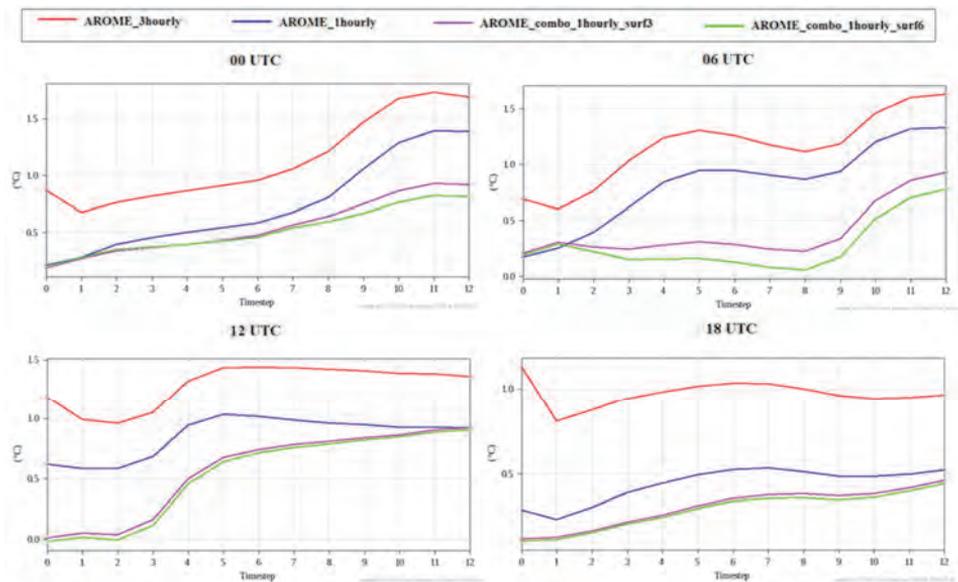
Fig 10. Bias of 2 m temperature for each configurations in function of lead-time in winter period.

Table 2: SAL results of each configuration for spring case. Lower radius values indicate better performance on precipitation forecasts. Green cells represent the best performance, redcells respresent the worst.

	00 UTC				06 UTC			
	5%	10%	20%	50%	5%	10%	20%	50%
AROME_3hourly	0.282	0.391	0.570	0.992	0.382	0.475	0.666	1.037
AROME_1hourly	0.276	0.365	0.506	1.075	0.297	0.454	0.666	1.026
AROME_combo_1hourly_surf3	0.274	0.373	0.578	1.117	0.325	0.492	0.652	1.051
AROME_combo_1hourly_surf6	0.261	0.410	0.570	1.128	0.369	0.484	0.655	1.016
	12 UTC				18 UTC			
	5%	10%	20%	50%	5%	10%	20%	50%
AROME-3hourly	0.366	0.447	0.665	1.096	0.357	0.534	0.684	1.157
AROME-1hourly	0.358	0.450	0.625	1.052	0.379	0.514	0.768	1.216
AROME-1hourly_surf3	0.307	0.424	0.648	1.094	0.369	0.484	0.643	1.159
AROME-1hourly_surf6	0.302	0.442	0.647	1.111	0.314	0.446	0.642	1.216

The biggest difference between the configurations can be seen on January 29, 2017. *AROME_3hourly* has more than five degrees Celsius RMSE, but *AROME_combo_1hourly_surf3* and *surf6* have only around one degree Celsius RMSE (*Fig. 11*). On this particular day (*Fig. 12*), the big difference in the RMSE, in favor of *AROME_combo_surf3* can be explained by the lack of cloud cover in *AROME_3hourly* and *AROME_1hourly* (*Fig. 13*). This usually happens in the Carpathian Basin when low-level clouds develop and remain during wintertime. In this situation, the NWP models usually are not able to serve accurate forecasts.
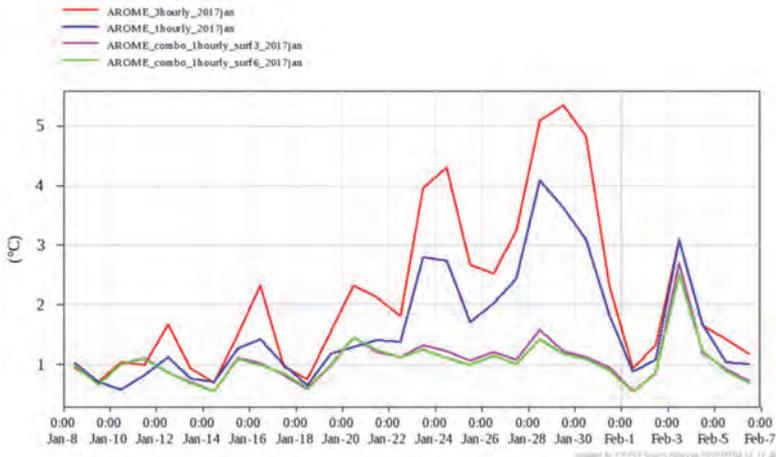
Fig. 11. RMSE of 2 m temperature for 12 UTC runs at 0 time step.
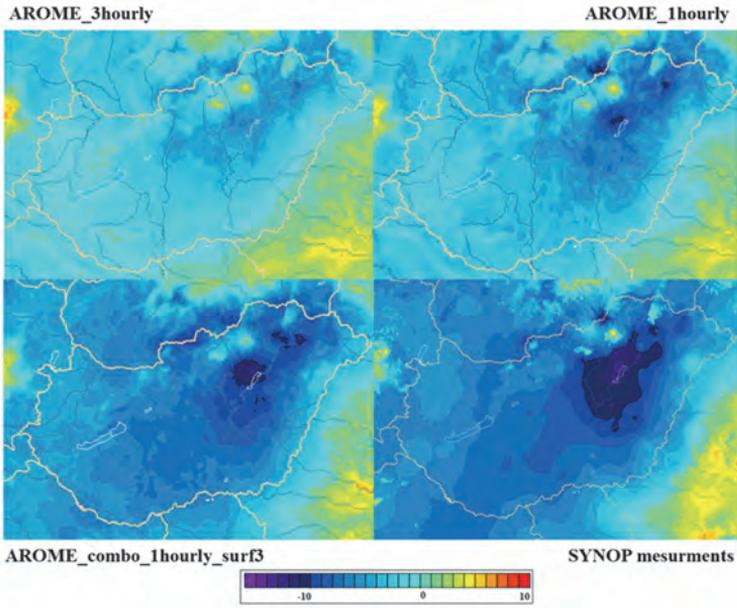
Fig. 12. Temperature fields provided by different configurations comparing to measurements at 12 UTC, on January 29, 2017.
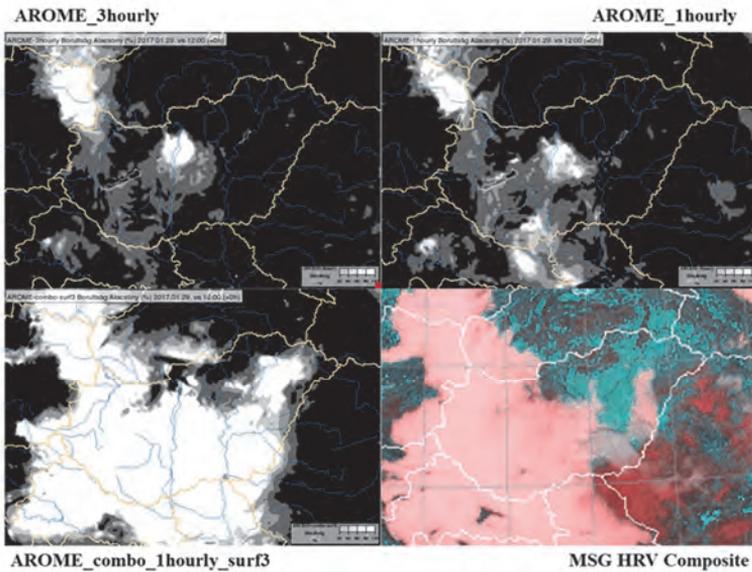
Fig. 13. Cloud cover fields provided by different configurations comparing to satellite observation at 12 UTC, on January 29, 2017.

Further examination was performed with increments of soil temperature (TG1, TG2) and soil moisture (WG1, WG2) in order to get a clear picture of the unexpected behavior of the model. The increments and soil variables were examined from January 18 to 31, 2017. Soil temperature increments looked normal, however, soil moisture increments were 0 during the whole period (not shown). This means, that the soil moisture was driven by the model only, no actual correction by the assimilation was performed, meanwhile, all configurations yielded different soil moisture contents. Further investigation is necessary to get the final conclusions.

4.2. Impact of Aircraft Mode-S MRAR data in AROME/HU

High resolution and high-density aircraft data are important and unmissable to improve the data assimilation system. Mode-S MRAR data can be used similarly to conventional AMDAR data and have similar quality as well. They are gathered through interrogation of suitable aircraft using specific (Mode-S TAR) radars, which means that only aircraft equipped with Mode-S transponders is able to return meteorological data. Smaller fraction of aircrafts is equipped for MRAR data, which contains specific meteorological parameters, like temperature and wind, but this relatively small amount of data is extremely valuable for data assimilation, as it contains meteorological data of similar quality as that of AMDAR data (*Strajnar*, 2012).

For the AROME/HU model, Slovenian Mode-S MRAR data was the first available for assimilation purposes. These observations are disseminated through the common preprocessing platform OPLACE (*Trojáková et al.*, 2019) since 2015. The first experiments in Hungary have started in the following year. In a case study, improved precipitation fields were experienced, and over a longer period, results showed mainly neutral impact with some improvement in the bias of wind gust and ETS score of precipitation. These data were introduced operationally at the end of 2016. Since 2019, Mode-S MRAR data from the Czech Republic are also available in OPLACE, which are also ready for assimilation. In case of Hungarian measurements, the air traffic control provided raw data, which has to be preprocessed in the first step. *Fig. 14* shows the area covered by the various Mode-S data.
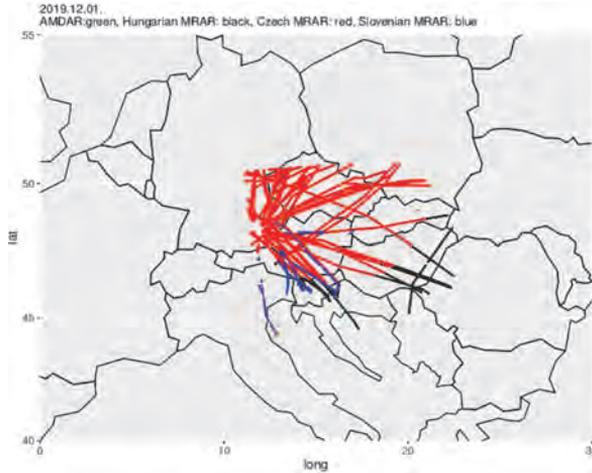
Fig. 14. Mode-S data collected by the Czech (red), Hungarian (black), and Slovenian (blue) radars over the AROME/HU domain.

4.2.1. Impact of Czech Mode-S data in AROME/HU

Two experiments were carried out to investigate the impact of Czech Mode-S MRAR data assimilation on the quality of the forecast. The first experiment covered a winter period (December 1 to 19, 2019), while the second one covered a summer period (June 1 to 30, 2020). Both experiments were based on the operational AROME/HU and the only difference was the inclusion of Czech Mode-S data, obtained from the OPLACE server. The two experiments differ from each other in regards to the forecast length (24 and 36 hours for the winter and summer periods, respectively) and the run hours (0, 6, 12, and 18 UTC runs in the winter experiment, and 0, 9, and 12 UTC runs in the summer experiment).

Observation monitoring shows that only a small fraction of the total number of Czech Mode-S data is active in the experiments (*Fig. 15*), which is likely due to the horizontal thinning. In the case of the winter experiment, the number of active Czech Mode-S data is very similar to the number of AMDAR data, which makes a reasonable comparison of their impact. In the case of the summer experiment, however, the number of Czech Mode-S observations is extremely low (*Fig. 15*), including several days with zero observations. This probably indicates the severe effect of the COVID-19 pandemic on the number of flights, and makes it much more difficult to evaluate the summer experiment.

It can be concluded that the assimilation of Czech Mode-S data improves slightly the forecast skill of AROME/HU. *Fig. 15* shows that the impact of the Mode-S dataset was quite substantial for specific days, at least for the summer period, but the difference is usually much smaller.

538
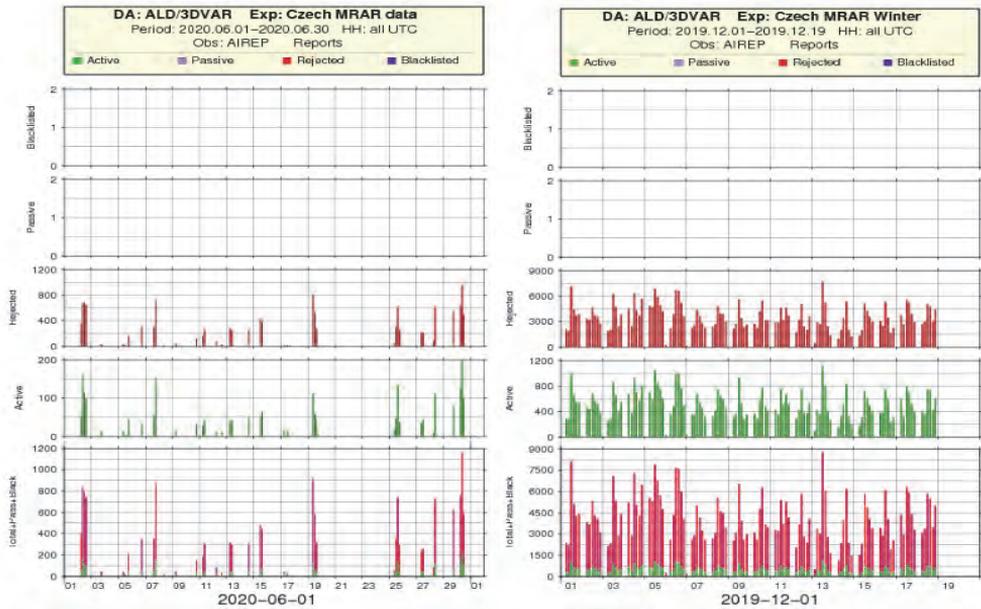
Fig. 15. Number of Czech Mode-S MRAR data over the AROME/HU domain for the summer (left) and the winter (right) experiment. Green and red columns represent the active and rejected observations, respectively.

Pointwise verification was performed for both periods against SYNOP and TEMP observations. The verification results show small improvement for the winter period, when scores are usually very close to the operational ones, although a slight improvement can be detected in most of the cases. A remarkable, albeit small positive impact can be seen in precipitation forecasts (*Fig. 16*).
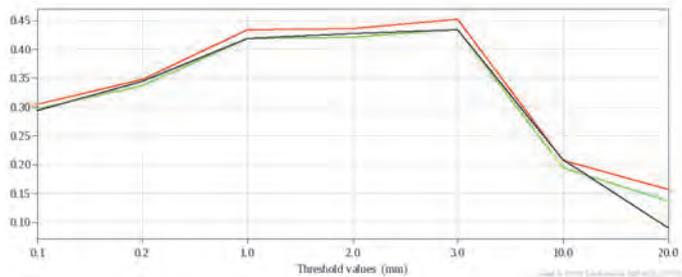
Fig. 16. ETS score of 12-hour accumulated precipitation in the 18 UTC runs from December 1 to 19, 2019. Red line: experiment with Czech Mode-S data, black line: experiment with Hungarian Mode-S data, green line: reference experiment without any Mode-S data.

For the summer period, the results are more varied, and show greater differences compared to the ones seen in the winter period. This can be attributed to the fact that there was a much greater amount of precipitation in the summer period. A case study of a convective event also shows that in specific cases, the inclusion of Mode-S data can significantly improve the precipitation forecast, especially regarding the spatial distribution of the amount of precipitation (*Fig. 17*). Verification scores are overall neutral, but in some cases, a significant improvement was obtained, especially for precipitation (*Fig. 18*). Other surface variables, however, show little or no improvement (not shown), therefore, the results are quite similar to the ones seen in the winter experiment.
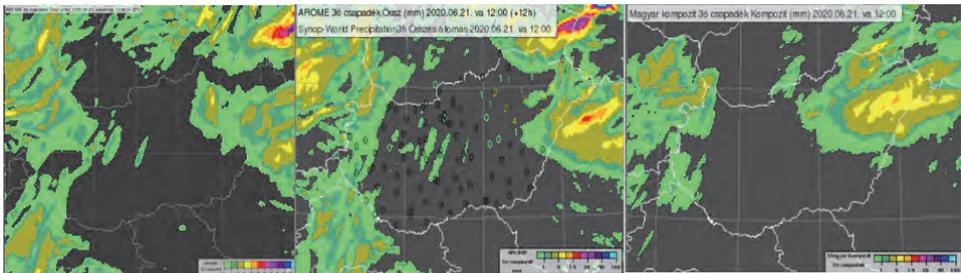
Fig. 17. 3-hour precipitation forecast of the experiment using Mode-S data (left), reference run (middle), and the observed precipitation (right) at 12 UTC, on June 21, 2020.
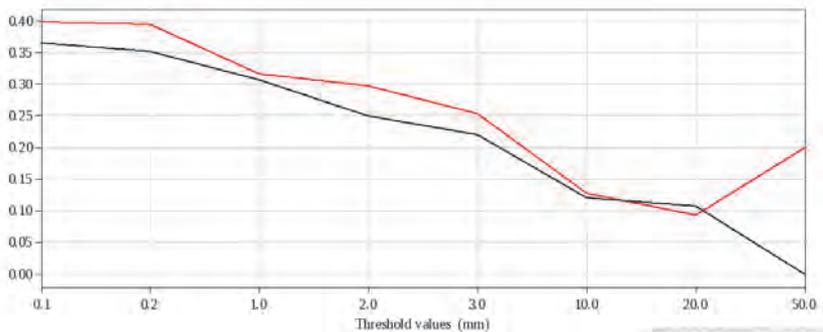
Fig. 18. ETS score of 12-hour accumulated precipitation in the 9 UTC runs from June 1 to 30, 2020. Red line: experiment with Czech Mode-S data, black line: reference run.

Regarding the upper-air variables, verification results are similarly varied. The inclusion of Mode-S MRAR data improves the forecast of some upper-air variables considerably, such as wind speed on different atmospheric levels

(*Fig. 19*), but in most cases, the improvement is smaller. Other variables, such as upper-air temperature or relative humidity show similar improvement, but in some cases, the verification results for these variables are worse than those yielded by the reference run.
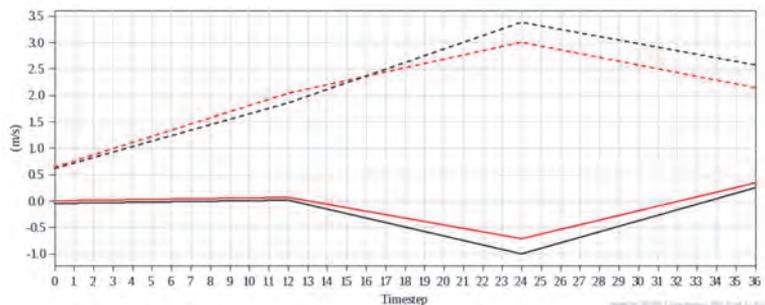
Fig. 19. Bias (solid line) and RMSE (dashed line) of 500 hPa wind speed in the 12 UTC runs from June 1 to 30, 2020. Black and red lines represent the reference run and the experiment using Mode-S data, respectively.

In conclusion, the assimilation of Czech Mode-S MRAR data has a small, but in most cases positive (or neutral) impact on AROME/HU forecasts. In the case of the summer experiment, the small differences can be attributed to the low number of active observations. The impact is greater at the upper atmospheric levels (for both experiments), while smaller on the surface. The assimilation of the Czech Mode-S MRAR data has been introduced operationally in AROME/HU from March 2021.

4.2.2. Impact of the Hungarian Mode-S MRAR dataset in AROME/HU

As a result of the positive experience with the Czech MRAR dataset, the Hungarian MRAR observations have also been investigated. Since the collection of Hungarian Mode-S data was started in November 2019, a proper preprocessing was needed on the raw dataset before their assimilation trial. Our first test period covered by the Hungarian MRAR data was between November 25, 2019 and March 31, 2020. First, a format conversion of the dataset was necessary to share the same format as other MRAR data distributed by the OPLACE system. Then a statistical quality filtering was applied, i.e., whitelisting procedure using an adopted criteria system through a passive assimilation cycle (*Table 3*). We only modified the minimum number of the measured data according to the flight numbers in the Hungarian flight area (*Table 4*).

Table 3. The applied whitelisting criteria.

	Temperature	Wind speed	Wind direction
Mean	1 K	1 m/s	10°
Standard deviation	2 K	5 m/s	100°
Minimum number of observations	1000	1000	1000

Table 4: Changes in the number of measurements and flights due to the whitelisting. Test period: November 25, 2019 to March 31, 2020.

	Temperature	Number of flights	Wind (speed and direction)	Number of flights
Total number	799452	238	798904	238
After statistical check	741480 (92.7%)	114	740962 (92.7%)	114
After quality check	577700 (72.3%)	75	507576 (63.5%)	61

The test forecasts with the quality-controlled MRAR dataset were running between December 1 and 18, 2019. Significant part of the Hungarian MRAR data has been rejected in the assimilation, only a few hundreds of them remained.

Only small differences have been detected in comparison with the reference upper air wind forecasts, which are more apparent in the 12 UTC runs, when there are more flights (*Fig. 20*). The use of Hungarian Mode-S MRAR data has a positive impact on the 2 m temperature and relative humidity analyses leading to small improvements in precipitation, relative humidity, total cloud cover, and wind gust forecasts. For other forecast variables, the impact is rather neutral.
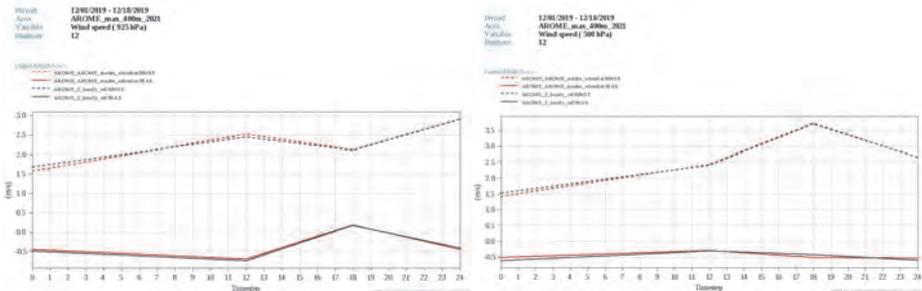
Fig. 20. RMSE (dashed line) and bias (solid line) of wind speed forecasts (left: 925 hPa, right: 500 hPa) at the 12 UTC runs with assimilated Hungarian Mode-S measurements (red) and reference forecast (black) for December 1-18, 2019.

542

To introduce the Hungarian Mode-S MRAR data into the operational assimilation, a further experiment is necessary on a period not (or less) affected by the pandemic.

4.3. Impact of AMDAR-humidity in AROME/HU

In 2015 and 2016, nine Lufthansa aircrafts were equipped with WVSS-II humidity sensors (*WMO*, 2019), and the measured data became part of the standard AMDAR report. As upper-air humidity observations in the assimilation system of AROME/HU are currently limited to radiosondes and GNSS ZTD, AMDAR-humidity data is important, especially, during the ascending or descending phases when the vertical humidity structure of the atmosphere is measured by the aircraft. The first experiments with AMDAR-humidity at OMSZ began in early 2016, and it was included in the operational assimilation system of AROME/HU in autumn 2016.

The impact of AMDAR-humidity on AROME forecasts was tested on a summer and winter period of one month each and on selected case studies. Verification scores show a generally neutral impact. Some small improvements can be observed for cloud cover in the first forecast hours and for upper-air humidity, especially for forecasts starting at 9 and 15 UTC, when no radiosonde observations are available on the AROME/HU domain (not shown).

Radiosonde and aircraft humidity data were compared when both observation types were available. Visual check of vertical profiles shows a good agreement between the two measurements (not shown). When a single specific humidity profile from AMDAR report was assimilated, the vertical profiles of the first guess and the analysis indicated that the humidity profile is closer to the observations, but without these measurements this is not the case (*Fig. 21*).
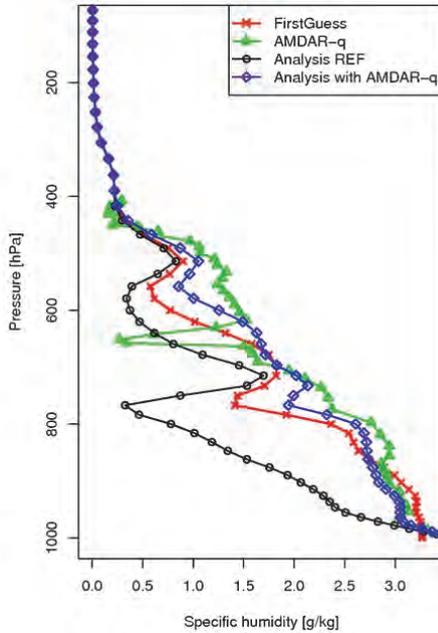
Fig. 21. Vertical profiles of specific humidity of AMDAR (green), first guess (red), analysis without AMDAR-q (black), and analysis with AMDAR-q (blue) at 18UTC, on March 25, 2016 over Budapest.

For case studies involving convection, impact of AMDAR-humidity can be more pronounced. *Fig. 22* shows AROME/HU forecasts for a day with intense summer convection. It can be noted that AMDAR-humidity improves the forecast of convective precipitation in the first forecast hours: convective cells missing in the control run over the southern part of Hungary are well forecasted in the run using AMDAR-humidity.
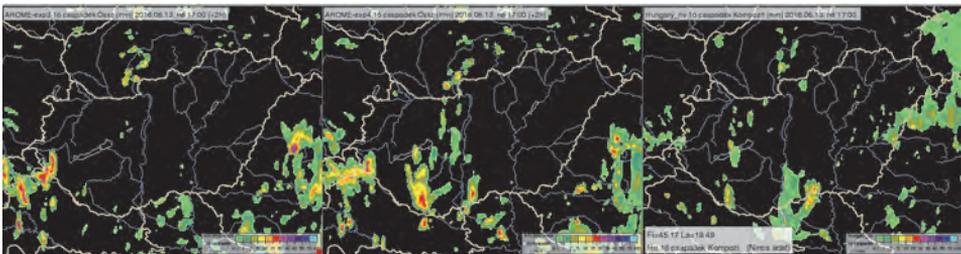
Fig. 22. Hourly precipitation sums at 17 UTC, on June 13, 2016. Right: Radar observation; left: AROME/HU run without AMDAR-humidity; middle: AROME/HU run with AMDAR-humidity (both forecasts started at 15 UTC on the same day).

Due to the COVID-19 pandemic in 2020, the air traffic has changed dramatically, which has affected the density of AMDAR data, as well as the quality of the forecasts (*Ingleby et al.*, 2020). As *Fig. 23* shows, a few measurements arrived over the AROME/HU domain during the European springtime lockdown, and although the number of observations began to increase during the summer, it has been gradually decreasing since autumn. Only a few aircraft are equipped with humidity sensors, so in the current situation, unfortunately, AMDAR humidity observations can be assimilated very rarely in the model.
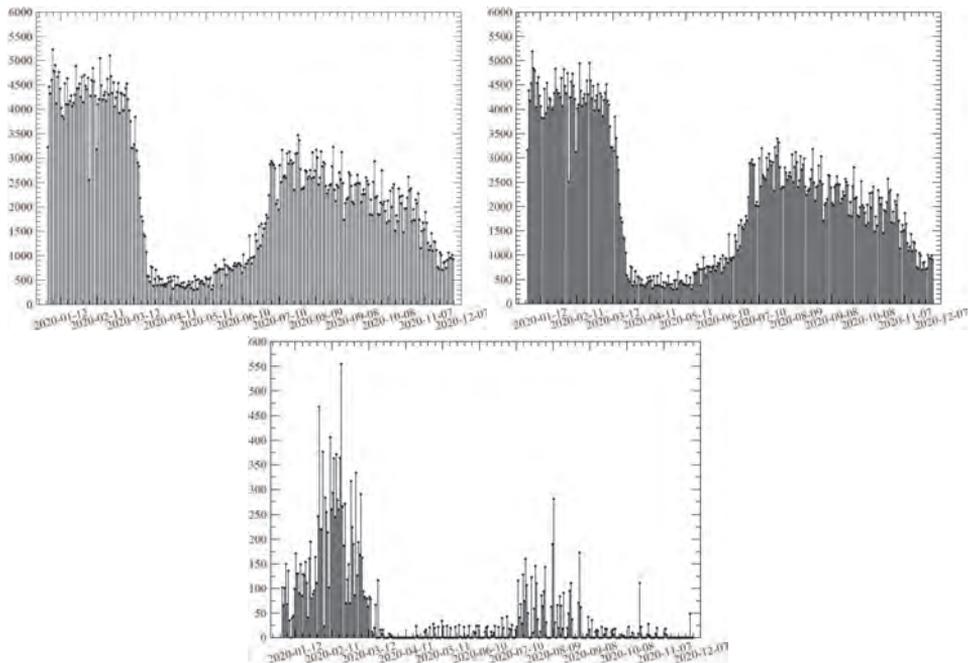
Fig. 23. Temperature (upper left), wind (upper right), and humidity (bottom) measurements over AROME/HU domain based on AMDAR reports from January to December, 2020.

4.4. Impact of atmospheric motion vectors

Atmospheric motion vectors (AMV) are retrieved from consecutive satellite images tracking coherent features thus estimating atmospheric wind at certain levels. AMVs have been used in data assimilation since the 1990s (*Schmetz et al.*, 1993). The European Organization for the Exploitation of Meteorological Satellites (EUMETSAT) provides hourly AMV products (geowind from now on)

using Meteosat Second Generation (MSG) visible, water-vapor, and infrared channel data (*Borde et al.*, 2014). These data are routinely received and preprocessed for OPLACE at the Hungarian Meteorological Service (OMSZ).

The Satellite Application Facility on Nowcasting and Short-Range Forecasting (NWCSAF) provides a software package to calculate products supporting nowcasting locally. One of these products is the high resolution wind (HRW) (*Garcia-Perada*, 2018) which is generated at OMSZ. HRW (from now on hrwind) is calculated using MSG visible, water-vapor, and infrared channel data.

AMVs are successfully used in both global and regional NWP models (*Forsythe et al.*, 2014). OMSZ has been operationally assimilating geowind in ALADIN-HU for many years (*Randriamampianina*, 2006). Experimental assimilation of both geowind and hrwind data were made in AROME/HU for different periods using the same settings described in *Mile et al.,* (2015). During the spring and summer experiments, we observed a very small, mostly neutral impact of the AMV data for the surface parameters (temperature, humidity, wind, pressure – not shown). In the convective period, a small, rather positive effect can be seen for the surface wind gust (*Fig. 24*).
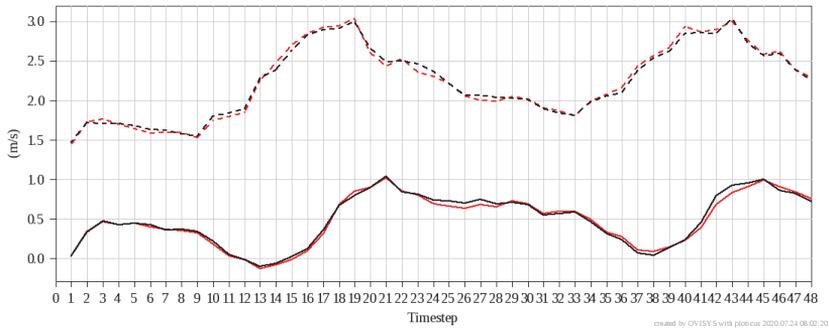
Fig. 24. Bias (solid line) and RMSE (dashed line) of wind gust forecasts in the 0 UTC runs from July 5 to August 7, 2019 as a function of lead time. Red and black lines: AROME/HU with and without AMVs, respectively.

In the precipitation, larger differences could be observed with and without AMVs. *Fig. 25* shows the SEDI parameter of 24-hour precipitation amount. For days with very small and large precipitation amounts, a positive impact can be seen, while for moderate precipitation amounts, the reference model run performed better.
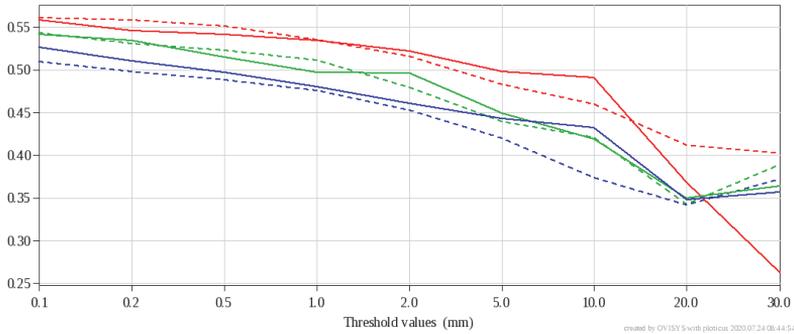
Fig. 25. SEDI of 24-hour precipitation forecasts in the 0 and 12 UTC runs from July 5 to August 7, 2019 as a function of precipitation amount at 24 (red), 36 (green), and 48 (blue) time steps. Dashed and solid lines: AROME/HU with and without AMVs, respectively.

In *Fig. 26* an example is shown, where cells with small precipitation were better formed when AMVs were assimilated. In this case, both the reference and the test version struggled to forecast the right location of the precipitation.
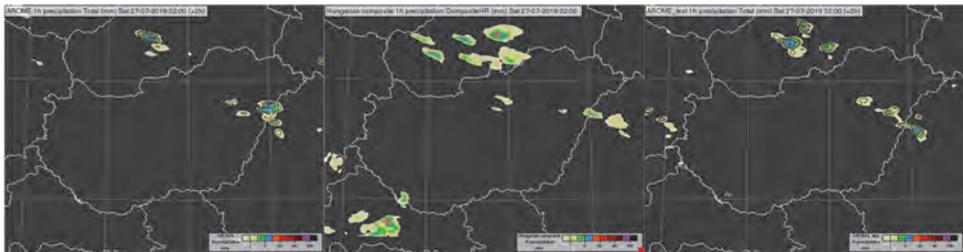
Fig. 26. 2-hour forecast of hourly precipitation without (left) and with (right) AMVs at 2 UTC, on July 27, 2019. Hourly precipitation sum based on radar data at 2 UTC, on July 27, 2019 (middle).

For the winter period, the impact of the used AMVs was mostly neutral for the surface pressure, wind speed, and wind gust. For the 2 m temperature and dew point, we observed a slightly negative effect (*Fig. 27*). Verification for the vertical levels was also done, where we could see a positive impact on wind speed (*Fig. 27*). However, since only a small number of radiosonde measurements are available besides 0 and 12 UTC over AROME/HU, the significance level of those results is not very high.
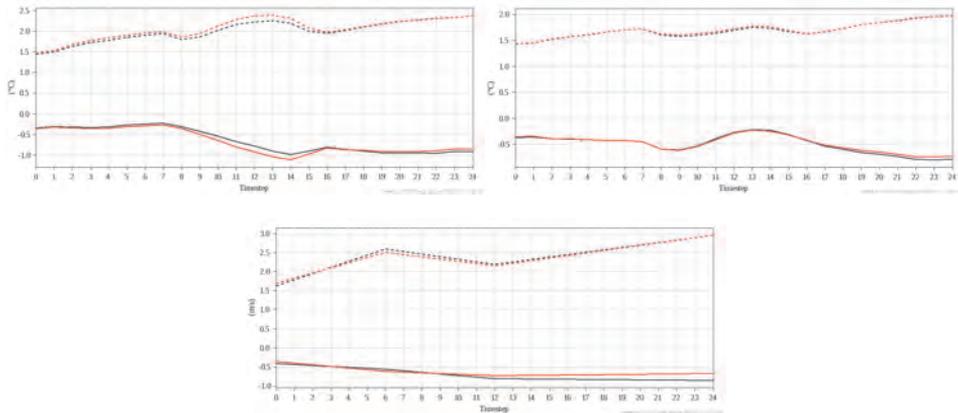
Fig. 27. Bias (solid line) and RMSE (dashed line) of 2 m temperature (upper left), dew point (upper right), and wind speed at 500 hPa (bottom) forecasts in the 0 UTC runs from December 1 to 18, 2019 as a function of lead time. Black and red lines: AROME/HU without and with AMVs, respectively.

For all experiments, the used blacklisting settings (*Mile et al.*, 2015) caused a relatively low number of active AMVs (*Fig. 28*). Additional experiments were configured and run to increase the number of active AMVs, and to check their distribution and characteristics. One experiment (called AMV8 hereafter) was for the activation of mid-tropospheric AMVs, which data were blacklisted a long time ago assuming their height assignment is less accurate, and another experiment (called AMVA hereafter) was carried out to allow even more previously blacklisted data into the assimilation system. *Table 5* describes the different settings and blacklisting details.
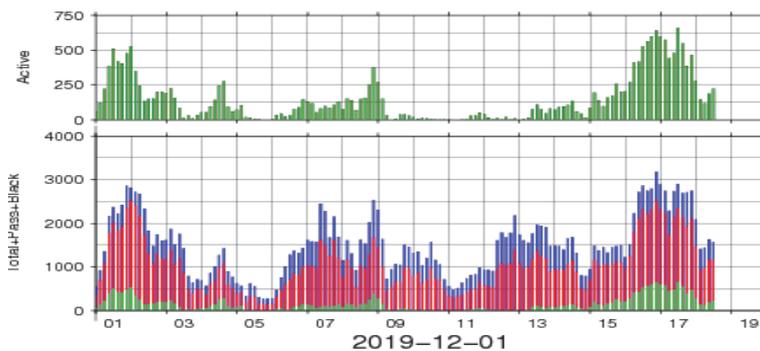
Fig. 28. Number of AMV observations over the AROME/HU domain from December 1 to 18, 2019. The numbers of blacklisted, rejected, and active observations are shown with blue, red, and green color.

548

Table 5: Blacklisting settings.

Setting	Reference	AMV8	AMVA
Quality index < 85 %	inactive	inactive	inactive
Data where p>700 hPa over land	inactive	inactive	active
Data where p<700 hPa for VIS	inactive	inactive	active
Data between 300 and 850 hPa	inactive	active	active
Data where p>400 hPa for WV	inactive	inactive	active

Fig. 29 shows that both AMVA and AMV8 runs activated more AMVs than the reference. AMVA uses more observation at lower levels, which may result in discrepancies due to orography. Observation minus background (O-B) statistics show no suspicious feature between 800 and 350 hPa (*Fig. 30*), so proceeding with AMV8 settings seems to be a better choice in the future.
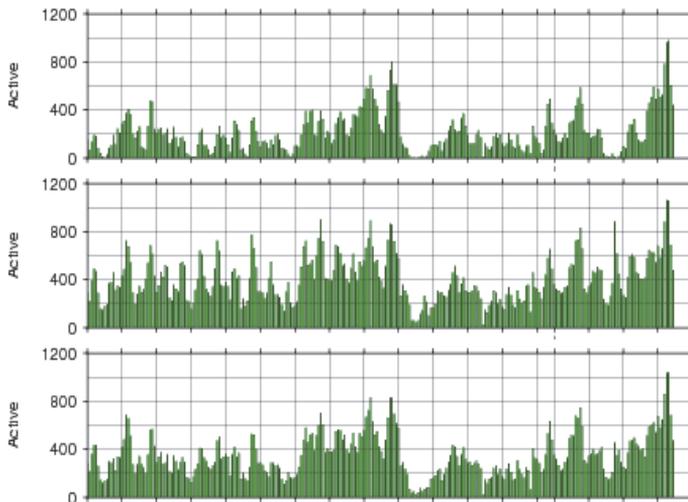
Fig. 29. Number of active AMV observations over the AROME/HU domain from July 5 to August 7, 2019 for the initial experiment (top), for experiment AMVA (middle), and for experiment AMV8 (bottom).
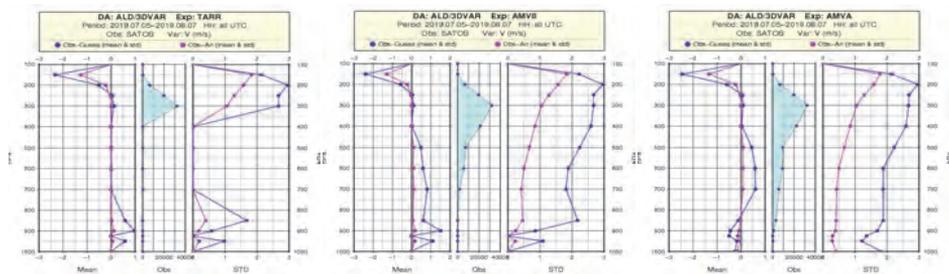
Fig. 30. The vertical distribution of the active observations for the initial experiment (left), for experiment AMV8 (middle), and for experiment AMVA (right) over the AROME/HU domain from July 5 to August 7, 2019.

5. Summary and conclusions

The latest developments of the AROME/HU data assimilation system were shown in this paper. First of all, the current operational DA system was described with a focus on the locally assimilated observations and special interest in the preparation mechanism of the analysis and forecast.

Then surface data assimilation developments were described. It was shown, that both the OI-main and the SEKF provided a positive impact on the screen-level parameters compared to the dynamical adaptation of AROME/HU, especially for nighttime periods. Very promising results were demonstrated by applying a 1-hour RUC configuration compared to the 3-hour ones. The reliability of the analyses and short-range forecasts were improved by employing more observations in the DA system. However, higher accuracy was provided by reduction of surface assimilation cycle frequency, the best results were found using a 3-hourly surface assimilation interval. Thereafter, upper-air DA impact studies were carried out using different kinds of observations to improve the analyses and forecasts. The impact of Czech and Hungarian Mode-S MRAR data assimilations was slightly positive or neutral regarding the analyses and the forecasts of surface parameters. The effect of AMDAR-humidity in AROME/HU forecasts was also tested, and generally, neutral impact was obtained. However, it can be noted that AMDAR-humidity improves the convective precipitation forecast in the first hours and helps to extend slightly the humidity related observations in the assimilation system. In addition to the assimilation of conventional data, non-conventional AMV data has been tested in AROME/HU DA system. Due to the outdated AMV blacklisting settings, an experiment was performed by the activation of mid-tropospheric AMVs to allow more data into the assimilation system. The upper-level innovation of this new experiment has shown promising results for further studies.

This paper indicated, that applying new methods, as SEKF, more frequent RUC, or increasing the number of new assimilated observations, like additional

aircraft or AMV observations, are future perspectives and powerful tools to improve the mesoscale analyses and forecasts. The AMDAR-humidity and the Czech Mode-S MRAR data are already part of the AROME 3D-Var operational system. The implementation of new, high resolution observations in the DA system, such as radar observations or satellite data, are becoming highly important, as the horizontal and vertical resolution of the meteorological model is continuously growing. In addition, we have to pay attention to modeling of the background error covariance matrix for the higher resolution model version, which is based on AROME ensemble DA method.

References

Albergel, C., Munier, S., Leroux, D. J., Dewaele, H., Fairbairn, D., Barbu, A. L., Gelati, E., Dorigo, W., Faroux, S., Meurey, C., Le Moigne, P., Decharme, B., Mahfouf, J.-F., and *Calvet, J.-C.*, 2017: Sequential assimilation of satellite-derived vegetation and soil moisture products using SURFEX_v8.0: LDAS-Monde assessment over the Euro-Mediterranean area, *Geosci. Model Dev. 10*, 3889–3912. https://doi.org/10.5194/gmd-10-3889-2017*

Barbu, A. L., Calvet, J.-C., Mahfouf, J.-F., and *Lafont, S.,* 2014: Integrated ASCAT surface soil moisture and GEOV1 leaf area index into the SURFEX modelling platform: a land data assimilation application over France, *Hydrol. Earth Syst. Sci. 18,* 173–192. https://doi.org/10.5194/hess-18-173-2014*

Benjamin, S.G., Dévényi, D., Weyandt, S.S., Brundage, K.J., Brown, J.M., Grell, G.A., Kim, D., Schwartz, B.E., Smirnova, T.G., Smith, T.L., and *Manikin, G.S.,* 2004: An hourly assimilation– forecast cycle: The RUC. *Mon. Weather Rev.,* 132, 495–518. https://doi.org/10.1175/1520-0493(2004)132<0495:AHACTR>2.0.CO;2*

Berre, L., 2000: Estimation of synoptic and mesoscale forecast error covariances in a limited area model. *Mon. Weather Rev. 128,* 644–667. https://doi.org/10.1175/1520-0493(2000)128<0644:EOSAMF>2.0.CO;2*

Borde, R.; Carranza, M.; Hautecoeur, O.; and *Barbieux, K.,* 2019: Winds of Change for Future Operational AMV at EUMETSAT. *Remote Sens. 11,* 2111. https://doi.org/10.3390/rs11182111*

Borde, R.; Doutriaux-Boucher, M.; Dew, G.; and *Carranza, M.*, 2014: A Direct Link between Feature Tracking and Height Assignment of Operational EUMETSAT Atmospheric Motion Vectors. *J. Atmos. Oceanic Technol. 31,* 33–46. https://doi.org/10.1175/JTECH-D-13-00126.1*

Bölöni, G., 2006: Development of a variational data assimilation system for a limited-area model at the Hungarian Meteorological Service. *Időjárás 110,* 309–327.*

Bölöni, G., Berre, L., and *Adamcsek, E.,* 2014: Comparison of static mesoscale background error covariances estimated by three different ensemble data assimilation techniques. *Q. J. Roy. Meteorol. Soc. 141,* 413–425. https://doi.org/10.1002/qj.2361*

Cardinali, C., Pezzuli, S., and *Andersson, E.,* 2004: Influence matrix diagnostic of data assimilation system. *Q. J. Roy. Meteorol. Soc. 130,* 2767–2786. https://doi.org/10.1256/qj.03.205*

Courtier, P., Thépaut, J.-N., and *Hollingsworth, A.,* 1994: A strategy for operational implementation of 4D-Var, using an incremental approach. *Q. J. Roy. Meteorol. Soc. 120,* 1367–1387. https://doi.org/10.1002/qj.49712051912*

Fischer, A., Homonnai, V., Mile, M., Sepsi, P., Szintai, B., and *Szűcs, M.,* 2017: Modelling activities at the Hungarian Meteorological Service. *ALADIN/HIRLAM Newsletter 8,* 64–68.

Fischer, A., Homonnai, V., Mester, M., Mile, M., Suga, R., Szintai, B., and *Szűcs, M.,* 2018: Modelling activities at the Hungarian Meteorological Service. *ALADIN/HIRLAM Newsletter 10,* 53–55.

Fischer, C., Montmerle, T., Berre, L., Auger, L., and *Ştefanescu, S.E.,* 2005: An overview of the variational assimilation in the ALADIN/France numerical weather-prediction system. *Q. J. Roy. Meteorol. Soc. 131,* 3477–3492. https://doi.org/10.1256/qj.05.115

Fischer, C., 2007: The variational computations inside ARPEGE/ALADIN: cycle CY32. http://www.umr-cnrm.fr/gmapdoc/spip.php?article11&var_lang=en, *18p*

Forsythe M, C Peubey, C Lupu, and J Cotton, 2014: Assimilation of wind information from radiances: AMVs and 4D-Var tracing, ECMWF Annual Seminar, September 2014, available in-line at: https://www.ecmwf.int/sites/default/files/elibrary/2015/9444-assimilation-wind-information-radiances-amvs-and-4d-var-tracing.pdf

García-Pereda, J., 2018: Algorithm Theoretical Basis Document for "High Resolution Winds" (NWC SAF/HRW v2018) https://doi.org/10.13140/RG.2.2.14679.91045

Giard, D. and *Bazile, E.,* 2000: Implementation of a New Assimilation Scheme for Soil and Surface Variables in a Global NWP Model. *Mon. Weather Rev. 128,* 997–1015. https://doi.org/10.1175/1520-0493(2000)128<0997:IOANAS>2.0.CO;2

Hágel, E., 2009: Development and operational application of a short-range ensemble prediction system based on the ALADIN limited area model. Ph. D. dissertation, Eötvös Loránd University, Faculty of Science, 127 p.

Hess, R., 2001: Assimilation of screen-level observations by variational soil moisture analysis. *Meteorol. Atmos. Phys. 77,* 145–154. https://doi.org/10.1007/s007030170023

Horányi, A., Ihász, I., and *Radnóti, G.,* 1996: ARPEGE/ALADIN: a numerical weather prediction model for Central-Europe with the participation of the Hungarian Meteorological Service. *Időjárás 100,* 277–301.

Ingleby, B., Candy, B., Eyre, J., Haiden, T., Hill, Ch., Isaksen, L., Kleist, D., Smith, F., Steinle, P., Taylor, S., Tennant, W., and Tingwell, Ch., 2020: The Impact of COVID-19 on weather forecasts: a balanced view. Geophys. Res. Lett. 48, e2020GL090699. https://doi.org/10.1029/2020GL090699

Jávorné Radnóczi, K., Várkonyi, A., and *Szépszó, G.*, 2020: On the way towards the AROME nowcasting system in Hungary. *ALADIN/HIRLAM Newslett., 14,* 65–69.

Lynch, P., D. Giard, and *V. Ivanovici,* 1997: Improving an efficiency of Digital Filtering Scheme for Diabatic Initialization. *Mon. Weather Rev. 125,* 1976–1982. https://doi.org/10.1175/1520-0493(1997)125<1976:ITEOAD>2.0.CO;2

Mahfouf J.-F., Viterbo P., Douville H., Beljaars A., and Saarinen S., 2000: A Revised land-surface analysis scheme in the Integrated Forecasting System. ECMWF Newslett. 88.

Mahfouf, J.-F., K. Bergaoui, C. Draper, F. Bouyssel, F. Taillefer, and *L. Taseva,* 2009: A comparison of two off-line soil analysis schemes for assimilation of screen level observations*, J. Geophys. Res., 114,* D08105. http://dx.doi.org/10.1029/2008JD011077 .

Masson, V., Le Moigne, P., Martin, E., Faroux, S., Alias, A., Alkama, R., Belamari, S., Barbu, A., Boone, A., Bouyssel, F., Brousseau, P., Brun, E., Calvet, J.-C., Carrer, D., Decharme, B., Delire, C., Donier, S., Essaouini, K., Gibelin, A.-L., Giordani, H., Habets, F., Jidane, M., Kerdraon, G., Kourzeneva, E., Lafaysse, M., Lafont, S., Lebeaupin Brossier, C., Lemonsu, A., Mahfouf, J.-F., Marguinaud, P., Mokhtari, M., Morin, S., Pigeon, G., Salgado, R., Seity, Y., Taillefer, F., Tanguy, G., Tulet, P., Vincendon, B., Vionnet, V., and Voldoire, A., 2013: The SURFEXv7.2 land and ocean surface platform for coupled or offline simulation of earth surface variables and fluxes. Geosci. Mod. Dev. 6, 929–960. https://doi.org/10.5194/gmd-6-929-2013.

Mile, M., Bölöni, G., Randriamampianina, R., Steib, R., and *Kucukkaraca, E.,* 2015: Overview of mesoscale data assimilation developments at the Hungarian Meteorological Service. *Időjárás 119,* 215–239.

Mile, M., Benáček, P., and *Rózsa, Sz.,* 2019: The use of GNSS zenith total delays in operational AROME/Hungary 3D-Var over a central European domain. *Atmos. Meas. Tech. 12,* 1569–1579. https://doi.org/10.5194/amt-12-1569-2019

Noilhan, J. and *S. Planton,* 1989: A simple parameterization of land surface processes for meteorological models. *Mon. Weather Rev. 117,* 536–549.
https://doi.org/10.1175/1520-0493(1989)117<0536:ASPOLS>2.0.CO;2

Noilhan, J. and *Mahfouf, J.-F.,* 1996: The ISBA land surface parameterisation scheme. *Glob. Planet. Change 13,* 145–159. https://doi.org/10.1016/0921-8181(95)00043-7.

Parrish, D.F. and *Derber, J.C.,* 1992: The National Meteorological Center's spectral statistical interpolation analysis system. *Mon. Weather Rev. 120,* 1747–1763.
https://doi.org/10.1175/1520-0493(1992)120<1747:TNMCSS>2.0.CO;2

Randriamampianina, R.., 2006: Impact of high resolution observations in the ALADIN/HU model. *Időjárás 110,* 329–349.

de Rosnay, P., Drusch, M., Vasiljevic, D., Balsamo, G., Albergel, C., and *Isaksen, L.*, 2013: A simplified Extended Kalman Filter for the global operational soil moisture analysis at ECMWF. *Q. J. Roy. Meteorol. Soc. 139,* 1199–1213. https://doi.org/10.1002/qj.2023

Rüdiger, C., C. Albergel, J.-F. Mahfouf, J.-C. Calvet, and *J. P. Walker,* 2010: Evaluation of the observation operator Jacobian for leaf area index data assimilation with an extended Kalman filter, *J. Geophys. Res. 115,* D09111. https://doi.org/10.1029/2009JD012912

Schmetz J, Holmlund K, Hoffman J, and *Strauss B*., 1993: Operational cloud-motion winds from Meteosat infrared images. *J. Appl. Meteorol. 32,* 1206–1225.
https://doi.org/10.1175/1520-0450(1993)032<1206:OCMWFM>2.0.CO;2

Seity, Y., Brousseau, P., Malardel, S., Hello, G., Bénard, P., Bouttier, F., Lac, C., and Masson, V., 2011: The AROME-France Convective-Scale Operational Model. Mon. Weather Rev. 139, 976–991.
https://doi.org/10.1175/2010MWR3425.1

Szintai, B., Szűcs, M.., *Randriamampianina, R.,* and *Kullmann, L..,* 2015: Application of AROME non-hydrostatic model at the Hungarian Meteorological Service: physical parametrizations and ensemble forecasting. *Időjárás 119,* 241–265.

Strajnar B., 2012: Validation of Mode-S Meteorological Routine Air Report aircraft observations. *J. Geophys. Res. 117,* D231110. https://doi.org/10.1029/2012JD018315

Taillefer, F., 2002: CANARI (Code for the Analysis Necessary for Arpege for its Rejects and its Initialization): Technical documentation. Internal CNRM/GMAP Report, 55 pp.

Tóth, H., 2004: Detailed case study of a dramatic winter temperature overestimation in the ALADIN/HU model. RC LACE Internal Report. 10pp, http://rclace.eu/?page=11)

Trojáková, A., Mile, M., and *Tudor, M.,* 2019: Observation Preprocessing System for RC LACE (OPLACE). *Adv. Sci. Res. 16,* 223–228., https://doi.org/10.5194/asr-16-223-2019

Wernli, H., Paulat, M., Hagen, M., and *Frei, C.* 2008:. SAL—A Novel Quality Measure for the Verification of Quantitative Precipitation Forecasts. *Month. Weather Rev. 136,* 4470–4487.
https://doi.org/10.1175/2008mwr2415.1

World Meteorological Organization, 2019: Tests, Comparisons and Operational Performance of the Water Vapor Sensing Systems (WVSS-II): CIMO Expert Team on Aircraft-based Observations.

IDŐJÁRÁS

Historical observation impact assessments for EUMETNET using the ALADIN/HU limited area model

Roger Randriamampianina[1,*], **András Horányi**[2], **Gergely Bölöni**[3], and **Gabriella Szépszó**[4]

[1]*Norwegian Meteorological Institute*
Henrik Mohns Plass 1, Oslo 0371, Norway

[2]*European Centre for Medium-Range Weather Forecasts*
Shinfield Park, RG2 9AX, Reading, UK

[3]*Deutscher Wetterdienst*
Frankfurter Str. 135, Offenbach, 63067, Germany

[4]*Hungarian Meteorological Service*
Kitaibel Pál u. 1., Budapest 1024, Hungary

[*]*Corresponding author's E-mail: rogerr@met.no*

(Manuscript received in final form August 30, 2021)

Abstract— Two historical Observing System Experiment (OSE) studies using the ALADIN limited area model and its assimilation system are described. The first study, using an OSE scenario that minimizes the impacts of observations through the lateral boundary conditions, demonstrated the importance of each assimilated terrestrial (radiosonde, aircraft, and wind profiler) observations on the analyses and short-range forecasts of the ALADIN/HU model and proved evidence, that the role of conventional observations cannot be even partly taken over by satellite measurements without degradation of the forecast quality. The second study demonstrated that the assimilation of radiosonde observations remains indispensable even with a progressively increasing amount of aircraft measurements.

Key-words: ALADIN, data assimilation, OSE, observations, limited area model, EUCOS

1. Introduction

Numerical weather prediction (NWP) models have developed enormously during the last three decades (*Bauer et al.*, 2015). Initialization of these models requires a lot of observations in time and (three dimensional) space. To be efficient, most of the observations are synchronized in time and shared between the NWP centers around the world through the Global Telecommunication System (GTS). The World Meteorological Organisation (WMO) is coordinating the management of the observation network on a global scale, while at European scale, EUMETNET provides recommendations and support for the development and maintenance of the terrestrial observing system.

NWP models require regular initialization of their initial condition taking into account all available observations through the data assimilation (DA) process (*Daley,* 1991; *Kalnay,* 2002). Therefore, well designed (spatially and temporally) observations are very important for an accurate NWP. For this reason, EUMETNET regularly initiates design studies that aim at evaluating the performance of the existing observation networks and their possible evolution. The Hungarian Meteorological Service (OMSZ) participated in some of these studies in 2006 (first study: EUCOS[1] Space/Terrestrial Link Study) and 2009 (second study: Upper Air Network Redesign Study), which involved also NWP centers in Europe such as the European Centre for Medium-range Weather Forecasts (ECMWF), Deutscher Wetterdienst (DWD), Met Office, Danish Meteorological Institute (DMI), and Norwegian Meteorological Institute (MET Norway). The evaluation of the "usefulness" of different observation networks is usually done through the examination of the relative impact of these networks on NWP analyses and forecasts. Usually, the following approaches are used for such an evaluation: forecast sensitivity to observation impact (FSOI: e.g., *Baker* and *Daley*, 2000; *Gelaro et al.,* 2007; *Cardinali*, 2009; *Soldatenko et al.*, 2018) and Observing System Experiments (OSEs: e.g., *Bouttier* and *Kelly,* 2001; *Amstrup,* 2008; *Benjamin et al.*, 2009; *Radnoti et al.*, 2012; *Bormann et al.*, 2019). In practice, in OSE the studied observations are either progressively added (e.g., *Randriamampianina et al.*, 2019) or taken out (data denial) (e.g., *Lawrence et al.,* 2019; *Randriamampianina et al.*, 2021) from the DA system, and the impact of such change is investigated.

This paper describes two OSEs initiated by the EUMETNET and realized at OMSZ using the ALADIN[2] model (*Bubnová et al.*, 1995; *Horányi et al.*, 1996; *Termonia et al.*, 2018) and its assimilation system (*Fischer et al.*, 2005; *Bölöni,* 2006; *Randriamampianina*, 2006b; *Mile et al.,* 2015). While the first study aimed at studying the benefits of terrestrial observing systems on top of the available satellite observations, the second study investigated the relative impact of different timely and spatially designed aircraft and radiosonde measurements.

---

[1]   EUMETNET Composite Observing System
[2]   Aire Limitée Adaptation dynamique Développement InterNational

A limited area model (LAM) requires lateral boundary conditions (LBC) to compute the forecasts for the region of interest, which are usually provided by a global model, also called the driving model. With respect to LAM data assimilation and OSEs, it is of particular importance what kind of observations are assimilated in the driving model. Practically, there are few possible options: 1) more observation types are used in the driving model compared to those used in LAM; 2) less observation types are used in the driving model compared to those used in LAM; 3) similar observation types are used in both driving model and LAM. Option 1) is valid for most of the operational LAMs in Europe. In the first study, 2) was used to minimize the impact of the observations assimilated in the driving model in LAM, while 3) was used in the second study to get full impact of the observations also through the LBCs in LAM. Although the relative impact of observations through LBCs were well considered in the presented two studies in this paper, their contribution in LAM was only evaluated in detail in recent studies (*Randriamampianina et al.*, 2021).

Section 2 describes the applied ALADIN/HU assimilation and forecast systems, the experimental designs, and the adopted verification approach. Section 3 presents the obtained results, while conclusions and some discussion are included in Section 4.

2. Data and methods

2.1. ALADIN/HU assimilation and forecast systems

In this study the hydrostatic ALADIN model was used for Hungary (ALADIN/HU; see *Fig. 1* for the model domain) (code version CY28T3 for the first and CY30 for the second study which were the operational model versions in 2006 and 2009, respectively) with slightly different configurations in the two OSEs (*Table 1*). Three-dimensional variational data assimilation (3D-Var – *Fischer et al.*, 2005) was applied to provide the atmospheric analysis using conventional (surface, radiosonde, aircraft, wind profiler) wind retrievals (atmospheric motion vectors: AMV) (*Randriamampianina*, 2006a) and satellite radiances (ATOVS: AMSU-A and AMSU-B) (*Randriamampianina*, 2005, 2006b) observations.
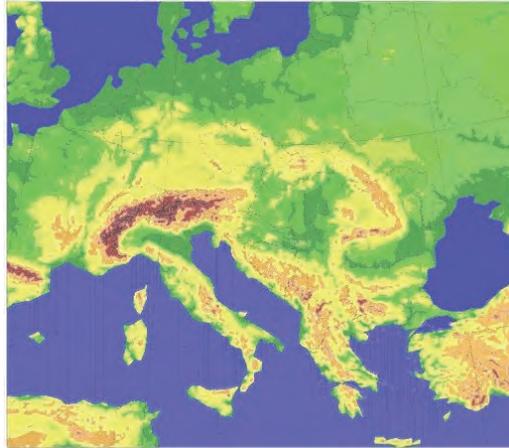
Fig. 1. The domain of the ALADIN/HU model

Table 1. The applied model setups in both studies

	First study	**Second study**
Horizontal resolution	12 km	8 km
Vertical resolution	37 vertical levels from the surface up to 5 hPa	49 vertical levels from the surface up to 5 hPa
Code version	CY28T3	CY30
Initial times and forecasts lengths	00 UTC (48h) 12 UTC (48h)	00 UTC (54h) 06 UTC (48h)

Although the use of observations was mainly determined by the scenarios of the OSE (see the next sections on the design of the experiment), here we describe some details on the use of observations, which might be important when interpreting the obtained results later on. Among the surface (SYNOP) observations, only geopotential data was used. From radiosondes (TEMP), geopotential, temperature, wind, and humidity data were assimilated. The AMDAR (Aircraft Meteorological Data Relay) aircraft data were assimilated with 25 km horizontal thinning within a +/- 1 hour observation window. The default thinning procedure of the aircraft data in ALADIN is done separately for each flight, which implies a risk of data being close to each other in space but measured

558

at different times. To avoid this problem, an additional filtering procedure was applied prior to aircraft data thinning. Wind profiler observations were used between 700 hPa and 400 hPa from the closest profile to the analysis time. This definitely results in a small amount of data in the experiments. The AMV (GEOWIND) data were used above 350 hPa and below 800 hPa over sea from the closest observation to the analysis time with a 25 km horizontal thinning (*Randriamampianina*, 2006a). Full grid ATOVS (AMSU-A and AMSU-B/MHS) data were assimilated within a +/- 3 hour observation window using 80 km horizontal thinning. In the experiments AMSU-A data from NOAA-15 and NOAA-16, and AMSU-B data from NOAA-16 and NOAA-17 were used (*Randriamampianina*, 2005 and 2006b). The data usage in the OSE experiments was carefully assessed through a web-based monitoring system.

For the first study, the surface fields were initialized by an interpolation of the corresponding ECMWF analysis to the ALADIN grid, while for the second study, an optimum interpolation (OI) scheme was used for the initialization of the surface fields. Concerning the assimilation of satellite radiances, the RTTOV-7 radiative transfer code was used to simulate the radiances from the model fields (*Saunders et al.*, 2002). The background error covariance matrix is computed using the NMC method (*Parrish* and *Derber*, 1992) in the first study and by the downscaled ensemble method (*Berre et al.*, 2006; *Bölöni* and *Horvath*, 2010) in the second study. A digital filter initialization is applied prior to the model integration. A six-hourly assimilation cycle generating analyses at 00, 06, 12, and 18 UTC was adopted. Three-hourly lateral boundary coupling was applied using the ECMWF analyses and short-range forecasts depending on the network time. At 00 and 12 UTC, the ECMWF analyses were used as the first boundary file, while at 06 and 18 UTC, the short-range forecasts (6-hour forecasts) of the ECMWF were used as the first coupling file. Longer forecasts were performed twice a day (see *Table 1*).

2.2. Design of the experiments

2.2.1. First study

The objective of the EUCOS Space/Terrestrial Link Study was to explore the relative benefit of various components of the terrestrial observing system on top of satellite observations. The chosen strategy for the study was to run a series of data denial experiments using different sets of observations within both global and LAM assimilation and forecasting systems. The NWP models taking part in the experiments were the global ECMWF, the global and the LAM version of the Unified Model (UK MetOffice), the Danish (*Amstrup*, 2008) and the Norwegian (*Thyness* and *Schyberg*, 2007) versions of the HIRLAM[3] model, and the ALADIN/HU model. Due to the different location of the LAM domains, the OSE

---

[3] HIRLAM: High Resolution Limited Area Model

scenarios differed slightly between the participants with LAM. For instance, in the Hungarian experiments the E-ASAP (EUMETNET Automated Shipboard Aerological Programme) observations were not used, because these observations cover mainly the northern part of the Atlantic ocean. Lateral boundary conditions for the ALADIN- and HIRLAM-model based experiments were taken from the ECMWF baseline (see below the description of baseline) experiment. The Unified LAM Model was coupled with its global version.

The experiments were conducted for both winter and summer periods. The winter period was from December 4, 2004 till January 20, 2005, while the summer period started on July 15 and lasted until September 5, 2005. The first 10 days of both periods were used for a warm up of the model and were not used for verification. The definitions and acronyms of the ALADIN/HU experiments are as follows:

Winter (EU)/Summer (ES) experiments:

EU01/ES01 – baseline (GSN[4] surface and GUAN[5] radiosonde + AMV + ATOVS radiances)

EU02/ES02 – baseline + aircraft,

EU03/ES03 – baseline + radiosonde wind profiles,

EU04/ES04 – baseline + radiosonde wind and temperature profiles,

EU05/ES05 – baseline + wind-profilers,

EU06/ES06 – baseline + radiosonde wind and temperature + aircraft,

EU07/ES07 – baseline + radiosonde wind, temperature and humidity,

EU08/ES08 – full observation (radiosonde + wind-profiler + aircraft).

2.2.2. Second study

The main objective of the Upper Air Network Redesign Study was to provide input for the definition of a European-wide network of ground-based upper-air observing systems with special emphasis on regional modeling. This study concentrated on the possible refinement of the upper-air observing network (radiosonde and aircraft) with respect to their optimal spatial and temporal distribution. For that end, six different observation scenarios were specified starting from the full operational data usage (control scenario) and ending with a baseline scenario, which was characterized by radical decrease of the number of radiosonde and aircraft profiles. The intermediate scenarios were focusing on the different thinning distances for the radiosonde and aircraft data with step-by-step degradation of their amounts. The scenarios were defined as follows:

Sc2 – Control: Full operational observation coverage.

---

4   GSN: GCOS (Global Climate Observing System) Surface Network
5   GUAN: GCOS Upper-Air Network

Sc3a: The radiosonde network is slightly reduced with a 100 km thinning distance, all aircraft data and the full remaining part of the observation networks.

Sc3b: Like Sc3a, but no thinning is performed for the 00 UTC radiosonde profiles.

Sc4: Like Sc3a but 250 km thinning distance for radiosondes and aircraft data.

Sc5: Like Sc4, but 500 km thinning distance.

Sc1 – Baseline: GUAN radiosonde network, flight level aircraft data, aircraft profiles of less than 3 hourly visited airports and full remaining part of the observation network.

The Observing System Experiments based on the above scenarios were performed by a global NWP center (ECMWF) and some National Meteorological Services (NMS) running LAMs. It was decided that the information on aircraft observations (which were created by a special blacklisting and thinning algorithms and provided by the EUCOS team) for each scenario was provided directly by ECMWF in order to ensure, that the same sets of observations are used in both global and limited area experiments. Concerning the radiosonde data, the same blacklisting decisions were applied at all centers. Other observation types were used as locally applied operationally. The experiments were carried out for a winter period between December 15, 2006 and January 31, 2007 and for a summer period between June 1st and July 15, 2007. The difference between the radiosonde and aircraft observation usage for all scenarios can be seen in *Fig. 2*, where (for the winter period) the amount of active data is displayed for each scenario. It can be seen that the control scenario is using more than double (rather 2.5) times more amount of radiosonde and roughly double aircraft data with respect to the baseline scenario (these are the two extreme scenarios), and the intermediate scenarios are situated between these two extremes as expected. In terms of aircraft data usage the control (Sc2), Sc3a, and Sc3b scenarios are equivalent. Therefore, it is expected that the best forecasting performance is going to be for Sc2 (control), which is followed by Sc3b, Sc3a, Sc4, Sc5, and Sc1 (baseline). It is interesting to notice the Christmas and New Year radical decrease in the amount of data especially for the aircraft observations.
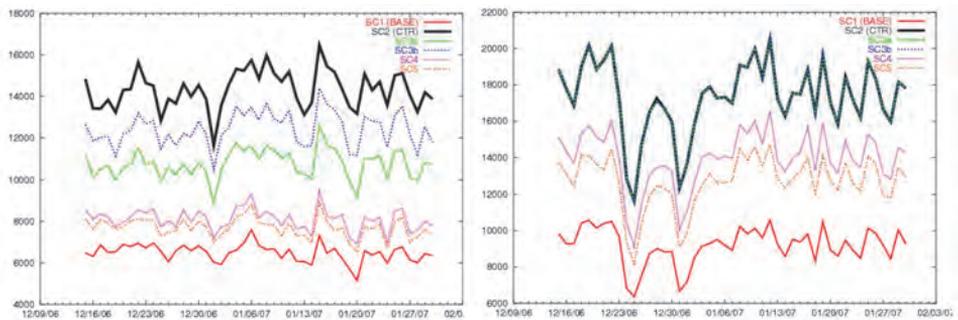
Fig. 2. Number of daily observations (temperature, wind, geopotential, and humidity for radiosondes, and temperature and wind for aircrafts) assimilated into the ALADIN/HU model using the six winter scenarios for radiosondes (left) and for aircraft (right) observations.

In order to be in agreement with the "real-life" situation, the LAM models were coupled with the corresponding global scenario runs (in contrary to the solution proposed for the previous space-terrestrial study – first study –, where the baseline scenario was used for all the runs in order to not mix the impacts of the initial and lateral boundary conditions). The LAM runs were performed by the HIRLAM group and the Hungarian Meteorological Service.

2.3. The applied verification method

In order to allow a meaningful comparison of the results from all participants, a common evaluation procedure was agreed, as follows. Computation of objective scores composed by bias and root-mean-square error (RMSE) of the simulated analyses and forecasts against observations (surface and radiosonde observations, using the so-called EWGLAM station list (*Hall*, 1987)) was mandatory for both studies. For the first study, we also performed a verification against the ECMWF analyses. *Geer* (2016) underlines the importance of significance of the RMSE differences. Significance tests of the objective verification scores were performed. The significance tests were computed on the normalized (by mean scores) mean difference in analyses and forecasts quality using the Student's t-test. The number of the analyzed and forecast parameters with the associated pressure levels was also agreed in advance. Further, an objective evaluation of two, a summer and a winter, case studies was performed focusing on interesting weather situations. Although, for the sake of the length of this article, the results of these case studies are not discussed.

562

3. Results

3.1. First study

The OSE technique applied in the first study was based on adding the studied observations in DA on top of the baseline system. For example, the impact of the aircraft observations was checked by comparing the verification scores for EU02/ES02 and EU01/ES01. The relative impact of the aircraft temperature and wind data was shown by plotting the verification scores of the above experiments together with the results of the run using the full observation set (EU08/ES08). Similarly, the impact of radiosonde wind data was checked by comparing the verification scores of EU03/ES03 with EU01/ES01, and so on for the impact of the radiosonde temperature, humidity, and the combined impact of radiosonde and aircraft data, as well as for the impact of the wind profilers. As an example, in *Fig. 3* we show the impact of the radiosonde temperature on analyses and forecasts of temperature fields.
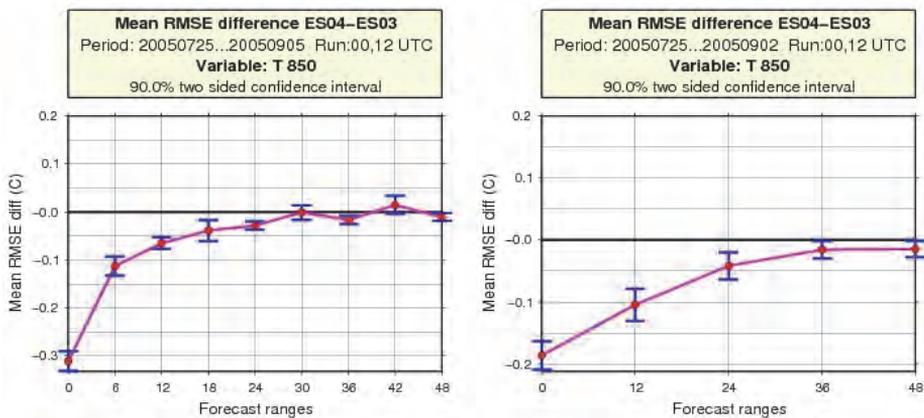
Fig. 3. The RMSE differences of temperature at 850 hPa between the experiment with radiosonde temperature and wind profiles (ES04) and the experiment with radiosonde wind profiles (ES03). The significance test is based on daily scores of temperature fields for both 00 and 12 UTC runs for the summer period July 25-September 2,2005). The graphs show the comparison against observations (left) and against the ECMWF analyses (right). Negative values mean reduction of the model errors when the radiosonde temperature was added in the DA, hence they show positive impact.

Table 2 shows the overall observed (from both against observations and the ECMWF analyses) verification results, which can be summarized as follows.

Objective verification against ECMWF analyses mostly showed a clear positive impact of the terrestrial observations on the analysis and forecasts of ALADIN/HU up to 2 days. Verification against observations showed that the impact is up to 24 hours. Case studies indicated clear improvement in the forecasts when adding the different components of the terrestrial observations in the assimilation system (not shown).

Table 2. Overall impact of the terrestrial observations during winter (in brackets) and summer (without brackets). + means significant positive impact.

Observing system	Parameters	Forecast ranges with impact				
		Neutral/Few hours	½ day	1 day	1.5 day	2 days
Radiosonde	Wind		(+)		+	
	Temperature			(+)		+
	Humidity	(+)			+	
Aircraft	Wind & temperature		(+)			+
Wind-profiler	Wind	(+)	+			

A more pronounced and long-lasting positive impact of the aircraft observations was found during summer compared to the winter period. Positive impact of the aircraft data on the forecast of humidity fields was observed during summer, while negative impact was found for the winter period, although it was significant only for a few hours (not shown). Positive impact of the aircraft data on the forecast of precipitation was observed for the summer period, while neutral (from 00 UTC) and negative (from 12 UTC) impacts were found for the winter period (not shown).

A clear positive impact of the radiosonde wind observation on the analysis and short-range forecasts was observed. A positive impact of the radiosonde temperature up to 24 and 48 hours was concluded during the winter and summer periods, respectively. Clear positive impact of the radiosonde temperature forecasts of the mean sea level pressure up to 24 hours was detected for summer, while neutral impact was found during the winter period (not shown). Neutral impact of the radiosonde humidity on the mean sea level pressure was observed during the summer period, while clear positive impact was seen during the winter period. Better impact of the radiosonde temperature on the geopotential was found

in the summer study. Large positive impact of the radiosonde humidity was observed for all forecast ranges of precipitation (see *Fig. 4*).
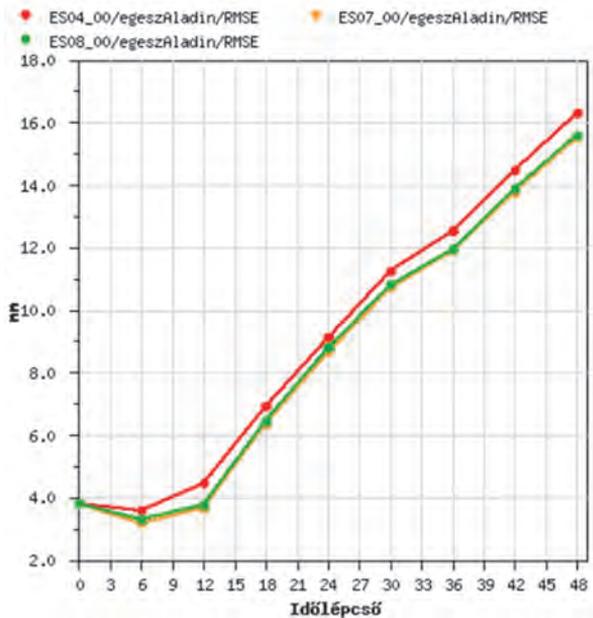
Fig. 4. RMSEs of 6-hourly cumulated precipitation at different forecast ranges (időlépcső – forecast ranges) for 00 UTC runs. Red line: forecasts initialized using radiosonde temperature and wind data (ES04_00), yellow line: forecasts initialized using radiosonde temperature, wind, and humidity data (ES07_00), green line: forecasts initialized with all available data (ES08_00).

The impact of the wind profilers on the analysis and forecasts is neutral for most of the meteorological parameters, but one can find examples with slightly positive impact as well (maximum up to 12 hours).

Our results showed that there is no problem of redundancy when using the aircraft observations on top of the radiosondes. Comparing the baseline (ES01), baseline and aircraft (ES02), and baseline and radiosonde wind and temperature (ES04) (summer study), we found that the impact of the aircraft (wind and temperature) observations was a bit larger than what we found during the winter study (half of the impact of radiosonde wind and temperature data). For the summer period, better scores were observed when comparing the impact of the aircraft data on top of the radiosonde wind and temperature data (ES04 vs ES06), while small deterioration was observed in the winter study.

3.2. Second study

Similarly to the first study, the impact on the ALADIN/HU analysis and forecasts was checked by comparing the verification scores of the different scenarios. *Table 3* summarizes the observed verification results focusing on the impact on the analyses and forecasts in the lower troposphere and focusing only on the model run from 00 UTC.

The control (Sc2) scenario significantly outperforms the baseline (Sc1) scenario during the first 24 hours of forecasts with the exception that the impact of temperature lasts up to one and half days in the winter case (*Table 3*, first comparisons).

Concerning scenarios 3 (3a and 3b), comparing the verification scores of the control with that of Sc3a showed clear importance of high resolution radiosonde network in LAM. Comparing the verification scores of Sc3a and Sc3b showed the importance of having a full network of radiosonde observations at 00 UTC. The obtained results showed also that Sc3b is better than the control (not shown in *Table 3*).

Table 3. Overall impact of observations with the different scenarios during winter (in brackets) and summer (without brackets). - means significant degradation and positive impact.

Observing system	Parameter	Forecast range with impact				
		Neutral/few hours	½ day	1 day	1.5 day	2 days
Control (Sc2 - Sc1)	Wind			(-) -		
	Temperature			-	(-)	
	Humidity			(-) -		
Radiosonde 100 km thinning (Sc2 - Sc3a)	Wind	(-) -				
	Temperature	-	(-)			
	Humidity	(-)	-			
Full radiosonde resolution at 00 UTC (Sc3b - Sc3a)	Wind	(-) -				
	Temperature	(-)		-		
	Humidity		(-) -			
Radiosonde and aircraft at 250 km resolution (Sc2 - Sc4)	Wind	(-) -				
	Temperature	-	(-)			
	Humidity		(-)		-	
Radiosonde and aircraft at 500km resolution (Sc2 - Sc5)	Wind	-	(-)			
	Temperature				(-) -	
	Humidity			(-)	-	

Further reducing the resolution of both radiosonde and aircraft networks (Sc4 and Sc5) showed clear degradation of the accuracy of analyses and forecasts of the ALADIN/HU model. While for the case of Sc4 (both radiosonde and aircraft networks at 250 km resolution), the degradation in wind and temperature forecast quality lasted up to 12 hours, for Sc5 (both radiosonde and aircraft network at 500 km resolution), the degradation lasted up one and half day for both temperature and humidity (see *Fig. 5*). Further, it was clearly shown that degradation of these observing networks significantly impacts the quality of the humidity forecasts of the ALADIN/HU model.
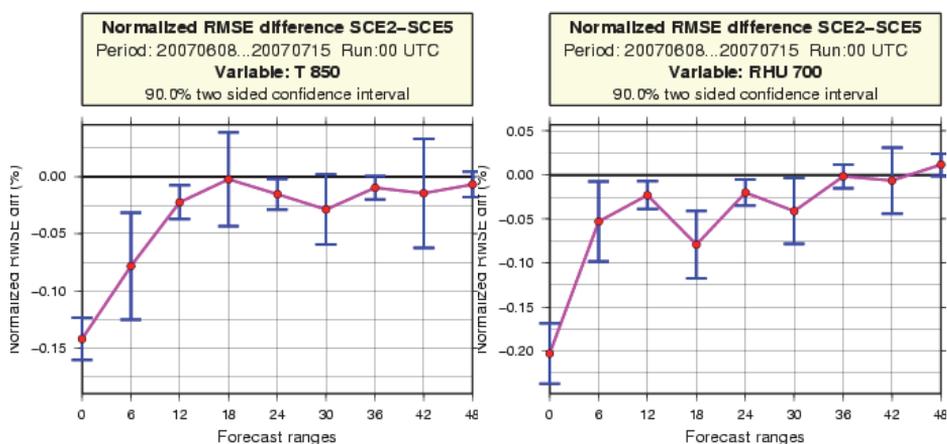
Fig. 5. The RMSE differences of temperature at 850 hPa (left) and relative humidity (right) between the control experiment (Sc2) and the one where radiosonde and aircraft data have been reduced with a 500 km thinning distance (Sc5). The graphs show the comparison against observations for the summer period of June 8 – July 15, 2007. Note that the full radiosonde network is mainly available at 00 and 12 UTC, and we have relatively less observations at 06 and 18 UTC. So, the relatively large error bars at 06, 18, 30, and 42 hour forecast ranges are due to use of less verifying observations and not due to the observation impact. Negative values mean reduction of the forecast errors due to the usage of radiosondes and aircraft data with a higher spatial density.

4. Summary and discussions

We presented two OSE studies performed several years ago in this paper. While the first one investigated the importance of the full terrestrial (radiosonde, aircraft and wind profiler) European networks, the second study evaluated the efficiency of the radiosonde and aircraft networks.

In the first study, the impact of the studied observations lasted longer during summer than during winter. All tested observations have clear positive impact on the ALADIN/HU analyses and forecasts. This study showed for the first time that the implemented data assimilation system is working properly, which means that, with the adopted experiment design - minimizing the impact coming through the lateral boundary conditions by using the baseline experiment from the coupling global model -, all the implemented observations showed clear positive impacts on the LAM model.

The second study showed that high resolution observing networks (both radiosonde and aircraft) are important for improving the LAM analyses and forecasts. The positive impacts of the studied observations were clearly shown thanks to the design of the experiments. In the second study, in each experiment the LAM was coupled with its global counterpart. Compared to the impact found in the first study, which was somehow maximized, we got the exact relative impacts of the studied observations through LAM DA. *Randriamampianina et al.* (2021) used the similar experiment design, and further computed as well the impacts of different observing networks through the LBCs on the LAM analyses and forecasts. They found that the total impacts of observations on LAM upper-air forecasts is dominated by the impacts through LBCs. This explains the "relatively weakened" (e.g., shorter lasting) impact shown in the second study compared to what is shown in the first one.

These studies demonstrated that the conventional (terrestrial) observations are still a very important component of the observing network. Despite the large amount of data from new observation techniques (especially satellites), the terrestrial network is indispensable for maintaining forecast quality even on a regional scale, and its redundancy is out of question. Additionally, the increasing number of aircraft data available does not mean that the radiosonde information would become redundant, and therefore, it is critical to keep (or even enhance) the present network of radiosondes.

This paper describes results of studies that were done 10–15 years ago accounting older model versions and relatively poorer observing networks. This is true for the aircraft observations where now we have on top of the AMDAR (Aircraft Meteorological Data Relay) network, the Mode-Selective (Mode-S) Enhanced Surveillance (EHS) and Meteorological Routine Air Report (MRAR) observations. Further, although with very limited numbers, over the Hungarian modeling area of interest, some aircrafts are equipped with humidity sensors. When available, the AMDAR humidity observations are assimilated in the operational convection-permitting AROME (Application of Research to Operations at Mesoscale) model at OMSZ (*Tóth et al.*, 2021). The implementation of the Mode-S (both EHS and MRAR) data is ongoing in AROME/HU (*Fischer et al.,* 2017). We expect different impacts of the individual and combined terrestrial observing networks in the current AROME operational model.

References

Amstrup, B., 2008: Assessment of the impact of key terrestrial observing systems using DMI-HIRLAM. *Quart. J. Roy. Meteor. Soc.* 134, 985–1001. https://doi.org/10.1002/qj.249

Baker, N. and *Daley, R.,* 2000: Observation and background adjoint sensitivity in the adaptive observation-targeting problem. *Quart. J. Roy. Meteor. Soc.* 126, 1431–1454. https://doi.org/10.1002/qj.49712656511

Bauer, P., Thorpe, A., and *Brunet, G.,* 2015: The quiet revolution of numerical weather prediction. *Nature* 525, 47–55. https://doi.org/10.1038/nature14956

Benjamin, S.G., Jamison, B.D., Moninger, W.R., Sahm, S.R., Schwartz, B.E., and *Schlatter, T.W.,* 2009: Relative short-range forecast impact from aircraft, profiler, radiosonde, VAD, GPS-PW, Metar, and Mesonet observations via the RUC hourly assimilation cycle. *Mon. Weather Rev. 138,* 1319–1343. https://doi.org/10.1175/2009MWR3097.1

Berre, L., Stefanescu, E.S., and *Belo Pereira, M.,* 2006: The representation of the analysis effect in three error simulation techniques. *Tellus 58,* 196–209. https://doi.org/10.1111/j.1600-0870.2006.00165.x

Bormann, N., Lawrence, H., and *Farnan, J.,* 2019: Global observing-system experiments in the ECMWF assimilation system. *ECMWF Tech. Memo. 839.*

Bouttier, F. and *Kelly, G.A.,* 2001: Observing-system experiments in the ECMWF 4D-Var assimilation system. *Quart. J. Roy. Meteor. Soc.* 127, 1469–1488. https://doi.org/10.1002/qj.49712757419

Bölöni, G., 2006: Development of a variational data assimilation system for a limited-area model at the Hungarian Meteorological Service, *Időjárás 110,* 309–329.

Bölöni, G. and *K. Horvath,* 2010: Diagnosis and tuning of background error statistics in a variational assimilation system. *Időjárás 114,* 1–21.

Bubnová, R., Hello, G., Bénard, P. and *Geleyn, J.-F.,* 1995: Integration of fully-elastic equations cast in the hydrostatic pressure terrain-following coordinate in the framework of the ARPEGE/ALADIN NWP system. *Mon. Weather Rev. 123,* 515-535. https://doi.org/10.1175/1520-0493(1995)123<0515:IOTFEE>2.0.CO;2

Cardinali, C., 2009: Monitoring the observation impact on the short-range forecast. *Quart. J. Roy. Meteor. Soc. 135,* 239–250. https://doi.org/10.1002/qj.366

Daley, R., 1991: Atmospheric Data Analysis. Cambridge Univ. Press.

EUCOS Space-Terrestrial Study Final Report: Observing System Experiments from the winter 2004 - 2005 and summer 2005. *METNO report:* 7/2007.

Fischer, A., Homonnai, V., Mile, M., Sepsi, P., Szintai, B., and *Szűcs, M.,* 2017: Modelling activities at the Hungarian Meteorological Service. *ALADIN-HIRLAM newslett. 8,* 64–68.

Fischer, C., Montmerle, T., Berre, L., Auger, L., and *Stefănescu, A.,* 2005: An overview of the variational assimilation in the ALADIN/FRANCE NWP system. *Quart. J. Roy. Meteor. Soc.131,* 3477–3492. https://doi.org/10.1256/qj.05.115

Geer, A.J., 2016: Significance of changes in medium-range forecast scores. *Tellus A 68,*1(30229), 1–21. https://doi.org/10.3402/tellusa.v68.30229

Gelaro, R., Zhu, Y., and *Errico, R.,* 2007: Examination of various-order adjoint-based approximations of observation impact. *Meteorol. Zeitsch. 16,* 685–692. https://doi.org/10.1127/0941-2948/2007/0248

Hall C., 1987: A common verification scheme for limited area models. *EWGLAM Newsletter 15,* 144–147.

Horányi, A., Ihász, I., and *Radnóti, G.,* 1996: ARPEGE/ALADIN: A numerical weather prediction model for Central-Europe with the participation of the HMS. *Időjárás 100,* 277–301.

Kalnay, E., 2002: Atmospheric Modeling, Data Assimilation and Predictability. Atmospheric Modeling. Cambridge University Press. https://doi.org/10.1017/CBO9780511802270

Lawrence, H., Bormann, N., Sandu, I., Day, J., Farnan, J., and *Bauer, P.,* 2019: Use and impact of arctic observations in the ecmwf numerical weather prediction system. *Quart. J. Roy. Meteorol. Soc., 145,* 3432–3454. https://doi.org/10.1002/qj.3628

Mile, M., Bölöni, G., Randriamampianina, R., Steib, R., and *Kucukkaraca, E.,* 2015: Overview of mesoscale data assimilation developments at the Hungarian Meteorological Service, *Időjárás 119,* 215–239.

Radnoti, G., Bauer, P., McNally, A., and *Horanyi, A.*, 2012: ECMWF study to quantify the interaction between terrestrial and space-based observing systems on numerical weather prediction skill. *ECMWF Techn. Memor.* 679.

Randriamampianina, R., 2005. Radiance-bias correction for a limited area model, *Időjárás 109,* 143–155.

Randriamampianina, R., 2006a: Investigation of the AMV data derived from meteosat-8 in theALADIN/HU assimilation system. 8th International Winds Workshop, 24–28 April 2006, Beijing, China. Access available on 09.05.2021, from:
https://www-cdn.eumetsat.int/files/2020-04/pdf_conf_p47_s2_06_randriama_v.pdf

Randriamampianina, R., 2006b: Impact of high resolution satellite observations in the ALADIN/HU model, *Időjárás 110,* 329–347.

Randriamampianina, R.; Schyberg, H.; and *Mile, M.,* 2019: Observing System Experiments with an Arctic Mesoscale Numerical Weather Prediction Model. *Remote Sens. 11,* 981; https://doi.org/10.3390/rs11080981

Randriamampianina, R., N. Bormann, M. A., Ø. Køltzow, H. Lawrence, I. Sandu, and *Z.-Q. Wang*, 2021: Relative impact of observations on a regional Arctic numerical weather prediction system, *Quart. J. Roy. Meteor. Soc.147,* 2212-2232. https://doi.org/10.1002/qj.4018

Parrish, D. and *J. Derber,* 1992: The National Meteorological Center's spectral statistical-interpolation analysis system. *Mon. Weather Rev. 120,* 1747–1763.
https://doi.org/10.1175/1520-0493(1992)120<1747:TNMCSS>2.0.CO;2

Soldatenko, S., Tingwell, C., Steinle, P., and *Kelly-Gerreyn, B.A.*, 2018: Assessing the impact of surface and upper-air observations on the forecast skill of the access numerical weather prediction model over Australia. *Atmosphere 9,* 23. https://doi.org/10.3390/atmos9010023

Saunders, R.W., Matricardi, M., Brunel, P., English, S.J., and *Deblonde, G.* ,2002: RTTOV-7: A Satellite Radiance Simulator for the New Millennium. Proceedings of the XIIth International TOVS Study Conference, Lorne, Australia, 28 February – 5 March 2002.

Termonia, P. Fischer, C., Bazile, E., Bouyssel, F., Brožková, R., Bénard, P., Bochenek, B., Degrauwe, D., Derková, M., El Khatib, R., Hamdi, R., Mašek, J., Pottier, P., Pristov, N., Seity, Y., Smolíková, P., Španiel, O., Tudor, M., Wang, Y., Wittmann, C., and *Joly, A.,* 2018: The ALADIN System and its canonical model configurations AROME CY41T1 and ALARO CY40T1. *Geosci. Model Dev. 11,* 257–281. https://doi.org/10.5194/gmd-11-257-2018

Tóth, H., Homonnai, V., Mile, M., Várkonyi, A., Kocsis, Zs., Szanyi, K., Tóth, G., Szintai, B. and *Szépszó, G.,* 2021: Recent developments in the data assimilation of AROME/HU numerical weather prediction model. *Időjárás 125,* 521–553. https://doi.org/10.28974/idojaras.2021.4.1

Thyness V.W. and *Schyberg H.,* 2007: EUCOS Space-Terrestrial Study Final Report: Observing System Experiments from the winter 2004 - 2005 and summer 2005. *METNO report*: 7/2007.

IDŐJÁRÁS

Numerical simulations of June 7, 2020 convective precipitation over Slovakia using deterministic, probabilistic, and convection-permitting approaches

André Simon[1,2],*, **Martin Belluš**[1], **Katarína Čatlošová**[1], **Mária Derková**[1],
Martin Dian[1], **Martin Imrišek**[1], **Ján Kaňák**[1], **Ladislav Méri**[1,3],
Michal Neštiak[1] and **Jozef Vivoda**[1,3]

[1] *Slovak Hydrometeorological Institute*
Jeséniova 17, 851 07 Bratislava, Slovakia

[2] *Hungarian Meteorological Service*
Kitaibel Pál u. 1, 1024 Budapest, Hungary

[3] *Department of Astronomy, Physics of the Earth, and Meteorology*
Comenius University in Bratislava
Mlynská Dolina, 842 48 Bratislava, Slovakia

*Corresponding author E-mail: andre.simon@shmu.sk

(Manuscript received in final form July 30, 2021)

Abstract— The paper presented is dedicated to the evaluation of the influence of various improvements to the numerical weather prediction (NWP) systems exploited at the Slovak Hydrometeorological Institute (SHMÚ). The impact was illustrated in a case study with multicell thunderstorms and the results were confronted with the reference analyses from the INCA nowcasting system, regional radar reflectivity data, and METEOSAT satellite imagery.

The convective cells evolution was diagnosed in non-hydrostatic dynamics experiments to study weak mesoscale vortices and updrafts. The growth of simulated clouds and evolution of the temperature at their top were compared with the brightness temperature analyzed from satellite imagery. The results obtained indicated the potential for modeling and diagnostics of small-scale structures within the convective cloudiness, which could be related to severe weather.

Furthermore, the non-hydrostatic dynamics experiments related to the stability and performance improvement of the time scheme led to the formulation of a new approach to linear operator definition for semi-implicit scheme (in text referred as NHHY). We demonstrate that the execution efficiency has improved by more than 20%.

The exploitation of several high resolution measurement types in data assimilation contributed to more precise position of predicted patterns and precipitation representation in the case study. The non-hydrostatic dynamics provided more detailed structures. On the other hand, the potential of a single deterministic forecast of prefrontal heavy precipitation was not as high as provided by the ensemble system. The prediction of a regional ensemble system A-LAEF (ALARO Limited Area Ensemble Forecast) enhanced the localization of precipitation patterns. Though, this was rather due to the simulation of uncertainty in the initial conditions and also because of the stochastic perturbation of physics tendencies. The various physical parameterization setups of A-LAEF members did not exhibit a systematic effect on precipitation forecast in the evaluated case. Moreover, the ensemble system allowed an estimation of uncertainty in a rapidly developing severe weather case, which was high even at very short range.

Key-words: numerical weather prediction, multicellular convection, convection-permitting modeling, GNSS ZTD (Global Navigation Satellite System – Zenith Total Delay) data assimilation, radial Doppler wind assimilation, probabilistic forecasting, mesovortex, cloud top temperature

1. Introduction

The history of NWP (numerical weather prediction) activities at SHMÚ is manifold, concerning research and development in the field of data assimilation, dynamics, physical parameterization, predictability as well as diagnostics (*Derková,* 2005). These were mostly focused on forecasting mesoscale events, such as the downslope windstorm in High Tatras on November 19, 2004 (*Simon et al.*, 2006). Arguably the most challenging task in mesoscale forecasting covers non-frontal thunderstorms, often accompanied by flash floods, hail, or other severe phenomena. A catastrophic flash flood in the year 1998 in the Malá Svinka basin (*Svoboda* and *Pekárová*, 1998) accelerated the endeavour to improve early diagnostics and prediction of such events. This resulted for example in local implementation and further development of the INCA nowcasting system (*Haiden et al.*, 2011) in the frame of the FLOODMED and INCA-CE (Integrated Nowcasting Comprehensive Analysis – Central Europe) projects (*Wang et al.*, 2017b).

Nevertheless, the possibility of nowcasting of local storms, which have basically multicellular character and undergo rapid development is very limited, when using only extrapolation methods. Early versions of the deterministic model at SHMÚ (called ALADIN/SHMU) were also not suitable for very short range forecasting in such cases, except for diagnostics of the convective environment. New opportunities were open after upgrading the physical parameterization of canonical model configuration ALARO (*Termonia et al.*, 2018) and after further improvements in the non-hydrostatic dynamics, which involved the

implementation of the iterative centered implicit (ICI) scheme (*Bénard et al.*, 2010). In ALARO, it was the so-called 3MT package, including mesoscale-oriented parameterization of convection (*Gerard*, 2009) and microphysics (after *Lopez*, 2002), which enabled more realistic simulation of local convective events.

Data assimilation procedures that provide realistic initial state for NWP model integration are equally important to obtain the correct model forecast. At SHMÚ, firstly the spectral blending by digital filter method was applied to improve the large scale representation of the upper air fields (*Derková* and *Belluš*, 2007). Advanced variational data assimilation schemes are not operationally used at SHMÚ, mostly due to lack of computer resources. Recently there are several data assimilation activities based on 3D-Var approach ongoing in parallel: assimilation of the Mode-S data (*Čatlošová* and *Derková*, 2020), assimilation of zenith total delay observations (*Imrišek et al.*, 2020), assimilation of Doppler weather radar measurements (*Čatlošová*, 2020) seemed to be promising in correcting the very short range forecasts at mesoscale, but these methods are still under development.

When forecasting severe mesoscale events, one has to deal with naturally large uncertainty already at nowcasting ranges or at very short lead times, which can be estimated with EPS (ensemble prediction system) methods. The SHMÚ EPS activities have been initiated in 2006 within the frame of the ALADIN-LAEF development, operational at the ECMWF HPCF (High-Performance Computing Facility) since 2011 (*Wang et al.*, 2011). Currently, ALADIN-LAEF is being replaced by a more sophisticated system based on the ALARO model with substantially higher spatial and vertical resolution called A-LAEF (*Belluš*, 2020a). Up to now, several case studies on severe weather were performed showing the potential of this system to identify even local flash floods (e.g., the flood on August 17, 2019 in Turkey) or windstorms (*Belluš*, 2020b). The A-LAEF system became operational at ECMWF HPCF as a Time Critical 2 application in July 2020, and its main objective is to provide reliable probabilistic forecasts at meso-synoptic scales for the national weather services of 8 RC LACE partners (Slovenia, Slovakia, Czech Republic, Croatia, Romania, Poland, Austria, Hungary) and Turkey.

The proper simulation of the initial conditions uncertainty as well as of the model uncertainty, together with the high-resolution physics well adapted to the local conditions, are crucial ingredients for the forecasting of convective events with generally low predictability. For this study a convective situation was chosen, which is rather typical in summer over Central Europe, and represents the above mentioned issues with forecasting non-organized, rapidly developing thunderstorms. Despite weak deep-layer shear and weak synoptic forcing, the thunderstorms on June 7, 2020 caused severe weather over Slovakia and the neighboring countries. It was mainly in the form of heavy precipitation or hail (ESWD, 2020) throughout the afternoon and evening hours. The operational ALADIN/SHMU forecasts used at that time predicted convective precipitation

rather in association with a cold front arriving toward the end of the day. SHMÚ forecasters issued preliminary warnings on prefrontal thunderstorms already on June 5 and 6 but with the lowest level of severity. These were updated after the development of storms had begun, and the second level of warning (on intense thunderstorms with hail and high precipitation) was issued mainly for districts in the western part of Slovakia. Concerning the eastern part of Slovakia, likelihood of severe storms during night hours was indicated by the ESTOFEX (*ESTOFEX,* 2020). For these reasons it was examined, whether assimilation of new data and higher-resolution non-hydrostatic models are capable of improving the precipitation forecasts, and what the limits of deterministic forecasting are in these types of situations. The experiments were compared with pre-operational forecasts of the A-LAEF system and its respective members. The EPS outputs were also used to evaluate the predictability of the event and the possible impact of various physical parameterizations. Apart from precipitation, distinguishing between different types of convection (e.g., multicell or supercell-type) is an important ingredient for severe weather forecasting. Thus, the ability to forecast small-scale structures (e.g., mesocyclones) with the convection-permitting configuration of the ALARO model was tested and compared with available radar and satellite observations.

Similar activities are ongoing at other national meteorological services over Europe where convection-permitting NWP deterministic models (AROME-France, *Seity et al.*, 2011; *Brousseau et al.*, 2016; HARMONIE-AROME, *Bengtsson et al.*, 2017; ALADIN at CHMI, *Brožková et al.*, 2019; COSMO, *Baldauf et al.*, 2011) as well as ensemble prediction systems (Arome-EPS, *Bouttier et al.*, 2012; C-LAEF, *Wastl et al.*, 2021; OMSZ AROME-EPS, *Szintai et al.*, 2015; AROME-MetCoOp, *Müller et al.*, 2017) are applied to improve forecast skills for high impact weather.

The presented study comprises description of used ALARO model versions in Section 2 and gives an overview of the experiments in Section 3. The case study description and results of respective experiments are shown in Section 4, whereas discussion and layout of further development in mesoscale forecasting follow in Section 5.

2. Methodology and description of used LAM NWP systems

2.1. LAM NWP systems used in the study

Four different versions of the ALARO NWP system have been used for experiments and diagnostics described in this paper. The basic setup of the systems is summarized in *Table 1*.

Table 1. Setup of four referenced ALARO versions.

label	ALADIN/SHMU	A-LAEF	ALADIN/CHMI	ALARO 2
status	operational	operational (common RC LACE)	operational (at CHMI)	run in testmode at SHMÚ
horizontal resolution	4.5 km	4.8 km	2.3 km	2.0 km
number of points	625 x 576	1250 x 750	1080 x 864	512 x 384
domain size	2813 x 2592 km	6000 x 3600 km	2511 x 2009 km	1024 x 768 km
number of vertical levels	63	60	87	87
coupling model	ARPEGE, 3 h coupling frequency	16+1 members of ECMWF EPS, 6 h coupling frequency	ARPEGE, 3 h coupling frequency	ARPEGE, 1 h coupling frequency
forecast ranges	78/72/72/60 h	72/-/72/- h	72/72/72/54 h	78/72/72/60 h
Initial times	00/06/12/18 UTC	00/12 UTC	00/06/12/18 UTC	00/06/12/18 UTC
upper air data assimilation	spectral blending by DF	spectral blending by DF for 16+1 members	BLENDVAR	none (dynamical downscaling)
surface data assimilation	CANARI optimal interpolation	Ensemble data assimilation based on CANARI OI	CANARI optimal interpolation	none (LBC downscaling)
initialization	none	none	Incremental digital filter in short cut-off production analysis	digital filter
model physics	ALARO-1vB	ALARO-1 multi-physics + surface stochastic physics (SPPT)	ALARO-1vB, adapted for convection-permitting scales	The same as ALADIN/CHMI
model dynamics	Hydrostatic formulation, spectral, semi-implicit, 2 time level semi-lagrangian scheme	The same as ALADIN/SHMU	Non-hydrostatic formulation, spectral, semi-implicit 2 time level iterative centered implicit scheme	The same as ALADIN/CHMI

2.1.1. ALADIN/SHMU model description

The main operational model used at SHMÚ is the ALARO configuration of the ALADIN NWP system (*Termonia et al.*, 2018) with 4.5 km horizontal resolution and 63 vertical levels. This version is hydrostatic with spectral, semi-implicit (*Simmons* and *Burridge,* 1981), 2-time-level semi-lagrangian scheme (*Hortal,* 2002).

The ALARO-1vB upper air physics setting (*Brožková et al.*, 2019) and ISBA surface scheme (*Noilhan* and *Planton,* 1989) with CY43t2_bf11 code version are largely applied. The parameterization of turbulence (sometimes modified in ALARO experiments described later) includes the emulated TKE-based scheme (*Ďurán et al.*, 2014; 2018) denoted as model II (MD2) and the Geleyn-Cedilnik formulation of the mixing length (*Cedilnik et al.*, 2005; *Geleyn et al.*, 2006). The global model ARPEGE provides lateral boundary condition (LBC) data 4 times/day with 3-hourly frequency. For initial conditions the operational ALADIN/SHMU system uses spectral blending by digital filter algorithm for upper air atmospheric fields (*Derková* and *Belluš*, 2007). For surface data assimilation, the optimal interpolation scheme denoted CANARI (*Giard* and *Bazile*, 2000) is applied. See *Derková et al.* (2017) for more details on the current operational version of ALADIN/SHMU.

2.1.2. A-LAEF system description

The former utilization of ensembles at SHMÚ has been restricted mostly to the global systems (ECMWF ENS, GEFS), which were used mainly for the medium-range forecasts. Recently, a new short-range ensemble weather forecasting system A-LAEF (ALARO Limited Area Ensemble Forecasting), available to our forecasters since July 2020 (*Belluš,* 2020a*; Belluš et al.,* 2019), can offer, among the other enhancements, a 4-times higher spatial resolution than its predecessor. Technically, it is a sequel to the former ALADIN-LAEF system developed within the RC LACE cooperation (Regional Cooperation for numerical weather modeling on Limited Area in Central Europe, *Wang et al.,* 2017a). The ALADIN-LAEF system had been operational at ECMWF since 2011 (*Wang et al.,* 2011) until recently, when it was replaced by the A-LAEF system. Moreover, the new A-LAEF system has increased horizontal and vertical resolution (4.8 km/60 L), and involves new perturbation techniques. The key components of the A-LAEF ensemble system are the followings:

- o Multi-physics based on ALARO-1 parameterizations, which can seamlessly operate on the horizontal scales from 2 to 10 km (*Termonia et al.,* 2018) and is capable of simulating the uncertainty on meso-synoptic scales. There are 4 different groups of settings for turbulence, microphysics, deep and shallow convection, and radiation parameterizations, hereafter referred to as MP clusters (*Belluš*, 2019);

o Ensemble of surface data assimilations ESDA (*Belluš et al.,* 2016) with the upper-air spectral blending by digital filter initialization (*Derková* and *Belluš,* 2007);

o The stochastic perturbation of physics tendencies for the surface prognostic fields (*Wang et al.,* 2019).

Concerning turbulence, the emulated QNSE parameterization of turbulent fluxes (*Sukoriansky et al.*, 2005) and the Geleyn-Cedilnik mixing length limited in stable regimes (*Ďurán*, 2014) are applied in MP clusters 2 and 3, whereas members of the clusters 1 and 4 run with the same turbulence scheme as ALADIN/SHMU. The integration domain of A-LAEF system covers large area including Europe, the whole Mediterranean Sea, and the part of Western Asia (*Fig. 1*). The ensemble comprises 16 perturbed members and 1 control run coupled to the ECMWF ENS, and the probabilistic products are available twice a day (based on the 00 and 12 UTC runs) for the next 3 days.
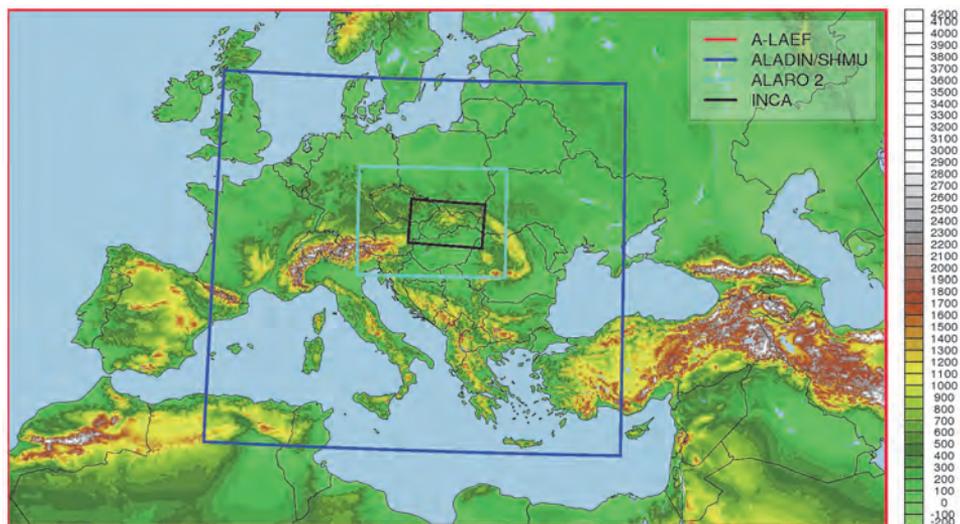
Fig. 1. Domains of the model configurations used in this study: A-LAEF (with model topography), and domain borders of ALADIN/SHMU, ALADIN/CHMI, ALARO 2 km, and of the INCA nowcasting system.

2.1.3. ALADIN/CHMI model description

The ALARO configuration run at CHMI (*Brožková et al.*, 2019, 2021) at 2.3 km horizontal resolution uses non-hydrostatic dynamics, spectral, semi-implicit 2-time-level iterative centered implicit scheme (*Bénard et al.,* 2010). The BLENDVAR method (*Bučánek et al.,* 2015) is applied for the analysis of the initial atmospheric fields. Incremental digital filter (*Fischer* and *Auger*, 2011) is applied for short cut-off production analysis.

The physical parameterization of this version is similar to ALADIN/SHMU but adapted for higher resolution (because deep convection and its effects are partially resolved, which is treated within the 3MT scheme). This ALARO version was used only for experiments with radar data assimilation (see Section 3), which is not available in ALADIN/SHMU yet.

2.1.4. ALARO 2 setup description

An ALARO version similar to ALADIN/CHMI is used at SHMÚ at horizontal resolution 2 km in dynamical adaptation mode without assimilation cycling and on a smaller domain (due to computational costs). The model uses digital filter initialization (*Lynch et al.,* 1997). The role of the digital filter is to filter out the noise introduced by the interpolation of LBCs into target resolution and to ensure higher numerical stability at the beginning of the run. Although running daily, the model is not considered to be fully operational, and its purpose is in testing and tuning of the physical parameterization and gaining experience with the convection-permitting mode (important for the future upgrade of the current ALADIN/SHMU to higher resolution). Several experiments in this study were based on the ALARO 2 experimental setup with certain modifications (described later).

2.2. Postprocessing and diagnostic methods

2.2.1. Parameters of convective environment

Processing of the ALADIN/SHMU outputs involved calculation of convective parameters and indices averaged for longer (3h) timescales, including surface-based convective available potential energy (SBCAPE), low-level divergence (average of the 980, 950, 925, 900, 875, 850 hPa divergence), relative humidity (average of the 2, 300, 500, 750, 1000, 1500, 2000, 3000 m AGL humidity) and 0-6 km wind shear. Averaging was used to characterize the prevailing conditions and environment of deep convection focusing on instability, humidity and saturation of the air, lift, shear during periods for which accumulated precipitation was calculated. These parameters were based on the forecasts of the operational ALADIN/SHMU model.

2.2.2. Cloud top height and temperature assessment

Cloud top height and cloud top temperature (CTT) were estimated from ALARO 2 outputs (simulated brightness temperature is not available as a diagnostic parameter yet). Cloud tops were identified upon thresholds of cloud ice (CLI) or cloud liquid water (CLW) mixing ratios forecast by the models. Further, extinction coefficients for ice were assessed from CLI (*Stoelinga* and *Warner*, 1999). It is often considered that CLW exceeds 0.01 gm^{-3} in water clouds (*Kokhanovsky*, 2004), and the extinction coefficient for ice in thick cirrus clouds is about 1.0 km^{-1} (*Platt*, 1997). However, in the presented case, the identification thresholds had to be higher (0.02 gm^{-3} for CLW and 2.5 km^{-1} for the CLI extinction coefficient) to better distinguish the top of a precipitating convective cloud from a cirrus cloud aloft. The algorithm also evaluated the depth of the cloudiness inferred from CLW and CLI profiles and the maxima of these parameters.

2.3. Observation data used for experiments evaluation

For evaluation of precipitation forecasts, analyses of the INCA nowcasting system (*Méri et al.*, 2018, 2021) were used, which process inputs from both AWS and radar observations. At SHMÚ, hourly analyses of precipitation are generated on a 1×1 km resolution domain. Radar reflectivity data were from the composite of Slovak, Hungarian, and Czech radars operated by SHMÚ, OMSZ, and ČHMÚ national meteorological services (*Jurašek et al.*, 2017; *Sipos et al.*, 2021; *Novák et al.*, 2019). These images have 660 m horizontal resolution and leaflet.js API was used for the visualisation with Wikimedia maps in the background (*Leaflet*, 2021; *Wikimedia*, 2021). Column maximum radar reflectivity data (Cmax) were retrieved with projections of the vertical profiles of the maximum reflectivity to four sides of the image (from the central axis toward the respective side). The constant altitude plan position indicator (CAPPI) horizontal cross-sections at 2 and 3 km height were generated for determination of the type and structure of convective cells. Doppler radar velocity measurements were analyzed from plan position indicator (PPI) data at 0.5, 1.0, 1.5, and 2.0 degree of antenna elevations measured by respective SHMÚ radars with 250 m gatewidth. The Nyquist velocity interval for these PPI data was ±40 m/s. Cloud top brightness temperature (CTB) data were inferred from 5 minute Rapid Scanning Service (RSS) satellite data from the METEOSAT 10 EUMETSAT IR 10.8 μm imagery with use of the MSGProc/ViewMSG programs (*Kaňák*, 2006). The horizontal resolution of the original data was nearly 3 × 3 km in the area of Slovakia. For better geolocation of the coldest cloud areas, the data were transformed to higher resolution with 0.0040 degrees per pixel in longitudinal and 0.0027 degrees per pixel in latitudinal direction with linear interpolation.

3. Description of experiments

Model experiments in the June 7, 2020 case were run with various types of input data or setups in data assimilation, dynamics, or physical parameterization (*Table 2*), which were sometimes different compared to the operational one. Data assimilation has been developed and tested mainly in the frame of the hydrostatic ALADIN/SHMU model (with radar data assimilation as exception). Predictability of the convective events in this case was studied with the operational version of the A-LAEF system. Here, the main focus was on the accuracy of the 3 h precipitation forecast, concerning both intensity and spatial distribution of precipitation. Experiments related to model dynamics and diagnostics applied the convection-permitting configuration, close to ALARO 2. These runs were used to explore the numerical stability and effectiveness/performance of such configuration, and concentrated on non-hydrostatic features and life-cycle of individual cells.

Table 2. Labelling and description of experiments.

Experiment label	Basic model version/domain	Description
P432	ALADIN/SHMU	Reference version for BLENDVAR experiments. No upper-air data assimilation, only blending by DF.
ZTDS	ALADIN/SHMU	BLENDVAR experiment with HRWIND AMV and GNSS ZTD with static whitelist in 3D-Var.
AWS1	ALADIN/SHMU	BLENDVAR experiment with HRWIND AMV and local AWS from OPLACE in 3D-Var.
ALLD	ALADIN/SHMU	BLENDVAR experiment with all available high-resolution data: HRWIND AMV, GNSS ZTD, local AWS, EMADDC and OPLACE Mode-S, high resolution BUFR TEMP in 3D-Var.
C-REF	ALADIN/CHMI	ALADIN/CHMI reference.
C-RAD	ALADIN/CHMI	ALADIN/CHMI, with OPERA radial winds.
ID00	ALARO 2	Reference ICI scheme without NHHY parameter, 73 model levels.
ID01	ALARO 2	SI scheme with NHHY=1.2.
IH00	ALARO 2	As ID00 but with 1 km resolution and 100 levels.
IH01	ALARO 2	As ID01 but with 1 km resolution and 100 levels.
SWDIAG	ALARO 2	73 model levels, ZTDS data for surface analysis, QNSE parameterization of turbulent fluxes, limitation for the Geleyn-Cedilnik mixing length.

3.1. Data assimilation experiments

As mentioned in Section 2.1, for initial conditions of the upper-air atmospheric fields, the operational ALADIN/SHMU system uses spectral blending by digital filter (DF) technique - without a direct use of observations. An extension of this operational setup is proposed by an introduction of the three-dimensional variational data analysis (3D-Var) step. 3D-Var is operationally used in similar ALADIN systems and many other LAM NWP models worldwide (*Gustafsson et al.*, 2018). Our goal is to use a combination of DF blending step and 3D-Var (BLENDVAR) configuration (*Bučánek et al.*, 2015). Such a combination enables us to benefit from large scale analysis provided by 4D-Var data assimilation of the global model Arpege via DF blending, and to improve the small scales description by using high resolution observations within ALADIN 3D-Var.

In the basic BLENDVAR prototype at SHMÚ, the conventional observations (AMDAR, SYNOP, TEMP) and AMV HRWIND are utilized in the upper-air 3D-Var. The observation data are taken from OPLACE – a common operational database of RC LACE (*Trojáková et al.*, 2019). Downscaled ensemble background error covariance matrix is applied (*Bučánek* and *Brožková,* 2017). No change in surface assimilation with respect to operational setup is made. Also, the operational 6-hourly assimilation cycling interval was kept. This BLENDVAR configuration is not yet superior to the operational versions in terms of the objective verification scores (not shown). Therefore, new sources of high resolution observations are being tested aiming to improve the small-scale features. These comprise:

o An extended set of about 500 national automatic weather stations (AWS) reports from OPLACE, that is not available in GTS;

o Zenith total delays (ZTD) data from almost 60 GNSS stations processed at the Slovak University of Technology (*Imrišek et al.*, 2020);

o The Mode-S aircraft measurements available from OPLACE, used with a thinning distance of 25 km, and 1500 Pa: EHS data from EMADDC and MRAR data from the Czech Republic and Slovenia;

o High resolution radiosonde data in BUFR format, that enables to take into account real positions of measurements both in space and time. Total increase of the assimilated data amount is quadrupled;

o Radial wind velocity data from the OPERA OIFS project, used with a thinning distance 8 km (*Čatlošová*, 2020).

A typical increase of data amount of individual datasets listed above compared to basic 3D-Var setup is shown in *Table 3*.

Table 3. Number of observation reports and number of individual data typically assimilated in a reference 3D-Var setup (left) and in the experiments with enhanced data sets (right) for the 12 UTC network

observations	reference 3D-Var setup		enhanced observations usage	
	No of reports	No of data	No of reports	No of data
SYNOP/AWS	~1500	~5000	~2000-2200	~6000
GNSS ZTD	-	-	~55	~55
AMDAR/Mode-S	~350	~1000	~4500	~13 000
HRWIND AMV	~50-100	~100-200	~50-100	~100-200
TEMP radiosonde	~60	~14 000	~60	~70 000
Radial wind velocities	-	-	~33 000	~370 000

The series of BLENDVAR experiments were run for the case study of June 7, 2020 and the impact on the precipitation forecast was evaluated. In each experiment a different high resolution observation set was utilized, as summarized in *Table 2*. The experiment setup consisted of 3 days of assimilation cycling starting from June 4, 2020, 00 UTC. Then the production forecast was launched for 00 and 12 UTC.

3.2. *Convection permitting experiments: non-hydrostatic dynamics*

For realistic simulation of phenomenon at kilometric and hectometric resolutions, the non-hydrostatic equation system must be exploited. The iterative centered implicit (ICI) integration scheme (*Bénard*, 2003) is implemented in the current dynamical core, because the original semi-implicit (SI) scheme with stable extrapolation SETTLS (*Hortal*, 2002) used for the hydrostatic system was found unstable.

In order to achieve stability of the ICI scheme already after the first iteration, the linear operator associated with the semi-implicit scheme must include two reference temperature profiles (*Bénard*, 2003, 2004). Because the real atmosphere can not have two profiles at the same time, the linear operator can not be obtained by linearization of the nonlinear system around the reference state.

This leads to the idea that there exists a class of linear operators that would stabilize the SI time stepping with SETTLS extrapolation for a non-hydrostatic model as well. To investigate the idea, a class of new operators was defined, where

each equation is written as the sum of hydrostatic linear operator terms plus non-hydrostatic departure terms. The departure terms in each equation are weighted by the unique constant parameter. When all parameters are set to 1, the non-hydrostatic linear operator is obtained. If the parameters are set to 0, the linear operator yields to the hydrostatic one. Therefore, the approach is called NHHY, when the linear operator is modified using an additional set of parameters. The feasibility of elimination into a single variable Helmholz solver for horizontal divergence provides constraints between parameters, and the final spectral solver contains only two additional tunable parameters concerning the existing state. The paper with detailed description is currently in preparation.

A set of experiments was performed to validate the stability of NHHY approach summarized in *Table 4*. Two model configurations were tested, derived from the experimental ALARO 2 setup. First configuration was run at the resolution of 2 km, 73 levels, and time step 120 s (experiments ID00 and ID01), and the second one with resolution 1 km, 100 levels, and time step 60 s (IH00 and IH01 experiments). The stability and efficiency of SI SETTLS scheme with NHHY parameters equal to 1.2 was compared against reference results obtained with the ICI scheme. The results are discussed in the Section 4.5.1.

Table 4. Performance of various experiments with ALARO model dynamics with 2 km and 1 km horizontal resolution, see *Table 1* and *Table 2* for the basic setup

Experiment	ID00	ID01	IH00	IH01
Integration time of 15 h forecast [s]	129	92	877	701

3.3. Convection-permitting experiments: structure and evolution of convective cells

The SWDIAG experiment applied the emulated QNSE parameterization of turbulent fluxes and the Geleyn-Cedilnik mixing length limited in stable regimes as in the A-LAEF 2nd MP cluster (see Section 2). The analysis of the ZTDS assimilation experiment (*Table 2*) was used as well. This combination provided better agreement with precipitation observation as the reference ALARO 2 setup (mainly in temporal and spatial distribution of intense convection), which was important for the diagnostics of severe weather (Section 4.5) and comparison of forecast and observed cloud properties.

4. Case study and results

4.1. General description

The region of Slovakia was situated in a moist, warm, and buoyant air mass ahead of a cold front, which was slowly propagating eastward (and reached the borders of the Czech Republic and Slovakia on June 7, 2020, at around 20 UTC). Deep convective clouds started to form after 08 UTC and propagated northward. Thunderstorms typically occurred along prefrontal convergence lines (*Fig. 2a*). The radar images and animations indicated lines of multicells and multicellular development. Mesocyclonic storms were not documented in Slovakia, although a tornado was reported from Kaniów, southern Poland, at around 12 UTC (ESWD, 2020). In the afternoon hours (12-14 UTC), the most intense thunderstorms were developing in the proximity of a very long convergence line over western Hungary and Slovakia, continuing to southern Poland (denoted line L1). These thunderstorms caused heavy rain and hail. There were numerous reports above all from Hungary, e.g., from the surrounding of Esztergom and Dorog at the border to Slovakia (*Dorog-Esztergom Időjárása*, 2020). Overall 30.8 mm of precipitation was reported from the close meteorological station at Tát (*OMSZ*, 2020). It is probable that these events can be attributed to the cell denoted C1. Later, convection dissipated along the L1 line, but another one (L2) formed over southwestern Slovakia at around 18 UTC causing local flash floods (*Fig. 2b*). A related car accident was noted near Tesárske Mlyňany probably in relation with a heavy thunderstorm denoted C2. Large hail was reported from Michalovce in the eastern part of Slovakia at around 20 UTC (cell C3). The numerical simulations of the event mostly concentrated on the above mentioned dominant features.
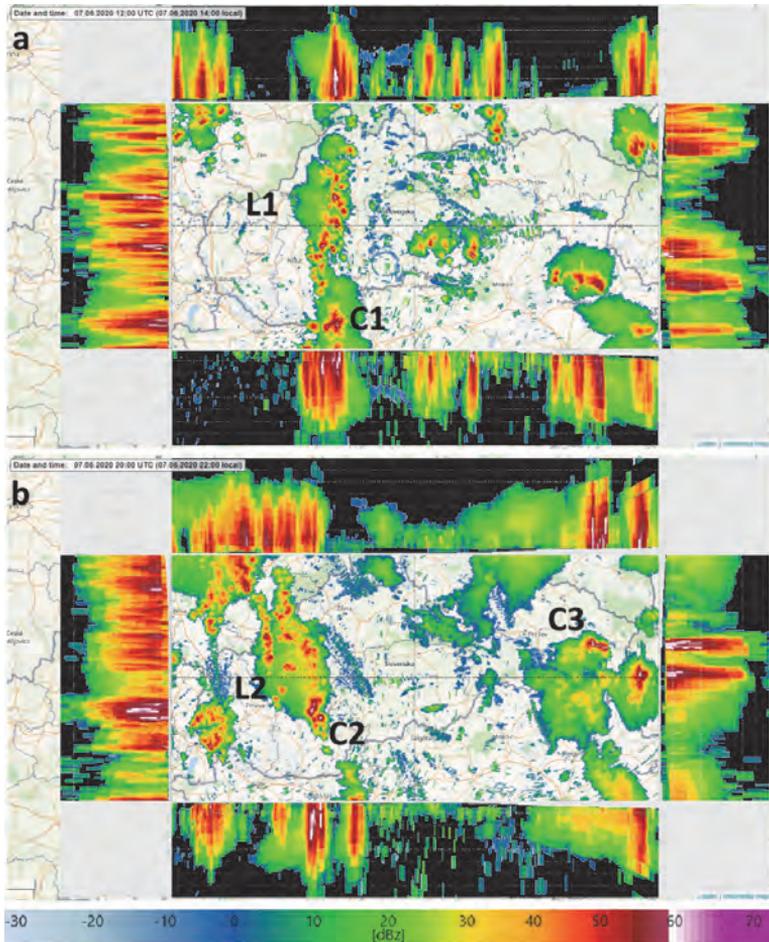
Fig. 2. Column maximum (Cmax dBz) radar reflectivity of the SHMÚ, ČHMÚ, and OMSZ composite imagery with side views (vertical profiles with 2 km mesh): a) valid for June 7, 2020, 12:00 UTC (L1 and C1 denote convergence line and cell investigated in the study); b) valid for June 7, 2020, 20:00 UTC (L2, C2, and C3 refer to significant convective features studied during this period).

4.2. Convective environment

The forecasts of the deterministic ALADIN/SHMU 00 UTC model run for the 12-15 UTC period of June 7 (*Fig. 3*, top left) showed high surface-based CAPE (mostly exceeding 1000 J/kg) over Slovakia, which also corresponded with TEMP rawinsonde reports (SBCAPE of 1523.6 J/kg assessed from Budapest and 810.26 J/kg from Gánovce soundings at 12 UTC). Moist areas could be seen on the averaged 0-3 km relative humidity image for the central part of Slovakia,

whereas the air over southwestern Slovakia was less saturated (*Fig. 3*, top right). The peak 0-500 m specific humidity (exceeding 12 g/kg) and total precipitable water (around 34 mm) was situated over the southern part of central Slovakia, east of L1 (not shown), which coincided with CAPE maxima, and the model development of the deep convection was also largely preferred in this region. It could be deduced that divergence of flow was rather prevailing in the southwestern flank of Slovakia and over its eastern part, while low-level convergence areas appeared more frequent over the central part of Slovakia – although its distribution was highly influenced by the rugged orography in this region (*Fig. 3*, bottom left). There was only little wind shear between the 10 m and 6 km heights over the western part of Slovakia (*Fig. 3*, bottom right), which probably explains the lack of organized convective systems in this region and the typically multicellular behavior of the convection.

In the evening hours (18-21 UTC), the air was still conditionally unstable with maximum SBCAPE just over the southern part of L2 (exceeding 1400 J/kg – not shown). The wind shear also slightly increased over this area – probably as a consequence of the approaching cold front.
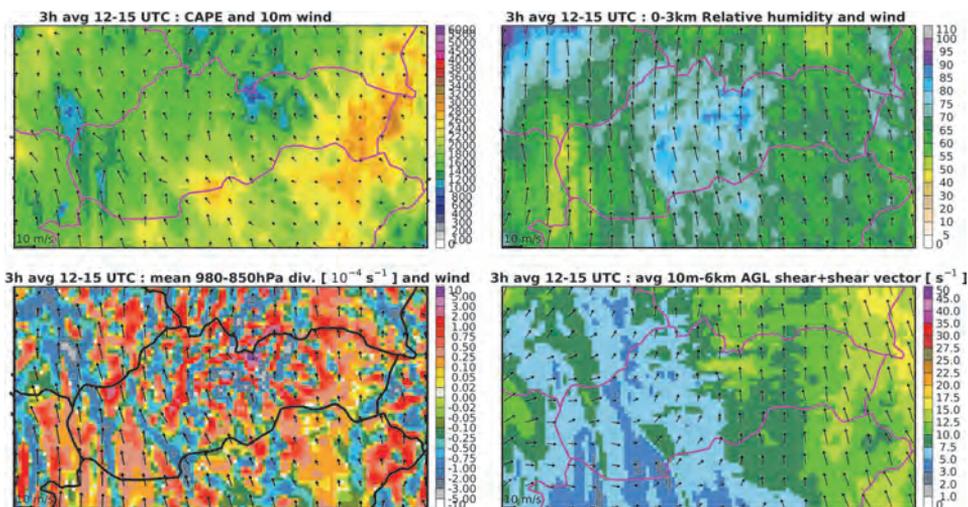
Fig. 3. Forecasts of the ALADIN/SHMU convective environment parameters based on June 7, 2020, 00:00 UTC and time-averaged for the 12-15 UTC period of the same day. Upper left: SBCAPE [J/kg] and 10 m wind [m/s], upper right: 0-3 km relative humidity [%] and wind [m/s], lower left: 980-850 hPa divergence [10^{-4} s^{-1}] and wind [m/s], lower right: 10m-6km AGL wind shear [s^{-1}] (absolute value in shades).

4.3. Operational models and data assimilation experiments

4.3.1. The 12-15 UTC period (along the line L1)

The most intense precipitation in this period occurred in the western part of Slovakia with a maxima exceeding 30 mm/3 h (*Fig. 4,* top left). The spatial coverage and intensity of the forecast precipitation was underestimated in the 00 UTC run of the operational SHMÚ model (*Fig. 4*, top right). In the operational A-LAEF output, the position of the intense precipitation fitted better the observed distribution in the western part of Slovakia in average (*Fig. 4*, bottom left) and coincided with the position of the L1 line. There was less certainty regarding the position and intensity of the extremes, but the EPS maxima predicted 20-30 mm peaks along the main convergence line (*Fig. 4,* bottom right). Operational deterministic forecast was improved using 3D-Var data assimilation of high resolution observations. Any of BLENDVAR experiments yield more realistic precipitation forecast against the reference P432 shown in *Fig. 5*, upper right plot – both the position of precipitation patterns and their intensities were captured better. The most promising experiment utilized humidity information from ZTD GNSS data (*Fig. 5*, middle left plot), although the most intense precipitation was situated at least 50-70 km south of the observed one. There were also more precipitation patterns over Hungary and northwestern Slovakia. Even stronger convective activity near the cell C1 of *Fig. 2a* was indicated in the AWS1 experiment with an enhanced number of assimilated automatic weather stations (*Fig. 5*, middle right plot). These results suggest, that this convective case was rather sensitive to initial conditions, where any change led to a slightly different forecast. The impact of utilization of radial wind velocity measurements from meteorological radars was checked independently, as those experiments were conducted using ALADIN/CHMI configuration within an RC LACE scientific stay. In this case the reference forecast (C-REF, *Fig. 5*, bottom left plot) was already much better than the ALADIN/SHMU one, also due to the higher resolution of ALADIN/CHMI (2.3 km/L87) and its non-hydrostatic dynamics. With assimilation of radial winds, the precipitation coverage was changed and more local precipitation patterns appeared - albeit not always correctly. The local maxima near the C1 cell on the border of Slovakia and Hungary were more realistic (C-RAD, *Fig. 5*, bottom right plot).
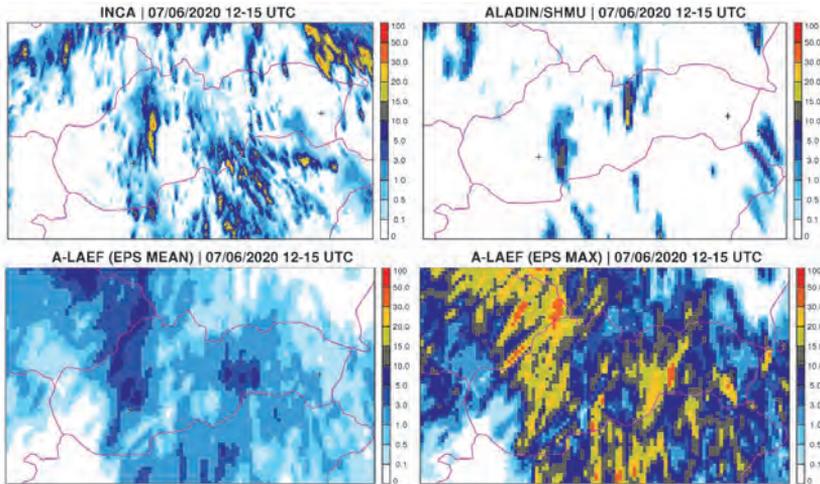
Fig. 4. 3-hourly precipitation accumulation [mm] for June 7, 2020, 12-15 UTC period: from INCA analysis (top left); ALADIN/SHMU operational forecast (top right); A-LAEF ensemble mean (bottom left); A-LAEF maximum of ensemble (bottom right). The model forecasts are based on the 00 UTC run.
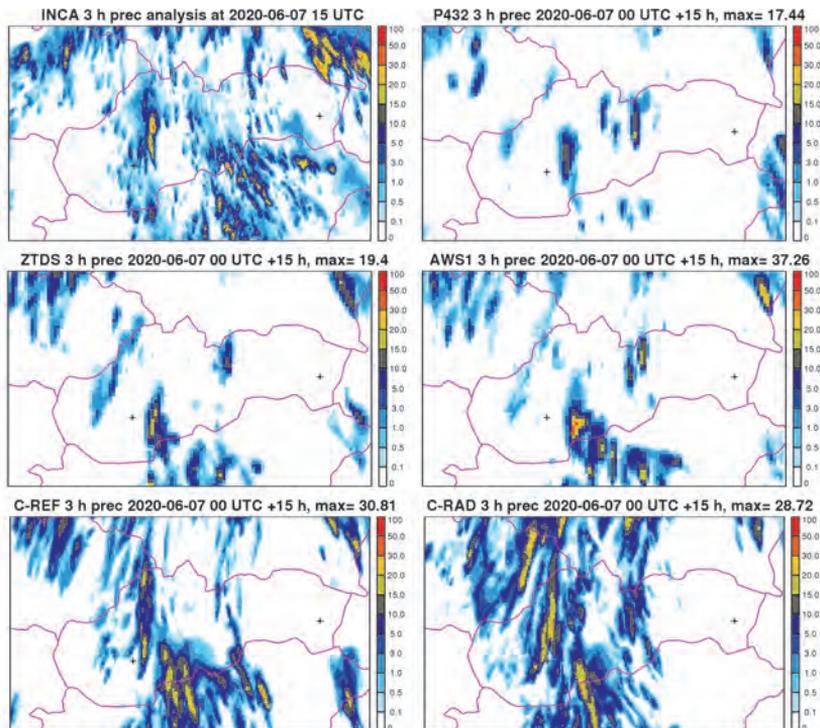
Fig. 5. 3-hourly precipitation accumulation [mm] for June 7, 2020, 12-15 UTC period: INCA analysis (top left); P432 reference experiment (top right); and BLENDVAR data assimilation experiments referred in *Table 2*: ZTDS (middle left), AWS1 (middle right), C-REF (bottom left), and C-RAD (bottom right). All model forecasts are based on the 00 UTC run.

4.3.2. The 18-21 UTC period (line L2, cells C2 and C3)

In the evening period, the operational SHMÚ forecast (based on both 00 and 12 UTC runs) predicted the cold front-related precipitation but not the heavy rainfall on the convergence line L2 (*Fig. 7*, second image in the first row). Some additional (but rather weak) patterns could be seen also in southeast Slovakia, in relation with C3. The BLENDVAR experiment with additional ZTD data (ZTDS, *Fig. 6*, middle left panel) remarkably improved the localization of precipitation along the convergence line L2, and indicated the presence of the convective cell C2 (to be compared to INCA analysis, *Fig. 6* top left panel, and P432 reference, *Fig. 6* top right panel). The false precipitation over Moravia and southwestern Slovakia were reduced. Precipitation forecasts based on the experiment, where 3D-Var comprises a whole enhanced set of data (ALLD, *Fig. 6*, middle right panel), maintained overall improvement with respect to the P432 reference, but some of the local features became lost. All BLENDVAR experiments failed to predict precipitation over central Slovakia and on the border with Poland. Experiment with radial wind velocity data assimilation succeeded to indicate convective precipitation in western Slovakia, albeit the maximum was shifted too westerly. Development of the convergence line L2 was clearly indicated with respect to the reference forecast. Precipitation patterns in central Slovakia were also present but easterly shifted, and a signal of convective activity in southern Poland and near the Ukrainian border was correct (*Fig. 6*, bottom right panel).
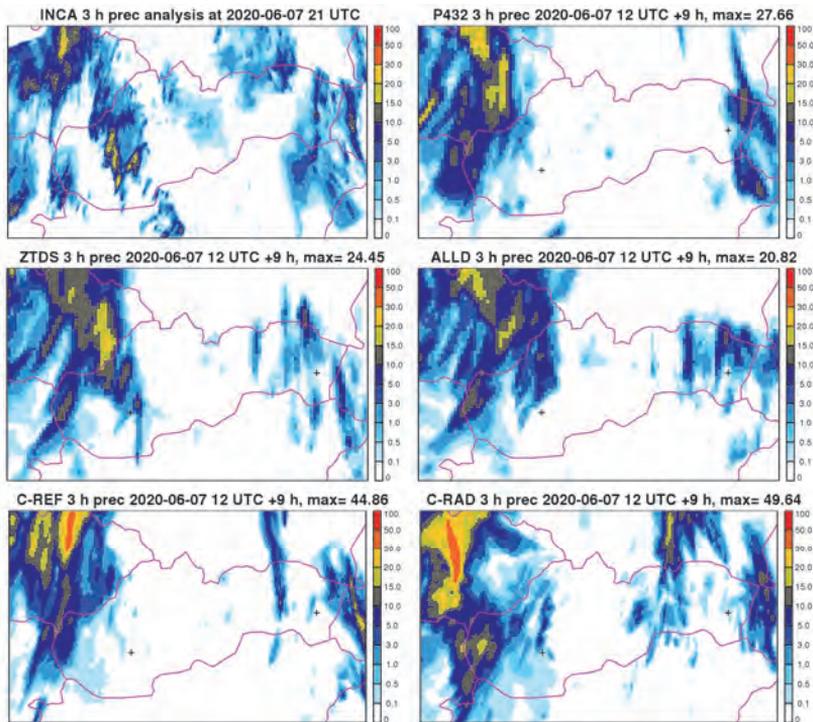
Fig 6. 3-hourly precipitation accumulation [mm] for June 7, 2020, 18-21 UTC period: INCA analysis (top left); P432 reference experiment (top right); and BLENDVAR data assimilation experiments referred in *Table 2*: ZTDS (middle left), ALLD (middle right), C-REF (bottom left), and C-RAD (bottom right). All model forecasts are based on the 12 UTC run. Position of Tesárske Mlyňany and Michalovce is marked by black crosses.

Some members of the A-LAEF system were able to provide a correct forecast of the heavy precipitation in the areas of C2 or C3 or very close to them (*Fig. 7*, except the first row). There were no significant systematic differences between the forecasts of EPS members belonging to respective MP clusters. Thus, in this situation it is likely that the differences related to ESDA or stochastic physics had an impact on the precipitation distribution in the respective members rather than the choice of the physical parameterization.
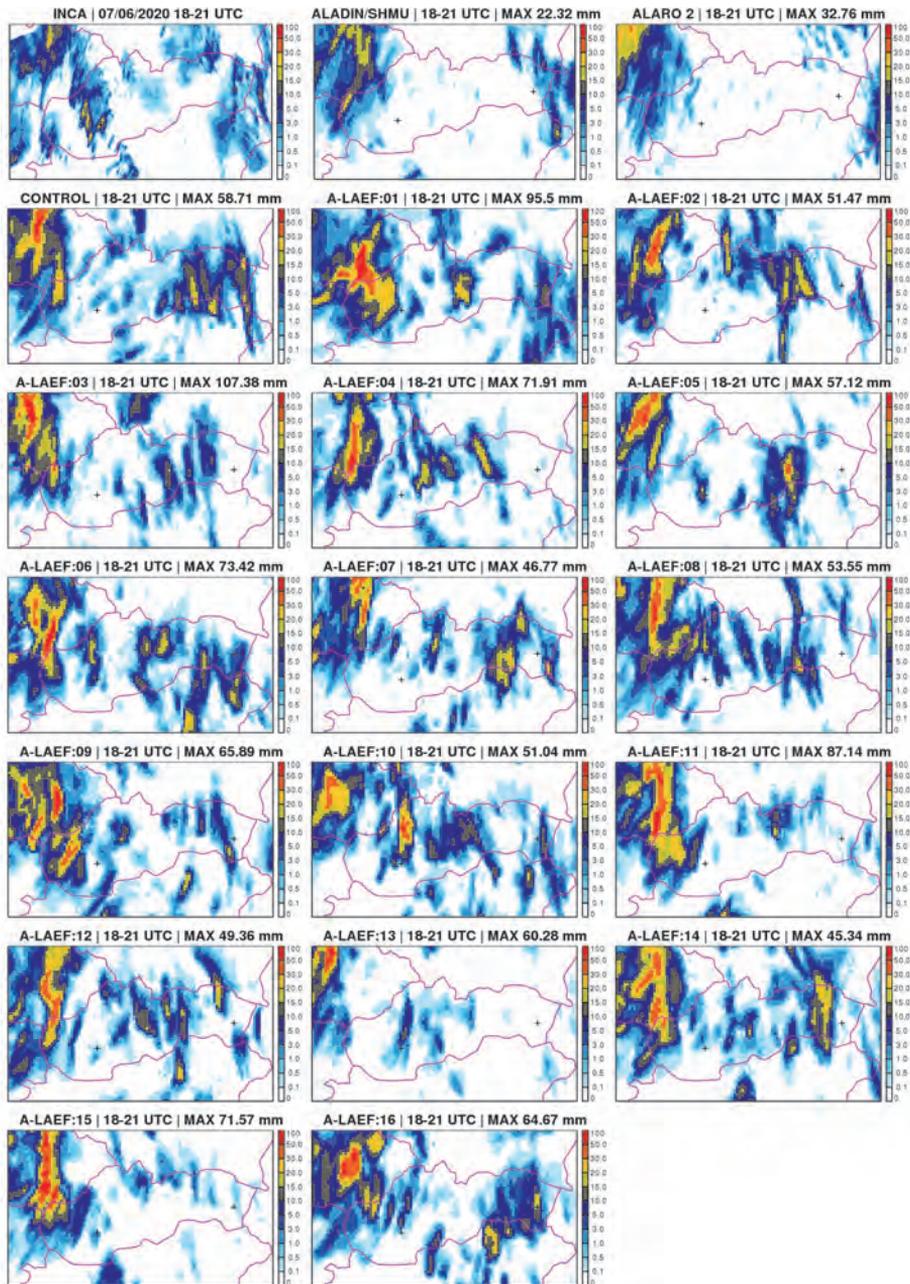
Fig. 7. 3-hourly precipitation accumulation [mm] of INCA analysis for June 7, 2020, 18-21 UTC period, corresponding forecasts of the operational ALADIN/SHMU and non-hydrostatic ALARO 2 km models based on the 12 UTC (first row), followed by the A-LAEF forecasts of EPS members based on the 12 UTC and valid for the same period as analysis. Several EPS members demonstrated the ability of forecasting precipitation near C2 and C3 related events at Tesárske Mlyňany and Michalovce (their position marked by crosses).

4.4. Probabilistic outputs and predictability of convective precipitation

As it was already discussed in the previous subsection (Section 4.3), the probabilistic approach of the A-LAEF system was clearly more successful in predicting the convective event of June 7, 2020 than the operational deterministic model. This is especially true for the evening period, when the deterministic forecasts failed to generate strong enough convective activity. Even the reference non-hydrostatic ALARO 2 model with higher spatial resolution was too dry in eastern Slovakia, where in reality a high precipitation event C3 occurred (*Fig. 7*, third image in the first row). Among the ensemble members of A-LAEF system there were different scenarios. In some of them the eastern Slovakia was similarly without precipitation - e.g. members 04 and 13, while the other members captured the C3 event in correspondence with INCA analysis pretty well - particularly members 01, 06, 09, 10, 14, 16 (*Fig. 7*). It can be concluded that small differences due to uncertainty simulation in the initial and boundary conditions as well as the stochastic perturbation of physics tendencies were the driving forces in this situation. Thus, taking into account the above-mentioned scenarios would be crucial for considering the predictability of this event. Furthermore, for June 7, 2020 situation it could be shown that along the convergence lines with highest assumed precipitation, there was also a high spread. While for the afternoon convection the spread was typically 5-10 mm along L1 (not shown) and the probability of at least low precipitation (exceeding 1 mm) was 70-80% (*Fig. 9*, left), the spread was higher (10-20 mm) in case of the evening, prefrontal convection along L2 (*Fig. 8*, left). This was partially because of the more intense convection and higher EPS maxima (*Fig. 8*, right) but probably also due to higher uncertainty in forecasting the precipitation occurrence concerning this event (note that the forecasts of L2- and C3-related precipitation were of shorter range than that of L1). The probability of precipitation exceeding 1 mm was mostly below 50% in the vicinity of L2 and C2, despite the high precipitation forecast by some EPS members (*Fig. 9*, right).
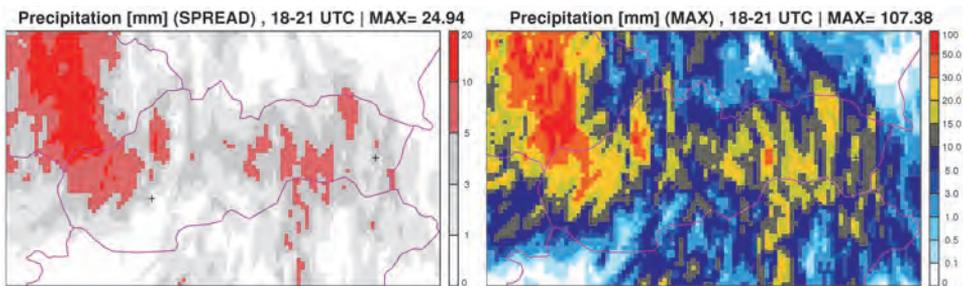
Fig. 8. Forecast of the A-LAEF EPS system based on June 7, 2020, 12 UTC and valid for the 18-21 UTC period: 3-hourly precipitation spread [mm] (left), EPS maximum of 3-hourly accumulated precipitation [mm] (right).
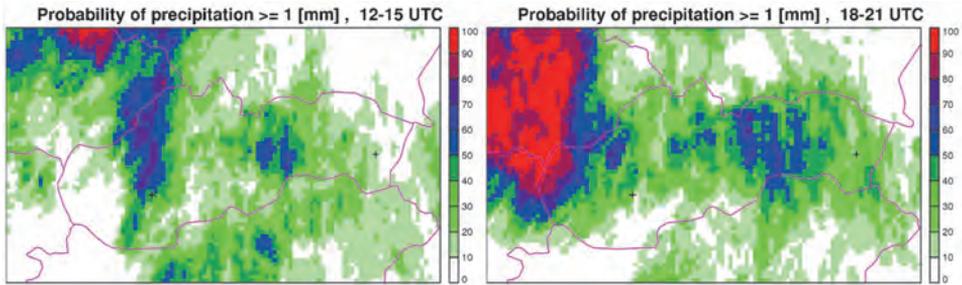
Fig. 9. Probability of precipitation for 1 mm threshold based on the A-LAEF EPS forecast from June 7, 2020, 00 UTC valid for the 12-15 UTC period (left), and from 12 UTC valid for the 18-21 UTC period (right).

4.5. Convection-permitting experiments

4.5.1. Dynamics optimization (from stability and performance perspective)

The experiments listed in *Tables 2* and *4* are described in this subsection. As it can be seen in *Fig. 10*, the SI SETTLS scheme was stabilized using NHHY parameters set to 1.2 at resolution 2 km (ID01). The overall character of the solution is the same as the one computed with ICI reference (ID00). First row presents the 3 h precipitation forecast from June 7, 2020 at 00 UTC for 12-15 h. There is no signal that would indicate instability in the solution. The green line on precipitation maps shows the direction of the vertical cross section via the line of convective cells. The cross sections are shown in the second row of *Fig. 10*. The structure of the cell is consistent in both experiments. The order of differences is typical for this kind of modification in advanced NWP systems, where complex feedback mechanisms are taking place under small forcing, especially in convective situations.

The same experiments were carried out with a 1 km version of the model as well (IH00 and IH01). The NHHY scheme was stable as well. The results are not presented here as qualitatively they were not relevant, because the physical parameterizations are scale-dependent and would require tuning, which was out of scope of this paper.
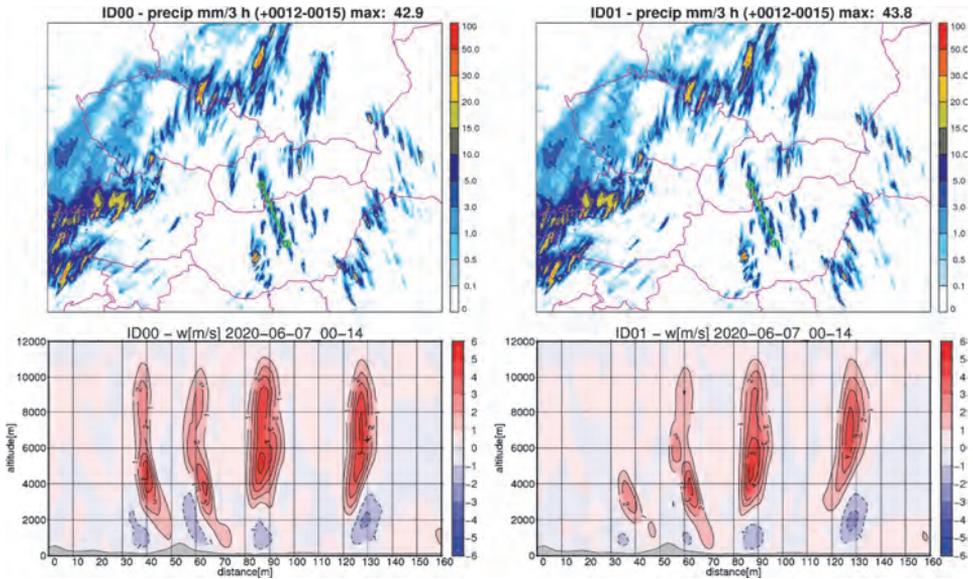
Fig. 10. The first column contains forecasts obtained with the reference ICI scheme and the second column with the NHHY scheme. In the first row, 3-hourly precipitation accumulation [mm] for June 7, 2020 is presented, 12-15 UTC period, left: ID00 with ICI scheme, right: ID01 with the NHHY scheme. The vertical cross section via convective cells (shown by green line in first row pictures) is at the second row.

4.5.2. Structure and evolution of convective cells

The non-hydrostatic experiments focused mainly on small-scale (meso-gamma) features, of which some could be observed on the radar imagery, mainly in the 12-15 UTC period (notably the C1 cell). The model runs produced several individual convective cells exhibiting 2-5 m/s vertical velocities at 700 hPa (extremes were up to 7 m/s in the levels above) and 2-3 m/s downdrafts. An intense and relatively persistent (could be traced between 11:50 and 13:30 UTC) updraft formation moved from Hungary toward southern Slovakia (*Fig. 11*, left). Initially, it was a cluster of several individual cells aggregating into one (not shown). The closest strong and relatively stable pattern in the radar reflectivity field was the C1 (*Fig. 11*, right), which could have also consisted of several updrafts. It could also have a WER (weak echo region) signature on its northwestern flank (could be seen as a shallow cave in the reflectivity field on several CAPPI 3 km images). Such signatures, when persistent, are sometimes associated with stronger updrafts or mesocyclonic circulation and inflow of the unsaturated environmental air (*Moller et al.*, 1994). One could see such

circulation in both storm-relative wind and vorticity fields in the vicinity of the strongest updrafts of the simulated cells, at mid-levels (mostly 700 and 500 hPa). The cyclonic vorticity was accompanied by lower geopotential (*Fig. 12*, left). For C1, one could identify weak azimuthal shear in the field of the radial Doppler velocity, close to the assumed WER signature (*Fig. 12*, right). Velocity differences of 5 m/s on 5 km distance were inferred between local maxima and minima, which corresponds to shear of about $0.001\ s^{-1}$. Not taking into account some noisy artifacts in the Doppler velocity, this shear could be rather a consequence of a weak cyclonic circulation than a supercellar MVS (mesocyclonic vorticity signature), which usually exhibits of about one order stronger shear (*AMS Glossary of Meteorology*, 2000). Similarly, the magnitude of vorticity of the simulated vortex was below $0.005\ s^{-1}$, and it could possibly be a kind of mesovortex (*Weisman* and *Trapp*, 2003) but rather confined to mid-levels. The simulated convection did not always propagate as an organized system, but new updrafts and cells were generated at the flanks of the downdrafts of older cells. For the investigated convective feature, a line of new updrafts emerged on the western and northern flanks of its outflow (*Fig. 13*, left). However, development of new rain patterns was rather sparse in the westward direction (not shown). On the radar imagery, one could see a line of new but weak cells westward of C1 (*Fig. 13*, right). These cells quickly decayed, probably as a result of unfavorable humidity and shear conditions over southwestern Slovakia.
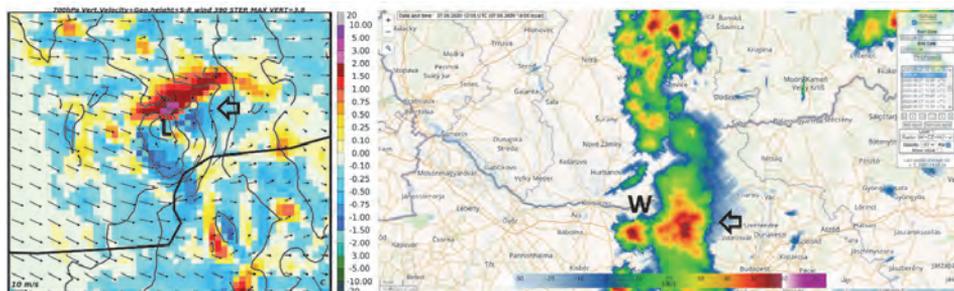
Fig. 11. Left: forecast of the ALARO 2 of the June 7,2020, 00 UTC run showing the field of 700 hPa vertical velocity (shades, m/s), geopotential height (lines, by 2 gpm), and storm-relative wind (m/s) valid for 13 UTC. The vector denoted "c" in the lower right corner depicts the storm motion vector. Right: CAPPI 3 km radar reflectivity (dBz) on June 7, 2020, 12:05 UTC. The arrow points toward the position of cell C1 defined by the vertical velocity on the left and toward the radar reflectivity maxima on the right. Letter W indicates the position of WER-like echo at the northwestern flank of C1. L highlights the local low in the geopotential field.
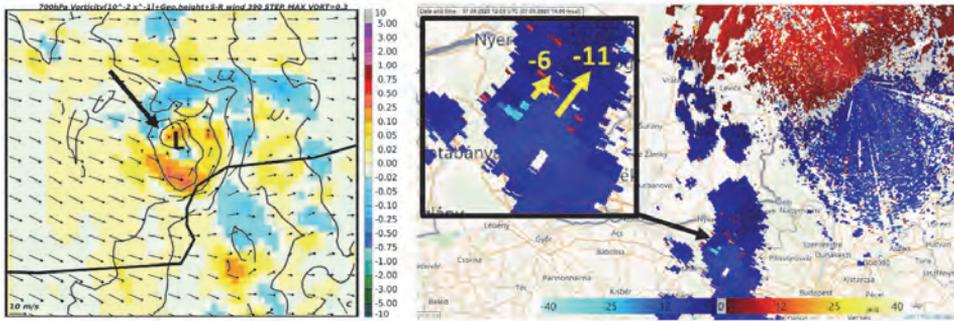
Fig. 12. Left: forecast of the ALARO 2 of the June 7, 2020, 00 UTC run showing the field of 700 hPa vertical vorticity (shades, 10^{-2} s^{-1}), geopotential height (lines, by 2 gpm), and storm-relative wind (m/s) valid for 13 UTC. Right: PPI 1.0° radial Doppler velocity (m/s) on June 7, 2020, 12:05 UTC. The arrow points toward the center of cyclonic circulation on the left and toward cyclonic shear in the radial Doppler velocity field on the right. Meaning of L as in *Fig. 11*. The enlarged detail depicts the region of azimuthal shear found in C1 in the Doppler velocity field (indicated by vectors and values in m/s).
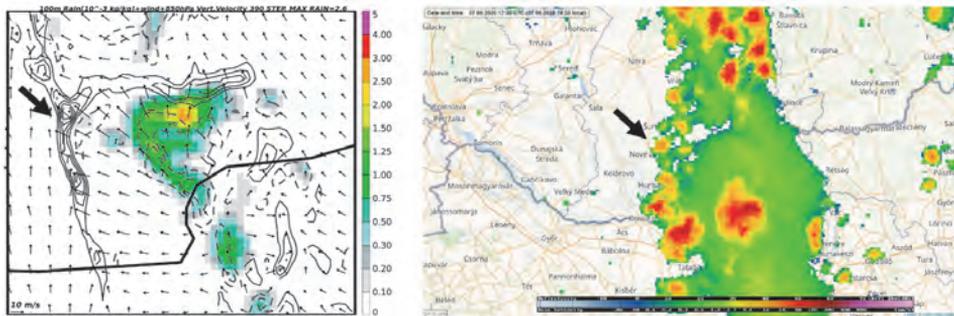
Fig. 13. Left: forecast of the ALARO 2 of the June 7, 2020, 00 UTC run showing the field of rain mixing ratio (shades, 10^{-3} kg/kg) , 850 hPa vertical velocity (lines by 0.5 m/s, solid – updrafts, dashed - downdrafts), and 100m wind (m/s) valid for 13 UTC. Right: Cmax radar reflectivity (dBz) on June 7, 2020, 12:30 UTC. The arrow points toward a line of updrafts generated on the leading edge of the cell outflow on the left, and a line of new cells emerging (and then quickly decaying) on the western flank of C1 on the right.

4.5.3. Comparison with satellite imagery

The speed of vertical growth of convective clouds depends on the intensity of their updrafts and vertical velocity, especially close to the top of the clouds. On the satellite imagery, the evolution of convection can be followed on the infrared

channels and CTB. The latter parameter is not exactly the temperature of the environment, but it largely depends on the air temperature at the same level (*Hanna et al.*, 2008). In fast evolving clouds with higher vertical velocities, the cooling of CTB is generally also faster. It was expected that in case that the magnitude of vertical velocities in the simulated clouds is similar to the real ones, one should also observe nearly similar CTT and CTB trends. The CTB and CTT comparison is reasonable during the rising phase of the convective cloud (thunderstorm), until it reaches its top and an anvil cloud is created. In case there is already a high cloudiness (cirrus clouds), the determination of the cloud top cooling rate becomes more difficult or not possible at all. There are also other limitations such as the resolution of the satellite imagery, which currently makes it difficult to trace the very early (cumulus) stage of the clouds.

For comparison, we selected rather isolated (not necessarily the most intense!) convective clouds on the satellite imagery, which had their counterparts in the SWDIAG experiment (developing at nearly the same time and place). An example was the convection over the southern part of central Slovakia, close to the Hungarian border (*Fig. 14*, left). The CTB of its clouds could be determined at 10:50 UTC, when it was -15 °C, and it reached its minimum (-55 °C) at 11:45 UTC (*Fig. 14*, right). According to the 12 UTC Budapest sounding, this temperature would be close to the air temperature at the tropopause (at 11 km height). The evolution of a similar cell in the model forecast started somewhat later (similar CTT as the satellite CTB appeared around 11:00 UTC). The minimum CTT (-53 °C) was reached in the mature stage of the cell and appeared 25 minutes later compared to CTB. The best agreement between CTT and CTB rate of cooling was in the temperature interval between -20 °C and -40 °C. Also in case of other cells (e.g., within L1) it could be seen, that the model cooling of the CTT is faster in the early stage of deep convection (i.e., the first 15-20 minutes of evolution) and it slowed down after, while opposite behavior was observed for the CTB course. Apart from technical reasons, this could also be related to the local environment and vertical distribution of buoyancy (e.g., presence of shallow inversions or stable layers, which slow down the growth of the thunderstorm clouds and which are often absent in the NWP forecasts).
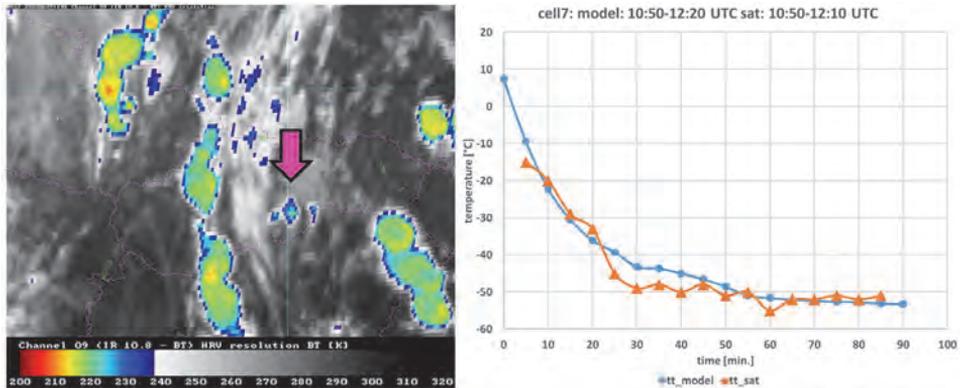
Fig. 14. Left: brightness temperature (K) from Meteosat 10 infrared 10.8μm channel over Slovakia on June 7, 2020, 11:45 UTC. The arrow points toward the convective cloud, of which the cloud-top temperature evolution was studied. Right: time-evolution of model-based cloud top temperature CTT in °C (blue line with circles) and satellite-based brightness temperature CTB in °C (orange line with triangles) of the cloud shown on the left. Both CTT and CTB curves start at 10:50 UTC. In the model, the evolution of a similar cell as investigated in the satellite imagery was delayed, but both curves were transposed in order to compare the rapid development phase of the convective cloud.

5. Conclusion and perspectives

In the presented situation, multicellular convection developed, occasionally causing severe weather. Especially point forecasts of such events is challenging, because the distribution of precipitation is very uneven, convection forms along relatively narrow convergence lines, which sometimes cannot be defined with sufficient precision in the model (due to the influence of orography but also outflows of previous convective cells and systems). Deterministic forecasting of heavy precipitation in such cases is difficult either by hydrostatic or higher resolution non-hydrostatic models – this is illustrated also by the fact that several model runs failed to forecast precipitation along the L2 line or near C3 even in very short time-range and despite favorable environment for deep convection.

In the presented case study, the initiation of convection has been better specified with enhanced assimilation of high resolution data from various sources, whose positive impact (bigger number of patterns, more intense precipitation) could be observed even after more than 18 h of integration (here illustrated only up to 15 h). Further improvement could be obtained with an advancement of the data assimilation setup. Ongoing work on the BLENDVAR configuration comprises diagnostics of observation and background error statistics according to *Desroziers et al.* (2005), increase of the analysis frequency, and employment of other types of observations. Revision of the background error statistics derivation

according to *Bučánek* and *Brožková* (2017) is planned as well when more HPC resources are available.

In the current study, even improved data assimilation or change of the lateral boundary conditions were mostly not sufficient to define the exact position of major convergence lines or the intensity of the heaviest precipitation. The non-hydrostatic dynamic adaptations based on ALARO 2 led to finer precipitation structures but did not substantially correct their position with respect to outputs of their driving hydrostatic models. Moreover, initiation of convective cells in non-hydrostatic models seems to be even more complicated – dependent not only on the environment but also on the interactions of the simulated cells and their outflows. Even if deep convection had developed, the resulting precipitation was often too weak with respect to both observation and precipitation parameterized by hydrostatic models. This could be also due to parameterizations setup in the non-hydrostatic models (e.g., for microphysics), for which further investigation is planned in the near future on more cases with deep convection and was only marginally studied here.

The forecasts of the A-LAEF system provided the most exact location of precipitation along lines L1 or L2, and several EPS members succeeded also to forecast local intense rainfall related to C2 and C3 cells. Comparison of results from respective MP clusters indicates that the influence of different setups of physical parameterization did not have a systematic effect (on the contrary to some other weather situations, e.g., winter temperature inversion, not presented here). More impact could be expected in relation with ESDA assimilation or application of stochastic perturbation, which possibly imitate local effects important for the initiation of deep convection and are absent in the deterministic model runs. The A-LAEF also provided useful information about the forecast uncertainty, which was particularly high for the heavy precipitation events. The probability of precipitation exceeding 10 mm was rarely bigger than 40%. Such outputs, even if correct, could be possibly underestimated by non-experts. Surveys among users (e.g., from civil protection) indicate that they prefer rather high probability thresholds to take measures, mostly above 50% chance of occurrence (*Kox* and *Ulbrich,* 2015). An issue to be investigated in the future is whether a bigger ensemble could possibly specify the local distribution of high precipitation with better precision and improve the forecast confidence.

The structure and evolution of convection simulated in the experiments with non-hydrostatic dynamics showed some traits similar to radar observations. Weak mesoscale vortices, which developed in the model in the vicinity of the most intense cells could exist in some significant thunderstorms (e.g., in the cell C1). Previous studies (e.g., *Csirmaz et al.*, 2013) suggested that mesocyclones can develop even in a weak-shear environment, although these vortices are sometimes confined only to a relatively shallow layer of the low- or mid- troposphere. Yet, it is uncertain whether these vortices also play a substantial role in the life cycle of these thunderstorms (e.g., concerning their longevity). One could also observe

similar multicellular behavior as in the observations, e.g., development of new updrafts on the outflow boundaries of older storms. However, the updrafts in the simulations were often relatively weak (in order of only a few m/s), though one should consider that these velocities represent an average in the given 2×2 km grid box. The CAPE values would indicate much higher (well exceeding 10 m/s) maximum updraft velocities, which are usually present either in observed or simulated multicell thunderstorms in other studies, even in weak shear conditions (*Kirkpatrick et al.*, 2009; *Fovell* and *Dailey*, 1995; *Fovell* and *Tan*, 1998). It is possible that the weaker updrafts in the ALARO 2 model simulations had also a consequence of underestimation of precipitation and lack of convection in certain areas (e.g., northwest Slovakia, southern Poland), but this would need further investigation.

The possibility of simulating the convection explicitly also raises the question of how to verify the magnitude of vertical velocity of convective cells generated in the model, which is usually not measured directly. One way is to compare the evolution of model clouds and their properties (e.g., cloud top temperature) with the rapidly updated satellite imagery. However, this is possible rather in case of isolated cells and despite some promising results, there are still large uncertainties in the algorithm concerning the microphysical properties of cloudiness at the top of the thunderstorms and its distinguishing from ordinary, non-convective cirrus clouds. Similarly, the determination of satellite CTB is also limited due to current resolution of the infrared imagery, which will be improved after launching the Meteosat Third Generation satellite (MTG).

Further progress in calculation efficiency of non-hydrostatic models is inevitable, as well as the stability of such computation. It was shown that the semi-implicit scheme with NHHY formulation could help to fulfil such goals being significantly faster than the current iterative centered implicit scheme. The execution times of 15 h forecast are shown in the *Table 4*. The relative speedup of model execution with NHHY scheme is 20% for the 1 km resolution experiment and 28% for the 2 km resolution one. Therefore, NHHY approach allows large improvement of execution efficiency at model resolutions around 2-1 km, and it potentially opens the possibility to run convection-permitting EPS systems also at meteorological centers where medium size HPC systems are installed. Certainly, more tests are needed in future in other conditions and different types of severe weather (including mesoscale convective systems and supercells) or even on continuous periods of time to examine the robustness of the new scheme and prediction capabilities of the non-hydrostatic version of ALARO.

All the above mentioned activities should be joined in the future in a form of convection-permitting EPS, using data assimilation with high resolution observations, run at short range and on sufficiently large domain (similarly to the current ALADIN/SHMU).

References

AMS Glossary of Meteorology, 2000: Mesocyclone (visited on 7 May 2021), Website
https://glossary.ametsoc.org/wiki/Mesocyclone

Baldauf, M., A. Seifert, J. Förstner, D. Majewski, M. Raschendorfer, and *T. Reinhardt*, 2011: Operational convective-scale numerical weather prediction with the COSMO model: Description and sensitivities. *Mon. Weather Rev. 139*, 3887–3905.
https://doi.org/10.1175/MWR-D-10-05013.1.

Belluš, M., Y. Wang, and *F. Meier*, 2016: Perturbing surface initial conditions in a regional ensemble prediction system. *Mon. Weather Rev. 144*, 3377–3390.
https://doi.org/10.1175/MWR-D-16-0038.1.

Belluš, M., F. Weidle, C. Wittmann, Y. Wang, S. Taşku, and *M. Tudor,* 2019: Aire Limitée Adaptation dynamique Développement InterNational – Limited Area Ensemble Forecasting (ALADIN-LAEF). *Adv. Sci. Res. 16*, 63–68. https://doi.org/10.5194/asr-16-63-2019

Belluš, M., 2019: Uncertainty simulation in ALADIN-LAEF, Presentation, ALARO-1 Working days 2019, Bratislava, Slovakia, 11-13 March 2019.
https://www.rclace.eu/File/ALARO/alaro1_wd19br/alaro1wd_MB_laef_mar19.pdf

Belluš, M., 2020a: New high-resolution ensemble forecasting system A-LAEF (in Slovak with English abstract). *Met. J. Slovak Hydromet. Inst. 23*, 75–86.

Belluš, M., 2020b: LAM-EPS activities in LACE, Presentation, Joint 30th ALADIN Workshop and HIRLAM ASM 2020, 30/03-03/04/2020, visio-conference.
http://www.umr-cnrm.fr/aladin/IMG/pdf/2020_04_ahw_online_eps_mbell.pdf

Bénard, P., 2003: Stability of semi-implicit and iterative centered-implicit time discretizations for various equation systems used in NWP. *Mon. Weather Rev. 131*, 2479–2491.
https://doi.org/10.1175/1520-0493(2003)131<2479:SOSAIC>2.0.CO;2.

Bénard, P., 2004: On the use of a wider class of linear systems for the design of constant-coefficients semi-implicit time schemes in NWP. *Mon. Weather Rev. 132*, 1319–1324.
https://doi.org/10.1175/1520-0493(2004)132<1319:OTUOAW>2.0.CO;2.

Bénard, P., Vivoda, J., Mašek, J., Smolíková, P., Yessad, K., Smith, C., Brožková, R., and *Geleyn, J. F.*, 2010: Dynamical kernel of the Aladin–NH spectral limited-area model: Revised formulation and sensitivity experiments. *Quart. J. Roy. Meteor. Soc. 136*, 155–169. https://doi.org/10.1002/qj.522

Bengtsson, L., Andrae, U., Aspelien, T., Batrak, Y., Calvo, J., de Rooy, W., Gleeson, E., Hansen-Sass, B., Homleid, M., Hortal, M., Ivarsson, K.-I., Lenderik, G., Niemelä, S., Nielsen, K. P., Onvlee, J., Rontu, L., 880 Samuelsson, P., Muñoz, D. S., Subias, A., Tijm, S., Tol, V., Yang, X., and Køltzow, M. Ødegaard., 2017: The HARMONIE-AROME model configuration in the ALADIN-HIRLAM NWP system. *Mon. Weather Rev., 145,* 1919–1935.
https://doi.org/10.1175/MWR-D-16-0417.1.

Bouttier, F., Vie, B. Nuissier, O., and *Raynaud, L.,* 2012: Impact of stochastic physics in a convection-permitting ensemble. *Mon. Weather Rev 140*, 3706–3721.https://doi.org/10.1175/mwr-d-12-00031.1.

Brousseau, P., Seity, Y., Ricard, D., and Léger, J., 2016: Improvement of the forecast of convective activity from the AROME-France system. *Quart. J. Roy. Meteor. Soc. 142*, 2231–2243. https://doi.org/10.1002/qj.2822

Brožková, R., Bučánek, A., Mašek, J., Smolíková, P., and Trojáková, A., 2019: Nová provozní konfigurace modelu Aladin ve vysokém rozlišení. *Meteorologické zprávy 72*, 129–139.http://www.cmes.cz/sites/default/files/chmu_mz_5-19_129-139.pdf (In Czech)

Brožková, R., Bučánek, A., Mašek, J., Němec, D., Smolíková, P., Šábik, F., and Trojáková, A., 2021: Numerical weather prediction activities at CHMI., ACCORD 1st AWS videoconference, 12–16 April 2021, poster presentation. https://doi.org/10.22233/20412495.0421.1

Bučánek, A., Brožková R., and Trojáková, A., 2015: Asimilační schéma BlendVar v ČHMÚ. *Meteorologické zprávy 68*, 180–185. (in Czech) https://www.chmi.cz/files/portal/docs/reditel/SIS/casmz/assets/2015/chmu_mz_6-15.pdf

Bučánek, A. and Brožková, R., 2017: Background error covariances for a BlendVar assimilation system. *Tellus A 69*, DOI: 10.1080/16000870.2017.1355718

Cedilnik, J., 2005: Parallel suites documentation. Regional Cooperation for Limited Area Modeling in Central Europe Rep. 2.http://www.rclace.eu/File/Physics/2005/cedilnik_stay_2005.pdf.

Csirmaz, K., Simon, A., Pistotnik, G., Polyánszky, Z., Neštiak, M., Nagykovácsi, Z. and Sokol, A., 2013: A study of rotation in thunderstorms in a weakly- or moderately-sheared environment. *Atmos. Res. 123*, 93–116. https://doi.org/10.1016/j.atmosres.2012.09.017

Čatlošová, K. and Derková, M., 2020: Exploitation of aircraft Mode-S data in AROME/SHMU numerical weather prediction model. *Meteorologický časopis 23 65-74*. http://www.shmu.sk/File/ExtraFiles/MET_CASOPIS/MC_2020-2.pdf.

Čatlošová, K., 2020: Assimilation of radial velocity from radars. RC LACE stay report, available at www.rclace.eu.https://www.rclace.eu/File/Data_Assimilation/2020/repStay_KCatlosova_Radi alWindAssimilaton_2020_07.pdf

Derková, M., 2005: Numerical Weather Prediction Activities at the Slovak Hydrometeorological Institute. *Meteorol. J. 8*, 53–64.

Derková, M. and Belluš, M., 2007: Various applications of the blending by digital filter technique in the ALADIN numerical weather prediction system. *Meteorologický časopis 10*, 27–36.

Derková, M., Vivoda, J., Belluš, M., Španiel, O., Dian, M., Neštiak, M., Zehnal, R., 2017: Recent improvements in the ALADIN/SHMU operational system. *Meteorologický časopis Vol. 20 No. 2*, 45-52. (in Czech) http://www.shmu.sk/File/ExtraFiles/MET_CASOPIS/2017-2__MC.pdf.

Desroziers, G., Berre, L., Chapnik, B. and Poli, P., 2005: Diagnosis of observation, background and analysis-error statistics in observation space. *Quart. J. Roy. Meteorol. Soc. 131*, 3385–3396. https://doi.org/10.1256/qj.05.108

Dorog-Esztergom Időjárása, 2020: Özönvíz zúdult térségünk nyugati felére vasárnap délután (In Hungarian), Website (Visited on 07 May 2021), https://dorog-esztergom-idojarasa.hu/hirek/ozonviz-zudult-tersegunk-tobb-pontjara-vasarnap-delutan/

Ďurán, I. B., Geleyn, J., and Váňa, F., 2014: A Compact Model for the Stability Dependency of TKE Production–Destruction–Conversion Terms Valid for the Whole Range of Richardson Numbers. *J. Atmos. Sci. 71*, 3004–3026. https://doi.org/10.1175/JAS-D-13-0203.1

Ďurán, I. B., 2014: Toucans. RCLACE stay report, Bratislava, 5 April – 2 May 2013, 12. http://www.rclace.eu/File/Physics/2014/bastakduran_toucans_bratislavaMay2014.pdf

Ďurán, I. B., Geleyn, J., Váňa, F., Schmidli, J., and Brožková, R., 2018: A Turbulence Scheme with Two Prognostic Turbulence Energies. *J. Atmos. Sci. 75*, 3381-3402. https://doi.org/10.1175/JAS-D-18-0026.1

ESTOFEX: 2020, Website: https://www.estofex.org/ (visited on 10 May 2021)

European Severe Weather Database, 2020: Website (visited on 7 May 2021).https://www.eswd.eu/

Fischer, C. and Auger, L., 2011: Some experimental lessons on digital filtering in the ALADIN-France 3DVAR based on near-ground examination, *Mon. Weather Rev. 139*, 774–785. https://doi.org/10.1175/2010MWR3388.1

Fovell, R. G. and Dailey, P. S., 1995: The temporal behavior of numerically simulated multicell-type storms. Part I: Modes of behavior. *J. Atmos. Sci. 52*, 2073–2095. https://doi.org/10.1175/1520-0469(1995)052<2073:TTBONS>2.0.CO;2

Fovell, R. G. and Tan, P.-H., 1998: The temporal behavior of numerically simulated multicell-type storms. Part II: The convective cell life cycle and cell regeneration. *Mon. Weather Rev. 126*, 551– 577.

Geleyn, J.-F., Váňa, F., Cedilnik, J., Tudor, M., and Catry, B., 2006: An intermediate solution between diagnostic exchange coefficients and prognostic TKE methods for vertical turbulent transport. In (Ed: *Côté, J.*) CAS/JSC WGNE "Blue Book" annual report: Research Activities in Atmospheric and Ocean Modelling. 4.11–4.12.

Gerard, L., Piriou, J.-M., Brožková, R., Geleyn, J.-F., and Banciu, D., 2009: Cloud and precipitation parameterization in a meso-gamma scale operational weather prediction model. *Mon. Weather Rev. 137*, 3960–3977. https://doi.org/10.1175/2009MWR2750.1

Gustafsson, N., Janjić, T., Schraff, C., Leuenberger, D., Weissmann, M., and *co-authors.* 2018*:* Survey of data assimilation methods for convective-scale numerical weather prediction at operational centres. *Quart. J. Roy. Meteorol. Soc. 144,* 1218–1256. https://doi.org/10.1002/qj.3179.

Giard, D. and Bazile, E., 2000: Implementation of a New Assimilation Scheme for Soil and Surface Variables in a Global NWP Model. *Mon. Weather Rev. 128,* 997–1015. https://doi.org/10.1175/1520-0493(2000)128<0997:IOANAS>2.0.CO;2

Haiden, T., Kann, A., Wittmann, C., Pistotnik, G., Bica, B., and Gruber, C., 2011 The integrated nowcasting through comprehensive analysis (INCA) system and its validation over the Eastern Alpine region. *Wea. Forecast. 26*, 166–183. https://doi.org/10.1175/2010WAF2222451.1

Hanna, J. W., Schultz, D.M., and Irving, A. R., 2008: Cloud-Top Temperatures for *P*recipitating Winter Clouds. *J. Appl. Meteor. Climatol. 47*, 351–359. https://doi.org/10.1175/2007JAMC1549.1

Hortal, M., 2002: The development and testing of a new two-time-level semi-Lagrangian scheme (SETTLS) in the ECMWF forecast model. *Quart. .J. Roy. Meteorol. Soc. 128*, 1671–1687. https://doi.org/10.1002/qj.200212858314

Imrišek, M., Derková, M., and Janák, J., 2020: Estimation of GNSS tropospheric products and their meteorological exploitation in Slovakia. *Cont. Geophys. Geodesy 50,* 83–111. https://doi.org/10.31577/congeo.2020.50.1.5

Jurášek, M., Kaňák, J., Okon, Ľ., Méri, L., 2017: Calibration and Monitoring of Slovak Weather Radar Network. Weather Radar Calibration and Monitoring workshop, 18-20 October, 2017, DWD, https://www.dwd.de/EN/specialusers/research_education/met_applications_specials/wxrcalmon 2017_presentations/poster_downloads/16_jurasek_wxrcalmon2017_poster.pdf?__blob=publicat ionFile&v=2

Kaňák, J., 2006: ViewMSG – An unconventional visualisation tool for MSG imagery. 2006 EUMETSAT Meteorological Satellite Conference, Helsinki, Finland. EUMETSAT Abstract brochure, 127, https://www.researchgate.net/publication/303975518_ViewMSG_- _An_unconventional_visualisation_tool_for_MSG_imagery

Kirkpatrick, C., McCaul, E. W. Jr., and Cohen, C., 2009: Variability of updraft and downdraft characteristics in a large parameter space study of convective storms. *Mon. Weather Rev. 137*, 1550–1561. https://doi.org/10.1175/2008MWR2703.1

Kokhanovsky, A., 2004: Optical properties of terrestrial clouds. *Earth-Sci. Rev. 64,* 189–241. https://doi.org/10.1016/S0012-8252(03)00042-4

Kox, L.G. and Ulbrich, U., 2015: Perception and use of uncertainty in severe weather warnings by emergency services in Germany. *Atmos. Res. 158-159*, 292–301. https://doi.org/10.1016/j.atmosres.2014.02.024

Leaflet, 2021: Website (visited on 7 May 2021).https://leafletjs.com/

Lopez, P., 2002: Implementation and validation of a new prognostic large-scale cloud and precipitation scheme for climate and data assimilation purposes. *Quart. J. Roy. Meteor. Soc. 128*, 229–257. https://doi.org/10.1256/00359000260498879

Lynch, P., Giard, D., and Ivanovici, V., 1997: Improving the Efficiency of a Digital Filtering Scheme for Diabatic Initialization. *Mon. Weather Rev. 125*, 1976–1982. https://doi.org/10.1175/1520-0493(1997)125<1976:ITEOAD>2.0.CO;2

Méri, L., Jurašek, M., Kaňák, J., and Okon, L., 2018: QUALITY-BASED RADAR DATA PROCESSING AND QPE AT THE SLOVAK HYDROMETEOROLOGICAL INSTITUTE. The 10th European Conference on Radar in Meteorology & Hydrology ERAD Ede-Wageningen, *T*he Netherlands. https://library.wur.nl/WebQuery/wurpubs/fulltext/454537

Méri, L.; Gaál, L.; Bartok, J.; Gažák, M.; Gera, M.; Jurašek, M.; and *Kelemen, M.,* 2021: Improved Radar Composites and Enhanced Value of Meteorological Radar Data Using Different Quality Indices. *Sustainability 13*, 5285. https://doi.org/10.3390/su13095285

Moller, A.R., Doswell, C.A. III, Foster, M.P., and *Woodall, G.R.,* 1994: The operational recognition of supercell thunderstorm environments and storm structures. *Wea. Forecast. 9*, 327–347. https://doi.org/10.1175/1520-0434(1994)009<0327:TOROST>2.0.CO;2

Müller, M., Homleid, M., Ivarsson, K.-I., Køltzow, M.A., Lindskog, M., Midtbø, K.H., Andrae, U., Aspelien, T., Berggren, L., Bjørge, D., Dahlgren, P., Jørn Kristiansen, J., Randriamampianina, R., Ridal, M., and *Vignes, O.,* 2017: AROME-MetCoOp: a nordic convective-scale operational weather prediction model. *Weather Forecast 32*, 609–627. https://doi.org/10.1175/WAF-D-16-0099.1

Noilhan, J. and *Planton, S.,* 1989: A simple parameterization of land surface processes for meteorological models. *Mon. Weather Rev., 117,* 536–549. https://doi.org/10.1175/1520-0493(1989)117<0536:ASPOLS>2.0.CO;2

Novák, P., Kyznarová, H., and *Fibich, O.,* 2019: Calibration and Monitoring of the Czech Weather Radar Network – Status Update 2019, 2nd Weather Radar Calibration & Monitoring workshop (WXRCalMon), DWD, 30 October-01 November 2019, DWD, Presentation. https://www.dwd.de/EN/specialusers/research_education/met_applications_specials/wxrcalmon 2019_presentations/presentation_downloads/06_czrad_wxrcalmon2019.pdf;jsessionid=5FE766 7701504FF420F2549A2110CD38.live21062?__blob=publicationFile&v=2

OMSZ, 2020: Időjárási napijelentés, 2020. június 8. Daily weather report of 8 June 2020, 133, OMSZ, Budapest. https://www.met.hu/idojaras/aktualis_idojaras/napijelentes/(in Hungarian)

Platt, C.M.R., 1997: A Parameterization of the Visible Extinction Coefficient of Ice Clouds in Terms of the Ice/Water Content. *J. Atmos. Sci. 54*, 2083–2098. https://doi.org/10.1175/1520-0469(1997)054<2083:APOTVE>2.0.CO;2

Seity, Y., Brousseau, P., Malardel, S., Hello, G., Bénard, P., Bouttier, F., Lac, C., and *Masson, V,* 2011: The AROME-France Convective-Scale Operational Model. *Mon. Weather Rev. 139*, 976–991. http://dx.doi.org/10.1175/2010MWR3425.1.

Simmons, A., J. and *Burridge, D., M.*, 1981: An energy and angular-momentum conserving vertical finite-difference scheme and hybrid vertical coordinates. *Mon. Wea. Rev. 109*, 758–766. https://doi.org/10.1175/1520-0493(1981)109<0758:AEAAMC>2.0.CO;2.

Simon, A., Horváth, Á., Vivoda, J., 2006: Case study and numerical simulations of the November 19, 2004 severe windstorm in Central Europe. *Időjárás*, 110, 91–123.

Sipos, Z., Simon, A., Csirmaz, K., Tünde, L., Mant,a R.-D., and *Kocsis, Zs.*, 2021: A case study of a derecho storm in dry, high-shear environment. *Időjárás 125*, 1–37. https://doi.org/10.28974/idojaras.2021.1.1

Stoelinga, M. T., and *Warner,* T. T., 1999: Nonhydrostatic, mesobeta-scale model simulations of cloud ceiling and visibility for an East Coast winter precipitation event. *J. Appl. Meteor. 38*, 385–404. https://doi.org/10.1175/1520-0450(1999)038<0385:NMSMSO>2.0.CO;2

Sukoriansky, S., Galperin, B., and *Staroselsky, I.,* 2005: A quasinormal scale elimination model of turbulent flows with stable stratification. *Phys. Fluids 17,* 085107. https://doi.org/10.1063/1.2009010.

Svoboda A. and *Pekárová P.*, 1998. The catastrophic flood of July 1998 in the Malá Svinka catchment – its simulation. *J. Hydrol. Hydromech., 46, 6,* 356–365. (in Slovak)

Szintai, B., Szűcs, M., Randriamampianina, R., and *Kullmann, L.*, 2015: Application of the AROME non-hydrostatic model at the Hungarian Meteorological Service: physical parameterizations and ensemble forecasting, *Időjárás 119*, 241–265.

Termonia, P., Fischer, C., Bazile, E., Bouyssel, F., Brožková, R., Bénard, P., Bochenek, B.,Degrauwe, D.,- Derková, M., El Khatib, R., Hamdi, R., Mašek, J., Pottier, P., Pristov, N. Seity, Y., Smolíková, P., Španiel, .O., Tudor, M., Wang, Y., Wittmann, C., and *Joly, A.,* 2018: The ALADIN System and its Canonical Model Configurations AROME CY41T1 and ALARO CY40T1. *Geosci. Model Dev. 11,* 257–281. https://doi.org/10.5194/gmd-11-257-2018.

Trojáková, A., Mile, M. and *Tudor, M.,* 2019: Observation Preprocessing System for RC LACE (OPLACE). *Adv. Sci. Res. 16,* 223–228.https://doi.org/10.5194/asr-16-223-2019.

Wang, Y., M. Belluš, A. Ehrlich, M. Mile, N. Pristov, P. Smolikova, O. Spaniel, A. Trojakova, R. Brozkova, J. Cedilnik, D. Klaric, T. Kovacic, J. Masek, F. Meier, B. Szintai, S. Tascu, J. Vivoda, C. Wastl, and *Ch. Wittmann*, 2017a: 27 years of Regional Co-operation for Limited Area Modelling in Central Europe (RC LACE), *Bull. Amer. Met. Soc. 99*, 1415–1432. https://doi.org/10.1175/BAMS-D-16-0321.1

Wang, Y., Meirold-Mautner, I., Kann, A., Slak, A. Š., Simon, A., Vivoda, J., Bica, B., Böcskör, E., Brezková, L., Dantinger, J., Giszterowicz, M., Heizler, G., Iwanski, R., Jachs, S., Bernard, T., Kršmanc, R., Merše, J., Micheletti, S., Schmid, F., Steininger, M., Haiden, T., Regec, A., Buzzi, M., Derková, M., Kozari´c, T., Qiu, X., Reyniers, M., Yang, J., Huang, Y., and Vadislavsky, E., 2017b: Integrating nowcasting with crisis management and risk prevention in a transnational and interdisciplinary framework. *Meteorol. Zeits. 26*, 459–473. https://doi.org/10.1127/metz/2017/0843

Wang, Y., Belluš, M., Wittmann, C., Steinheimer, M., Weidle, F., Kann, A., Ivatek-Šahdan, S., Tian, W., Ma, X., Tascu, S., and Bazile, E., 2011: The Central European limited-area ensemble forecasting system ALADIN-LAEF. *Quart. J. Roy. Meteor. Soc. 137*, 483–502. https://doi.org/10.1002/qj.751

Wang, Y., M. Belluš, F. Weidle, Wittmann, C., , Tang, J., Meier, F., Xia, F., and Keresturi, E., 2019: Impact of land surface stochastic physics in ALADIN-LAEF. *Quart. J. Roy. Meteorol. Soc. 145*, 1–19. https://doi.org/10.1002/qj.3623.

Wastl, C., Wang, Y., Atencia, A., Weidle, F., Wittmann, Ch., Zingerle, Ch., Keresturi, E., 2021: C-LAEF - Convection-permitting Limited Area Ensemble Forecasting System. *Quart. J. Roy. Meteorol. Soc. 147*, 1431–1451. https://doi.org/10.1002/qj.3986.

Weisman, M.L. and Trapp, R. J., 2003: Low-level mesovortices within squall lines and bow echoes. Part I: Overview and sensitivity to environmental vertical wind shear. *Mon. Weather Rev. 131*, 2779–2803. https://doi.org/10.1175/1520-0493(2003)131<2779:LMWSLA>2.0.CO;2

Wikimedia maps, 2021: website (visited on 7 May 2021), https://www.mediawiki.org/wiki/Wikimedia_Maps

ABBREVIATIONS

A-LAEF	ALARO - Limited Area Ensemble Forecasting
AGL	above ground level
ALADIN	Aire Limitée Adaptation dynamique et Développement InterNational
ALADIN-LAEF	Aire Limitée Adaptation dynamique et Développement InterNational - Limited Area Ensemble Forecasting
ALARO	ALadin - AROme
AMDAR	Aircraft Meteorological Data Relay
AMV HRWIND	Atmospheric Motion Vector High-Resolution WINDs
AROME	Applications of Research to Operations at MEsoscale
ARPEGE	Action de Recherche Petite Echelle Grande Echelle
AWS	Automatic Weather Station
BLENDVAR	combination of DF blending step and 3D-Var configuration
BUFR	Binary Universal Form for the Representation of meteorological data
C-LAEF	Convection-permitting - Limited Area Ensemble Forecasting
CANARI	Code for the Analysis Necessary for Arpege for its Rejects and its Initialization
CAPE	Convective Available Potential Energy
CAPPI	Constant Altitude Plan Position Indicator

CTB	Cloud top brightness temperature
CTT	Cloud top temperature
CHMI	Czech Hydrometeorological Institute
CLI	Cloud ice
CLW	Cloud liquid water
Cmax	Column maximum (radar reflectivity data)
COSMO	Consortium for Small Scale Modelling
DF	Digital Filter
ECMWF	European Centre for Medium-Range Weather Forecasts
ECMWF ENS	European Centre for Medium-Range Weather Forecasts Ensemble Forecast
ECMWF HPCF	ECMWF High-Performance Computing Facility
EDA	Ensemble Data Assimilation
EHS	Enhanced surveillance
EMADDC	European Meteorological Aircraft Derived Data Center
EPS	Ensemble Prediction System
ESDA	Ensemble of Surface Data Assimilation
ESTOFEX	European Storm Forecast Experiment
ESWD	European Severe Weather Database
EUMETSAT	European Organisation for the Exploitation of Meteorological Satellites
FLOODMED	Monitoring, forecasting and best practices for FLOOD Mitigation and prevEntion in the CADSES region
GEFS	Global Ensemble Forecast System
GNSS	Global navigation satellite system
GTS	Global Telecommunication System
HARMONIE-AROME	HIRLAM–ALADIN Research on Mesoscale Operational NWP in Euromed - AROME
HPC	High-Performance Computing
HY	hydrostatic
ICI scheme	iterative centred implicit scheme
INCA	Integrated Nowcasting through Comprehensive Analysis
INCA-CE	Integrated Nowcasting through Comprehensive Analysis for the Central European area
ISBA	Interactions between Soil, Biosphere, and Atmosphere
LAM	Limited area model
LBC	Lateral Boundary Conditions

METEOSAT	meteorological satellites operated by EUMETSAT
MD2	So-called Model II turbulence parameterization in *Ďurán et al.,* 2014
MODE-S	Secondary Surveillance Radar Mode-Selective data
MP	multi-physics
MRAR	Meteorological routine air report
MSG	Meteosat Third Generation
MVS	Mesocyclonic Vorticity Signature
NH	Non-hydrostatic
NHHY	name of innovative formulation of linear operator used in semi-implicit time stepping (to be published)
NMS	National Meteorological Service
NWP	Numerical Weather Prediction
OI	Optimal Interpolation
OMSZ	Országos Meteorológiai Szolgálat (Hungarian Meteorological Service)
OPERA OIFS	Operational Program on the Exchange of Weather Radar Information Internet File System
OPLACE	Observation Preprocessing System for RC LACE
PPI	Plan Position Indicator
QNSE	Quasi-Normal Scale Elimination
RC LACE	Regional Cooperation for numerical weather modeling on Limited Area in Central Europe
RSS	Rapid Scanning Service
SBCAPE	Surface-Based Convective Available Potential Energy
SI scheme	semi-implicit scheme
SETTLS	Stable extrapolation of two time level scheme
SHMÚ	Slovak Hydrometeorological Institute
SYNOP	surface synoptic observations
TEMP	upper air soundings
TKE	Turbulence Kinetic Energy
WER	Weak Echo Region
ZTD	Zenith Total Delay
3D-Var	Three-dimensional Variational data analysis
3MT package	Modular Multi-scale Microphysics and Transport
4D-Var	Four-dimensional Variational data analysis

IDŐJÁRÁS

Calibration of wind speed ensemble forecasts for power generation

Sándor Baran* and **Ágnes Baran**

Faculty of Informatics, University of Debrecen
Kassai út 26, H-4028 Debrecen, Hungary

*Corresponding author E-mail: baran.sandor@inf.unideb.hu

Abstract— In the last decades, wind power became the second largest energy source in the EU covering 16% of its electricity demand. However, due to its volatility, accurate short range wind power predictions are required for successful integration of wind energy into the electrical grid. Accurate predictions of wind power require accurate hub height wind speed forecasts, where the state-of-the-art method is the probabilistic approach based on ensemble forecasts obtained from multiple runs of numerical weather prediction models. Nonetheless, ensemble forecasts are often uncalibrated and might also be biased, thus require some form of post-processing to improve their predictive performance. We propose a novel flexible machine learning approach for calibrating wind speed ensemble forecasts, which results in a truncated normal predictive distribution. In a case study based on 100m wind speed forecasts produced by the operational ensemble prediction system of the Hungarian Meteorological Service, the forecast skill of this method is compared with the predictive performance of three different ensemble model output statistics approaches and the raw ensemble forecasts. We show that compared with the raw ensemble, post-processing always improves the calibration of probabilistic and accuracy of point forecasts, and from the four competing methods, the novel machine learning based approach results in the best overall performance.

Key-words: ensemble calibration, ensemble model output statistics, multilayer perceptron, wind energy, wind speed

1. Introduction

The increasing challenges caused by consequences of air pollution and emission of greenhouse gases highlight the importance of transition of energy production towards renewable energy sources. Besides the classical hydro power, in the last decades, photovoltaic and wind energy fulfilled larger and larger part of energy demand. In 2020, the world set a new record by adding 93 GW of new wind turbines, so the total capacity of wind farms reached 744 GW covering 7% of the global electricity demand (*World Wind Energy Association,* 2021). In the EU (United Kingdom included), this proportion reached 16%, and the (world) record is held by Denmark, where wind accounted for 48% of the electricity consumed in 2020 (*Wind Europe,* 2021). However, wind energy poses serious challenges to traditional electricity markets, so accurate short range (between several minutes and a couple of days) prediction of wind power is of utmost importance for wind farm managers and electric grid operators.

Although the relation between wind speed and produced wind energy is nonlinear and might also be nonstationary, more reliable wind speed forecasts obviously result in more reliable predictions of produced electricity. Wind speed forecasts, similar to other meteorological variables, are based on numerical weather prediction (NWP) models describing atmospheric processes via systems of partial differential equations. The state of the art approach is to run an NWP model several times with different initial conditions which results in an ensemble of forecasts (*Bauer et al.,* 2015). Ensemble forecasts enable estimation of situation dependent probability distributions of future weather variables, which opens the door for probabilistic weather forecasting (*Gneiting* and *Raftery,* 2005), where besides getting a point forecast, the forecast uncertainty is also assessed.

Recently, all major weather centres operate their own ensemble prediction system (EPS), e.g., the 35-member Prévision d'Ensemble ARPEGE[1] (PEARP) EPS of Méteo France (*Descamps et al.,* 2015) or the 11-member Applications of Research to Operations at Mesoscale EPS (AROME-EPS; *Jávorné Radnóczi et al.,* 2020) of the Hungarian Meteorological Service (HMS), whereas the largest ensemble size corresponds to the 51-member EPS of the European Centre for Medium-Range Weather Forecasts (*Buizza et al.,* 1998). Nowadays ensemble weather forecasts are also popular inputs to probabilistic forecasts of renewable energy (*Pinson* and *Messner,* 2018).

However, ensemble forecasts often appear to be uncalibrated and/or biased, this feature has been observed in several operational ensembles (see, e.g., *Buizza et al.,* 2005). A possible solution is the use of some form of statistical post-processing (*Buizza,* 2018), where nonparametric methods usually capture predictive distributions via estimating their quantiles (see, e.g., *Friederichs* and *Hense,* 2007; *Bremnes,* 2019), whereas parametric post-processing approaches

---

[1] Action de Recherche Petite Echelle Grande Echelle (i.e. Research Project on Small and Large Scales)

provide full predictive distributions of the future weather quantities (see, e.g., *Gneiting et al.,* 2005; *Raftery et al.,* 2005). Recently, machine learning based methods also gain more and more popularity (see, e.g., *Rasp* and *Lerch,* 2018; *Taillardat* and *Mestre,* 2020); for a detailed overview of statistical calibration techniques we refer to *Wilks* (2018) or *Vannitsem et al.* (2021).

Here we focus on a weather quantity important in energy production and investigate statistical post-processing of ensemble forecasts of wind speed measured at hub height (100m). In this context, *Tailor et al.* (2009) proposes kernel dressing with Gaussian kernel left truncated at zero (TN; truncated normal), while *Messner et al.* (2013) considers forecasts based on inverse power curves and applies a censored normal predictive distribution. However, any post-processing method appropriate for wind speed can be applied, and we concentrate on the ensemble model output statistic (EMOS; *Gneiting et al.,* 2005) approach, where the predictive distribution is a single parametric probability law with parameters depending on the ensemble forecasts via appropriate link functions. To account for the non-negativity and right skew of wind speed, *Thorarinsdottir* and *Gneiting* (2010) proposes a TN, *Baran* and *Lerch* (2015) a log-normal (LN), whereas *Baran et al.* (2021) a truncated generalized extreme value (TGEV) predictive distribution, and several methods for combining these probabilistic forecasts have also been developed (see, e.g., *Lerch* and *Thorarinsdottir,* 2013; *Baran* and *Lerch,* 2016, 2018).

In the present paper we test the forecast skill of TN, LN, and TGEV EMOS approaches on AROME-EPS forecasts of hub height wind speed. We also introduce a novel model with TN predictive distribution, where using the ideas of *Rasp* and *Lerch* (2018) and *Ghazvinian et al.* (2021), location and scale parameters of the TN law are connected to the ensemble members via a multilayer perceptron neural network (MLP; *Goodfellow et al.,* 2016). Compared with the case of fixed link functions, this latter approach allows more flexibility in modeling and straightforward inclusion of new covariates as well. Note that TN, LN, and TGEV EMOS approaches and some of their combinations have already been successfully applied for calibration of surface wind speed forecasts of the 11-member Aire Limitée Adaptation dynamique Développement International-Hungary Ensemble Prediction System of the HMS (*Horányi et al.,* 2006), see, e.g., *Baran et al.* (2014).

The paper is organized as follows. In Section 2, the detailed description of the AROME-EPS is given, while in Section 3, the applied post-processing methods and considered verification tools are reviewed. The results of our case study is presented in Section 4 followed by a concluding discussion in Section 5.

2. Data

The 11-member AROME-EPS of the HMS covers the Transcarpathian Basin with a horizontal resolution of 2.5 km (*Jávorné Radnóczi et al., 2020*). It consists of a control member and 10 ensemble members obtained from perturbed initial conditions. The dataset at hand contains ensemble forecasts of wind speed (m/s) at hub height (100m) together with the corresponding validation observations for three wind farms in the northwestern part of Hungary (Ács, Jánossomorja, and Pápakovácsi) for the period May 7, 2020 to March 28, 2021. All forecasts are initialized at 0000 UTC with a temporal resolution of 15 minutes and maximal forecast horizon of 48 h resulting in a total of 192 forecast lead times.

3. Post-processing methods and verification tools

Non-homogeneous regression or EMOS is one of the most popular parametric post-processing approaches, probably due to its computational efficiency and excellent performance for a wide range of weather variables. EMOS models for different weather quantities differ in the parametric family specifying the predictive distribution; however, most of the existing EMOS models are implemented in the ensembleMOS package of R (*Yuen et al., 2018*).

   In the following sections let $f_1, f_2, ..., f_{11}$ denote the 11-member AROME-EPS hub height wind speed forecast for a given location, time, and lead time, where $f_1 = f_{CTRL}$ is the control forecast, while $f_2, f_3, ..., f_{11}$ correspond to the 10 statistically indistinguishable (and thus exchangeable) ensemble members $f_{ENS,1}, f_{ENS,2}, ..., f_{ENS,10}$ generated using random perturbations. Further, let $\overline{f}$ denote the ensemble mean, $\overline{f}_{ENS}$ denote the mean of the 10 exchangeable members, and S^2 and MD denote the ensemble variance and ensemble mean absolute difference, respectively, defined as

$$S^2 := \frac{1}{10}\sum_{k=1}^{11}(f_k - \overline{f})^2 \quad \text{and} \quad \text{MD} := \frac{1}{11^2}\sum_{k=1}^{11}\sum_{\ell=1}^{11}|f_k - f_\ell|.$$

3.1. Truncated normal EMOS model

Let $\mathcal{N}_0(\mu, \sigma^2)$ denote the TN distribution with location μ, scale $\sigma > 0$, and lower truncation at 0, having probability density function (PDF)

$$g(x|\mu, \sigma) := \frac{1}{\sigma}\varphi((x - \mu)/\sigma)/\Phi(\mu/\sigma), \quad \text{if } x \geq 0,$$

and $g(x|\mu, \sigma) := 0$, otherwise, where φ is the PDF; while Φ denotes the cumulative distribution function (CDF) of a standard normal distribution. The proposed TN EMOS predictive distribution for hub height wind speed based on the AROME-EPS ensemble forecast is

$$\mathcal{N}_0(a_0 + a_{\text{CTRL}}^2 f_{\text{CTRL}} + a_{\text{ENS}}^2 \overline{f}_{\text{ENS}}, b_0^2 + b_1^2 \text{MD}), \qquad (1)$$

where $a_0, a_{\text{CTRL}}, a_{\text{ENS}}, b_0, b_1 \in \mathbb{R}$. The same model is applied by *Hemri et al.* (2014) to model square root of 10m wind speed, and the suggested method is a slight modification of the TN EMOS approach of *Thorarinsdottir* and *Gneiting* (2010), where the square of the scale parameter is an affine function of the ensemble variance, that is $\sigma^2 = b_0^2 + b_1^2 S^2$. Exploratory tests with the dataset at hand show that neither modelling the square root of the data, nor linking location to the ensemble variance result in better forecast skill than the use of Eq. (1).

3.2. Log-normal EMOS model

As an alternative to the TN EMOS approach, we consider the EMOS model of *Baran* and *Lerch* (2015), where the mean m and variance v of the LN predictive distribution are affine functions of the ensemble members and the ensemble variance, respectively, that is

$$m = \alpha_0 + \alpha_{\text{CTRL}}^2 f_{\text{CTRL}} + \alpha_{\text{ENS}}^2 \overline{f}_{\text{ENS}} \qquad \text{and} \qquad v = \beta_0^2 + \beta_1^2 S^2,$$

where $\alpha_0, \alpha_{\text{CTRL}}, \alpha_{\text{ENS}}, \beta_0, \beta_1 \in \mathbb{R}$. The heavier upper tail of the LN distribution allows a better fit to high wind speed values.

3.3. Truncated generalized extreme value EMOS model

Another possible solution to address reliability of probabilistic forecasts for high wind speed is the use of the GEV EMOS approach proposed by *Lerch* and *Thorarinsdottir* (2013). The GEV distribution $\mathcal{GEV}(\mu, \sigma, \xi)$ with location μ, scale $\sigma > 0$, and shape ξ is defined by CDF

$$G(x|\mu, \sigma, \xi) := \begin{cases} \exp(-[1 + \xi(\frac{x-\mu}{\sigma})]^{-1/\xi}), & \text{if } \xi \neq 0; \\ \exp(-\exp(-\frac{x-\mu}{\sigma})), & \text{if } \xi = 0, \end{cases}$$

for $1 + \xi(\frac{x-\mu}{\sigma}) > 0$ and $G(x|\mu, \sigma, \xi) := 0$, otherwise. However, as demonstrated by *Lerch* and *Thorarinsdottir* (2013) and *Baran* and *Lerch* (2015), the GEV EMOS model might assign positive predicted probability to negative wind

speed. To correct this deficiency, *Baran et al.* (2021) proposed to truncate the GEV distribution from below at zero and considered a TGEV predictive distribution $\mathcal{TGEV}(\mu, \sigma, \xi)$ with location μ, scale $\sigma > 0$, and shape ξ defined by CDF

$$G_0(x|\mu, \sigma, \xi) := \begin{cases} \frac{G(x|\mu,\sigma,\xi) - G(0|\mu,\sigma,\xi)}{1 - G(0|\mu,\sigma,\xi)}, & \text{if } G(0|\mu, \sigma, \xi) < 1; \\ 1, & \text{if } G(0|\mu, \sigma, \xi) = 1, \end{cases}$$

for $x \geq 0$, and $G(x|\mu, \sigma, \xi) := 0$, otherwise.

For the 11-member AROME-EPS, location and scale parameters of the TGEV EMOS model are

$$\mu = \gamma_0 + \gamma_{\text{CTRL}} f_{\text{CTRL}} + \gamma_{\text{ENS}} \overline{f}_{\text{ENS}} \quad \text{and} \quad \sigma = \sigma_0^2 + \sigma_1^2 \overline{f},$$

with $\gamma_0, \gamma_{\text{CTRL}}, \gamma_{\text{ENS}}, \sigma_0, \sigma_1 \in \mathbb{R}$, while the shape parameter ξ does not depend on the ensemble members. In order to ensure a finite mean and positive skewness, the shape is kept in the interval $]-0.278, 1/3[$.

3.4. Parameter estimation

Parameter estimation in the TN, LN, and TGEV EMOS models described in Sections 3.1 – 3.3 is based on the optimum score principle of *Gneiting* and *Raftery* (2007). The estimates are obtained as minimizers of the mean value of a proper scoring rule over an appropriate training dataset. Here we consider one of the most popular proper scores in atmospheric sciences, namely the continuous ranked probability score (CRPS; *Wilks,* 2019, Section 9.5.1). Given a (predictive) CDF F and a real value (observation) x, the CRPS is defined as

$$\text{CRPS}(F, x) := \int_{-\infty}^{\infty} [F(y) - \mathbb{I}_{\{y \geq x\}}]^2 \mathrm{d}y = \mathrm{E}|X - x| - \frac{1}{2}\mathrm{E}|X - X'|, \quad (2)$$

where $\mathbb{I}_H$ denotes the indicator function of a set H, while X and X' are independent random variables distributed according to F and having a finite first moment. CRPS is a negatively oriented score, that is the smaller the better, and the right-hand side of Eq. (2) implies that it can be expressed in the same units as the observation. Note that the CRPS for TN, LN, and TGEV distributions can be expressed in closed form (see *Thorarinsdottir* and *Gneiting* (2010), *Baran* and *Lerch* (2015), and *Baran et al.* (2021), respectively), which allows an efficient optimization procedure.

A crucial issue in statistical calibration is the selection of training data. Here the different forecast horizons are treated separately, and we use rolling training periods, which is a standard approach in EMOS modeling. In this training scheme, parameters for a given lead time are estimated with the help of

corresponding forecast–observation pairs from the preceding n calendar days. Further, both regional (or global) and local EMOS models are investigated. In the regional approach, all data from the training period are considered together, providing a single set of EMOS parameters for all three wind farms. In contrast, local estimation results in different parameter estimates for different wind farms by using only data of the given location. In general, local models outperform their regional counterparts (see, e.g., *Thorarinsdottir* and *Gneiting,* 2010), provided the training period is long enough to avoid numerical stability issues (*Lerch* and *Baran,* 2017).

3.5. *Machine learning based approach to wind speed modeling*

As mentioned in the Introduction, based on works of *Rasp* and *Lerch* (2018) and *Ghazvinian et al.* (2021), we applied a machine learning approach to estimate the parameters of the predictive distribution in a TN model. In this case, instead of looking for the parameters $a_0, a_{CTRL}, a_{ENS}, b_0, b_1$ in Eq. (1), location and scale are estimated directly, without assuming that they depend on the ensemble in a prescribed way. Practically this means, that some features derived from the ensemble (e.g., the control member, or the ensemble standard deviation) are used as inputs of a multilayer perceptron (MLP), while the trained network provides a two-dimensional vector corresponding to the location and scale parameters. Similar to the previous models, the network is trained by minimizing the mean CRPS over the training data.

In an MLP. some hidden layers connect the input layer and the output one, the number of layers and the number of neurons in the different hidden layers are tuning parameters of the network. Starting from the first hidden layer, each neuron of the given layer computes a weighted sum of the values provided by the neurons in the previous layer, adds a bias, and via a so-called transfer function, applies a transformation to the result.

In the present work we train an MLP with one hidden layer containing 25 neurons, the applied transfer functions are the exponential linear unit (ELU; see e.g., *Ghazvinian et al.,* 2021) function in the hidden layer, and the linear function in the output layer. After some experiments, in the final training we decided to use the control forecast, the mean of the exchangeable ensemble members, and the standard deviation of the 11 members as input features of the network. Based on *Ghazvinian et al.* (2021), to ensure the positivity of the location and scale parameters, their estimates are given by $\exp(\theta_1)$ and $\exp(\theta_2)$, where θ_1 and θ_2 are the values provided by the two neurons of the output layer.

By the training of a network, the number of the training samples is always a critical point: a relatively small training set can easily result in overfitting, which means a weak performance on the test set. In order to avoid this problem, we apply a regional estimation, moreover, we do not handle the different lead times separately; for a given training period we train only two networks, one for the 0–

24h forecasts, another for the 24–48h forecasts. We made a trial to take into account the lead time in the training by extending the features with a fourth one, containing the ranks of the lead times; however, this modification did not improve the predictive performance of the network. The lack of significance of the forecast horizon might be explained by the diurnal cycle in the ensemble standard deviation, which indicates a direct relation between forecast uncertainty and lead time.

3.6. Verification tools

As argued by *Gneiting et al.* (2007), the aim of probabilistic forecasting is to maximize the sharpness of the predictive distribution subject to calibration. The former refers to the concentration of the predictive distribution, whereas the latter means a statistical consistency between the validating observation and the corresponding predictive distribution. These goals can be addressed simultaneously using proper scoring rules quantifying the forecast skill by numerical values assigned to pairs of probabilistic forecasts and validating observations. In the case study of Section 4, for a given lead time, competing forecasts in terms of probability distribution are compared with the help of the mean CRPS over all forecast cases in the verification data. The improvement in terms of CRPS of a probabilistic forecast F with respect to a reference forecast F_{ref} can be assessed with the continuous ranked probability skill score (CRPSS; see, e.g., *Gneiting* and *Raftery*, 2007) defined as

$$\text{CRPSS} := 1 - \frac{\overline{\text{CRPS}_F}}{\overline{\text{CRPS}_{F_{\text{ref}}}}},$$

where $\overline{\text{CRPS}_F}$ and $\overline{\text{CRPS}_{F_{\text{ref}}}}$ denote the mean score values corresponding to forecasts F and F_{ref}, respectively. Here larger values indicate better forecast skill compared to the reference method.

Calibration and sharpness can also be quantified by the coverage and average width of the $(1 - \alpha)100\,\%$, $\alpha \in\,]0,1[$, central prediction interval, where calibration is defined as the proportion of validating observations located between the lower and upper $\alpha/2$ quantiles of the predictive distribution. For a well calibrated forecast, this value should be around $(1 - \alpha)100\,\%$, and in order to provide a fair comparison with the 11-member AROME-EPS, α should be chosen to match the nominal coverage of 83.33 % ($10/12 \times 100\,\%$) of the raw ensemble.

Simple graphical tools for assessing calibration of probabilistic forecasts are the verification rank histogram of ensemble predictions and its continuous counterpart, the probability integral transform (PIT) histogram. Verification rank is defined as the rank of the verifying observation with respect to the corresponding ensemble forecast (*Wilks,* 2019, Section 9.7.1), whereas PIT is the value of the predictive CDF evaluated at the observation (*Wilks,* 2019, Section 9.5.4). For a

properly calibrated ensemble, all ranks should be equally likely, while calibrated predictive distributions result in standard uniform PIT values.

Finally, the accuracy of point forecasts, such as median and mean, is quantified with the help of mean absolute errors (MAEs) and root mean squared errors (RMSEs), respectively.

4. Results

We start our analysis by determining the appropriate training-period length for our post-processing approaches. We consider a fixed verification period from July 8, 2020 to March 28, 2021 (264 calendar days) and compare the forecast skill of both local and regional TN EMOS models estimated using $20, 21, \ldots, 60$ day rolling training-periods. *Fig. 1* shows the mean CRPS taken over all forecast cases and lead times and the MAE of median forecasts as functions of the training-period length. Both plots clearly demonstrate that for longer training periods, the local TN EMOS is more skillful than the regional one. CRPS and MAE of the latter stabilize after day 51, while the corresponding scores of the local TN EMOS also seem to level off there. Hence, for TN EMOS modeling, a 51-day training-period seems to be a reasonable choice, and the same training-period length is applied for LN and GEV EMOS models as well. A detailed data analysis confirmed that this length is also appropriate for the machine learning approach of Section 3.5 (TN MLP), this choice of training data leaves a total of 273 calendar days (period June 29, 2020 – March 28, 2021) for model verification. Further, as in general, local versions of the tested EMOS approaches slightly outperform the regional ones, thus, in what follows, only the scores of the local models are reported.
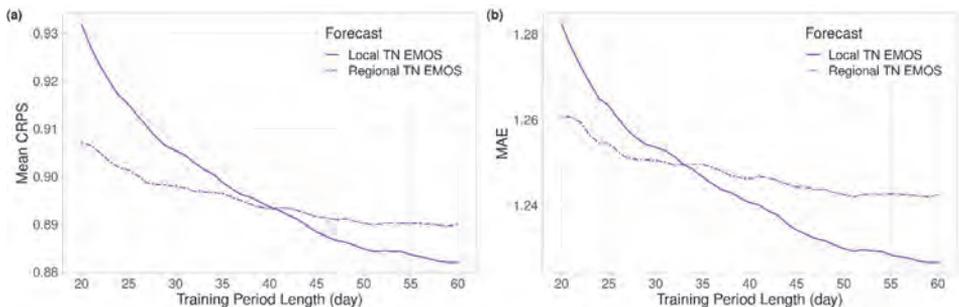
Fig. 1. Mean CRPS of probabilistic (a) and MAE of median (b) forecasts for local and regional TN EMOS models as functions of training-period length.

Fig. 2a shows the mean CRPS of post-processed and raw ensemble forecasts as functions of the lead time, whereas in *Fig. 2b*, the corresponding CRPSS values with respect to the raw ensemble are plotted. In general, all post-processing approaches outperform the raw ensemble for all lead times, but the advantage of post-processing decreases with the increase of the forecast horizon. The best overall CRPSS taken over all lead times and forecast cases belongs to the TN MLP model (0.111), followed by the local TN EMOS method (0.103); however, there are certain forecast horizons (especially around 20h and 23h), where the latter exhibits slightly better predictive performance. For the TGEV and LN EMOS approaches, these overall CRPSS values are 0.091 and 0.095, respectively.
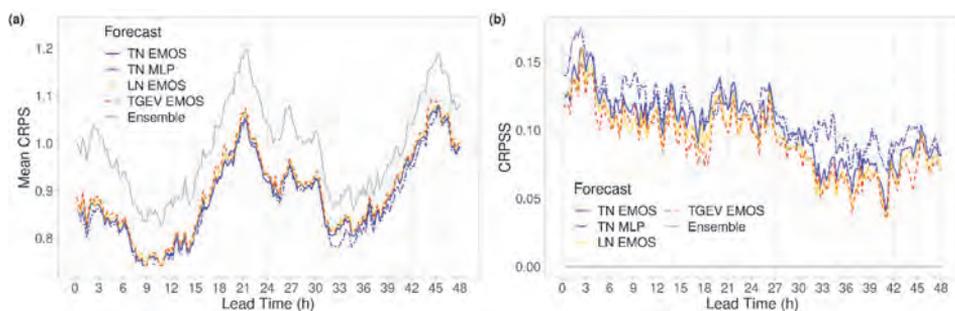
Fig. 2. Mean CRPS of post-processed and raw ensemble forecasts of wind speed (a) and CRPSS with respect to the raw ensemble (b) as functions of lead time.

The improved calibration of post-processed forecasts can also be observed in *Fig. 3a* showing the coverage of the nominal 83.33% central prediction intervals for different lead times. The coverage of the AROME-EPS ranges from 50% to 70%, and in general, increases with the increase of the lead time, whereas all post-processed forecasts for all lead times result in coverage values that are rather close to the nominal level. In particular, there is no visible systematic difference in the coverage values of the three investigated EMOS models, whereas the TN MLP approach seems to exhibit some kind of diurnal cycle. However, as depicted in *Fig. 3b*, the cost of the better calibration should be paid in the deterioration of the sharpness. The raw ensemble produces far the narrowest central predictive intervals, there is no difference in sharpness between the competing EMOS models, whereas the diurnal cycle in sharpness of the TN MLP is completely in line with the corresponding coverage. Note that similar diurnal cycles can be observed in the ensemble standard deviation and ensemble mean difference as well.
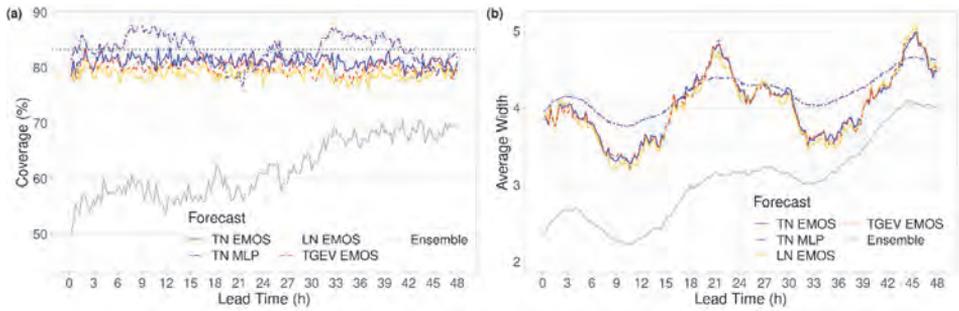
Fig. 3. Coverage (a) and average width (b) of the nominal 83.33 % central prediction intervals of post-processed and raw forecasts as functions of lead time.

While statistical post-processing substantially improves the calibration of probabilistic forecasts, it does not really effect the accuracy of point predictions. In *Fig. 4a*, the difference in MAE of the median forecasts of the various calibration methods from the MAE of the raw ensemble are plotted as functions of the lead time. Similar to the mean CRPS, models with TN predictive distribution show the best performance for all lead times; however, even the largest difference in MAE is less than 0.1 m/s. The same behavior can be observed in *Fig. 4b* displaying the difference in RMSE of the mean forecasts. This can indicate that the raw AROME-EPS forecasts are already unbiased and indeed, the mean biases of the ensemble mean and median taken over all forecast cases of the whole available period May 8, 2020 to March 28, 2021 and all lead times are just 0.136 m/s and 0.122 m/s, respectively, while the overall MAE equals 1.285 m/s and the overall RMSE is 1.669 m/s.
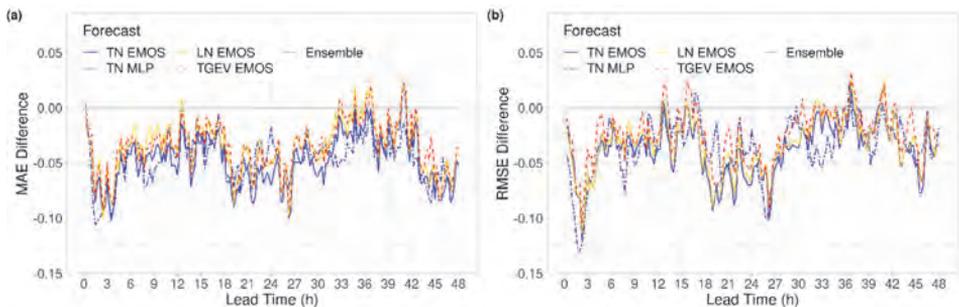
Fig. 4. Difference in MAE of the median forecasts (a) and in RMSE of the mean forecasts (b) from the raw ensemble as functions of lead time.

Finally, *Fig. 5* shows the verification rank histograms of raw and PIT histograms of post-processed forecasts for four different lead time intervals. The U-shaped verification rank histograms clearly indicate the underdispersive character of the raw ensemble; however, the dispersion improves with the forecast lead time. This behavior is completely in line with the increasing coverage and high sharpness of the raw forecasts (see *Fig. 3*). Further, the depicted rank histograms are rather symmetric, which is consistent with the small overall MAE and RMSE and illustrates the lack of bias in the raw ensemble. All post-processing approaches substantially improve calibration; models based on TN predictive distributions result in almost flat PIT histograms, whereas the histograms of TGEV and LN EMOS approaches indicate slight biases. Kolmogorov–Smirnov (KS) test rejects the uniformity of the PIT for all models; however, based on the values of the KS test statistic, one can provide a clear ranking of the methods. PIT values of the TN MLP approach fit best the uniform distribution, followed by the TN, TGEV, and LN EMOS models, which order nicely reflects the shapes of the corresponding histograms of *Fig. 5*.
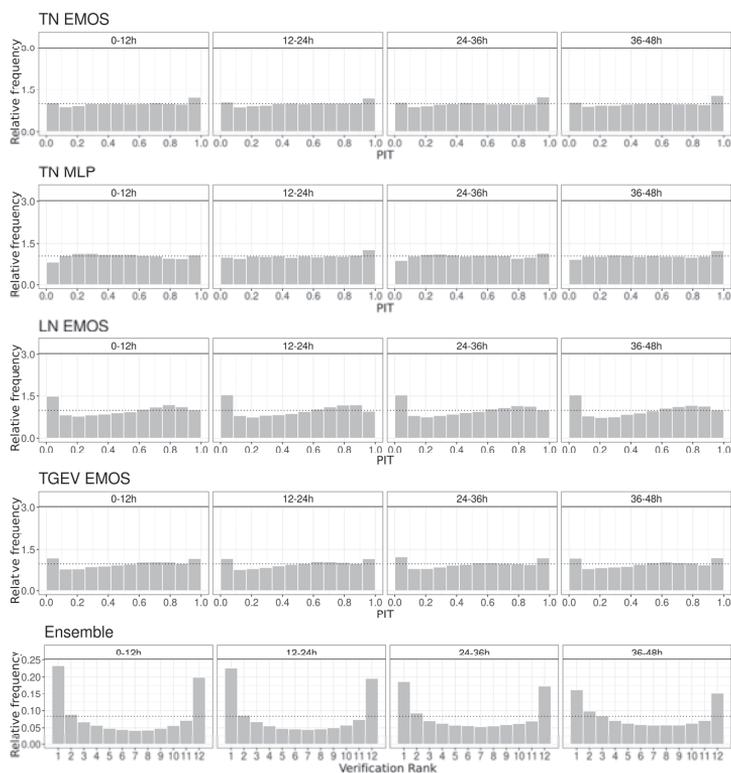
Fig. 5. PIT histograms of post-processed and verification rank histograms of raw ensemble forecasts of wind speed for the lead times 0-12h, 12-24h, 24-36h, and 36-48h.

Based on the above results, one can conclude that models with TN predictive distributions provide the best forecast skill, and the machine learning based TN MLP approach outperforms the TN EMOS model. Hence, one might be interested in the dissimilarities of the corresponding predictive distributions. According to *Fig. 6a*, there is no fundamental difference in the location, and the station-wise time series plots of this parameter also provide matching curves (not shown). Thus, the linear model of the location given in Eq. (1) seems to be optimal. A completely different picture can be observed in *Fig. 6b*, showing the mean of the scales of the TN predictive distributions as function of lead time. The diurnal cycle for TN MLP is far less pronounced than for the TN EMOS, and the corresponding time series (not shown) exhibit completely different behavior, too. Hence, the superior performance of the TN MLP approach is due to the more general modeling of the scale of the TN predictive distribution.
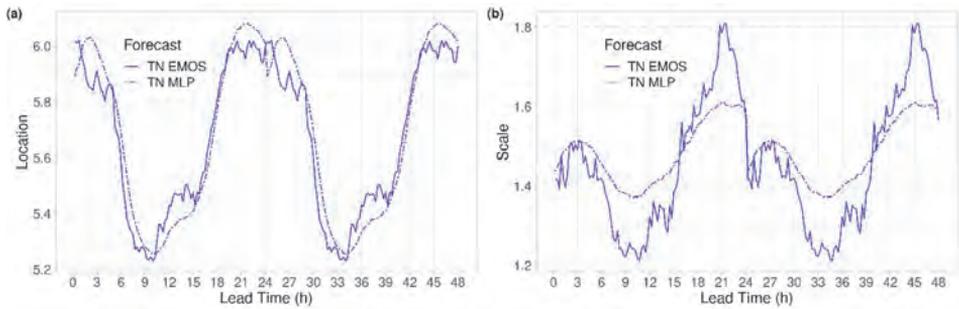
Fig. 6. Mean of the location (a) and scale (b) of the truncated normal predictive distributions of TN EMOS and TN MLP models as functions of lead time.

5. Conclusions

We investigate post-processing of ensemble forecasts of 100m wind speed, as this variable is of crucial interest in wind energy production. Three different EMOS models based on truncated normal, log-normal, and truncated generalized extreme value distributions are considered, and we also propose a novel method where the probabilistic forecasts are obtained in the form of a truncated normal predictive distribution with parameters linked to the ensemble via a multilayer perceptron neural network. The forecasts skill of the competing calibration methods is tested on the 11-member AROME-EPS hub height wind

speed ensemble forecasts of the HMS for three wind farms in Hungary and verified against observations provided by the wind farm operators. Only short-term predictions are considered with forecast horizons ranging up to 48 h with a temporal resolution of 15 minutes. Using the raw ensemble as reference, we compare the mean CRPS of probabilistic, MAE of median, and RMSE of mean forecasts, and the coverage of central prediction intervals corresponding to the nominal 83.33% coverage. We also study the shapes of the PIT histograms of the calibrated forecasts for different lead times and compare with the corresponding verification rank histograms of the raw ensemble. Based on our case study we can conclude, that compared with the raw ensemble, post-processing always improves the calibration of probabilistic and accuracy of point forecasts. From the four competing methods, the novel machine learning based TN MLP approach exhibits the best overall performance; moreover, in contrast to the investigated EMOS models, it provides a single universal model for several forecast horizons. The superior performance of the TN MLP model is explained by its ability to represent more complex nonlinear relations between the ensemble forecasts and the parameters of the TN predictive distribution, and our results are consistent with the findings of *Rasp* and *Lerch* (2018) and *Ghazvinian et al.* (2021).

The present work highlights several directions of potential future research. From the one hand, one might consider the machine learning approach to parameter estimation in the case of other predictive distribution families such as the LN and TGEV investigated here. From the other hand, a neural network allows a very flexible choice of input features, providing a simple and straightforward opportunity of involving predictions of other weather variables in wind speed modeling.

References

Baran, S., Horányi, A. and *Nemoda, D.,* 2014: Comparison of the BMA and EMOS statistical methods in calibrating temperature and wind speed forecast ensembles. *Időjárás 118*, 217–241.

Baran, S. and *Lerch, S.,* 2015: Log-normal distribution based Ensemble Model Output Statistics models for probabilistic wind speed forecasting. *Q. J. R. Meteorol. Soc. 141*, 2289–2299. https://doi.org/10.1002/qj.2521

Baran, S. and *Lerch, S.,* 2016: Mixture EMOS model for calibrating ensemble forecasts of wind speed. *Environmetrics 27*, 116–130. https://doi.org/10.1002/env.2380

Baran, S. and *Lerch, S.,* 2018: Combining predictive distributions for statistical post-processing of ensemble forecasts. *Int. J. Forecast. 34*, 477–496. https://doi.org/10.1016/j.ijforecast.2018.01.005

Baran, S., Szokol, P., and *Szabó, M.,* 2021: Truncated generalized extreme value distribution based EMOS model for calibration of wind speed ensemble forecasts. *Environmetrics 32,* e2678. https://doi.org/10.1002/env.2678

Bauer, P., Thorpe, A. and Brunet, G., 2015: The quiet revolution of numerical weather prediction. *Nature 525*, 47–55. https://doi.org/10.1038/nature14956

Bremnes, J.B., 2019: Constrained quantile regression splines for ensemble postprocessing. *Mon. Weather Rev. 147*, 1769–1780. https://doi.org/10.1175/MWR-D-18-0420.1

Buizza, R., 2018: Ensemble forecasting and the need for calibration. In (eds. *Vannitsem, S., Wilks, D. S., Messner, J.W.*), Statistical Postprocessing of Ensemble Forecasts, Elsevier, Amsterdam, 15–48. https://doi.org/10.1016/B978-0-12-812372-0.00002-9

Buizza, R., Houtekamer, P. L., Toth, Z., Pellerin, G., Wei, M., and Zhu, Y., 2005: A comparison of the ECMWF, MSC, and NCEP global ensemble prediction systems. *Mon. Weather Rev. 133*, 1076–1097. https://doi.org/10.1175/MWR2905.1

Buizza, R., Petroliagis, T., Palmer, T., Barkmeijer, J., Hamrud, M., Hollingsworth, A., Simmons, A., and Wedi, N., 1998: Impact of model resolution and ensemble size on the performance of an Ensemble Prediction System. *Q. J. R. Meteorol. Soc. 124*, 1935–1960. https://doi.org/10.1002/qj.49712455008

Descamps, L., Labadie, C., Joly, A., Bazile, E., Arbogast, P., and Cébron, P., 2015: PEARP, the Météo-France short-range ensemble prediction system. *Q. J. R. Meteorol. Soc. 141*, 1671–1685. https://doi.org/10.1002/qj.2469

Friederichs, P. and Hense, A., 2007: Statistical downscaling of extreme precipitation events using censored quantile regression. *Mon. Weather Rev. 135*, 2365–2378. https://doi.org/10.1175/MWR3403.1

Ghazvinian, M., Zhang, Y., Seo, D-J., He, M., and Fernando, N., 2021: A novel hybrid artificial neural network - parametric scheme for postprocessing medium-range precipitation forecasts. *Adv. Water Resour. 151*, paper 103907. https://doi.org/10.1016/j.advwatres.2021.103907

Gneiting, T., Balabdaoui, F., and Raftery, A.E., 2007: Probabilistic forecasts, calibration and sharpness. *J. R. Stat. Soc. B 69*, 243–268. https://doi.org/10.1111/j.1467-9868.2007.00587.x

Gneiting, T. and Raftery, A.E., 2005: Weather forecasting with ensemble methods. *Science 310*, 248–249. https://doi.org/10.1126/science.1115255

Gneiting, T. and Raftery, A.E., 2007: Strictly proper scoring rules, prediction and estimation. *J. Amer. Statist. Assoc. 102*, 359–378. https://doi.org/10.1198/016214506000001437

Gneiting, T., Raftery, A.E., Westveld, A.H., and Goldman, T., 2005: Calibrated probabilistic forecasting using ensemble model output statistics and minimum CRPS estimation. *Mon. Weather Rev. 133*, 1098–1118. https://doi.org/10.1175/MWR2904.1

Goodfellow, I., Bengio, Y., and Courville, A., 2016: Deep Learning. MIT Press, Cambridge.

Hemri, S., Scheuerer, M., Pappenberger, F., Bogner, K., and Haiden, T., 2014: Trends in the predictive performance of raw ensemble weather forecasts. *Geophys. Res. Lett. 41*, 9197–9205. https://doi.org/10.1002/2014GL062472

Horányi, A., Kertész, S., Kullmann, L., and Radnóti, G., 2006: The ARPEGE/ALADIN mesoscale numerical modeling system and its application at the Hungarian Meteorological Service. *Időjárás 110*, 203–227.

Jávorné Radnóczi, K., Várkonyi, A., and Szépszó, G., 2020: On the way towards the AROME nowcasting system in Hungary. *ALADIN-HIRLAM Newsletter 14*, 65–69.

Lerch, S. and Baran, S., 2017: Similarity-based semi-local estimation of EMOS models. *J. R. Stat. Soc. C 66*, 29–51. https://doi.org/10.1111/rssc.12153

Lerch, S. and Thorarinsdottir, T.L., 2013: Comparison of non-homogeneous regression models for probabilistic wind speed forecasting. *Tellus A* 65, paper 21206. https://doi.org/10.3402/tellusa.v65i0.21206

Messner, J.W., Zeileis, A., Bröcker, J., and Mayr, G.J., 2013: Probabilistic wind power forecasts with an inverse power curve transformation and censored regression. *Wind Energy 17*, 1753–1766. https://doi.org/10.1002/we.1666

Pinson, P. and Messner, J.W., 2018: Application of Postprocessing for Renewable Energy. In (eds. *Vannitsem, S., Wilks, D.S., Messner, J.W.*) Statistical Postprocessing of Ensemble Forecasts, Elsevier, 241–266. https://doi.org/10.1016/B978-0-12-812372-0.00009-1

Raftery, A. E., Gneiting, T., Balabdaoui, F., and Polakowski, M., 2005: Using Bayesian model averaging to calibrate forecast ensembles. *Mon. Weather Rev. 133*, 1155–1174. https://doi.org/10.1175/MWR2906.1

Rasp, S. and Lerch, S. (2018) Neural networks for postprocessing ensemble weather forecasts. *Mon. Weather Rev. 146*, 3885–3900. https://doi.org/10.1175/MWR-D-18-0187.1

Taillardat, M. and *Mestre, O.,* 2020: From research to applications – examples of operational ensemble post-processing in France using machine learning. *Nonlin. Proc. Geophys. 27*, 329–347. https://doi.org/10.5194/npg-27-329-2020

Taylor, J., McSharry, P. and *Buizza, R.,* 2009: Wind power density forecasting using ensemble predictions and time series models. *IEEE Trans. on Energy Convers. 24*, 775–782. https://doi.org/10.1109/TEC.2009.2025431

Thorarinsdottir, T. L. and *Gneiting, T.,* 2010: Probabilistic forecasts of wind speed: Ensemble model output statistics by using heteroscedastic censored regression. *J. R. Stat. Soc. A 173*, 371–388. https://doi.org/10.1111/j.1467-985X.2009.00616.x

Vannitsem, S., Bremnes, J. B., Demaeyer, J., Evans, G. R., Flowerdew, J., Hemri, S., Lerch, S., Roberts, N., Theis, S., Atencia, A., Ben Boualègue, Z., Bhend, J., Dabernig, M., De Cruz, L., Hieta, L., Mestre, O., Moret, L., Odak Plenkovič, I., Schmeits, M., Taillardat, M., Van den Bergh, J., Van Schaeybroeck, B., Whan, K., and *Ylhaisi, J.,* 2021: Statistical postprocessing for weather forecasts – review, challenges and avenues in a big data world. *Bull. Amer. Meteorol. Soc. 102*, E681–E699. https://doi.org/10.1175/BAMS-D-19-0308.1

Wilks, D.S., 2018: Univariate ensemble forecasting. In (eds. *Vannitsem, S., Wilks, D.S., Messner, J.W.*), Statistical Postprocessing of Ensemble Forecasts, Elsevier, 49–89. https://doi.org/10.1016/B978-0-12-812372-0.00003-0

Wilks, D.S., 2019: Statistical Methods in the Atmospheric Sciences. 4th ed. Elsevier, Amsterdam.

Wind Europe, 2021: Wind energy in Europe 2020. Statistics and the outlook for 2021-2025. Available at: https://windeurope.org/intelligence-platform/product/wind-energy-in-europe-in-2020-trends-and-statistics/ [Accessed on 17 August 2021]

World Wind Energy Association, 2021: Worldwide wind capacity reaches 744 gigawatts – an unprecedented 93 gigawatts added in 2020. Available at: https://wwindea.org/worldwide-wind-capacity-reaches-744-gigawatts/ [Accessed on 17 August 2021]

Yuen, R. A., Baran, S., Fraley, C., Gneiting, T., Lerch, S., Scheuerer, M., and *Thorarinsdottir, T.L.,* 2018: R package ensembleMOS, Version 0.8.2: Ensemble Model Output Statistics. Available at: https://cran.r-project.org/package=ensembleMOS [Accessed on 17 August 2021]

IDŐJÁRÁS

Effect of the uncertainty in meteorology on air quality model predictions

Zita Ferenczi*, **Emese Homolya**, **Krisztina Lázár**, and **Anita Tóth**

Hungarian Meteorological Service
Kitaibel P. str. 1, H-1024 Budapest, Hungary

*Corresponding author's E-mail: ferenczi.z@met.hu

Abstract— An operational air quality forecasting model system has been developed and provides daily forecasts of ozone, nitrogen oxides, and particulate matter for the area of Hungary and three big cites of the country (Budapest, Miskolc, and Pécs). The core of the model system is the CHIMERE off-line chemical transport model. The AROME numerical weather prediction model provides the gridded meteorological inputs for the chemical model calculations. The horizontal resolution of the AROME meteorological fields is consistent with the CHIMERE horizontal resolution. The individual forecasted concentrations for the following 2 days are displayed on a public website of the Hungarian Meteorological Service. It is essential to have a quantitative understanding of the uncertainty in model output arising from uncertainties in the input meteorological fields. The main aim of this research is to probe the response of an air quality model to its uncertain meteorological inputs. Ensembles are one method to explore how uncertainty in meteorology affects air pollution concentrations. During the past decades, meteorological ensemble modeling has received extensive research and operational interest because of its ability to better characterize forecast uncertainty. One such ensemble forecast system is the one of the AROME model, which has an 11-member ensemble where each member is perturbed by initial and lateral boundary conditions. In this work we focus on wintertime particulate matter concentrations, since this pollutant is extremely sensitive to near-surface mixing processes. Selecting a number of extreme air pollution situations we will show what the impact of the meteorological uncertainty is on the simulated concentration fields using AROME ensemble members.

Key-words: chemical transport model, uncertainty in meteorology, ensemble technic, smog

1. Introduction

Air pollution is a major environmental risk of our times, the reduction of which poses a great challenge on professionals and decision-makers equally (*Lelieveld*, 2017). High concentrations of air pollutants may directly impair human health (*Landrigan,* 2017), ecosystems (*De Marco et al.*, 2019), and the built environment (*Kucera* and *Fitz,* 1995). Deposition processes may lead to harmful material getting into the surrounding environmental media – into the vegetation, waters, or soil –, where it can cause further damage (*Moiseenko et al.*, 2018). Today a widening range of attention is given to air quality, and we have more and more advanced methodologies to assess the current status (*EEA*, 2019) and tendencies of, and the expected changes in air pollution (*Apte et al.*, 2017).

Although the most accurate information regarding the actual conditions in the air is gained by direct measurements, a comprehensive assessment of air quality today requires the use of specific air quality models (*Rybarczyk* and *Zalakiviciute*, 2018). Based on a mathematical interpretation of physical and chemical processes taking place in the air, air quality models define a relationship between the emitted pollutants and concentrations measured in the environment (*Baklanov et al.*, 2014).

Therefore, they provide a suitable way for the tracking of the dispersion, chemical reactions, and deposition of air pollutants. Modern air quality models take many kinds of environmental processes into account, and their evolving complexity makes it possible for them to describe the real behavior of the natural systems more and more profoundly. However, no matter how sophisticated a model is, due to the high complexity of the natural systems and the feedbacks and non-linearities they involve, it is not able to describe all processes fully accurately, it is bound to use approximation and parameterization in its methods. Simulations of the models are therefore generally accompanied by a certain amount of uncertainty, that is dependent on the calculation methods, the accuracy of the input data, the geographical environment, the weather situation, and the resolution as well (*Borrego et al., 2*008). In the issue of the response of the air quality model to varying input data, it is essential to evaluate the reaction of the model to the changes in the emission or the meteorological data. The better understanding we have regarding the behavior, characteristics, and limits of our models, the more precisely we can define this uncertainty, which then provides us with the opportunity to estimate the expectable accuracy of our calculations beforehand.

One of the most important input data of the chemical transport models comes from the emission inventories, which latter are static databases for a specific year. Furthermore, emissions are not possible to be measured in most cases. The emission estimate is inevitably an inaccurate representation of the emission that actually occurred. In addition to the simulations, emission data with fine temporal (*Menut et al.,* 2012) and spatial variations are expected. The uncertainty of the emission data depends not only on the category of the emission source but also on

the contributing emission sources and their quantity. The assessment of uncertainty in the modeled forecasts in relation to the input uncertainty of the emission dataset has been analyzed in many papers (*Napelenok et al., 2*011; *Holnicki* and *Nahorski,* 2015).

The aim of this research was to analyze the Hungarian air quality from different aspects using up-to-date tools based on model simulations, where we focused primarily on weather elements that mostly influence dispersion processes in the air (*Angevine*, *et al.,* 2014), their effects on concentrations evolving in the environment, and the modeling of critical air quality situations rising in special meteorological conditions. In our previous work (*Homolya,* 2021), a sensitivity analysis was carried out using the CHIMERE chemical transport model in order to examine, to what extent and how the key meteorological elements affect the evolving concentrations in the course of the modeling process. For this study, the values of the meteorological parameters were artificially modified. This modification was not physically consistent, but at that time ensemble members from AROME model were not available.

As a result of developments at the Hungarian Meteorological Service in recent years, AROME EPS has become available for sensitivity analyses. Using this new meteorological driver, physically consistent meteorological fields were available for our examination. In this work, we focus on wintertime particulate matter concentrations, since this pollutant is extremely sensitive to near-surface mixing processes. Three extreme air pollution situations were selected to examine the impact of the meteorological uncertainty on the simulated concentration fields.

2. Materials and methods

2.1. Models

For the examinations with the CHIMERE chemical transport model (*Mailler et al.,* 2017), a domain covering Hungary and extending to almost the whole territory of the Carpathian Basin, with the borders of latitudes 45° and 50° and longitudes 14° and 25° (*Fig. 1*) was chosen to be the target area. The area bounded by the red line in *Fig. 1* shows the calculation domain. The grid was defined the way that the spatial resolution fits that of the emission inventory data of EMEP – 0.1° – which corresponds to roughly 10 km in the region of the Carpathian Basin. We have to emphasize that the analyses presented in this work refer to the area bounded by the blue line, which is smaller than the area bounded by the red line. The reason for this choice was that some unbalances might occur close to the border of the domain, arising from the boundary conditions.
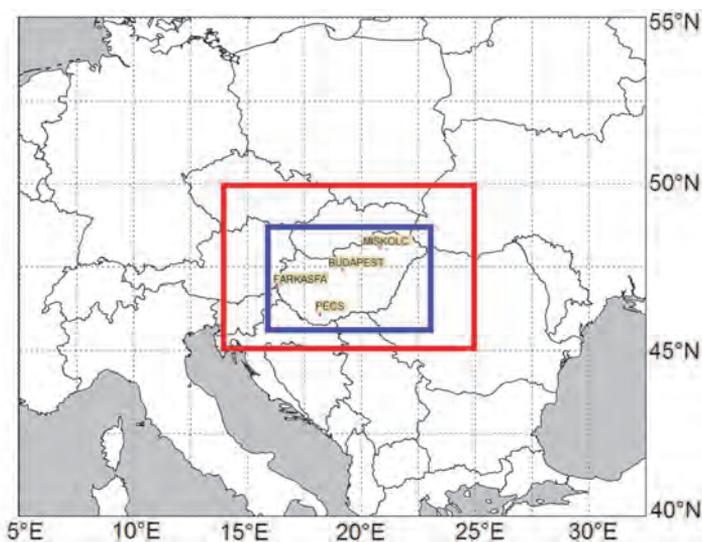
Fig. 1. The target domain for the analyses using the CHIMERE model and the location of the monitoring sites.

The gridded emission inventory of EMEP for the year 2015 was used in the simulations. The inventory data for nitrogen-oxides, volatile organic compounds, sulphur dioxide, ammonia, fine aerosol particles ($PM_{2.5}$), coarse aerosol particles ($PM_{10} - PM_{2.5}$), and carbon-monoxide were taken into account in a 0.1° spatial resolution. The EMEP emissions inventory, which includes annual total data, has to be converted to hourly data (*Menut et al.,* 2012). During the time distribution of the emission data, seasonal, weekly, and hourly factors are used.

Data of biogenic emission was calculated by the MEGAN model (*Guenther et al.,* 2006), which is a global model with a base resolution of ~ 1 km.

Meteorological data were provided by the AROME non-hydrostatic numerical weather prediction model of the Hungarian Meteorological Service in a 1-hour temporal and the 0.1^0 spatial resolution of the EMEP grid. For CHIMERE, data is prepared by the built-in meteorological pre-processor, using the model's own diagnostic tool. One file in the database contains data for one single day. AROME/HU (*Szintai et al.,* 2015) runs 8 times per day up to 36–48 hours at 2.5 km horizontal resolution using 60 vertical levels over a domain including the Carpathian Basin. The initial conditions are prepared by optimal interpolation on the surface and local 3D-Var assimilating SYNOP, TEMP, AMDAR, GNSS ZTD measurements, and Mode-S MRAR data from the Slovenian network. The hydrometeors and snow evolve through the data assimilation (DA) cycle. Hourly lateral boundary conditions are taken from the ECMWF HRES forecast in time lagged mode. AROME-EPS is an 11-member forecast coupled to 18 UTC ECMWF ENS with a frequency of 3

hours. The model runs at horizontal resolution of 2.5 km over a domain covering the Carpathian Basin. The forecasts are initialized at 00 UTC and range up to 48 hours.

For our chemical transport model calculations, the AROME and AROME-EPS run at 00 UTC and the model results of 00–24 UTC have been used. In our model simulations, the deterministic model is considered as benchmark results because this data is used in the operational air quality prediction. The originally fine resolution meteorological fields of the AROME and AROME-EPS model were interpolated to the CHIMERE grid, which was defined by the EMEP gridded emission data.

Boundary and initial conditions are needed to get appropriate model results. In our test cases, in the case of the first day, climatological data were used as initial conditions, and then the previous simulation produced the initial conditions for the next simulation. The climatological set of boundary conditions has been provided by the LMDz-INCA global model (Laboratoire de Météorologie Dynamique General Circulation Model coupled with INCA: Interaction with Chemistry and Aerosols) (*Hourdin et al.,* 2006; *Hauglustaine et al.,* 2004). Information concerning land cover has been provided by the USGS database (*Loveland et al.,* 2000).

2.2. Measurements

Four monitoring stations with significantly different characteristics (population, type of station) were selected for the detailed analysis of three cities, Budapest, Miskolc, Pécs, and Farkasfa background monitoring station. The locations of the monitoring stations can be seen in *Fig. 1*.

At several locations in Budapest (525.1 km^2, 1 756 000 inhabitants), the monitoring of PM$_{10}$ with fine temporal resolution started in 2007. Among the monitoring sites, the Gilice tér urban background station (located in the southeastern part of Budapest) was selected for our analysis, which is a standard meteorological and air quality monitoring station providing PM$_{10}$ concentrations and detailed meteorological observations with good data coverage. This location is in the area of the Marczell György Main Observatory of the Hungarian Meteorological Service. The classification of this air quality monitoring site is suburban with a significant influence from major sources from the greater Budapest area.

Miskolc (236.7 km^2, 159 000 inhabitants) is represented by the Búza tér station. The classification of the site is urban traffic with a significant contribution from traffic-related sources. Moreover, the whole city is located in an unfavourable geographical location in the valley of Sajó River surrounded by the Bükk Mountains. Its special orography contributes to the development of long-lasting (several days up to weeks) and severe air pollution episodes.

In Pécs (162.8 km^2, 148 000 inhabitants), the selected station (Boszorkány utca) is located in a suburban environment. The hourly PM$_{10}$ data for our complex analysis have been available since 2009. One of the major industrial emission

sources in this area is a coal-fueled power plant equipped with two modern electrostatic precipitators. This development further decreases the PM_{10} emissions in the city. However, compared to Miskolc, the city of Pécs has more favorable orography: the northern part of the city is bordered by the Mecsek Mountains, but the southern side is open and flat.

Farkasfa background air pollution monitoring station is located in the western part of Hungary, at the area of the Őrség National Park. The station is surrounded by forest and no essential local source of air pollutants can be found nearby.

2.3. Episode situations

Three episode situations (January 6–13, 2020, January 17–22, 2020, and November 9–14, 2020) were analyzed in depth, when PM_{10} concentrations were over the threshold limit in Hungary. The synoptic events were anticyclonal in Central Europe during these periods (*Fig. 2*). A cold pool is a special meteorological situation that is related to inversion in the upper atmosphere and is coupled with low surface air temperatures. It most frequently evolves in areas that are surrounded by chains of mountains. Events in anticyclones trigger the development of cold pool as they foster downward motions in the air. By serving as a barrier for mixing motions, inversion causes the air to stabilize, and it hinders the movement of the air mass out of the basin.
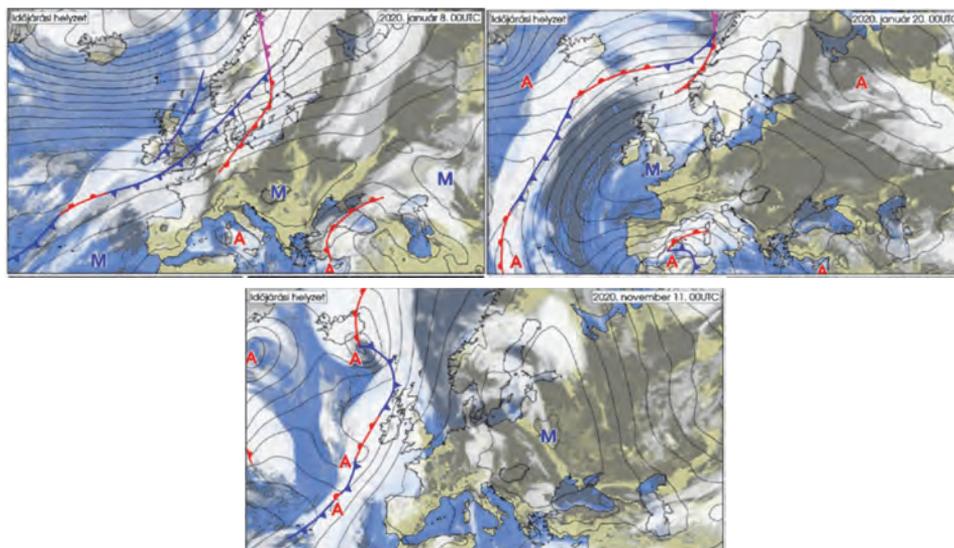
Fig. 2. Typical weather situations during the analyzed episode situations. (source: www.met.hu)

During the time period January 6–13, 2020, an anticyclone was observed in Central Europe. The weather was quiet and uneventful in the first days of this time period, the sky was variably cloudy and the sun was quite often shining everywhere in the country. The sky was weakly cloudy, at night but temporary fog spots formed at dawn. In the middle of the period, the influence of a warm front was observed, and warm, moist air came into Hungary. Subsequently, a layer of clouds and fog formed during the nights in many places, which did not break up or only broke up later during the day in the eastern and northeastern parts of the country. In the rest of the country, the sky was clear due to the strengthening NW wind, but the extension of the clear region decreased day by day.

The following period (January 17–22, 2020) was heavily cloudy with misty, foggy weather, both at nights and during the days. It is important to mention that on January 19, a weak cold front arrived over the western counties and disbanded there, but it did not cause a significant change in the weather. The change was brought by another cold front, which arrived on January 22 from the north. It had already passed over the country, leaving a weakly cloudy, sunny weather behind.

During the next period (November 9–14, 2020), an extensive anticyclone was located again over Central Europe. It stretched from the Scandinavian Peninsula to the Balkans. A classic cold pool developed over the target area. The permanently cloudy, misty, foggy weather across the country was only interrupted during the day in some places in the western parts of the country. The turning point was a passing cold front that brought drier air.

3. Results and discussion

In this section, the effect of the meteorological parameters on the PM_{10} concentration values calculated by an air quality model will be presented. In our previous work (*Ferenczi et al.,* 2020) we found, that the wind speed, the boundary layer (PBL) height, and the precipitation affected the prediction of the PM_{10} concentrations the most. In this work, the impact of the meteorological uncertainty on the simulated concentration fields was determined using AROME numerical weather prediction model's ensemble members. The analysis focused on the effects of the wind speed and the boundary layer height. In this work, the effect of precipitation was not examined, because in these episode situations no precipitation was reported. Three episode situations were selected for the analysis. The characteristics of these episode situations were described in the previous section.

3.1. Effect of the uncertainty in meteorology on air quality model predictions

We calculated the areal average differences between the various EPS and the deterministic values of the meteorological parameters and the PM_{10} concentration over the domain covering Hungary. All the three episode situations have been

analyzed with this method. The time series of these areal average differences and also of the deterministic values are visualized in graphs.

First we conclude the results of the six-day period in November 2020. (*Fig. 3*) On the last two days, the deterministic PBL heights are much higher than the EPS values in the middle of the day, that is why we see large negative differences in the figure around noon. That means that the maximum PBL height was underestimated by the EPS members. At the end of the day on November 13, all the EPS areal averages are above the deterministic value. The maximum of the positive areal average differences was +49 m and the largest negative deflection was –93 m. Referring to the wind speed areal averages we can say, that the differences stayed mostly between +/– 0.1 m/s in the first and between+/– 0.2 m/s in the second half of the period. On November 13, during the first 8 hours, the deterministic areal averages were lower than all the other EPS values. The maximum value of the positive differences is +0.3 m/s and the maximum of the negative differences is –0.2 m/s. When the PBL height or wind speed differences were large, all the EPS members were deflected in the same direction from the deterministic value. The areal average PM_{10} concentrations of the EPS members differ mostly between +/– 1 μg/m³ from the deterministic values in the first part of the period. With time, larger values appear, and the EPS members also differ more from each other. The maximum deflection is +2.4 μg/m³in the positive direction and in –3.3 μg/m³ the negative direction. In the morning (from 6 to 12) of November 13, all the EPS values were lower than the deterministic concentration. This can be explained by the behavior of the areal average wind speeds: on this day, during the first 8 hours, the deterministic wind speeds were lower than any other EPS wind speeds. We were interested in how the daily averages of the PBL height, wind speed, and PM_{10} concentration changed on this day over the country. We visualized the deterministic daily averages and the differences between the EPS daily averages and deterministic values on maps. The maps relating to the PM_{10} concentration can be seen in *Fig. 4*. In the first map we see, that the daily, deterministic PM_{10} concentrations were above 40–50 μg/m³ in the eastern half of the country. In the other, difference-maps we see, that the EPS values differed with more than +/−8 μg/m³ in this eastern part of the modeled region. Where the deterministic PM_{10} concentrations are relatively high, there the EPS members show larger differences. Although there are extended areas showing positive differences, we can still have an impression, that over the country the negative differences (green colours) dominate.

A)
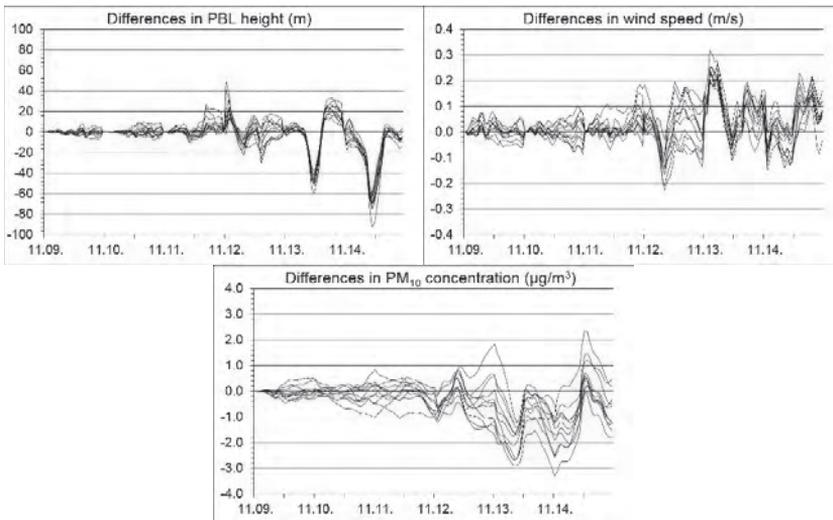
B)
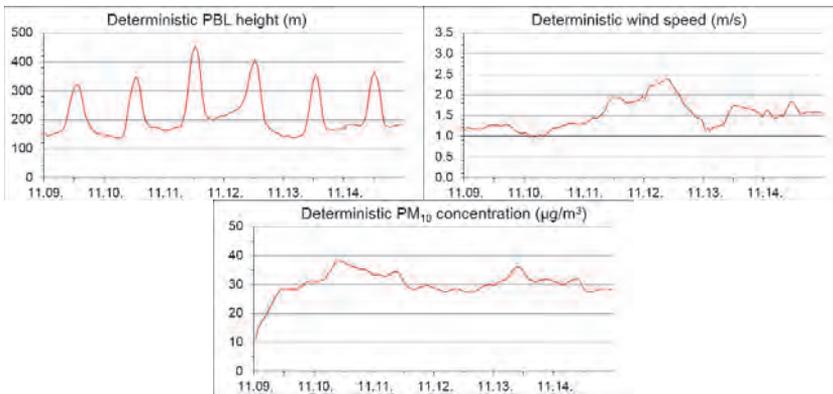
Fig. 3. A) Boundary layer height, wind speed, and PM$_{10}$ differences between EPS members and deterministic values. B) Deterministic boundary layer height, wind speed, and PM$_{10}$ values (areal averages, November 9–14, 2020).
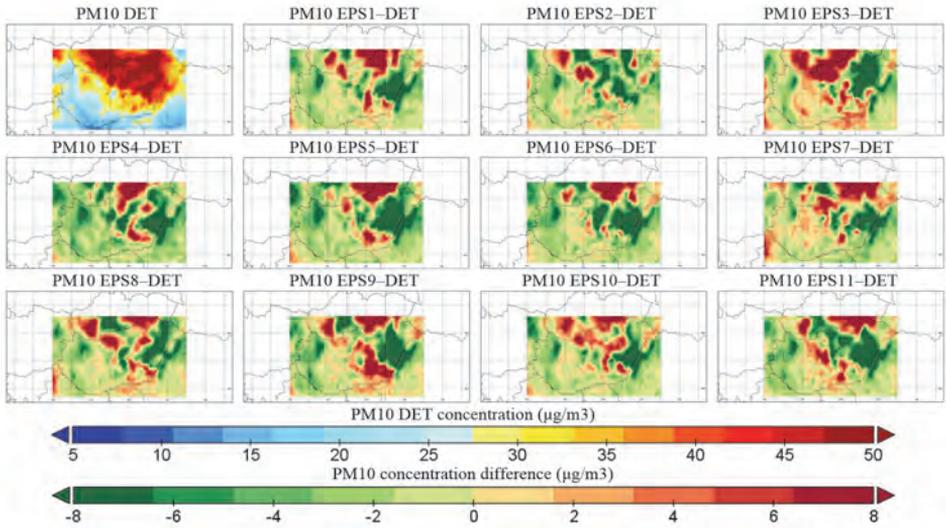
Fig. 4. Maps of deterministic daily average PM$_{10}$ concentrations (first) and the difference between the EPS and the deterministic daily averages (others). Positive differences are red, negative differences are green. November 13, 2020.

The next period is the January 6–13, 2020. (*Fig. 5*) The PBL height differences stayed mostly between +/–20 m, only on January 11 were larger differences. On this day, the extent of the deterministic planetary boundary layer was the largest. The maximum value of the positive differences is +43 m, in the negative direction the largest deflection was – 38 m. The wind speed areal average differences are mostly between +/–0.2 m/s. On January 11, the differences are higher, there are some EPS members which differ nearly +/–0.3 m/s from the deterministic value. The maximum of the positive wind speed differences was +0.3 m/s, in the negative direction the maximum deflection was –0.3 m/s. The differences in the PM$_{10}$ concentrations stayed mostly between +/–1 μg/m^3, but in some hours, the differences are near to the +/–2 μg/m^3 values. The maximum of the positive differences was +1.9 μg/m^3 and of the negative differences was –3.5 μg/m^3. To conclude, we can say that the largest differences were on January 11. This can be due to a cold front reaching the country on this day. We can see, that the deterministic wind speed and also the PBL height reached maximum values on this day, and the EPS members showed high variability around these maximum values. However, we could not detect especially large spread in the EPS PM$_{10}$ concentrations on this day.

A)
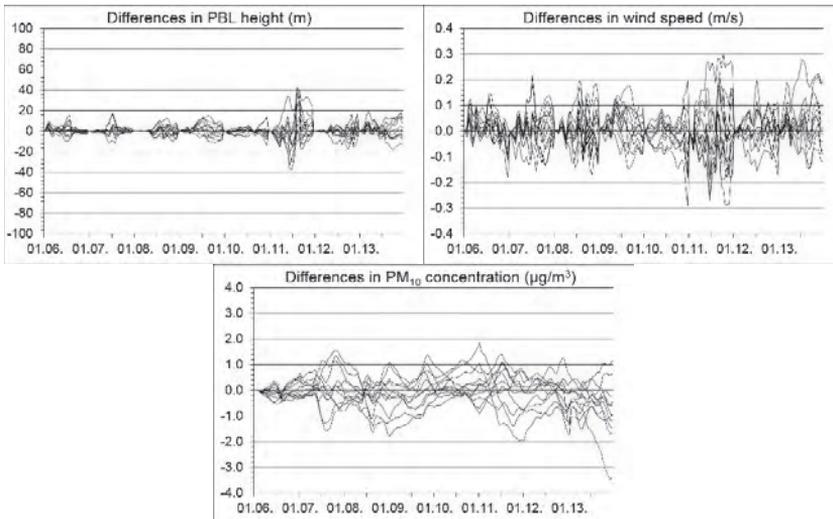
B)
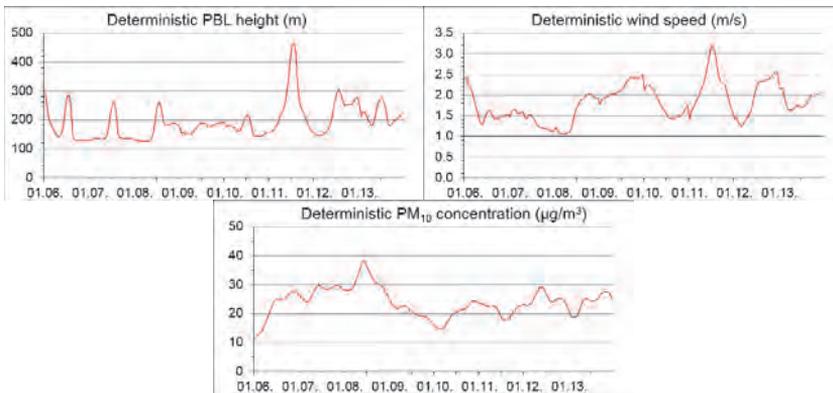
Fig. 5. A) Boundary layer height, wind speed, and PM₁₀ differences between EPS members and deterministic values. B) Deterministic boundary layer height, wind speed, and PM₁₀ values (areal averages, January 6–13, 2020.).

Lastly we conclude the information about the period January 17–22, 2020. (*Fig. 6*) Usually the PBL height deflections stayed between +/–20 m, but there are EPS members which differ in a larger magnitude mostly near the end of the day. The largest difference was +121 m, in the other direction –46 m was the highest difference. Most of the wind speed differences are in the range of +/–0.2 m/s. The largest, positive deflection was +0.6 m/s, the largest negative

difference was –0.5 m/s. In case of the PM_{10} concentrations, the variation between the EPS members stayed large during the whole period apart from the first few hours. The differences did not cross the 2 $\mu g/m^3$ value in the positive direction. The largest positive difference was +1.5 $\mu g/m^3$ and the largest negative was –2.5 $\mu g/m^3$ during the period. To conclude we can say, that most of the EPS members which on average showed positive areal average differences in PBL height and wind speed compared to the deterministic value, are the members, which showed negative PM_{10} differences. In the end of the period, the PBL height and wind speed differences are large and show high variability, but we see that the PM_{10} concentration differences are smaller than on the days before.

A)
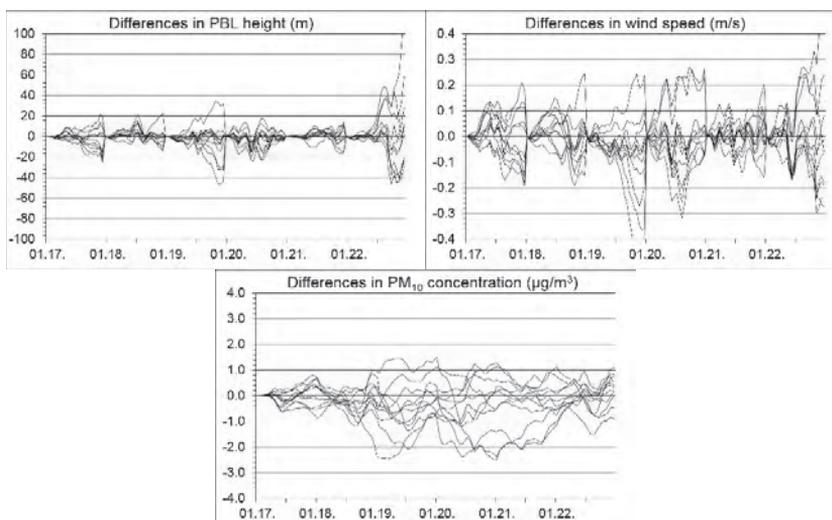
B)
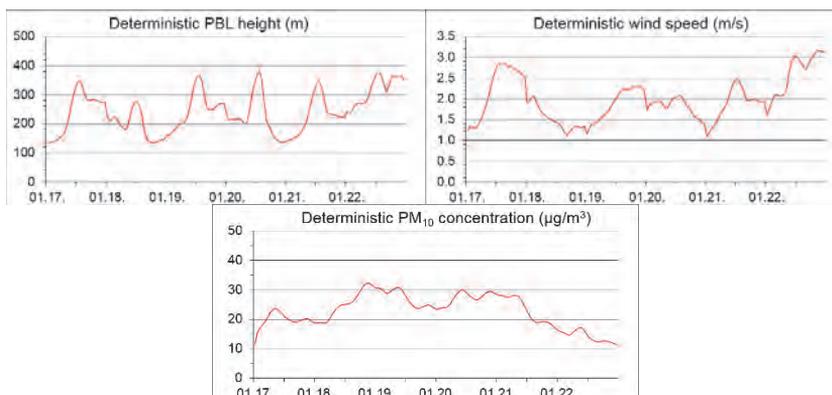
Fig. 6. A) Boundary layer height, wind speed, and PM_{10} differences between EPS members and deterministic values. B) Deterministic boundary layer height, wind speed, and PM_{10} values (areal averages, January 17–22, 2020).

In terms of the areal averages, the variability in the meteorological data is showing itself in the PM_{10} concentration predictions. While the differences between the meteorological inputs (deterministic and EPS) in case of the PBL height and wind speed decrease in some hours during the examined periods, the implied PM_{10} concentration differences are large circa from the second day of each period, and the spread of the differences stays large until the end of the period. It is important to mention that the differences in wind fields could impact the advection or transport of pollutants from the sources. The differences which occur in the trajectories of the air parcels lead to changes in the concentration fields.

Finally, we examined the behavior of the EPS and deterministic PBL height, wind speed, and PM_{10} concentration values in four monitoring stations: Budapest, Miskolc, Pécs, and Farkasfa. To sum up we can say that the PBL height differences varied between +/–200 m on the 4 monitoring stations, the wind speed differences stayed mostly between +/–1 m/s, and the differences of the PM_{10} concentrations fell usually in the +/–10 μg/m^3 range. It is difficult to say that the differences in the gridcells of the stations got generally larger with time, because there were some cases relating to all of the examined parameters, when larger deflections from the deterministic values and larger variety within the values of the different EPS members arose in the first part of the period. In case of the PBL height, the differences were in general always large in the hours around noon. The various EPS members differed more in the maximum extension of the PBL from the deterministic value. Generally, there is a smaller variation in case of Farkasfa, however, large differences from the deterministic values can occur here too. The variation of the differences was smaller in Pécs than in the other urban stations. From the examined parameters the wind speed differences showed the largest variation during the three episode situations. Variations in the wind speed values had a more significant effect on the variation in the PM_{10} concentrations. Small differences in wind fields over areas with high emission can have notable impact on dilution and air parcel composition.

3.2. Effect of the EPS meteorology on the air quality forecast

The impact of EPS meteorology was investigated at three urban and one background stations. The three city stations are Gilice tér in Budapest, Búza tér in Miskolc, and Boszorkány utca in Pécs, and the background station is Farkasfa. We chose points far apart. The type, geographical location, and emission impact of the designated stations are also different, as shown in the previous chapter.

First, we examined the timelines to see if we could improve PM_{10} forecasting using EPS meteorology. AROME-EPS prediction is made with perturbed initial and lateral boundary conditions. The set of forecasts, produced in this way, presents several scenarios. From these we can also deduce the probability and uncertainty of weather events. Ensemble predictions also have the advantage of predicting extreme events, such as predicting air pollution peaks.

In our case, we examined only three periods and four locations, but the standard deviation of EPS members did not prove to be widespread enough to adequately predict certain concentrations of pollutants. The application of EPS meteorology did not significantly improve the prediction of PM_{10} (*Fig. 7*). The results of this examination demonstrate that the success of air pollution forecast is affected by not only the accurate meteorological parameters but the perfect emission pattern of sources as well. The presented examples show that we have to improve or rethink how to prepare hourly emission data from the yearly amount. Of course, the accurate meteorological forecast is also a basis of a good air quality forecast, but in our case, the emission data is the weakness of our forecasting system.
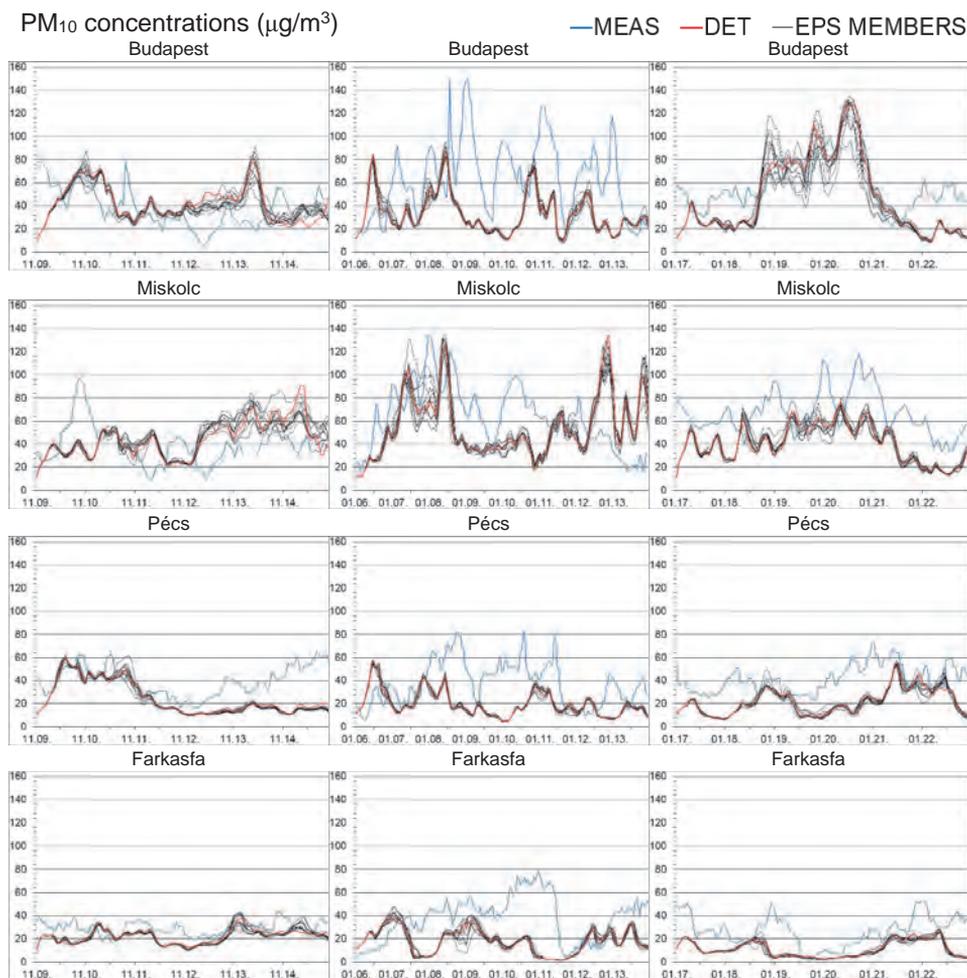
Fig. 7. Modeled and measured PM_{10} concentrations at Budapest, Gilice tér, Miskolc, Búza tér Pécs, Boszorkány utca, and Farkasfa stations (Source of measured data: Hungarian Air Quality Network).

Generally, winter weather patterns provide more favorable conditions for critical air quality situations coupled with high concentrations of PM_{10} to occur than summer weather patterns, which can basically be put down to the different emission and meteorological characteristics. Next, we carried out a sensitivity analysis with the aim to prove that the role of meteorology is significant in the formation of air pollution in winter. It should be emphasized, that the performance of a model may depend on the geographical domain, which makes the target area relevant in the process of investigating the model characteristics. The sensitivity analysis proved to be an efficient method to demonstrate the strong effects of local meteorological parameters including the parameters principally responsible for the dispersion and dilution processes of air pollutants, namely wind speed and planetary boundary layer height on the evolving concentrations in the environment.

Time series were selected from the 3 episode situations for every 4 geographical points, when there was light and strong wind speed and low and high PBL height values (*Tables 1* and *2*). For these time periods, the differences between the two wind speed EPSs and PBL height EPSs extremes were determined and than compared to the appropriate PM_{10} concentrations. By extremes we mean which EPS gave the lowest values most often and which EPS gave the highest values most often compared to the other EPS members. With this analysis, the effects of wind speed and PBL height on PM_{10} concentrations were demonstrated. The used definition of light wind: < 2 m/s, strong wind: > 2 m/s, low PBL height: < 400 m, and high PBL height: > 400 m.

Table 1. Analyzed time periods for the effect of wind speed

	Budapest	**Miskolc**	**Pécs**	**Farkasfa**
Light wind	January 19–21, 2020	November 13–15, 2020	January 21–22, 2020	November 12–15, 2020
Strong wind	November 12–13, 2020	January 09–12, 2020	November 12–13, 2020	January 19–20, 2020

The effect of wind speed is to cause the accumulated air pollutants to diffuse, thereby leading to an improvement in air quality and vice versa, decreasing wind speeds favor the accumulation of pollutants and induce a decline in air quality. First the effect of light wind on the PM_{10} concentration was analyzed (*Fig. 8*). The first line of Figure 8 shows the two EPSs that gave the lowest wind speed value most often and the highest wind speed value most often when low wind speed was examined. The same graphs show the PM_{10} concentrations for these EPSs. The second line of the figure shows the difference between the wind speeds and the difference between the PM_{10} concentrations of the aforementioned EPSs. Thus, the change in PM_{10} concentration caused by wind speed is illustrative. In the case

of light wind, the PM$_{10}$ concentration responds to small changes in wind speed with a significant adjustment. In the case of the presented examples, a 1 m/s increase in wind speed can result in a decrease in the PM$_{10}$ concentration up to 10 μg/m^3. On the contrary, a 1 m/s decrease in wind speed can result in an increase in the PM$_{10}$ concentration up to 5 μg/m^3. Based on *Fig. 8*, it can be said, that in the case of light wind, the prediction of PM$_{10}$ concentration is very sensitive to changes in wind speed.
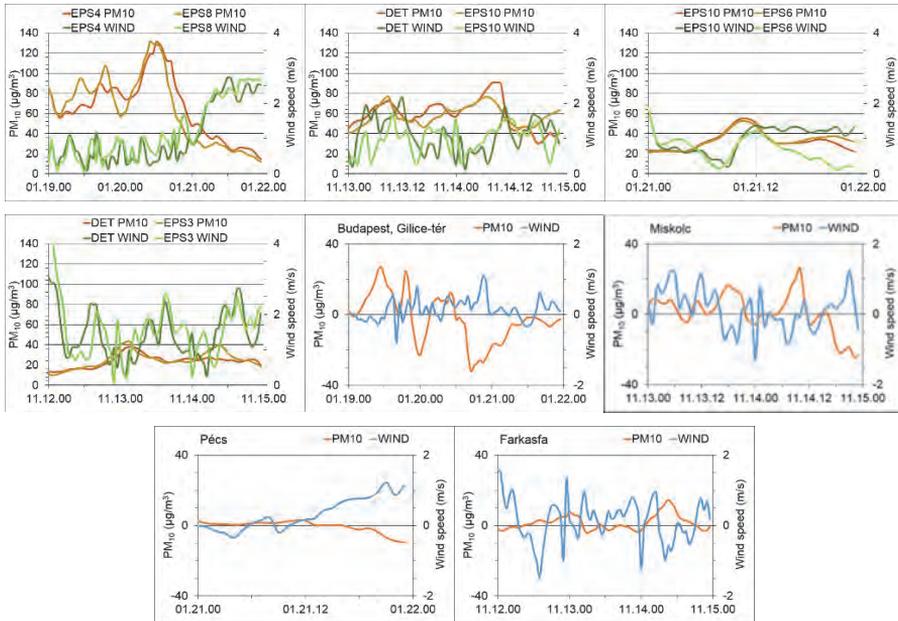
Fig. 8. Effect of the wind speed change on the change in PM$_{10}$ concentration at several geographic locations (in case of light wind speed).

Then the effect of strong wind on the PM$_{10}$ concentration was also analyzed (*Fig. 9*). The first line of *Fig. 9* shows the EPSs giving most often the highest and most often the lowest wind speeds, as well as PM$_{10}$ values for the same EPSs. The second line shows the difference between the wind speeds and the difference between the PM$_{10}$ concentrations. In this case, the response of the PM$_{10}$ concentration change to the wind speed change is not as clear as in the case of light wind speed change, but it can be noted that the effect is not negligible. However, in some cases, a strong wind speed can also increase PM$_{10}$ concentrations, as a result of an increased suspension of particles from ground surfaces (*Kukkonen et al.,* 2005).
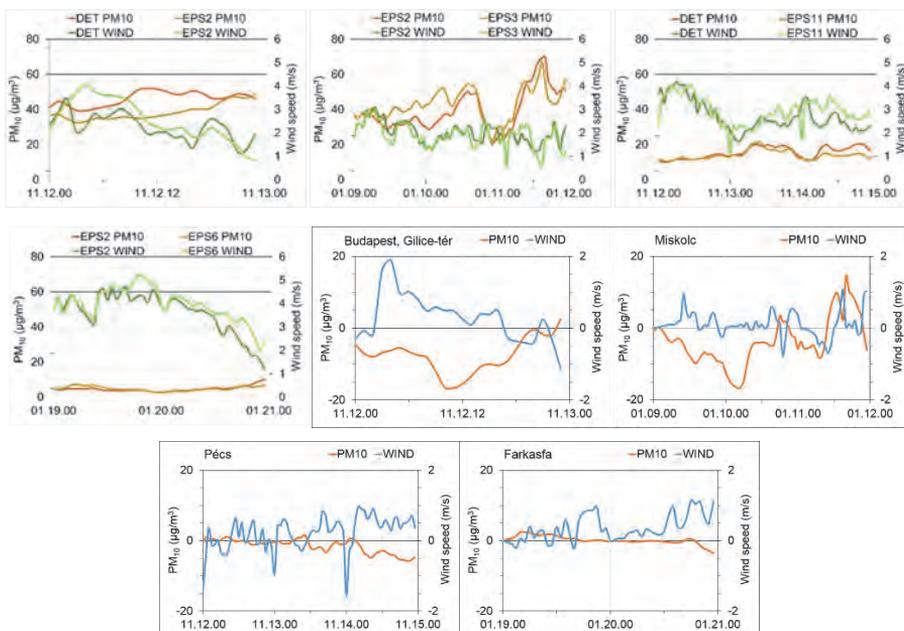
Fig. 9. Effect of the wind speed change on the change in PM$_{10}$ concentration at several geographic locations (in case of strong wind speed).

Results show that differences in the concentration fields due to the modified meteorology (using EPS members) are more pronounced in the case of lower wind speeds than they are in the case of higher wind speeds. We have to note that the changes in PM$_{10}$ concentrations were the most significant at the Budapest location. It is well trackable in model simulations that by low wind speeds pollutants start accumulating in the air rapidly, and it could be the explanation of this effect.

Table 2. Analyzed time periods for the effect of PBL height

	Budapest	**Miskolc**	**Pécs**	**Farkasfa**
Low PBL height	January 21–23, 2020	January 17–19, 2020	November 13–15, 2020	November 13–15, 2020
High PBL height	November 13–15, 2020	January 21–23, 2020	January 19–21, 2020	November 11–13, 2020

Pollutant, especially PM concentrations in the environment are largely affected by the boundary layer height as well (*Du et al.,* 2013). Results show that an increasing boundary layer height is coupled with the decrease of pollutant concentrations and, on the other hand, a decrease in the planetary boundary layer height leads to a definite increase in concentrations. However, this general conclusion can be modified by the very extreme meteorological situation during cold pools, when the predicted planetary boundary layer height is extremely low (< 400 m). First, the effect of low PBL height was analyzed on the PM_{10} concentration (*Fig. 10*). The expected effect that the increasing boundary layer height can cause decreasing PM_{10} concentration and vice versa is not clear in all cases in the case of low PBL height. A low boundary layer would constrain pollutants to the low surface layer and restrict the diffusion and dispersion of air pollutants. Our examination showed that a small change in the boundary layer height has a small effect on PM_{10} concentration. In our case studies, the negative connection was the strongest in the case of Pécs and the weakest in the case of Farkasfa. The first row of *Fig. 10* shows the EPSs with most often the highest and most often the lowest PBL heights and the associated PM_{10} concentrations. The second line shows the difference between the PBL heights and the difference between the PM_{10} concentrations.
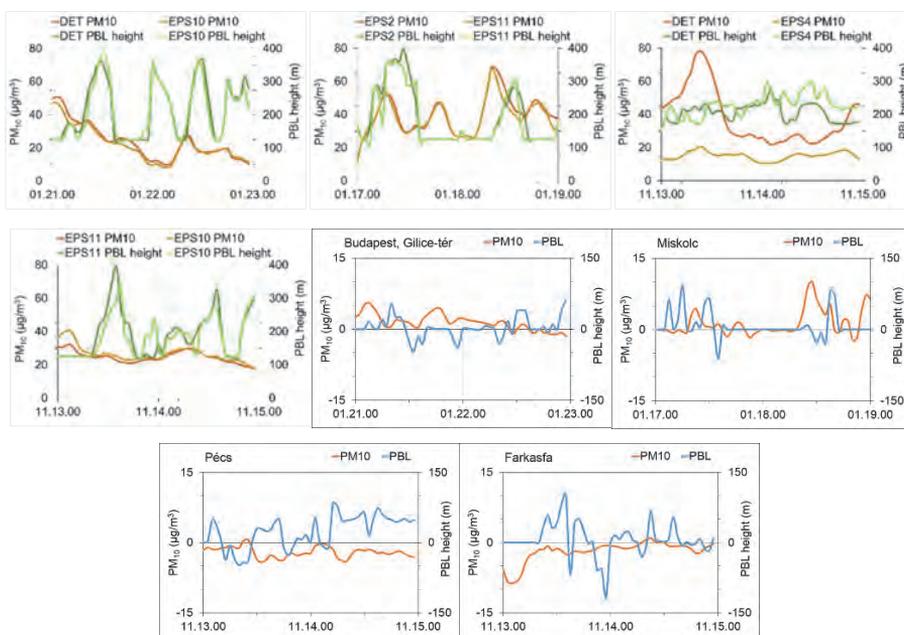
Fig. 10. Effect of the PBL height change on the change in PM_{10} concentration at several geographic locations (in case of low PBL height).

As a next step, the effect of higher PBL height was also analyzed on the PM_{10} concentration (*Fig. 11*). Inverse relationship between boundary layer depth and PM_{10} concentration was found. This relationship is stronger when the PBL height is higher than 400 m, because in this situation the decrease or increase of this layer could be more significant. The first row of *Fig. 11* shows the EPSs with the most common highest and the most common lowest PBL heights, in the case of high PBL heights, and the corresponding PM_{10} concentrations. The second line of the figure shows the difference between these values.
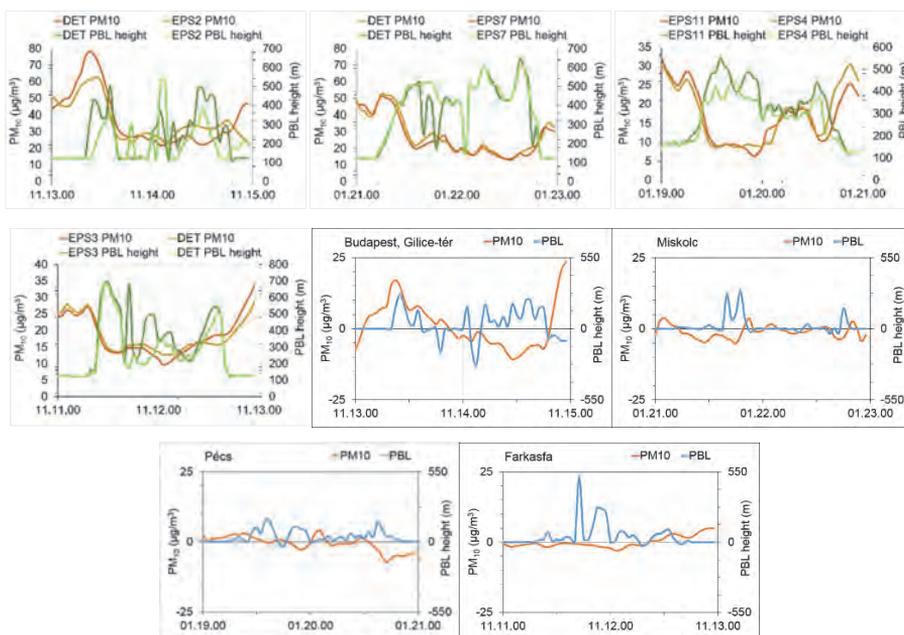
Fig. 11. Effect of the PBL height change on the change in PM_{10} concentration at several geographic locations (in case of high PBL height)

According to simulation results of the CHIMERE model, it is apparent that the response of the model is stronger for the decrease than for the increase of the boundary layer height, which means that the accumulation of air pollutants is more intense with the diminishing boundary layer than the dilution of pollutants is when the boundary layer height increases. We also have to note that the numerical weather prediction models determine the PBL height using different parameterization schemes, this fact can also affect the results of this type of analysis. The AROME numerical weather prediction model calculates the PBL height using the TKE scheme (*Szintai et al.,* 2015).

In this section, the effect of meteorological parameters on the PM_{10} concentration was analyzed separately. The effect of different meteorological situations (represented by a given EPS member in this analysis) on the calculated PM_{10} concentration can be analyzed a more complex way, when the effect of different parameters are taken into account simultaneously. This type of analysis is our next plan.

4. Conclusion

Results confirm that the chemical transport model is suitable for the detailed examination of the relationship between air pollutant concentrations and meteorological elements. Through model simulations, we demonstrated that a local accumulation of air pollutants significantly depends on the current meteorological conditions. A modification of the values of key meteorological variables that dominate in the dispersion processes – such as precipitation, wind speed, and planetary boundary layer height – brings about a consistent change in air concentrations.

The strengthening of wind speed causes the accumulated air pollutants to diffuse, thereby leading to an improvement in air quality and vice versa, decreasing wind speeds favor the accumulation of pollutants and induce a decline in air quality. Our studies showed that the differences in the concentration fields due to the modified meteorology are more pronounced in the case of lower wind speeds than they are in the case of higher wind speeds. Boundary layer characteristics play also a crucial role in the dilution of air pollutants near the surface. Increasing boundary layer height is coupled with the decrease of pollutant concentrations and, on the other hand, a decrease in the planetary boundary layer height leads to a definite increase in concentrations. Our studies showed that the differences in the concentration fields due to the modified meteorology are more pronounced in the case of higher boundary layer than they are in the case of lower boundary layer height.

Concerning the examined weather elements, the general conclusion can be deducted that they fundamentally influence the formation of air pollution and affect air concentrations significantly. The wind speed, being in connection with the intensity of mixing in the air and the height of the planetary boundary layer are both inversely proportional to the amount of pollutants in the air. Weather situations coupled with low wind speed, low boundary layer height, and without precipitation favor the accumulation of air pollutants the most. On the other hand, stronger winds and an increase in the boundary layer height cause concentrations to decrease. Based on the results, the role of local meteorology is therefore significant in the formation of air pollution. The more knowledge we have about the relationship between local weather and the evolving air concentrations, the more accurate assessments we are able to accomplish regarding both the current air quality and air quality forecasts.

Therefore, a detailed exploration of these relations is of fundamental significance. Naturally, the geographical environment, that makes the individual local conditions diverse, is also an important factor in this issue. The Carpathian Basin is unique in this respect with strong characteristics as a basin, but within its boundaries very different local conditions may exist in connection with the diverse topography, that is necessary to be taken into account.

The investigation of similar cases is essential in order to explore weather situations in which we can only reservedly rely on the results of air quality models. Being aware of the limitations of our models and the situations in which their calculations might become imprecise, and knowing what to expect concerning the differences between the real situation and the model results – whether the model over- or underestimates the real concentrations – make it possible for us to assign an uncertainty to the results and also to make a more accurate assessment of the current situation by taking the expectable inaccuracies into account, based on which we can introduce more adequate measures.

References

Apte, J.S., Messier, K.P., Gani, S., Brauer, M., Kirchstetter, T.W., Lunden, M.M., Marshall, J.D., Portier, C.J., Vermeulen, R.C.H., and *Hamburg, S.P.*, 2017: High-resolution air pollution mapping with Google street view cars: exploiting big data. *Environ. Sci. Technol. 51*, 6999–7008. https://doi.org/10.1021/acs.est.7b00891

Angevine, W.M., Bioude, J., McKeen, S., and *Holloway, J.S.*, 2014: Uncertainty in Lagrangian pollutant transport simulations due to meteorological uncertainty from a mesoscale WRF ensemble. *Geosci. Model Develop. 7*, 2817–2829. https://doi.org/10.5194/gmd-7-2817-2014

Baklanov, A., Schlünzen, K., Suppan, P., Baldasano, J., Brunner, D., Aksoyoglu, S., Carmichael, G., Douros, J., Flemming, J., Forkel, R., Galmarini, S., Gauss, M., Grell, G., Hirtl, M., Joffre, S., Jorba, O., Kaas, E., Kaasik, M., Kallos, G., Kong, X., Korsholm, U., Kurganskiy, A., Kushta, J., Lohmann, U., Mahura, A., Manders-Groot, A., Maurizi, A., Moussiopoulos, N., Rao, S.T., Savage, N., Seigneur, C., Sokhi, R.S., Solazzo, E., Solomos, S., Sørensen, B., Tsegas, G., Vignati, E., Vogel, B., and *Zhang, Y.*, 2014: Online coupled regional meteorology chemistry models in Europe: current status and prospects. *Atmos. Chemis. Phys. 14*, 317–398. https://doi.org/10.5194/acp-14-317-2014

Borrego, C., Monteiro, A., Ferreira, J., Miranda, A. I., Costa, A.M., Carvalho, A.C., and *Lopes, M.*, 2008: Procedures for estimation of modelling uncertainty in air quality assessment. *Environ. Int. 34*, 613–620. https://doi.org/10.1016/j.envint.2007.12.005

De Marco, A., Proietti, C., Anav, A., Ciancarella, L., D'Elia, I., Fares, S., Fornasierb, M.F., Fusaroe, L., Manese, M.G.F., Marchettof, A., Mirceac, M., Paolettig, E., Piersantic, A., Rogoraf, M., Salvatid, L., Salvatorie, E., Screpantih, A., Vialettoc, G., Vitalee, M., and *Leonardi, C.*, 2019: Impacts of air pollution on human and ecosystem health, and implications for the National Emission Ceilings Directive: Insights from Italy. *Environ. Int. 125*, 320–333. https://doi.org/10.1016/j.envint.2019.01.064

Du, C., Liu, S., Yu, X., Li, X., Chen, C., Peng, Y., Dong, Y., Dong, Z., and *Wang, F.*, 2013: Urban Boundary Layer Height Characteristics and Relationship with Particulate Matter Mass Concentrations in Xi'an, Central China. *Aerosol Air Qual. Res. 13*, 1598–1607. https://doi.org/10.4209/aaqr.2012.10.0274

EEA (European Environment Agency), 2019: Air quality in Europe – 2019 report. EEA Report, No. 10/2019, ISSN 1977-8449, ISBN 978-92-9480-088-6, doi: 10.2800/822355

Ferenczi Z., Homolya E., and *Bozó L.*, 2020: Detailed Assessment of a Smog Situation Detected in the Sajó Valley, Hungary. In (eds. *Mensink C., Gong W., Hakami A.*) Air Pollution Modeling and its Application XXVI. ITM 2018. Springer Proceedings in Complexity. Springer, Cham. https://doi.org/10.1007/978-3-030-22055-6_56

Guenther, A., Karl, T., Harley, P., Wiedinmyer, C., Palmer, P.I., and *Geron, C.*, 2006: Estimates of global terrestrial isoprene emissions using MEGAN (Model of Emissions of Gases and Aerosols from Nature). *Atmos. Chem. Phys. 6*, 3181–3210. https://doi.org/10.5194/acp-6-3181-2006

Hauglustaine, D.A., Hourdin, F., Jourdain, L., Filiberti, M.-A., Walters, S., Lamarque, J.-F., and *Holland, E.A.*, 2004: Interactive chemistry in the Laboratoire de Meteorologie Dynamique general circulation model: Description and background tropospheric chemistry evaluation. *J. Geophys. Res. 109*, D04314. https://doi.org/10.1029/2003JD003957

Holnicki, P. and *Nahorski, Z.*, 2015: Emission data uncertainty in urban air quality modeling—case study. *Environ. Model. Assess. 20*, 583–597. https://doi.org/10.1007/s10666-015-9445-7

Homolya, E., 2021: A levegőminőség várható alakulásának vizsgálata újgenerációs diszperziós modellek alkalmazásával, PhD Thesis, Hungarian University of Agriculture and Life Sciences (In Hungarian)

Hourdin, F., Musat, I., Bony, S., Braconnot, P., Codron, F., Dufresne, J.L., Fairhead, L., Filiberti, M.A., Friedlingstein, P., Grandpeix, J.Y., Krinner, G., LeVan, P., Li, Z.X., and *Lott, F.*, 2006: The LMDZ4 general circulation model: climate performance and sensitivity to parametrized physics with emphasis on tropical convection. *Climate Dynam. 27*, 787–813. https://doi.org/10.1007/s00382-006-0158-0

Kucera, V. and *Fitz, S.*, 1995: Direct and indirect air pollution effects on materials including cultural monuments. *Water, Air Soil Pollut 85*, 153–165. https://doi.org/10.1007/BF00483697

Kukkonen, J., Pohjola, M., Sokhi, R. S., Luhana, L., Kitwiroon, N., Fragkou, L., Rantamäki, M., Berge, E., Ødegaard, V., Slørdal, L. H., Denby, B., and *Finardi, S.*, 2005: Analysis and evaluation of selected local-scale PM10 air pollution episodes in four European cities: Helsinki, London, Milan and Oslo. *Atmos. Environ. 39*, 2759–2773. https://doi.org/10.1016/j.atmosenv.2004.09.090

Landrigan, P.J., 2017: Air pollution and health. *Lancet Publ. Health 2*, e4–e5. https://doi.org/10.1016/S2468-2667(16)30023-8

Lelieveld, J., 2017: Clean air in the Anthropocene. *Faraday Discuss. 200*, 693–703. https://doi.org/10.1039/C7FD90032E

Loveland, T.R., Reed, B.C., Brown, J.F., Ohlen, D.O., Zhu, Z., Yang, L.W.M.J., and *Merchant, J.W.*, 2000: Development of a global land cover characteristics database and IGBP DISCover from 1 km AVHRR data. *Int. J. Remote Sens. 21*, 1303–1330. https://doi.org/10.1080/014311600210191

Mailler, S., Menut, L., Khvorostyanov, D., Valari, M., Couvidat, F., Siour, G., Turquety, S., Briant, R., Tuccella, P., Bessagnet, B., Colette, A., Létinois, L., Markakis, K., and *Meleux, F.*, 2017: CHIMERE-2017: from urban to hemispheric chemistry-transport modeling. *Geosci.Model Develop. 10*, 2397–2423. https://doi.org/10.5194/gmd-10-2397-2017

Menut, L., Goussebaile, A., Bessagnet, B., Khvorostyanov, D., and *Ung, A.*, 2012: Impact of realistic hourly emissions profiles on air pollutants concentrations modelled with CHIMERE. *Atmos. Environ. 49*, 233–244. https://doi.org/10.1016/j.atmosenv.2011.11.057

Moiseenko, T.I., Dinu, M.I., Gashkina, N.A., Jones, V., Khoroshavin, V.Y., and *Kremleva, T.A.*, 2018: Present status of water chemistry and acidification under nonpoint sources of pollution across European Russia and West Siberia. *Environ. Res. Lett. 13*, 105007. https://doi.org/10.1088/1748-9326/aae268

Napelenok, S.L., Foley, K.M., Kang, D., Mathur, R., Pierce, T., and *Rao, S.T.*, 2011: Dynamic evaluation of regional air quality model's response to emission reductions in the presence of uncertain emission inventories. *Atmos. Environ. 45*, 4091–4098. https://doi.org/10.1016/j.atmosenv.2011.03.030

Rybarczyk, Y. and *Zalakeviciute, R.*, 2018: Machine learning approaches for outdoor air quality modelling: A systematic review. *Appl. Sci. 8*, 2570. https://doi.org/10.3390/app8122570

Szintai, B., Szűcs, M., Randriamampianina, R., and *Kullmann, L.*, 2015: Application of the AROME non-hydrostatic model at the Hungarian Meteorological Service: Physical parameterizations and ensemble forecasting. *Időjárás 119*, 241–265.

IDŐJÁRÁS

ALADIN-Climate at the Hungarian Meteorological Service: from the beginnings to the present day's results

Beatrix Bán[*,1], **Gabriella Szépszó** [1], **Gabriella Allaga-Zsebeházi** [1], and **Samuel Somot** [2]

[1] *Hungarian Meteorological Service*
Kitaibel Pál u. 1; H-1024 Budapest, Hungary

[2] *CNRM (Centre National de Recherches Météorologiques)*
Université de Toulouse, Météo-France, CNRS, Toulouse, France
42 avenue Coriolis, 31057 Toulouse, France

[*] *Corresponding author e-mail: ban.b@met.hu*

(Manuscript received in final form October 2, 2021)

Abstract— This study is focusing on the past and, in particular, the present of the ALADIN-Climate model used at the Hungarian Meteorological Service. The currently applied model version is 5.2 (HMS-ALADIN52). In the recent experiments, the CNRM-CM5 global model outputs were downscaled in two steps to 10 km horizontal resolution over Central and Southeast Europe using RCP4.5 and RCP8.5 scenarios. Temperature and precipitation projections are analyzed for 2021-2050 and 2071–2100 with respect to the reference period of 1971–2000 with focus on Hungary. The results are evaluated in comparison to 26 simulations selected from the 12 km horizontal resolution Euro-CORDEX projection ensemble (including two additional versions of ALADIN-Climate: CNRM-ALADIN53 and CNRM-ALADIN63) to get more information about the projection uncertainties over Hungary and to assess the representativeness of HMS-ALADIN52.

The HMS-ALADIN52 simulations project a clear warming trend in Central and Southeast Europe, which is more remarkable in case of greater radiative forcing change (RCP8.5). From the 2040s, the Euro-CORDEX simulations start to diverge using different scenarios. The total range of the annual change over Hungary is 1.3–3.3 °C with RCP4.5 and 3.2–5.7 °C with RCP8.5 by the end of the 21st century. HMS-ALADIN52 results are approximately near to the median: 2.9 °C with RCP4.5 and 4 °C with RCP8.5. CNRM-ALADIN53 shows generally similar results to HMS-ALADIN52, but simulations with CNRM-ALADIN63 indicate higher changes compared to both. In terms of seasonal mean precipitation change, the HMS-ALADIN52 simulations assume an increase between 9% and 33% (less in spring, more in autumn) over Hungary in both periods and with both scenarios. Most of the selected Euro-CORDEX simulations show a precipitation increase, apart from summer, when growth and reduction can be equally expected in 2021–2050, and the drying tendency continues towards the end of the century. Increase projected by HMS-ALADIN52 is mostly confirmed by CNRM-ALADIN53, while CNRM-ALADIN63

predicts precipitation decrease in summer. Precipitation results do not show a significantly striking difference between the scenarios, likely due to the fact that internal variability and model uncertainty are more relevant sources of uncertainty in precipitation projections over our region.

1. Introduction

During the early 2000s, it was decided at the Hungarian Meteorological Service (HMS) to start working in the field of regional climate modeling in order to provide a firm basis for climate change adaptation in Hungary. A pragmatic approach was taken in the search of regional climate models (RCM) to be used, and the ALADIN model was selected in addition to the REMO model (*Szépszó and Horányi*, 2008). The ALADIN limited area numerical weather prediction (NWP) model (*Termonia et al.*, 2018) has been developed through an international cooperation, and for now the ALADIN model family is the most widely used limited area model in Europe (it has been used also in operational practice of HMS since the 1990s). Its two specific versions were considered in these early days. The first one was basically the short-range NWP version of the model (*Farda et al.*, 2010), which included only minor changes for the climate version. The second one was a dedicated model version called ALADIN-Climate (*Radu et al.*, 2008), which was built by merging the physical parameterization package of the ARPEGE-Climat global climate model (*Déqué et al.*, 1994) and the dynamics of the ALADIN model. That version was more tailored for climate use and was adapted at the Hungarian Meteorological Service. This model has been used for various climate experiments including some shorter (few years) experimentation to establish the most appropriate model version, domain, horizontal resolution, and the spin-up time.

At HMS, the first longer experiments were performed by reanalysis lateral boundary conditions (LBCs) and then using global climate model (ARPEGE-Climat) LBCs in order to understand the behavior of the model for the past. While the ERA-40 (*Uppala et al.*, 2005) driven experiment was achieved at 25 km resolution over Central Europe, the ARPEGE-driven simulation covered only the Carpathian Basin with 10 km resolution. The validation demonstrated that the domain size affects the results: using the smaller integration area led to an overestimation in summer precipitation and an underestimation in temperature (*Csima* and *Horányi*, 2008).

The first climate change run with ALADIN-Climate 4.5 was carried out in the framework of the CECILIA EU FP6 project (*Halenka*, 2007) between 2006 and 2009. The experiment was accomplished for two future time slices (2021–2050 and 2071–2100) using the medium A1B SRES scenario (*Nakicenovic et al.*, 2000) to provide RCM outputs for assessment of the climate change effects on extreme

events, air pollution, agriculture, water- and energy management in Central and Eastern Europe. The ALADIN-Climate results showed significant temperature increase and strong summer and lower winter reduction in precipitation over the Carpathian Basin for the 21st century (however, the latter outcome was neither confirmed by the results of the REMO model applied also at the Hungarian Meteorological Service nor by the available results of other European RCMs; *Krüzselyi et al.*, 2011; *Belda et al.*, 2015; *Christensen et al.*, 2007a).

In the early 2010s, outputs of four locally run regional climate models were available in Hungary (*Krüzselyi et al.*, 2011). A National Adaptation Geo-information System (NAGiS; *Kajner et al.*, 2017) was created in 2013 to support climate adaptation and related decision making in Hungary with coordinated impact studies. Their model basis for the future climate projections are the ALADIN-Climate and RegCM (*Torma et al.*, 2008) RCMs. The climate information available in NAGiS is utilized in vulnerability assessments in many sectors, e.g., tourism, hydrology, human health (*Kovács et al.*, 2015; *Bede-Fazekas et al.*, 2017; *Homolya et al.*, 2017; *Lepesi et al.*, 2017).

Parallel to the vulnerability assessments, HMS aimed to update the climate simulation base of NAGIS in a side-project of NAGiS and later in the EU-funded KlimAdat project from 2016. A new version (5.2) of the ALADIN-Climate model was applied over a domain covering Central and Eastern Europe with 10 km resolution. For the evaluation and control runs, ERA-Interim reanalysis (*Dee et al.*, 2011) and the 5th version of ARPEGE-Climat, which is the atmospheric part of the CNRM-CM5 general global circulation model (*Voldoire et al.*, 2013) provided the lateral boundary conditions, respectively. The magnitude of the temperature underestimation and the summer precipitation overestimation over Hungary reduced in the new experiments (*Illy et al.*, 2015). New, transient climate change simulations are also accomplished using the RCP (Representative Concentration Pathways) anthropogenic scenario family defined for the Fifth Assessment Report of the IPCC (*Moss et al.*, 2010).

In order to properly describe future climate change, uncertainties of climate projections need to be taken into account. Therefore, other model results have been considered besides the ALADIN-Climate simulations. The World Climate Research Program established the CORDEX (Coordinated Regional Downscaling Experiment, http://cordex.org; *Giorgi et al.*, 2009) collaboration which provides an internationally coordinated framework to improve regional climate scenarios over every continent. Simulations are performed mostly at 50 km (EUR-44) resolution over the predefined continent-sized domains until the end of the 21st century, but in the framework of Euro-CORDEX initiative (http://www.euro-cordex.net/; *Jacob et al.*, 2014), experiments over Europe are performed also at a finer 12.5 km (EUR-11) resolution. The regional simulations downscale the CMIP5 global climate projections (*Taylor et al.*, 2012) and take into account the RCP scenarios.

The aim of this study is to present the projection results of the ALADIN-Climate regional climate model for Hungary, and to examine how these simulations relate to a Euro-CORDEX EUR-11 (*Jacob et al.*, 2014) model ensemble. The latter question is important for practical reasons as well, since future climate change uncertainties can be best quantified with multi-model and multi-scenario ensembles, and in Hungary, the computing capacities are limited to run several simulations with different models. After the historical overview, in Section 2, first the current model version adapted at HMS and the selected Euro-CORDEX ensemble are introduced, emphasizing the included ALADIN-Climate 5.3 and 6.3 RCM versions. Then, experiments achieved with ALADIN-Climate 5.2, the analyzed Euro-CORDEX simulations, and the evaluation methods are also presented. Section 3 is dedicated to assess the temperature and precipitation projection results of the latest 10 km simulations of ALADIN-Climate 5.2, prepared with two different scenarios and the comparison to the Euro-CORDEX ensemble. Finally, a summary is given in Section 4.

2. Data and methodology

2.1. The studied ALADIN-Climate model versions

ALADIN-Climate is a hydrostatic, spectral regional climate model, which 5.2 version (*Colin et al.*, 2010; hereinafter HMS-ALADIN52) is currently applied at the Hungarian Meteorological Service. The dynamic core of this model version is based on the cycle 32 of the ALADIN numerical weather prediction model, while the physical parameterization package is originated from the 5th version of the ARPEGE-Climat global climate model. The horizontal grid type of the model is a Lambert conformal conic projection, while the model applies the hybrid (terrain-following near the surface, that continuously turns into pressure levels at higher altitudes) coordinate system. The prognostic variables are the horizontal components of wind speed, temperature, specific humidity on model levels, and the surface air pressure. A combination of semi-implicit and semi-Lagrangian schemes are applied to determine the temporal evolution of the prognostic variables, which allows the use of a longer integration time step. The lateral boundary conditions and the RCM fields are smoothed to each other in the relaxation zone (an 8-gridpoint bound around the RCM central domain; *Davies*, 1976).

The main physical parameterization schemes are the followings: longwave radiation is described by the RRTM scheme (Rapid Radiation Transfer Model; *Mlawer et al.*, 1997) which takes into account the emission and absorption of longwave radiation and the effects of particular atmospheric gases and aerosols. The calculation of the shortwave radiation flux is done by the *Fouquart* and *Bonnel* (1980) scheme, which describes the reflection, scattering, and absorption of shortwave radiation, and also considers the absorption of each atmospheric

trace gas and the modifying effect of cloud cover. *Ricard* and *Royer*'s (1993) scheme is used for large scale cloudiness and *Smith*'s scheme (1990) for large scale precipitation. The parameterization of convection is based on the scheme of *Bougeault* (1985). The land surface processes are described by the SURFEX land surface model (*Masson et al.*, 2013) that applies different schemes over the natural land, inland water, sea, and town surfaces. In the present model configuration, the ISBA scheme (Interaction of Soil Biosphere Atmosphere; *Noilhan* and *Planton*, 1989) was applied over the natural land surfaces, urban surfaces were described as rocks, while over water surfaces the simple Charnock formula (*Charnock*, 1955) gives surface fluxes using prescribed surface temperature.

The impact of human activity is considered through the annual global mean evolution of the atmospheric concentrations of greenhouse gases (CO_2, CH_4, N_2O, CFC-11, CFC-12) and certain types of aerosols (black coal, organic aerosol, sulphate, sea salt, dust). Aerosols are described in monthly distributions for 10-year periods in the historical period (*Tegen et al.*, 1997), as well as in the scenario periods (*Szopa et al.*, 2013).

ALADIN-Climate version 5.3 and 6.3 (also known as CNRM-ALADIN53; *Colin et al.*, 2010 and CNRM-ALADIN63; *Nabat et al.*, 2020) have been developed and applied for regional climate model simulations, e.g., in the Euro-CORDEX framework by the Centre National de Recherches Météorologiques (CNRM), the research department of the French national weather service, Météo-France. CNRM-ALADIN53 is very close to the version 5.2 used at HMS and it was described above. The main difference is that CNRM-ALADIN53 does not use the SURFEX land surface model (but a similar version of ISBA for the natural surfaces). For completeness, note that the HMS-ALADIN52 version is relatively different from the ALADIN5 version used by CNRM in Med-CORDEX (*Tramblay et al.*, 2013) and the MENA domain (*Driouech et al.*, 2020), but is identical to the CNRM version used for CORDEX North America (*Lucas-Picher et al.*, 2013).

On the contrary, CNRM-ALADIN63 is a very different version as more than 10 years of model development occurred between version 5 and version 6 of ALADIN. It is described in detail in *Nabat et al.* (2020) and the main differences between ALADIN5 and ALADIN6 are summarized in *Ivusic et al.* (2021, in rev.) CNRM-ALADIN53 and CNRM-ALADIN63 are part of the latest 12 km-resolution Euro-CORDEX ensemble that has been assessed in *Vautard et al.* (2021) and *Coppola et al.* (2021).

2.2. Experiments with HMS-ALADIN52

Two simulations (*Table 1*) have been created for the future with ALADIN52 at the Hungarian Meteorological Service using the high-emission RCP8.5 and the intermediate emission RCP4.5 scenarios for greenhouse gases. The numbers in the scenario names indicate the expected change in radiative forcing (i.e.,

8.5 W/m^2 and 4.5 W/m^2, respectively) by the end of the 21st century compared to the pre-industrial level. The associated aerosol distributions were determined from simulations with global air chemistry (INCA Chemistry model) and general circulation models (*Szopa et al.*, 2013). The lateral boundary conditions have 1.4 degree (approximately 150 km on our latitudes) horizontal resolution and are provided by the CNRM-CM5 general global circulation model, that was dynamically downscaled to 50 km resolution with HMS-ALADIN52 to the Euro-CORDEX domain. CNRM-CM5 includes the ARPEGE-Climat atmospheric model, the NEMO ocean model (*Madec*, 2008), the ISBA land surface scheme (*Noilhan* and *Planton*, 1989), and the GELATO sea ice model (*Salas y Melia*, 2002) coupled through the OASIS system (*Valcke*, 2006). The 50 km horizontal resolution fields are then downscaled to 10 km (0.09 degree) on a domain covering Central and Southeast Europe (*Fig. 1, left*). An error has been recently reported concerning the CNRM-CM5 GCM files that were used as atmospheric lateral boundary conditions for the ALADIN52 and ALADIN53 runs (www.umr-cnrm.fr/cmip5/spip.php?article24&lang=en), but this likely has no significant effect on the long-term climate change signal. Sea surface temperature (SST) is derived from the CNRM-CM5 model, which is used directly by the 50 km resolution HMS-ALADIN52 simulations. The SST forcing of the 10 km HMS-ALADIN52 is more complex, which takes into account the 50 km HMS-ALADIN52 results and the use of SURFEX (sea-surface ratio). In our HMS-ALADIN52 experiments, there is no ocean/sea coupling.

Table 1. Features of the HMS-ALADIN52 simulations

	HMS-ALADIN52
Lateral boundary conditions	50 km resolution HMS-ALADIN52 driven by CNRM-CM5
Projection	Lambert
Horizontal resolution	10 km
Number of vertical levels	31
Time interval	1950-2100
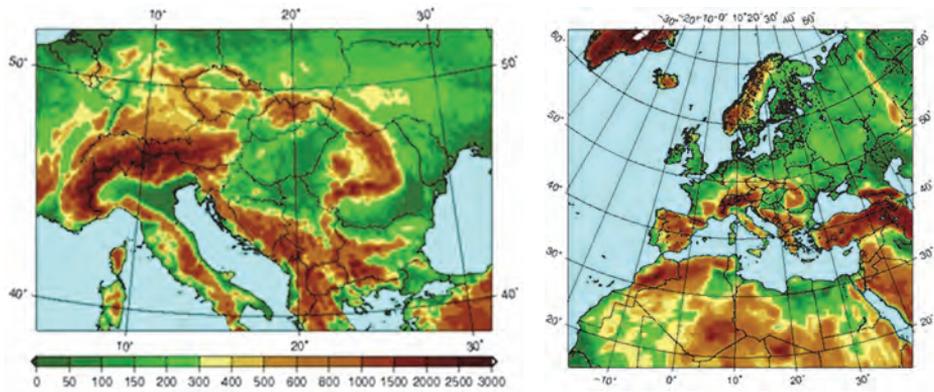
Fig 1. The integration domains of the 10 km horizontal resolution HMS-ALADIN52 regional climate model (left) and the 12.5 km horizontal resolution Euro-CORDEX regional climate models (right).

2.3. The selected Euro-CORDEX simulations

In addition to the assessment of HMS-ALADIN52 results, the projections of several Euro-CORDEX simulations are jointly evaluated, assuming that all of them are equally possible realizations of climate change. A multi-model and multi-scenario ensemble consisting of 26 simulations from the 12.5 km (0.11° × 0.11°) Euro-CORDEX RCM set is selected to quantify the uncertainties originated from the GCM-RCM differences and the scenario choice. Eight RCMs driven by five GCMs (13 model combinations) using the RCP4.5 and RCP8.5 scenarios have been applied in this study (*Table 2*). The simulations (except two with CNRM-ALADIN63) were chosen several years ago based on the following criteria applied for the assessed variables: 1) the simulations should include the study period, 2) the historical and the two RCP scenario simulations should be available, 3) the simulations should be achieved on 0.44° and 0.11° resolution as well. The CNRM-ALADIN63 simulations were added afterwards in order to further explore the differences amongst the ALADIN versions. More details on the individual RCMs can be found in the reference articles. The domain of the simulations is presented in the right panel of *Fig. 1*.

Table 2. The ensemble selected from Euro-CORDEX with 13 model combinations driven by RCP4.5 and RCP8.5 scenarios (26 simulation members). The two ALADIN versions analyzed in detail are indicated with bold.

RCM	Driving GCM	Reference
ALADIN53	**CNRM-CM5**	***Colin et al.* (2010)**
ALADIN63	**CNRM-CM5**	***Nabat et al.* (2020)**
CCLM4-8-17	MPI-ESM-LR	*Rockel et al.* (2008)
HIRHAM5	EC-EARTH	*Christensen et al.* (2006)
RACMO22E	EC-EARTH	*Meijgaard van et al.* (2012)
	HadGEM2-ES	
RCA4	CNRM-CM5	*Kupiainen et al.* (2011)
	HadGEM2-ES	
	MPI-ESM-LR	
	IPSL-CM5A-MR	
	EC-EARTH	
REMO2009	MPI-ESM-LR	*Jacob et al.* (2012)
WRF331F	IPSL-CM5A-MR	*Skamarock et al.* (2008)

2.4. Evaluation method

The assessment concentrates on temperature and precipitation. First, the projections of HMS-ALADIN52 were thoroughly evaluated both over the whole model domain and Hungary. The annual and seasonal mean changes have been quantified in two future periods: 2021–2050 for the near future and 2071–2100 for the far future relative to the 1971–2000 model reference period. The Welch-test for both temperature and precipitation was performed to identify significant changes at grid points over Hungary.

In addition, the model results have been corrected by the delta method (*Maraun*, 2016; *Maraun* and *Widmann*, 2018) to filter out the systematic error of HMS-ALADIN52 (assuming that the past and future bias is unchanged), considering the CARPATCLIM-HU (*Bihari et al.*, 2017) as a reference database.

CARPATCLIM-HU is a daily gridded observation database on 0.1 degree horizontal resolution covering Hungary. The dataset was generated by the MASH homogenization (*Szentimrey*, 2008; 2014) and the MISH interpolation (*Szentimrey* and *Bihari*, 2007; 2014) methods specially developed for meteorological purposes, and it incorporates station measurements from Hungary and the neighboring countries For correction of the RCM results, the simulated monthly mean changes for each year in the projection time periods were combined with the observed 30-year monthly mean of the reference period (originated from CARPATCLIM-HU) in an additive way (according to Eq.(1)) for temperature and in a multiplicative way (according to Eq.(2)) for precipitation:

$$X(t)'_{sim,f} = \bar{X}_{obs,p} + \left(X(t)_{sim,f} - \bar{X}_{sim,p} \right), \tag{1}$$

$$X(t)'_{sim,f} = \bar{X}_{obs,p} \times \left(\frac{X(t)_{sim,f}}{\bar{X}_{sim,p}} \right), \tag{2}$$

where $X(t)'_{sim,f}$ is the bias-corrected future monthly mean value for the given year, $\bar{X}_{obs,p}$ is the average of the observations for the reference period, $X(t)_{sim,f}$ is the simulated raw future value for a given year, and $\bar{X}_{sim,p}$ is the average of simulated past values for the reference period. The yearly monthly means averaged over Hungary in the past and in the two future 30-year periods are shown in box-whisker diagrams (also known as boxplot; *Williamson et al.*, 1989), in order to investigate how the range and distribution of monthly means change between the different 30-year periods. Five statistical attributes are visualized in a box-whisker diagram: the median, the lower and upper quartiles (i.e., the 25th and 75th percentiles), and the minimum and maximum values.

Finally, the HMS-ALADIN52 results have been compared to the Euro-CORDEX experiments to examine how HMS-ALADIN52 fits into the uncertainty range of a larger ensemble, thus providing information on the representativeness of HMS-ALADIN52 in terms of temperature and precipitation changes over Hungary. This is an important step as there are limited opportunities to adapt and run several regional climate models in Hungary. The projected evolution of changes was assessed by using moving averages over 30-year time windows with one-year steps (e.g., 2021–2050, 2022–2051, etc.) throughout the 21st century. Moreover, the mean temperature and precipitation changes for all models are presented together on scatter plots. The far future period in the case of Euro-CORDEX ensemble had to be slightly shifted to 2070–2099 instead of 2071–2100, because for some RCM simulations the year 2100 was missing due to the lack of GCM data. Nevertheless, shifting the 30-year period by one year does not affect the climate change signal significantly.

3. Results and discussion

3.1. In-house simulations with HMS-ALADIN52

Temperature

A gradual warming can be detected towards the end of the century, which is more intense with the RCP8.5 than with the RCP4.5 scenario and in winter compared to summer (*Fig. 2*). Considering first the spatial pattern of temperature change on the model domain, the warming is increasing from southwest to northeast in summer. This also suggests that the continental parts are expected to experience higher temperature increases than the western, ocean-influenced parts. The temperature rise in the Ukrainian area (eastern part of the domain) could reach 5 °C by the end of the century with the RCP8.5 scenario and 3–3.5 °C with RCP4.5. The smallest temperature rise (0.5–1 °C) can occur in 2021-2050 with RCP4.5 over the central part of Germany and the northwestern part of Switzerland. Moreover, the Alps are emerging with higher temperature increase (reaching around 7 °C for the RCP8.5 scenario) from its surrounding areas as well. In general, the spatial differences are larger with both scenarios at the end of the century in contrast to the middle of the century. In winter, the Alpine chains do not appear as prominent as in summer, but the largest temperature increase is expected also over Ukraine, and several smaller regions (e.g., Po Plain, South Germany, Czech Republic) may face remarkable warming too, reaching 7–8 °C by 2071–2100 with RCP8.5 and 5–6 °C with RCP4.5.

The mean temperature increase for the area of Hungary is summarized in *Table 3*. Annually 1.3 °C in 2021–2050, 2.9 °C in 2071–2100 with RCP4.5 is obtained, respectively, which could reach 4 °C by the end of the century with RCP8.5. The largest seasonal temperature increase occurs in winter: 3.6 °C and 4.8 °C by the end of the century with RCP4.5 and RCP8.5, respectively. A slight zonality in the warming can be noticed in winter with all scenarios and for all periods with higher values over the northern and northeastern parts of the country, especially over the North Hungarian Mountains (*Fig. 2*). The second most warming season is summer: 2.9 °C and 4.4 °C by the end of the century with RCP4.5 and RCP8.5, respectively, and the warming in this season is almost homogeneous in terms of the spatial pattern. The change is mostly significant at both annual and seasonal scales at all grid points (not shown).

Monthly mean temperature values averaged over Hungary are analyzed to gain information on the variability within the selected 30-year periods. The warming in February, August, September, and December using the RCP8.5 scenario (red boxes in *Fig. 3*) is so large, that the monthly values between the 25th and 75th percentiles (which are in the boxes) do not even overlap in the two 30-year periods. The highest value among the mean temperatures of July – which month was the warmest in the reference period – was 23.2 °C, this can exceed 29 °C by the end of the century. Based on the percentiles, for both future periods

and both scenarios, the mean temperature in July may become much more variable compared to the reference period: the wider boxes indicate that the range of values between the 25th and 75th percentiles may become extended. August can compete with July in terms of the hottest month in the year on average (max. 30.1 °C) in 2071–2100 with the higher emission scenario. Mean temperature values not exceeding 0 Celsius degree are still possible to occur in the winter months in 2021–2050 with both scenarios and in 2071–2100 with RCP4.5, but the 75% of the monthly means will reach 0 degree considering all the three months.

The key difference of temperature increase with RCP4.5 and RCP8.5 scenarios, that is especially clear in the far future, reveals the strong correlation between the radiative forcing and the temperature change.
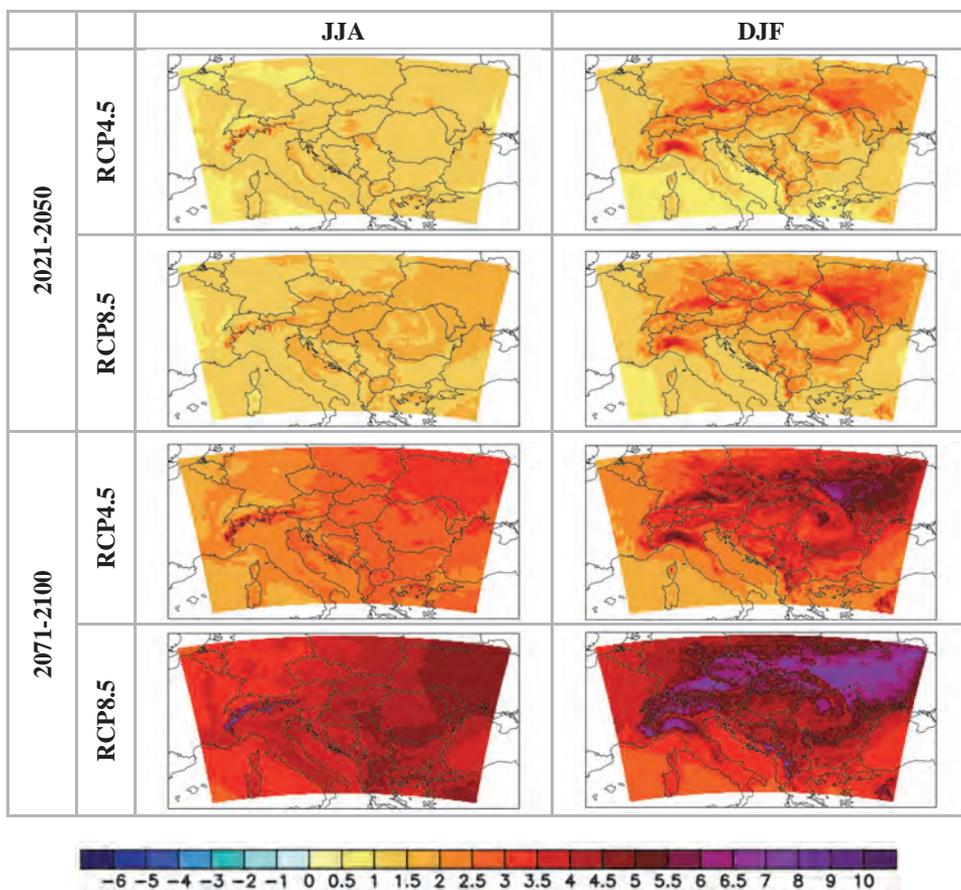
Fig. 2. Summer (JJA) and winter (DJF) temperature changes (°C) projected for 2021–2050 and 2071–2100 over the domain of HMS-ALADIN52 in case of RCP4.5 and RCP8.5 scenarios (reference period: 1971–2000).

Table 3. Annual and seasonal mean temperature changes (°C) in Hungary for 2021–2050 and 2071–2100 compared to 1971–2000, based on the results of HMS-ALADIN52 model simulations with RCP4.5 and RCP8.5 scenarios, below them the corresponding minimum and maximum changes are in parentheses based on 26 Euro-CORDEX (EC) ensemble simulations.

		Annual	MAM	JJA	SON	DJF
2021–2050	**RCP4.5**	1.3 [0.9 – 2.2]	1.1 [0.5 – 2.4]	1.4 [1.0 – 2.1]	0.8 [0.5 – 2.0]	1.8 [0.6 – 2.5]
	RCP8.5	1.7 [0.8 – 2.4]	1.3 [0.9 – 2.2]	1.7 [0.8 – 2.5]	1.5 [0.8 – 2.7]	2.1 [0.2 – 2.8]
2071–2100 (EC: 2070–2099)	**RCP4.5**	2.9 [1.3 – 3.3]	2.7 [1.1 – 3.1]	2.9 [1.5 – 3.3]	2.3 [1.1 – 3.5]	3.6 [1.0 – 3.9]
	RCP8.5	4.0 [3.2 – 5.7]	3.4 [2.6 – 5.0]	4.4 [3.2 – 5.8]	3.5 [2.7 – 5.9]	4.8 [3.4 – 6.1]
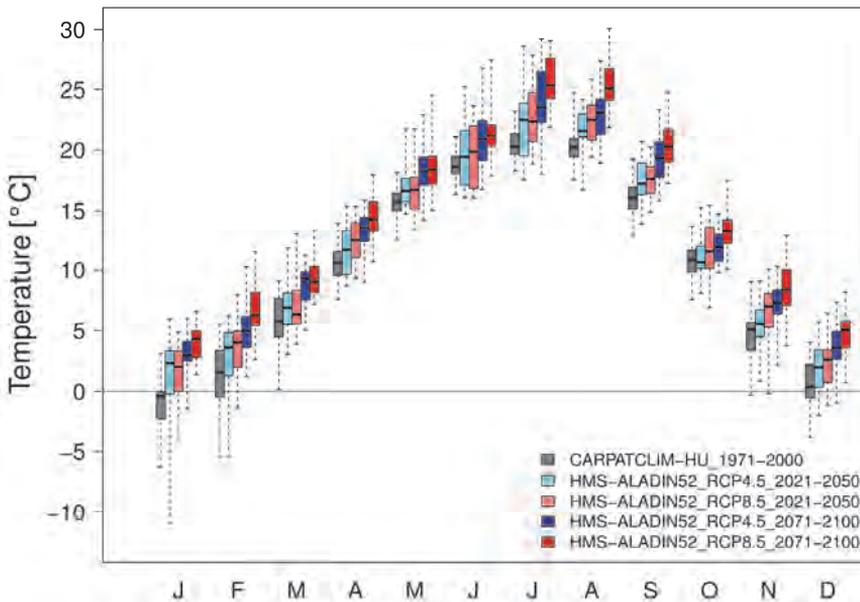
Fig. 3. Box-whisker diagram of the bias-corrected monthly mean temperature values (°C) area-averaged over Hungary for every year of 2021–2050 and 2071–2100 (light and dark colors respectively) obtained with the RCP4.5 and RCP8.5 scenarios driven HMS-ALADIN52 (blue and red, respectively). The observations (CARPATCLIM-HU) for 1971–2000 are indicated with grey. The lower and upper boundaries of the rectangles (the "boxes") represent the lower and upper quartiles of the dataset (25th and 75th percentiles, respectively), while the line in the boxes shows the median value. The vertical dashed lines below and above the boxes show the minimum and maximum values of the dataset.

Precipitation

The winter and summer mean precipitation changes over the model domain are presented for both future time periods considering both scenarios in *Fig. 4*. The simulation results suggest a precipitation increase both in summer and winter, for a large part of the domain, including Hungary. In summer, heavy increase (>70%) – which can be caused by an inaccuracy in the SST forcing field (CNRM, personal communication) – is projected over the Black Sea, Adriatic Sea, and Aegean Sea with both scenarios.

Over Hungary, the relative precipitation increase can reach 16–24% by the end of the century on annual scale (*Table 4*), which is significant in most of the grid cells for both future periods with RCP4.5 and RCP8.5, except above Lake Balaton in 2071–2100 and over a western region in Hungary in 2021–2050 with the RCP4.5 scenario (not shown). Considering seasonal mean changes, relative precipitation increase occurs in all seasons, moreover, larger increase is expected in the far future period and with RCP8.5, except in spring and summer with RCP4.5, when the magnitude of precipitation change remains nearly the same between the two future periods. Precipitation change between 2021–2050 and 2071–2100 is the strongest in autumn, and considering RCP8.5, this season may face the most precipitation surplus in the year (23 and 33% in the near and far future, respectively). The smallest increase is expected in spring with the RCP4.5 scenario: 9% for 2021–2050 and 10% for 2071–2100. Note that gridpoints with higher relative seasonal increase (reaching around 20%) are generally significant areas, while areas of decrease occurring only with RCP4.5 are not significant (except 1–2 grid cells) and may appear over small regions like Lake Balaton in summer and spring of both future period, and like some parts of the Somogyi Hills and the North Hungarian Mountains in autumn of 2021–2050 (not shown). It should also be noted that no explicit lake parameterization is used in the model, so, for example, results over Lake Balaton should be treated with caution in terms of both temperature and precipitation.

The monthly means for each year of the 30-year period indicates large inter-annual variability (*Fig. 5*) according to the spread of the values. The maximum for the future is expected in June like in the reference period, but it can be even wetter in the 21st century: the amount can reach 65–120 mm considering the 25th and 75th percentiles for the end of the century, while it varied between 50-85 mm in 1971–2000 according to the CARPATCLIM-HU. In addition, HMS-ALADIN52 simulations show the largest spread of monthly precipitation amounts in August. February was usually the driest month in the past, and it seems likely to be shifted to March in future. September was also a particularly dry month on average in 1971–2000, while a secondary maximum occurred in November. In comparison, the future monthly values suggest that mainly September is responsible for the autumn precipitation increase, moreover, the secondary maximum appears also in this month. The very low (near-zero) monthly precipitation sums occurred between 1971 and 2000 are not likely to disappear in

the 21st century, moreover, near-zero monthly sums are possible both in the near and far future. The maximums can vary between 50 and 240 mm depending on the considered month, and it suggests that much higher monthly precipitation amounts could occur even in the near future than have been observed in the past.
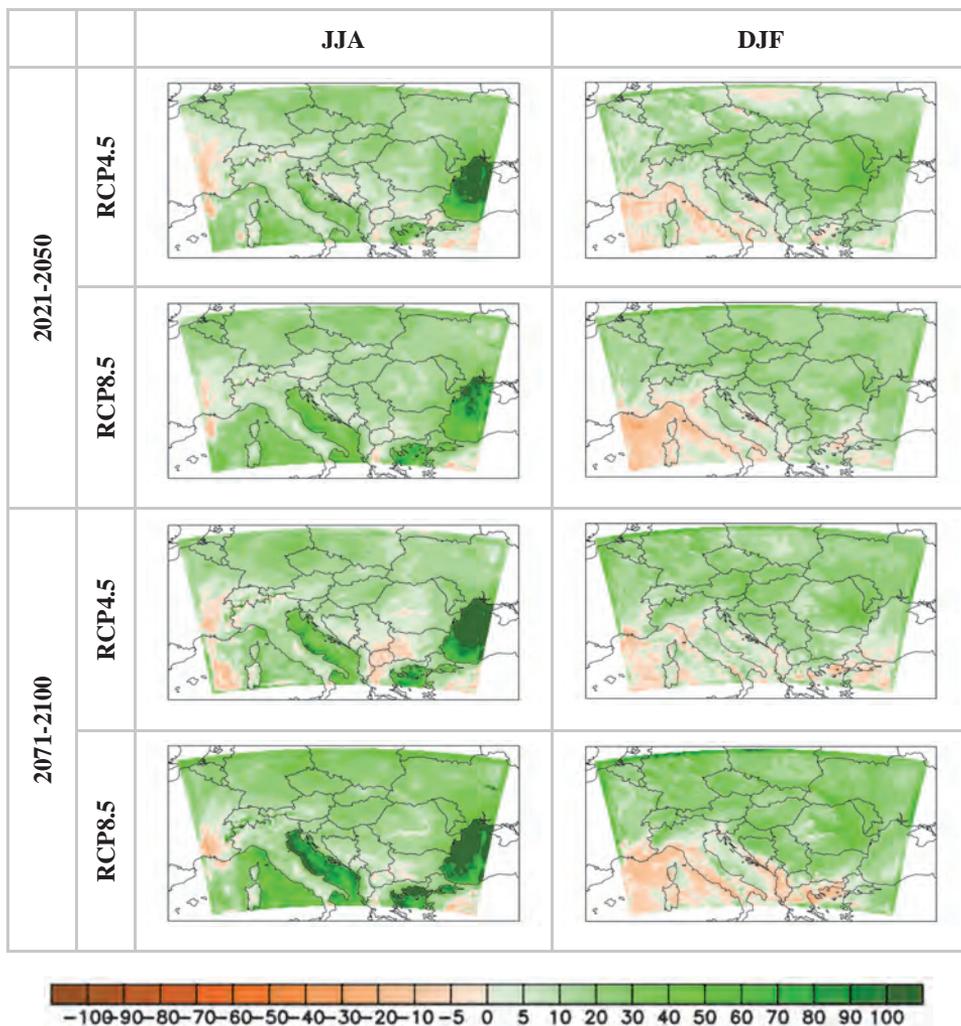
Fig. 4. Summer (JJA) and winter (DJF) relative precipitation changes (%) projected for 2071–2100 over the domain of HMS-ALADIN52 in case of RCP4.5 and RCP8.5 scenarios (reference period: 1971–2000).

Table 4. Annual and seasonal mean precipitation relative changes (%) in Hungary for 2021–2050 and 2071–2100 compared to 1971–2000, based on the results of HMS-ALADIN52 model simulations with RCP4.5 and RCP8.5 scenarios, below them the corresponding minimum and maximum changes are in parentheses based on 26 Euro-CORDEX (EC) RCM simulations.

		Annual	MAM	JJA	SON	DJF
2021-2050	**RCP4.5**	13 [-4 – 13]	9 [-5 – 21]	17 [-16 – 15]	9 [-11 – 21]	18 [5 – 24]
	RCP8.5	17 [0 – 16]	13 [-1 – 26]	15 [-8 – 23]	23 [-7 – 19]	19 [-5 – 26]
2071–2100 (EC: 2070–2099)	**RCP4.5**	16 [0 – 18]	10 [1 – 29]	16 [-16 – 17]	23 [-1 – 25]	22 [4 – 29]
	RCP8.5	24 [3 – 37]	19 [-2 – 32]	24 [-19 – 48]	33 [0 - 60]	24 [17 - 53]
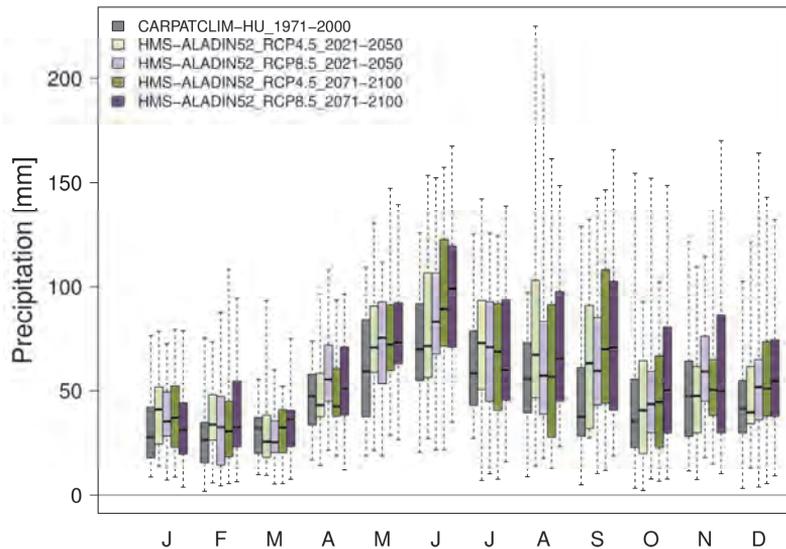
Fig. 5. Box-whisker diagram of the bias-corrected monthly precipitation sums (mm/month) area-averaged over Hungary for every year of 2021-2050 and 2071-2100 (light and dark colors, respectively), obtained with the RCP4.5 and RCP8.5 scenarios driven HMS-ALADIN52 (green and purple, respectively). The observations (CARPATCLIM-HU) for 1971-2000 are indicated with grey. The lower and upper boundaries of the rectangles (the "boxes") represent the lower and upper quartiles of the dataset (25th and 75th percentiles, respectively), while the line in the boxes shows the median value. The vertical dashed lines below and above the boxes show the minimum and maximum values of the dataset.

3.2. Comparison to Euro-CORDEX model ensemble

Based on the results of the selected Euro-CORDEX simulations (for the calculated minimum-maximum ranges of the annual and seasonal mean temperature and precipitation changes for the investigated 30-year periods see *Tables 3 and 4*), the projected annual mean temperature change for Hungary lies approximately in the same range (within 0.8 °C and 2.4 °C) with both scenarios for the near future, while for 2070–2099, their ranges seem to be almost disjoint: 1.3–3.3°C for RCP4.5 and 3.2–5.7 °C for RCP8.5 (see *Table 3* and also the box-whisker on the right side of *Fig. 8*). *Jacob et al.* (2014) also concluded that a robust and statistically significant warming, in the range of 1–4.5 °C for RCP4.5 and of 2.5–5.5 °C for RCP8.5 is likely to occur on a European scale, with regional differences.

Considering the maxima of the projected temperature changes by the Euro-CORDEX models (*Table 3*), the largest warming may occur in winter in both future periods, with both scenarios. However, the spread of the model results is also the highest in this season (except with the RCP8.5 in the end of the century), which makes winter a highly uncertain season in terms of the magnitude of changes. In contrast, the lowest change is seen in spring (except in 2021–2050 with RCP4.5 scenario). Recall, that the largest warming was projected in winter by HMS-ALADIN52 as well, while the least warming season was spring and autumn using RCP8.5 and RCP4.5, respectively.

The projected precipitation change for both scenarios in the near future and also for the RCP4.5 scenario in 2070–2099 lies in the same range, namely between -16% and +29%. (*Table 4*). Only the RCP8.5 for the far future projects somewhat higher values: except for spring, the maximum of the Euro-CORDEX ensemble is between 48–60% depending on the seasons, but it must be added that only one model is responsible for such high values in each season (*Fig. 7*). For both future periods, most of the model simulations show seasonal precipitation increase (reinforcing the HMS-ALADIN52 precipitation projections) except autumn in 2021-2050 and summer. The sign of the summer change is uncertain in the Euro-CORDEX results, i.e., both increase and decrease are projected. The concluded tendencies are in good agreement with the findings of *Kis et al.* (2020) on a monthly scale, even though they performed their analysis for a different multi-model ensemble – 10 RCMs driven by 4 different GCMs with 3 RCPs (RCP2.6, RCP4.5, and RCP8.5).

Looking at the scatter plots of projected precipitation and temperature changes over Hungary, we hardly see any correlation between them neither for 2021–2050 (*Fig. 6*) nor for 2070–2099 (*Fig. 7*), and the sign of precipitation change is uncertain in some seasons. *Hawkins* and *Sutton* (2011) showed that the internal variability and model uncertainty have higher contribution to the total uncertainty of the near-future temperature projections, while the scenario choice has higher role in the second half of the century. This is valid also for Hungary:

while the symbols representing the changes are grouped in a small circle for 2021–2050 *in Fig. 6*, for 2070–2099 *in Fig. 7* they are clearly distributed between two groups based on the applied RCP scenarios in each season. *Szabó* and *Szépszó* (2016) proved using global climate model results, that the main uncertainty source of precipitation projections over the Carpathian Basin is the internal variability along the whole century, and the scenarios choice has the smallest contribution to the total uncertainty range. Our results coincide with this for Hungary: low and high precipitation change as well as positive and negative precipitation changes are equally projected both using RCP4.5 and RCP8.5 scenarios. The only exception is winter in the far future: higher precipitation increase is shown mostly by RCP8.5 simulations (accompanied also by higher temperature change). This outcome for winter contradicts the conclusion of *Szabó* and *Szépszó* (2016) which did not show any impact of the scenario choice on the winter precipitation change signal over the Carpathian Basin, however, their study was based solely on GCM outputs.
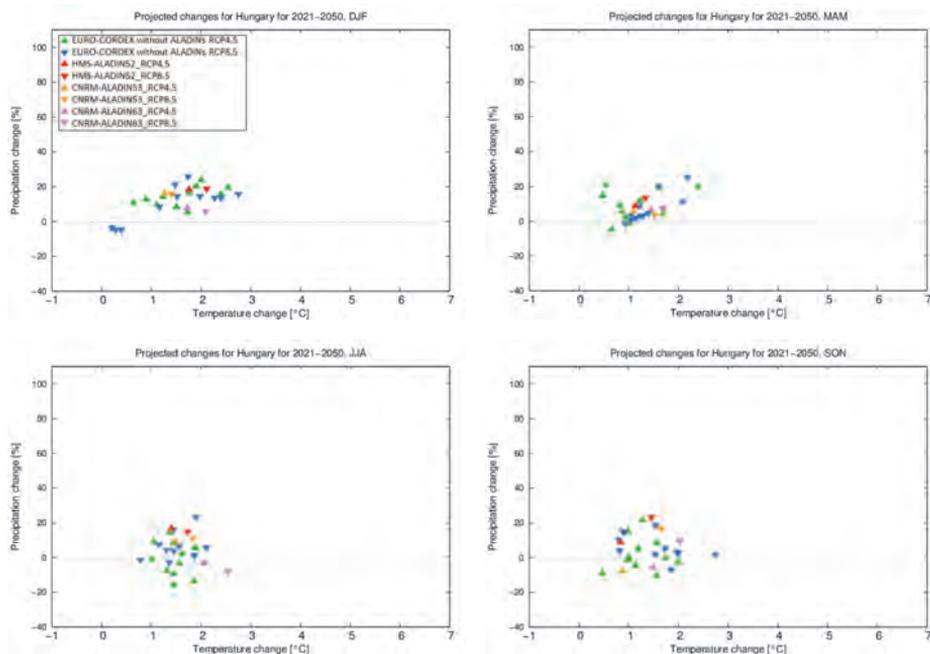
Fig. 6. Scatter plots of projected seasonal (winter-DJF: upper left, spring-MAM: upper right, summer-JJA: lower left, autumn-SON: lower right) changes of precipitation (y-axis; in %) and temperature (x-axis; in °C) over Hungary according to the different RCP scenarios (represented by different shapes) for 2021–2050 based on 26 Euro-CORDEX RCM simulations (highlighting CNRM-ALADINs) and HMS-ALADIN52. The reference period is 1971–2000.
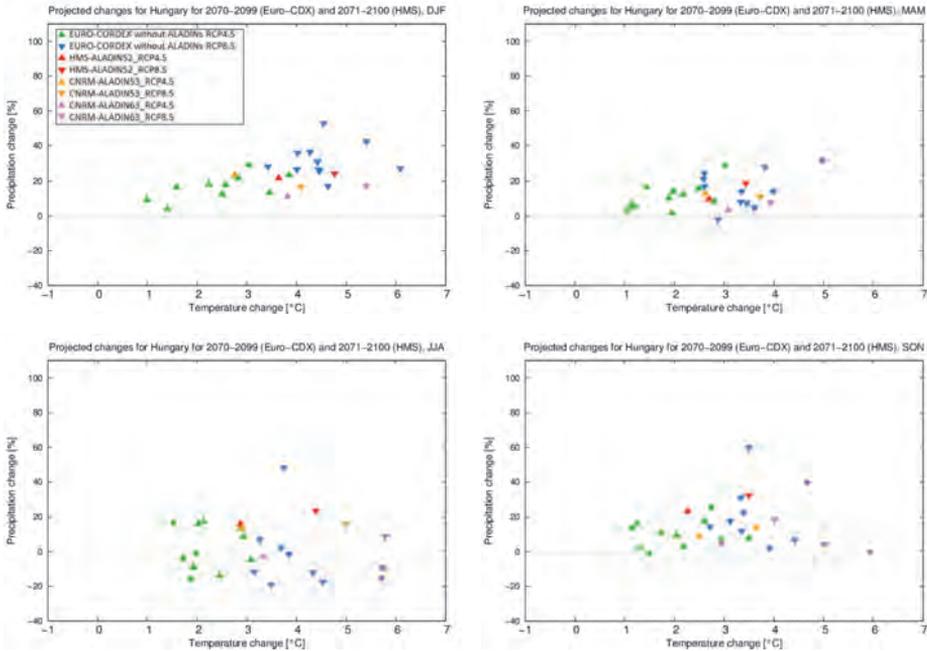
Fig. 7. Scatter plots of projected seasonal (winter-DJF: upper left, spring-MAM: upper right, summer-JJA: lower left, autumn-SON: lower right) changes of precipitation (y-axis; in %) and temperature (x-axis; in °C) over Hungary according to the different RCP scenarios (represented by different shapes) for 2070–2099 based on 26 Euro-CORDEX RCM simulations (highlighting CNRM-ALADINs) and for 2071-2100 for HMS-ALADIN52. The reference period is 1971–2000.

Finally, results of the three ALADIN versions are assessed and compared to the Euro-CORDEX subset. Focusing on the annual temperature change (*Fig. 8*), CNRM-ALADIN53 with the RCP4.5 is quite similar to HMS-ALADIN52, but the former one projects somewhat lower temperature change throughout the 21st century. In contrast, with the RCP8.5 scenario, CNRM-ALADIN53 produces almost the same warming as HMS-ALADIN52. Looking at the scatter plots of seasonal changes (*Figs. 6* and *7*), it is clear that the largest difference between the two model versions occurs in winter with both scenarios. Note that the RCP8.5 driven HMS-ALADIN52 projects lower temperature increase than CNRM-ALADIN53 in spring, summer, and autumn, which may contribute to the very similar results on annual scale. Considering all the ALADINs, the RCP4.5 scenario driven simulations indicate more intense warming compared to the RCP8.5 driven counterparts in the early part of the century (*Fig. 8*).

Comparing the temperature projections of the different ALADIN versions to the 26 members Euro-CORDEX ensemble in the 21st century over Hungary (see *Fig. 8*), while HMS-ALADIN52 with RCP4.5 tends to alternate around the median of the Euro-CORDEX ensemble during the whole time span, with the RCP8.5 scenario it remains below the median till 2040, but then increasingly exceeds it. CNRM-ALADIN63's projection is above the ensemble median, both with RCP4.5 and RCP8.5 scenarios thanks to its larger warming. The concluded features seem to be logical, because HMS-ALADIN52 and CNRM-ALADIN53 are consistent regarding the physical parameterization package, while CNRM-ALADIN63 is quite different, as large part of the parameterization has been changed in that version. We also should remember that HMS-ALADIN52 and CNRM-ALADIN53 share the same LBC error during the historical period, whereas this error was corrected in CNRM-ALADIN63 (see Section 2.2).
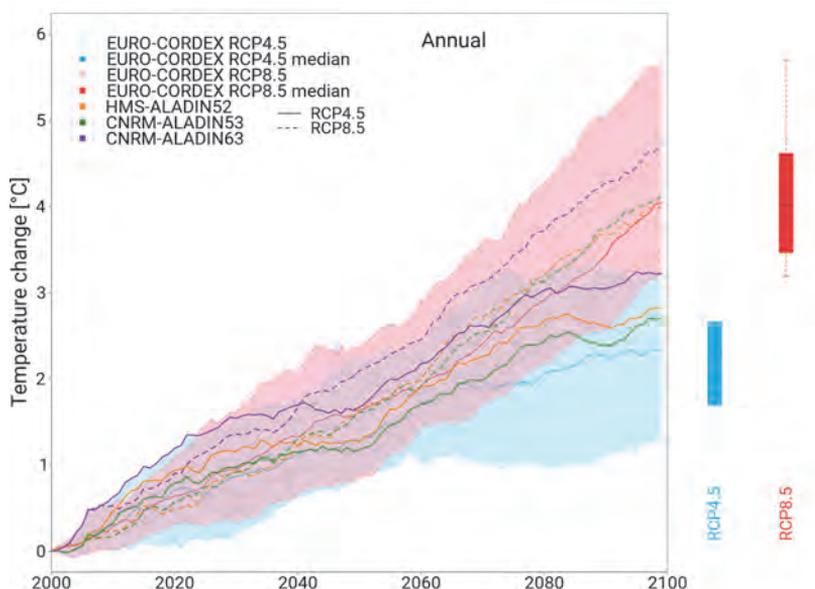
Fig. 8. The temporal evolution of the annual mean temperature change (°C) over Hungary in the 21st century under the RCP4.5 and RCP8.5 scenarios based on 26 Euro-CORDEX RCM simulations, smoothed with a 30-year window moving average. The median of these simulations is indicated with blue and red lines, the spread of these simulations is indicated with blue and pale red shades for the RCP4.5 and RCP8.5 scenarios, respectively. The thin blue and pale red lines represent the 25th and 75th percentiles. HMS-ALADIN52, CNRM-ALADIN53, and CNRM-ALADIN63 with RCP4.5 (solid line) and RCP8.5 (dashed line) are indicated with different colors. (The calculated average values are plotted at the final year of the time interval.) On the right, the box-whisker diagram of the Euro-CORDEX simulations sorted by the different scenarios is shown for 2070–2099. The reference period is 1971–2000.

Regarding the temporal evolution of the precipitation changes in the 21st century, two seasonal examples are shown (*Fig. 9*). In winter, CNRM-ALADIN63 is below the ensemble median with both scenarios. HMS-ALADIN52 and CNRM-ALADIN53 behave similarly to each other, and project larger precipitation increase than CNRM-ALADIN63, which difference is reduced by the end of the century. Note that at the beginning of the century, HMS-ALADIN52 shows higher mean precipitation values than even the maximum of the Euro-CORDEX ensemble. By the end of the century, the HMS-ALADIN52 and CNRM-ALADIN53 versions project approximately the same winter precipitation increase as the median of the Euro-CORDEX ensemble considering RCP4.5 scenario. This is also true for the RCP8.5-driven HMS-ALADIN52, but CNRM-ALADIN53 is shifted away from the median and projects lower values. During summer, CNRM-ALADIN63 indicates precipitation decrease with both RCPs in 2021–2050 and 2071–2100 (*Figs. 6* and *7*) in contrast to HMS-ALADIN52 and CNRM-ALADIN53. However, looking at the whole century (*Fig. 9*), especially with RCP8.5, a few 30-year time periods may face precipitation surplus compared to the past. Assessing the ALADIN versions in light of the Euro-CORDEX ensemble, HMS-ALADIN52 with the RCP8.5 scenario sticks out from the spread for some short time intervals. The extent of the uncertainties is much larger for the summer season than for winter (just as the box-whisker diagrams on the right side of *Fig. 9* clearly indicate this for 2070–2099). The RCP8.5 results completely cover the ensemble uncertainty by the end of the century, underlining the irrelevance of the scenario choice. However, it is also important to note that the maximum of the summer change is provided by the WRF331F simulation which is responsible for about the upper 20% of the range from 2080 in case of RCP8.5 scenario. In autumn (not shown) and winter, this member gives also the maximum of the RCP8.5 range. The WRF331F simulation should be treated with caution, as it has been removed from several national and international model ensembles due to its problematic behavior (*Giorgi et al.*, 2016; *Vautard et al.*, 2021).
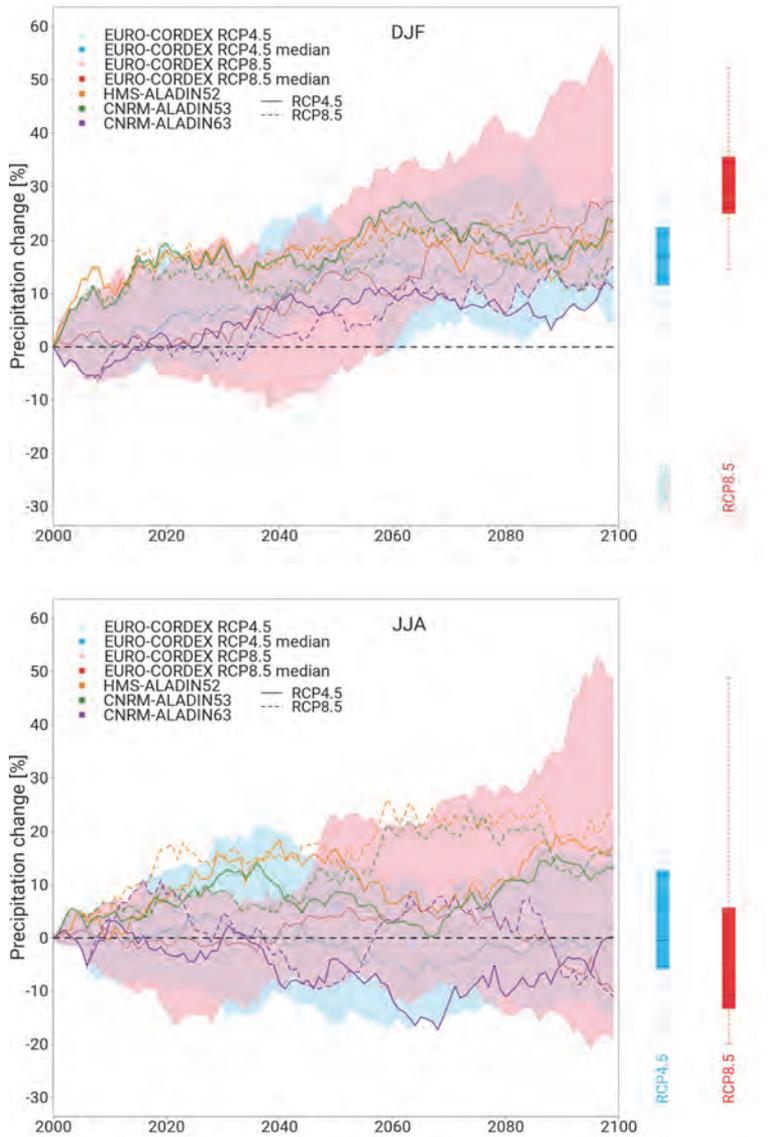
Fig. 9. The temporal evolution of the winter (DJF, top) and summer (JJA, bottom) mean precipitation changes (%) over Hungary in the 21st century under the RCP4.5 and RCP8.5 scenarios based on 26 Euro-CORDEX RCM simulations, smoothed with a 30-year window moving average. The median of these simulations is indicated with blue and red lines, the spread of these simulations is indicated with blue and pale red shades for the RCP4.5 and RCP8.5 scenarios, respectively. The thin blue and pale red lines represent the 25th and 75th percentiles. HMS-ALADIN52, CNRM-ALADIN53, and CNRM-ALADIN63 with RCP4.5 (solid line) and RCP8.5 (dashed line) are indicated with different colors. (The calculated average values are plotted at the final year of the time interval.) On the right, the box-whisker diagram of the Euro-CORDEX simulations sorted by the different scenarios is shown for 2070–2099. The reference period is 1971–2000.

4. Summary and conclusions

In this paper, the history and some recent temperature and precipitation results of the ALADIN-Climate regional climate model used at HMS have been summarized. In addition to HMS-ALADIN52 simulations, a Euro-CORDEX ensemble (which includes two additional versions of ALADIN-Climate) has been studied in order to evaluate the climate change expected in Hungary and to assess the representativeness of HMS-ALADIN52. The results of three ALADIN-Climate models (HMS-ALADIN52, CNRM-ALADIN53, CNRM-ALADIN63) included in this study were evaluated with special focus. Temperature and precipitation changes are analyzed mainly for 2021–2050 and 2071–2100 (2070–2099 for Euro-CORDEX) with respect to 1971–2000 but for the whole 21th century as well along RCP4.5 and RCP8.5 scenarios.

The HMS-ALADIN52 results for Hungary can be considered representative for temperature: the gradual increase is significant, the annual mean change is close to the median of the Euro-CORDEX simulations. The main source of uncertainty in the second half of the century is the scenario choice (*Szabó* and *Szépszó*, 2016) which is confirmed by the results. According to the Euro-CORDEX, the annual mean temperature increase is more moderate with RCP4.5 varying between 1.3 °C and 3.3 °C (2.9 °C in HMS-ALADIN52), while with RCP8.5, the increase is between 3.2 °C and 5.7 °C (4 °C in HMS-ALADIN52) by the end of the 21st century.

Earlier studies based on SRES scenarios showed that Hungary lies in a very uncertain area in Europe concerning the future evolution of precipitation (*Christensen et al.,* 2007b; *Coppola et al.*, 2021), but the majority of the simulations projected summer reduction and winter increase in the Carpathian Basin. *Szabó* and *Szépszó* (2016) proved the key role of the internal variability in projection uncertainty for this region. HMS-ALADIN52 simulations suggest a definite increase exceeding 10% in all seasons with RCP4.5 scenario. The Euro-CORDEX simulations project a precipitation increase in winter and spring for both future 30-year periods, and in autumn at the end of the century, however, the sign of the summer change is uncertain. Summer precipitation decrease may occur for both scenarios, but higher temperature change values are associated with those using the RCP8.5 scenario. Considering the whole century, HMS-ALADIN52 simulations are in the "upper" part of the spread (indicating higher values than the median), especially in the first part of the 21st century, and also completes the Euro-CORDEX range in a positive direction.

The three ALADIN RCMs show similar evolution of annual temperature change, though CNRM-ALADIN63 indicates higher changes throughout the 21th century. CNRM-ALADIN63 shows lower precipitation increase compared to HMS-ALADIN52 and CNRM-ALADIN53. Moreover, and contrary to the other versions, CNRM-ALADIN63 assumes decrease in autumn with RCP4.5 in the near future, and in summer for both future periods with both scenarios (e.g., by

the end of the century -0.5% and -11% relative change with RCP4.5 and RCP8.5, respectively). CNRM-ALADIN63 shows a nearly systematic lower precipitation amounts in summer compared to HMS-ALADIN52 and CNRM-ALADIN53 (which are relatively close to each other) from the 2010s till the end of the 21st century. The differences are likely related to the changes in physical parameterizations made between ALADIN5 and ALADIN6 as a result of a 10-year model development. Only further investigations implying sensitivity simulations for each parameterization may be able to reveal the specific reasons behind the simulated differences. This is far out of the scope of the current study.

Our further plans include the investigation of climate indices and extremes in HMS-ALADIN52 projections as well as in the Euro-CORDEX ensemble, and a joint evaluation of HMS-ALADIN52 and REMO2015 – also adapted at HMS – results.

References

Bede-Fazekas, Á., Czúcz, B., and *Somodi, I.*, 2017: Vulnerability of natural landscapes to climate change – a case study of Hungary. *Időjárás 121*, 392–414.

Belda, M., Skalák, P., Farda, A., Halenka, T., Déqué, M., Csima, G., Bartholy, J., Torma, Cs., Boroneant, C., Caian, M., and *Valery, V.*, 2015: CECILIA Regional Climate Simulations for Future Climate: Analysis of Climate Change Signal. Advances in Meteorology. https://doi.org/10.1155/2015/354727

Bihari, Z., Lakatos, M., and *Szentimrey, T.*, 2017: Felszíni megfigyelésekből készített rácsponti adatbázisok az Országos Meteorológiai Szolgálatnál, *Légkör 62*, 148–151. (in Hungarian)

Bougeault, P., 1985: A simple parameterization of the large-scale effects of cumulus convection. *Mon. Weather. Rev. 113*, 2108–2121.
https://doi.org/10.1175/1520-0493(1985)113<2108:ASPOTL>2.0.CO;2

Charnock, H., 1955: Wind stress on a water surface. *Quart. J. Roy. Meteor. Soc. 81*, 639–640.
https://doi.org/10.1002/qj.49708135027

Christensen, O.B., Drews, M., Christensen, J.H., Dethloff, K., Ketelsen, K., Hebestadt, I., and *Rinke, A.*, 2006: The HIRHAM regional climate model, version 5. Technical Report, Danish Meteorological Institute, Copenhagen, 6–17.

Christensen, J.H., Carter, T.R., Rummukainen, M., and *Amanatidis, G.*, 2007a: Evaluating the performance and utility of climate models: the PRUDENCE project. *Climat. Change 81*, (PRUDENCE Special Issue), 1–6. https://doi.org/10.1007/s10584-006-9211-6

Christensen, J.H., Hewitson B., Busuioc, A., Chen, A., Gao, X., Held, I., Jones, R., Kolli, R.K., Kwon, W.-T., Laprise, R., Magaña Rueda, V., Mearns, L., Menéndez, C.G., Räisänen, J., Rinke, A., Sarr, A., Whetton, P., 2007: Regional Climate Projections. In (Eds. *Solomon, S., D. Qin, M. Manning, Z. Chen, M. Marquis, K.B. Averyt, M. Tignor* and *H.L. Miller)* Climate Change 2007b: The Physical Science Basis. Contribution of Working Group I to the Fourth Assessment Report of the Intergovernmental Panel on Climate Change. Cambridge University Press, Cambridge, United Kingdom and New York, NY, USA.

Cinquini, L., Crichton, D., Mattmann, C., Harney, J., Shipman, G., Wang, F., Ananthakrishnan, R., Miller, N., Denvil, S., Morgan, M., Pobre, Z., Bell, M.G., Doutriaux, C., Drach, R., Williams, D., Kershaw, P., Pascoe, S., Gonzalez, E., Fiore, S., and *Schweitzer, R.*, 2014: The Earth System Grid Federation: an open infrastructure for access to distributed geospatial data. *Fut. Generat. Comput. Syst. 36*, 400–417. https://doi.org/10.1016/j.future.2013.07.002

Colin, J., Déqué, M., Radu, R., and *Somot, S.*, 2010: Sensitivity study of heavy precipitations in Limited Area Model climate simulation: influence of the size of the domain and the use of the spectral nudging technique. *Tellus-A 62*, 591–604. https://doi.org/10.1111/j.1600-0870.2010.00467.x

Coppola, E., Nogherotto, R., Ciarlò, J.M., Giorgi, F., van Meijgaard, E., Kadygrov, N., Iles, C., Corre, L., Sandstad, M., Somot, S., Nabat, P., Vautard, R., Levavasseur, G., Schwingshackl, C., Sillmann, J., Kjellström, E., Nikulin, G., Aalbers, E., Lenderink, G., Christensen, O.B., Boberg, F., Lund Sørland, S., Demory, M.-E., Bülow, K., Teichmann, C., Warrach-Sagi, K., and *Wulfmeyer, V.*, 2021: Assessment of the European Climate Projections as Simulated by the Large EURO-CORDEX Regional and Global Climate Model Ensemble. *J. Geophys. Res. Atmos. 126*, e2019JD032356. http://doi.org/10.1029/2019JD032356

Csima, G. and *Horányi, A.*, 2008: Validation of the ALADIN-Climate regional climate model at the Hungarian Meteorological Service. *Időjárás 112*, 155–177.

Davies, H.C., 1976: A lateral boundary formulation for multi-level prediction models. *Quart. J. Roy. Meteorol. Soc. 102*, 405–418. https://doi.org/10.1002/qj.49710243210

Dee, D.P., Uppala, S.M., Simmons, A.J., Berrisford, P., Poli, P., Kobayashi, S., Andrae, U., Balmaseda, M. A., Balsamo, G., Bauer, P., Bechtold, P., Beljaars, A.C.M., van de Berg, L., Bidlot, J., Bormann, N., Delsol, C., Dragani, R., Fuentes, M., Geer, A.J., Haimberger, L., Healy, S.B., Hersbach, H., Hólm, E.V., Isaksen, L., Kållberg, P., Köhler, M., Matricardi, M., McNally, A. P., Monge-Sanz, B.M., Morcrette, J.-J., Park, B.-K., Peubey, C., de Rosnay, P., Tavolato, C., Thépaut, J.-N., and *Vitart, F.*, 2011: The ERA-Interim Reanalysis: Configuration and Performance of the Data Assimilation System. *Quart. J. Roy. Meteorol. Soc.* 137, 553–597. https://doi.org/10.1002/qj.828

Déqué, M., Dreveton, C., Braun, A., and *Cariolle, D.*, 1994: The ARPEGE-IFS atmosphere model: a contribution to the French community climate modelling. *Clim. Dynam. 10*, 249–266. https://doi.org/10.1007/BF00208992

Driouech, F., ElRhaz, K., Moufouma-Okia, W., Arjdal, K., and *Balhane, S.*, 2020: Assessing future changes of climate extreme events in the CORDEX-MENA region using regional climate model ALADIN-climate. *Earth Syst. Environ. 4*. 477–492. https://doi.org/10.1007/s41748-020-00169-3

Farda, A., Déué, M., Somot, S., Horányi, A., Spiridonov, V., and *Tóth, H.*, 2010: Model ALADIN as regional climate model for Central and Eastern Europe. *Studia Geophysica et Geodaetica 54*, 313–332. https://doi.org/10.1007/s11200-010-0017-7

Fouquart, Y. and *Bonnel, B.*, 1980: Computations of solar heating of the Earth's atmosphere: A new parameterization. *Contrib. Atmos. Phys. 53*, 35–62.

Giorgi, F., Jones, C., and *Asrar, G.*, 2009: Addressing climate information needs at the regional level: the CORDEX framework. *WMO Bull. 54*, 175–183

Giorgi, F., Torma, Cs., Coppola, E., Ban, N., Schär, C., and *Somot, S.*, 2016: Enhanced summer convective rainfall at Alpine high elevations in response to climate warming. *Nat. Geosci. 9*, 584–589. https://doi.org/10.1038/ngeo2761

Halenka, T., 2007: CECILIA keeping a close eye on climate change. eStrategies, Science, Technology and Innovation Projects, British Publishers, 12.

Hawkins, E. and *Sutton, R.*, 2011: The potential to narrow uncertainty in projections of regional precipitation change. *Clim. Dynam. 37*, 407–418. https://doi.org/10.1007/s00382-010-0810-6

Homolya, E., Rotárné Szalkai, Á., and *Selmeczi, P.*, 2017: Climate impact on drinking water protected areas. *Időjárás 121*, 371–392.

Illy, T., Sábitz, J., and *Szépszó, G.*, 2015: Az ALADIN-Climate modellkísérletek eredményeinek validációja. RCMTéR (EEA-C13-10) project report.

Ivusic, S., Güttler, I., Horvath, K., Somot, S., Guérémy, J.-F., and *Alias, A.*, 2021: Modelling the extreme precipitation over the Dinaric Alps: evaluation of the CNRM-ALADIN regional climate model. *Quart. J. Roy. Meteorol. Soc.* (in rev.)

Jacob, D., Elizalde, A., Haensler, A., Hagemann, S., Kumar, P., Podzun, R., Rechid, D., Remedio, A.R., Saeed, F., Sieck, K., Teichmann, C., and *Wilhelm, C.*, 2012: Assessing the transferability of the regional climate model REMO to different coordinated regional climate downscaling experiment (CORDEX) regions. *Atmosphere 3*, 181–199. https://doi.org/10.3390/atmos3010181

Jacob, D., Petersen, J., Eggert, B., Alias, A., Christensen, O.B., Bouwer, L.M., Braun, A., Colette, A., Déqué, M., Georgievski, G., Georgopoulou, E., Gobiet, A., Menut, L., Nikulin, G., Haensler, A., Hempelmann, N., Jones, C., Keuler, K., Kovats, S., Kröner, N., Kotlarski, S., Kriegsmann, A., Martin, E., van Meijgaard, E., Moseley, C., Pfeifer, S., Preuschmann, S., Radermacher, C., Radtke, K., Rechid, D., Rounsevell, M., Samuelsson, P., Somot, S., Soussana, J-F., Teichmann, C., Valentini, R., Vautard, R., Weber, B., and *Yiou, P.*, 2014: EURO-CORDEX: new high-resolution climate change projections for European impact research. Reg. *Environ. Change 14*, 563–578. https://doi.org/10.1007/s10113-013-0499-2

Kajner, P., Czira, T., Selmeczi, P., and *Sütő A.*, 2017: National Adaptation Geo-information System in climate adaptation planning. *Időjárás 121*, 345–370.

Kis, A., Pongrácz, R., Bartholy, J., Gocic, M., Milanovic, M., and *Trajkovic, S.*, 2020.: Multi-scenario and multi-model ensemble of regional climate change projections for the plain areas of the Pannonian Basin. *Időjárás, 124,* 157–190. https://doi.org/10.28974/idojaras.2020.2.2

Kovács, A., Unger, J., and *Szépszó, G.*, 2015: Adjustment of tourism climatological indicators for the Hungarian population in assessing exposure and vulnerability to climate change. In (eds.: *Demiroğlu, O.C. et al.*) Proceedings of the 4th International Conference on Climate, Tourism and Recreation – CCTR2015, Istanbul Policy Center, Istanbul, Turkey, 71–76. ISBN 978-605-9178-18-1.

Krüzselyi, I., Bartholy, J., Horányi, A., Pieczka, I., Pongrácz, R., Szabó, P., Szépszó, G., and *Torma, Cs.*, 2011: The future climate characteristics of the Carpathian Basin based on a regional climate model mini-ensemble. *Adv. Sci. Res. 6*, 69–73. https://doi.org/10.5194/asr-6-69-2011

Kupiainen, M., Samuelsson, P., Jones, C., Jansson, C., Willén, U., Hansson, U., Ullerstig, A., Wang, S., and *Döscher, R.*, 2011: Rossby Centre regional atmospheric model, RCA4. *Rossby Centre Newsletter.*

Lepesi, N., Bede-Fazekas, Á., Czúcz, B., and *Somodi, I.*, 2017: Adaptive capacity of climate sensitive habitats to climate change in Hungary. *Időjárás 121*, 415–436.

Lucas-Picher, P., Somot, S., Déqué, M., Decharme, B., and *Alias A.*, 2013: Evaluation of the regional climate model ALADIN to simulate the climate over North America in the CORDEX framework. *Clim. Dynam. 41,*1117–1137. https://doi.org/10.1007/s00382-012-1613-8

Madec, G., 2008: NEMO ocean engine. Note du Pole de modélisation, Institut Pierre-Simon Laplace (IPSL), France, No 27 ISSN:1288–1619.

Maraun, D., 2016: Bias correcting climate change simulations – a critical review. *Curr. Climate Change Rep. 2*, 211–220. https://doi.org/10.1007/s40641-016-0050-x

Maraun, D. and *Widmann, M.*, 2018: Statistical downscaling and bias correction for climate research, Cambridge University Press. https://doi.org/10.1017/9781107588783

Masson, V., Le Moigne, P., Martin, E., Faroux, S., Alias, A., Alkama, R., Belamari, S., Barbu, A., Boone, A., Bouyssel, F., Brousseau, P., Brun, E., Calvet, J.-C., Carrer, D., Decharme, B., Delire, C., Donier, S., Essaouini, K., Gibelin, A.-L., Giordani, H., Habets, F., Jidane, M., Kerdraon, G., Kourzeneva, E., Lafaysse, M., Lafont, S., Lebeaupin Brossier, C., Lemonsu, A., Mahfouf, J.-F., Marguinaud, P., Mokhtari, M., Morin, S., Pigeon, G., Salgado, R., Seity, Y., Taillefer, F., Tanguy, G., Tulet, P., Vincendon, B., Vionnet, V., and *Voldoire, A.*, 2013: The SURFEXv7.2 land and ocean surface platform for coupled or offline simulation of earth surface variables and fluxes. *Geosci. Model Dev. 6*, 929–960. https://doi.org/10.5194/gmd-6-929-2013

671

Meijgaard, E. v., Ulft, L.H. v., Lenderink, G., Roode, S.R. d., Wipfler, E.L., Boers, R., and Timmermans, R. M. A. v., 2012: Refinement and application of a regional atmospheric model for climate scenario calculations of Western Europe. Wageningen: Royal Netherlands Meteorological Institute.

Mlawer, E.J., Taubman, S.J., Brown, P.D., Iacono, M.J., and Clough, S.A., 1997: Radiative transfer for inhomogeneous atmospheres: RRTM, a validated correlated-k model for the longwave. J. Geophys. Res. 102D, 16663–16682. https://doi.org/10.1029/97JD00237

Moss, R.H., Edmonds, J.A., Hibbard, K.A., Manning, M.R., Rose, S.K., van Vuuren, D.P., Carter T.R., Emori, S., Kainuma, M., Kram, T., Meehl, G.A., Mitchell, J.F.B., Nakicenovic, N., Riahi, K., Smith, S.J., Stouffer, R.J., Thomson, A.M., Weyant, J.P., and Wilbanks, T.J., 2010: The next generation of scenarios for climate change research and assessment. Nature 463, 747–756. https://doi.org/10.1038/nature08823

Nabat, P., Somot, S., Cassou, C., Mallet, M., Michou, M., Bouniol, D., Decharme, B., Drugé, T., Roehrig, R., and Saint-Martin, D., 2020: Modulation of radiative aerosols effects by atmospheric circulation over the Euro-Mediterranean region. Atmos. Chem. Phys. 20, 8315–8349, https://doi.org/10.5194/acp-20-8315-2020

Nakicenovic, N., Alcamo, J., Davis, G., de Vries, B., Fenhann, J., Gaffin, S., Gregory, K., Grübler, A., Jung, T.Y., Kram, T., La Rovere, E.L., Michaelis, L., Mori, S., Morita, T., Pepper, W., Pitcher, H., Price, L., Raihi, K., Roehrl, A., Rogner, H.H., Sankovski, A., Schlesinger, M., Shukla, P., Smith, S., Swart, R., van Rooijen, S., Victor, N., and Dadi, Z., 2000: IPCC special report on emissions scenarios. Cambridge University Press, Cambridge, USA.

Noilhan, J. and Planton, S., 1989: A simple parameterization of land surface processes for meteorological models. Mon. Weather Rev. 117, 536–549.
https://doi.org/10.1175/1520-0493(1989)117<0536:ASPOLS>2.0.CO;2

Radu, R., Déqué, M., and Somot, S., 2008: Spectral nudging in a spectral regional climate model. Tellus 60A, 885–897. https://doi.org/10.1111/j.1600-0870.2008.00343.x

Ricard, J.L. and Royer, J.F., 1993: A statistical cloud scheme for use in an AGCM. Annal. Geophysicae 11, 1095–1115.

Rockel, B., Will, A., and Hense, A. (eds.), 2008: Special issue Regional climate modelling with COSMO-CLM (CCLM). Met. Zeitsch. 17. https://doi.org/10.1127/0941-2948/2008/0309

Salas y Melia, D., 2002: A global coupled sea ice–ocean model. Ocean Model. 42. 137–172.
https://doi.org/10.1016/S1463-5003(01)00015-4

Skamarock, W.C., Klemp, J.B., Dudhia, J., Gill, D.O., Duda, D.M.B.M.G., Huang, X.Y., Wang, W., and Powers, J.G., 2008: A description of the advanced research WRF version 3. NCAR Tech. Note 475.

Smith, R.N.B., 1990: A scheme for predicting layer clouds and their water content in a general circulation model. Quart. J. Roy. Meteorol. Soc. 116, 435–460. https://doi.org/10.1002/qj.49711649210

Szabó, P. and Szépszó, G., 2016: Quantifying Sources of Uncertainty in Temperature and Precipitation Projections over Different Parts of Europe. In: (eds.: Bátkai, A., Csomós, P., Faragó, I., Horányi, A., Szépszó, G.) Mathematical Problems in Meteorological Modelling, 239–261.
https://doi.org/10.1007/978-3-319-40157-7_12

Szentimrey, T., 2008: Development of MASH homogenization procedure for daily data. In: Proceedings of the Fifth Seminar for Homogenization and Quality Control in Climatological Databases, Budapest, Hungary, 2006. WCDMP-No.71, WMO/TD-No. 1493, 123–130.

Szentimrey, T., 2014: Manual of homogenization software MASHv3.03, Hungarian Meteorological Service.

Szentimrey, T. and Bihari, Z., 2007: Mathematical background of the spatial interpolation methods and the software MISH (Meteorological Interpolation based on Surface Homogenized Data Basis). In: Proceedings from the Conference on Spatial Interpolation in Climatology and Meteorology, Budapest, Hungary, 2004, COST Action 719, COST Office, 17–27.

Szentimrey, T. and Bihari, Z., 2014: Manual of interpolation software MISHv1.03. Hungarian Meteorological Service.

Szépszó, G. and Horányi, A., 2008: Transient simulation of the REMO regional climate model and its evaluation over Hungary. Időjárás 112, 203–231.

Szopa, S., Balkanski, Y., Schulz, M., Bekki, S., Cugnet, D., Fortems-Cheiney, A., Turquety, S., Cozic, A., Déandreis, C., Hauglustaine, D., Idelkadi, A., Lathière, J., Lefevre, F., Marchand, M., Vuolo, R., Yan, N., and Dufresne, J.-L., 2013: Aerosol and ozone changes as forcing for climate evolution between 1850 and 2100. Clim. Dynam. 40, 2223–2250. https://doi.org/10.1007/s00382-012-1408-y

Taylor, K., Stouffer, R.J., Meehl, G.A., 2012: An overview of CMIP5 and the experiment design. Bull. Amer. Meteorol. Soc. 93, 485–498. https://doi.org/10.1175/BAMS-D-11-00094.1

Tegen, I., Hollrig, P., Chin, M., Fung, I., Jacob, D., and Penner, J., 1997: Contribution of different aerosol species to the global aerosol extinction optical thickness: Estimates from model results, J. Geophys. Res., 102, 23895–23915. https://doi.org/10.1029/97JD01864

Termonia, P., Fischer, C., Bazile, E., Bouyssel, F., Brožková, R., Bénard, P., Bochenek, B., Degrauwe, D., Derková, M., El Khatib, R., Hamdi, R., Mašek, J., Pottier, P., Pristov, N., Seity, Y., Smolíková, P., Španiel, O., Tudor, M., Wang, Y., Wittmann, C., and Joly, A., 2018: The ALADIN System and its canonical model configurations AROME CY41T1 and ALARO CY40T1. Geosci. Model Dev. 11, 257–281. https://doi.org/10.5194/gmd-11-257-2018

Torma, Cs., Bartholy, J., Pongrácz, R., Barcza, Z., Coppola, E., and Giorgi, F., 2008: Adaptation and validation of the RegCM3 climate model for the Carpathian Basin. Időjárás 112, 233–247.

Tramblay, Y., Ruelland, D., Somot, S., Bouaicha, R., and Servat, E., 2013: High-resolution Med-CORDEX regional climate model simulations for hydrological impact studies: a first evaluation of the ALADIN-Climate model in Morocco. Hydrol. Earth Syst. Sci., 17, 3721–3739. https://doi.org/10.5194/hess-17-3721-2013

Uppala, S.M., KÅllberg, P.W., Simmons, A.J., Andrae, U., Bechtold, V.D.C., Fiorino, M., Gibson, J.K., Haseler, J., Hernandez, A., Kelly, G.A., Li, X., Onogi, K., Saarinen, S., Sokka, N., Allan, R.P., Andersson, E., Arpe, K., Balmaseda, M.A., Beljaars, A.C.M., Berg, L.V.D., Bidlot, J., Bormann, N., Caires, S., Chevallier, F., Dethof, A., Dragosavac, M., Fisher, M., Fuentes, M., Hagemann, S., Hólm, E., Hoskins, B.J., Isaksen, L., Janssen, P.A.E.M., Jenne, R., Mcnally, A.P., Mahfouf, J.-F., Morcrette, J.-J., Rayner, N.A., Saunders, R.W., Simon, P., Sterl, A., Trenberth, K.E., Untch, A., Vasiljevic, D., Viterbo, P., and Woollen, J., 2005: The ERA-40 re-analysis. Quart. J. Roy. Meteorol. Soc., 131, 2961–3012. https://doi.org/10.1256/qj.04.176

Valcke, S., 2006: OASIS3 user guide (prism_2-5). Technical report TR/CMGC/06/73, CERFACS, Toulouse, France.

Vautard, R., Kadygrov, N., Iles, C., Boberg, F., Buonomo, E., Bülow, K., Coppola, E., Corre, L., van Meijgaard, E., Nogherotto, R., Sandstad, M., Schwingshackl, C., Somot, S., Aalbers, E., Christensen, O.B., Ciarlo, J.M., Demory, M.-E., Giorgi, F., Jacob, D., Jones, R.G., Keuler, K., Kjellström, E., Lenderink, G., Levavasseur, G., Nikulin, G., Sillmann, J., Solidoro, C., Lund Sørland, S., Steger, C., Teichmann, C., Warrach-Sagi, K., and Wulfmeyer, V., 2021: Evaluation of the large EURO-CORDEX regional climate model ensemble. J. Geophys. Res. – Atmospheres 126, e2019JD032344. https://doi.org/10.1029/2019JD032344

Voldoire, A., Sanchez-Gomez, E., Salas y Mélia, D., Decharme, B., Cassou, C., Sénési, S., Valcke, S., Beau, I., Alias, A., Chevallier, M., Déqué, M., Deshayes, J., Douville, H., Fernandez, E., Madec, G., Maisonnave, E., Moine, M.-P., Planton, S., Saint-Martin, D., Szopa, S., Tyteca, S., Alkama, R., Belamari, S., Braun, A., Coquart, L., and Chauvin, F., 2013: The CNRM-CM5.1 Global Climate Model: Description and Basic Evaluation. Clim. Dyn. 40, 2091–2121. https://doi.org/10.1007/s00382-011-1259-y

Williamson, D.F., Parker, R.A., and Kendrick, J.S., 1989: The boxplot: a simple visual method to interpret data. Ann. Int. Medicine 110, 916–921. https://doi.org/10.7326/0003-4819-110-11-916

IDŐJÁRÁS

Future temperature and urban heat island changes in Budapest: a comparative study based on the HMS-ALADIN and SURFEX models

Gabriella Allaga-Zsebeházi

Hungarian Meteorological Service
P.O. Box 38, H-1525 Budapest, Hungary

Corresponding author E-mail: zsebehazi.g@met.hu

Abstract— Cities, due to their warmer and dryer local climate in addition to their dense population, are subjected to large future climate change risks. Land surface models, with detailed urban parameterization schemes, serve as an adequate tool to refine the rough regional climate projections over the cities. In this study, the future temperature conditions in Budapest are studied with the SURFEX land surface model (LSM), driven by the HMS-ALADIN5.2 regional climate model (RCM) and considering the high-emission RCP8.5 scenario. Special attention is dedicated to explore the differences between the RCM and LSM in terms of the results, their interpretation, and further use in impact models. According to the investigated model combination, the winter season may warm the most, with 1.9 °C in 2021–2050 and 4.3 °C in 2071–2100, although the magnitude of this change is smaller in SURFEX than in ALADIN. Besides the mean changes, four climate indices, based on high and low temperature thresholds, were studied, and it was found that the low temperature indices (frost days and very cold days) may relatively decrease more in SURFEX compared to ALADIN over Budapest, and in the city center compared to the suburbs and rural areas. In addition, the urban heat island (UHI) intensity is projected to decrease in SURFEX mainly in spring and summer (by 2071–2100 with 0.35 °C and 0.32 °C, respectively). Finally, a simple method is provided to correct the SURFEX temperature fields, using the ALADIN model, with eliminated systematic biases and the simulated UHI field.

Key-words: urban climate, urban heat island, climate projection, land surface model, regional climate model

1. Introduction

The physical characteristics of cities (i.e., impervious surfaces, large heat capacity, narrow streets, high buildings) in addition to their anthropogenic activities (e.g., internal heating and transportation) result in warmer, drier, and more polluted air in cities than in natural areas (*Oke*, 1982). One of the most studied phenomena of urban climate is the urban heat island (UHI), the temperature difference between the city and its environment, which is the largest at summer calm nights. Such unfavorable conditions may be exacerbated in the future due to climate change (*Revi et al.,* 2014), which - align with the increasing population (*UN,* 2014) –, expose cities to severe heat related risks in the future.

Future climate change in urbanized areas is assessed at several levels of complexity. *Wilby* (2008) applied a statistical downscaling approach on general circulation models and revealed that the nocturnal UHI of London may be further strengthen by 2050 considering a medium-high (A2) emission scenario. Similar conclusion was drawn for the British cities by *Lo et al.* (2020) using HadREM3-GA7–05 (the regional climate configuration of the Hadley Centre Global Environmental Model), and for Berlin by *Langendijk et al.* (2019) using a subset of RCM simulations achieved in the frame of the Euro-CORDEX (the European branch of the Coordinated Regional Downscaling Experiments). In contrast, *Lauwet et al.* (2015) showed that the nocturnal UHI will decrease in the future based on the UrbClim urban boundary layer model simulations. This is reinforced by *Hamdi et al.* (2014), using the SURFEX (Surface Externalisée) land surface model (LSM) in offline mode driven by the ARPEGE-Climat (Action de Recherche Petite Echelle Grande Echelle-Climat) global climate model (the offline mode means, that the interaction between the GCM and the RCM is one-way). Therefore, the future change of UHI intensity is uncertain and more research is needed to better explore and understand the contributing physical processes.

In the Carpathian Basin, Budapest is the most populated capital, with its 1.75 million inhabitant and 525 m^2 territory (*Tatai et al.,* 2018). In the downtown of the city, the population density is between 10 000 and 20 000 people/km^2, while its outer rim is less built-in (here the population density does not exceed 2000–2500 people/km^2).

From 1901 to present, the annual mean temperature has increased more than 1.1 °C in Budapest, which is comparable with the county-wise warming (*Tatai et al.*, 2021). However, considering the change of extreme events, the frequency of warm temperature extremes has increased much more in Budapest, compared to the measurements of other centennial stations in Hungary. E.g., between 1901 and 2009, the number of heatwave days (*Table 1*) and hot days (when the maximum daily temperature reaches 30 °C) has increased 17 and 11 days, respectively, while the second largest increase is 13 days in case of heatwave days (in Szombathely, situated in the western part of Hungary) and 8 days in case of hot days (in Szeged, situated in the southern part of Hungary, *Lakatos* and *Bihari*, 2011). Therefore,

the UHI effect superimposed on the regional climate change may explain the outstanding increase of warm temperature indices in the capital. Moreover, *Dian et al.* (2020) showed that the summer surface temperature in the downtown of Budapest may be 5 °C warmer compared to rural areas. The contribution of urbanization to regional climate change has been quantified in *Bassett et al.* (2020), and it was found that the cities' expansion in Great Britain between 1975 and 2014 explains 3.4% of the mean warming that reach up to 9.8% at the heavily urbanized southeastern part of the country.

At the Hungarian Meteorological Service (HMS), the SURFEX model is used for urban climate modeling in offline mode coupled to the HMS-ALADIN5.2 (the 5.2 version of the Aire Limitée Adaptation dynamique Dévéloppement International RCM adapted at the HMS). This model chain has been previously subjected to thorough validation, regarding the spatial and temporal characteristics of surface and 2m UHI (SUHI and UHI, respectively), and it was found that compared to satellite measurements, SURFEX overestimates the SUHI extent especially during the day (*Zsebeházi* and *Mahó*, 2021). However, gridpoint validation with respect to station measurement showed that inherited from the driving ALADIN model, the LSM heavily overestimates the summer mean temperature, but apart from this and from the aspect of UHI, the model reasonably simulates urban temperature characteristics (*Zsebeházi* and *Mahó*, 2021; *Zsebeházi* and *Szépszó*, 2020).

Following the validation process, the SURFEX was applied for projection simulations, i.e., experiment covering the 1950–2100 period was achieved, taking into account the high-emission RCP8.5 scenario (*Riahi et al.,* 2011). The urban climate projection may contribute to impact studies (e.g., in the field of health and tourism) to provide a more detailed realizations of future meteorological conditions, than an RCM is capable for. However, all models are loaded with biases, that are usually corrected before implemented in the impact model (*Ehret,* 2012). Since the resolution of an LSM (~ 1 km) may be higher with at least one order compared to the gridded observational datasets, generally used for correcting the RCMs (~ 10 km), such post-processing of urban climate simulation require somewhat new methods compared to the classical methodology developed for RCMs and GCMs.

The aim of this paper is 1) to assess the future climate change of Budapest from the aspect of temperature and UHI, 2) to explore how different the projected changes are compared to the ALADIN, and 3) to provide a simple postprocessing method to eliminate the biases of SURFEX.

In Section 2, the SURFEX and ALADIN models are briefly presented, and the experimental design and evaluation methods are explained. Next, in Section 3, the change of mean temperature, a few climate indices, and the UHI are studied in SURFEX, and the temperature and climate indices are compared to ALADIN as well. Also in this Section, a simple method is presented to produce detailed future temperature fields that are free from systematic biases. Finally, our conclusions and future plans are given in Section 4.

2. Data and methods

2.1. The SURFEX land surface model

In the present study the 5.1 version of the SURFEX (*Masson et al.*, 2013) multilayer land surface model is used in offline mode. This set-up allows to obtain much higher resolution at low computing costs compared to the online coupling, since the computation is realized in one dimension (vertically, for each gridcell separately), therefore, the stability criterions for waves and advection are irrelevant. SURFEX is responsible for simulating the land surface processes in the constant flux layer of the planetary boundary layer, called surface layer. Four different surfaces (natural land, inland water, sea, and town) can be differentiated by the model, with dedicated schemes applied for each of them. The model can be used for a wide variety of horizontal resolutions (from the order of 100 m to the order of 100 km resolution) in a way, that the subgrid-scale surface heterogeneity is handled by the tiling method (*Avissar* and *Pielke*, 1989). The land cover information is provided for SURFEX by the 1st version of the ECOCLIMAP database (*Masson et al.,* 2003) that reflects the land use, land cover characteristics of the 90s. Among the four surface types, the town and natural land surfaces are the most relevant from the perspective of Budapest, therefore, the corresponding schemes are presented hereinafter.

Over natural land surfaces, the ISBA-3L (Interaction Soil Biosphere Atmosphere model with 3 layers; *Boone et al.,* 1999) scheme is used, that computes the surface and soil temperature and moisture with the force-restore method (*Noilhan* and *Planton,* 1989).

The urban physical properties are calculated with the TEB (Town Energy Balance) scheme (*Masson;* 2000) that follows the canyon concept. The surface conditions of roof, wall, and road are treated separately with prognostic equations; moreover, the surfaces are divided into three layers in order to take heat conductivity into account. Only domestic heating is considered in our model set-up as anthropogenic heat source, by preventing indoor temperature to fall below 19 °C. The near surface variables (e.g., 2m temperature, humidity, 10m wind speed) are calculated with the Surface Boundary Layer (SBL) scheme (*Hamdi* and *Masson*, 2008; *Masson* and *Seity,* 2009).

2.2. The driving RCM: HMS-ALADIN5.2

The atmospheric forcings of the SURFEX are temperature, humidity, wind speed, and wind direction at a few tenth of m above ground level, downward shortwave and longwave radiation, surface pressure, snow, and rain. In our case, the forcings are provided by the HMS-ALADIN5.2 (*Bán et al.,* 2021) hydrostatic spectral RCM. The physical parameterization package of ALADIN is derived from the ARPEGE-Climat version 5 (*Voldoire et al.,* 2013) atmospheric GCM. The longwave radiation transfer is described by the RRTM (Rapid Radiation Transfer

Model; *Mlawer et al.,* 1997) scheme, while the shortwave radiation transfer is parameterized according to *Fouquart* and *Bonnel* (1980). The large-scale precipitation is determined by the Smith scheme (*Smith*, 1990), and the convective cloud and precipitation formation are described in *Bougeault* (1985). The surface scheme of ALADIN is SURFEX version 5, in which ISBA-3L was applied over natural land surfaces. The vertical profiles of temperature, humidity, and wind speed in the surface layer are parameterized according to *Geleyn* (1988). Urbanized areas are substituted with rocks, and the physical processes are described by the ISBA scheme.

2.3. Experimental design

In this study, a century-long urban climate simulation is assessed, performed with the 5.1 version of SURFEX for Budapest driven by the HMS-ALADIN5.2 and using the RCP8.5 scenario, that estimates strong greenhouse gas (GHG) increase throughout the 21st century. The simulation period of SURFEX was 1960–2100, and the forcings are provided at 30 m above ground level by the ALADIN, achieved at 10 km horizontal resolution on a domain covering Central and Southeastern Europe (top panel of *Fig. 1*) for the period of 1951–2100. The lateral boundary conditions of ALADIN are obtained from the CNRM-CM5 (Centre National de Recherches Météorologiques Coupled global climate Model; *Voldoire et al.,* 2013), that was downscaled in two steps to the 10 km resolution domain. On the period of 1951–2005, the RCM considered observed greenhouse-gas concentrations (*Meinshausen et al.,* 2011), while from 2006 to 2100, the concentrations followed the RCP8.5 scenario. RCP8.5 foresees 8.5 W/m^2 global radiative forcing increase by 2100 with respect to the preindustrial level.

The integration domain of SURFEX consists of 61x61 gridpoints with 1 km horizontal resolution and covers Budapest and its vicinity (*Fig. 1*). The ALADIN simulations are interpolated from 10 km to 1 km resolution using the 927 configuration of ALADIN (which is responsible for preparing the lateral boundary conditions for the RCM). The integration timestep of SURFEX is 300 s, to which the 3-hour forcings are linearly interpolated.
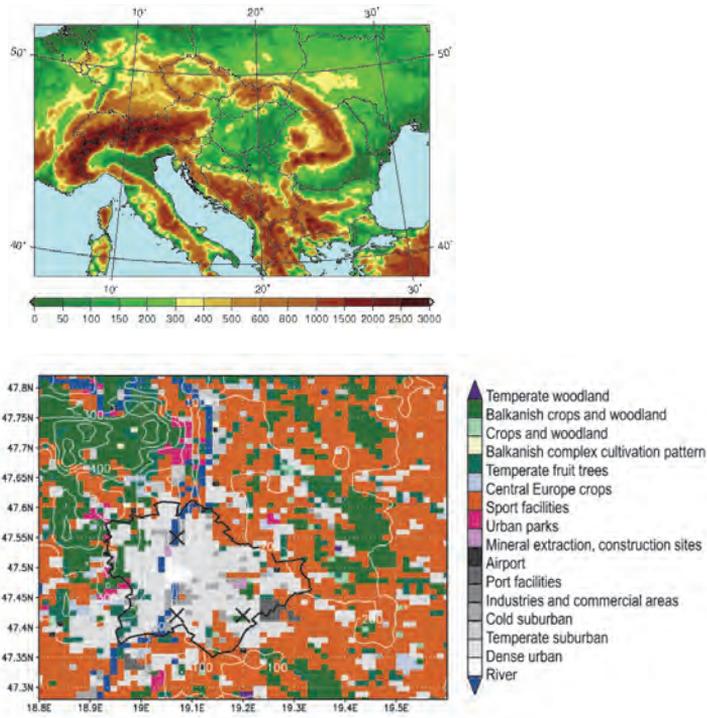
Fig. 1. Top: integration domain and orography (m) of the HMS-ALADIN5.2 regional climate model. Bottom: land cover categories over the SURFEX integration domain according to ECOCLIMAP (colored gridcells) and orography (m; white isolines). The administrative border of Budapest is marked with black line, and the included ALADIN gridpoints are marked with black x.

2.4. Evaluation methods

First, the temperature change and the change of four climate indices (heatwave days, tropical nights, frost days, and very cold days, *Table 1*) are studied and compared in SURFEX and ALADIN on 30-year periods, particularly 2021–2050 and 2071–2100, with respect to 1971–2000. The future change of climate indices are mainly presented in relative form, since in this way, differences between urban and rural areas are better revealed than considering mean changes in days.

Besides considering the climate projections for the entire SURFEX domain, the results over Budapest are scrutinized to assess the future climate change of Budapest according to the RCM and LSM. Therefore, in ALADIN and SURFEX the gridpoints outside of the administrative border of the city were masked out. Note that in the case of ALADIN, only 3 gridpoints fall over the area of Budapest (see *Fig. 1*).

In addition to the change of temperature and climate indices, the future evolution of UHI intensity was also studied in SURFEX. The UHI intensity was computed as the following: in every timestep and every gridpoint the 2m temperature value was subtracted from the mean rural temperature, which latter was determined as the average temperature of pure rural grid cells.

Table 1. Name and definition of presented climate indices

Name of climate indices	Definition
Heatwave days	daily mean temperature ≥ 25 °C
Tropical nights	daily minimum temperature > 20 °C
Frost days	daily minimum temperature < 0 °C
Very cold days	daily minimum temperature < -10 °C

Finally, a simple bias adjustment method is applied in order to investigate the expected mean future temperatures of Budapest, compared to its natural environment. The adjustment was performed for the 30-year mean temperature of ALADIN, using the 10 km resolution CARPATCLIM-HU gridded observation dataset (*Bihari et al.,* 2017) as reference. CARPATCLIM-HU was constructed based on homogenized and interpolated station measurements according to the MASH (*Szentimrey*, 2008) and MISH (*Szentimrey* and *Bihari*, 2007) methods, and widely used for regional climate model evaluation for Hungary. In the next step, the UHI intensity field of SURFEX is added to the bias adjusted ALADIN according to the following equation:

$$\overline{T}_{corr} = (\overline{T}_{RCM,f} - \overline{T}_{RCM,p}) + \overline{T}_{obs,p} + UHI_f, \qquad (1)$$

where $\overline{T}_{RCM,f}$ and $\overline{T}_{RCM,p}$ stand for the future and past 30-year area means of ALADIN, $\overline{T}_{obs,p}$ refers for the past 30-year area mean of CARPATCLIM-HU, while UHI_f means the future 30-year mean UHI field.

3. Results and discussion

3.1. Change of temperature and extreme events

First, the 2 m temperature change over Budapest is investigated in SURFEX and compared with the 10 km resolution ALADIN projections. The most warming season according to SURFEX is winter with 1.9 °C in 2021–2050 and 4.3 °C in 2071–2100, while the smallest temperature change is expected in spring (*Fig. 2, Table 2*). Looking at the seasonal warming trend in the ALADIN, it is clear that the LSM projects lower temperature change than the RCM in all seasons except autumn (*Fig. 3, Table 2*). The largest difference (0.5–0.6 °C) is obtained in spring and summer in both future periods, and in winter in 2071–2100. In addition, it is mentioned that this departure is increasing in the beginning of the 21st century (until 2030–2040), then it remains nearly constant except winter, when this process continues until 2060s. Since the abovementioned findings are valid over the whole domain as well (not shown), this behavior is rather attributed to the LSM itself and not limited to the TEB scheme over the urbanized areas.
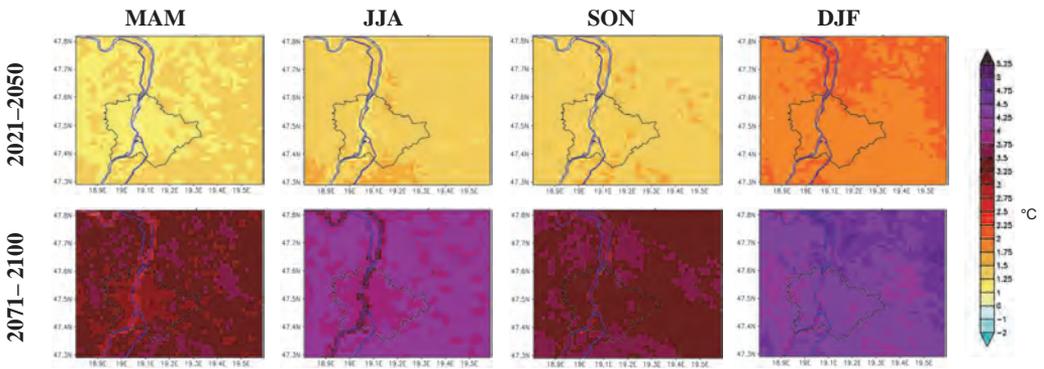
Fig. 2. Seasonal mean temperature change (°C) in 2021–2050 and 2071–2100 simulated by SURFEX. Reference: 1971–2000.

Table 2. Annual and seasonal mean temperature change (°C) in 2021–2050 and 2071–2100 simulated by ALADIN and SURFEX over Budapest. Reference: 1971–2000

		Annual	**MAM**	**JJA**	**SON**	**DJF**
ALADIN	**2021–2050**	1.7	1.5	1.7	1.5	2.2
	2071–2100	4.1	3.7	4.4	3.6	4.8
SURFEX	**2021–2050**	1.5	1.1	1.3	1.4	1.9
	2071–2100	3.7	3.2	3.9	3.4	4.3
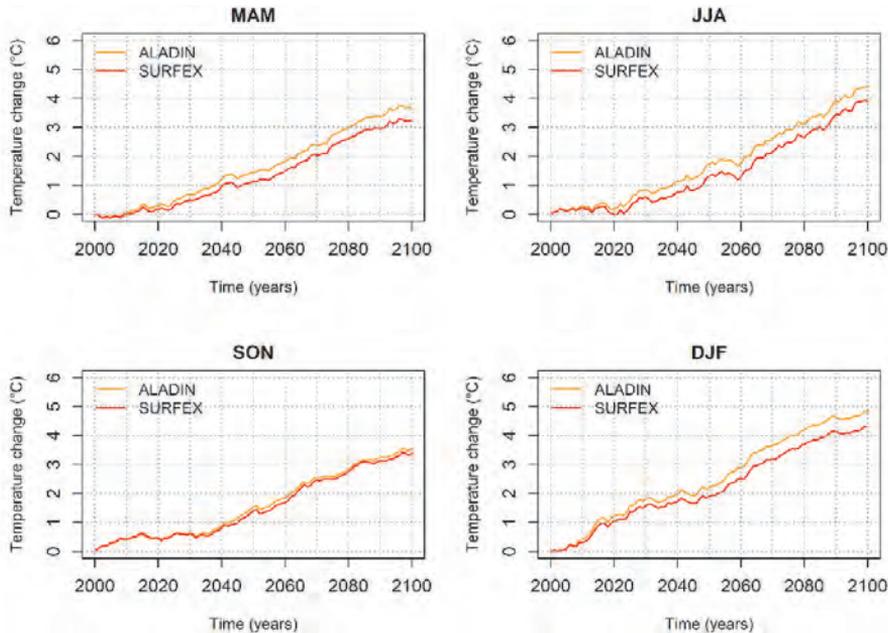
Fig. 3. Seasonal temperature change (°C) in SURFEX and ALADIN between 2000 and 2100 averaged over Budapest. The year-to-year variability is smoothed with 30-year running average (in each year the precedent 30-year mean is indicated). Reference: 1971–2000.

Regarding the spatial distribution of temperature change in SURFEX, the city and its rural vicinity portrays similar warming tendency, except in spring and summer by the end of the century, when the temperature increase is 0.25 °C less in Budapest, compared to the other parts of the domain (*Fig. 2*). Similar pattern is seen only in the minimum temperature change fields, the maximum temperature change does not affected significantly by the land cover type (not shown).

The future change of climate indices portrays different relationship between the projected values in ALADIN and SURFEX in some cases, compared to the conclusions based on the mean temperature changes. While ALADIN indicates larger relative changes of heatwave days and tropical nights with respect to SURFEX, which is especially notable for tropical nights (the difference between the two models is 66% and 207% in 2021–2050 and 2071–2100, respectively); the indices, representing low temperatures, decrease to a greater extent in SURFEX. Although it is noted that the change expressed in days is always larger in ALADIN, i.e., SURFEX projects 1–3 days less heatwave days and tropical nights in both future periods, 10 days less frost days in 2071–2100, and 6–9 days less very cold days in the near and far future, respectively. The controversies for low temperature indices can be explained by that they are less frequent in

SURFEX than in ALADIN in the reference period (with 34 days for frost days and with 9 days for very cold days; *Table 3*) partly due to the warming effect of the city, while the projected future changes in the two models are less different.

Considering the spatial distribution of the relative change of climate indices in SURFEX, the downtown of Budapest (that is a small central area on the right side of the Danube) may encounter larger relative decrease of frost days (in 2021–2050 30–35%, in 2071–2100 more than 70% reduction is projected) than in the outer districts or in the rural areas of the domain (*Fig. 4*). In contrast, the heatwave days change the least in the downtown and in Budapest compared to the other parts of the domain.
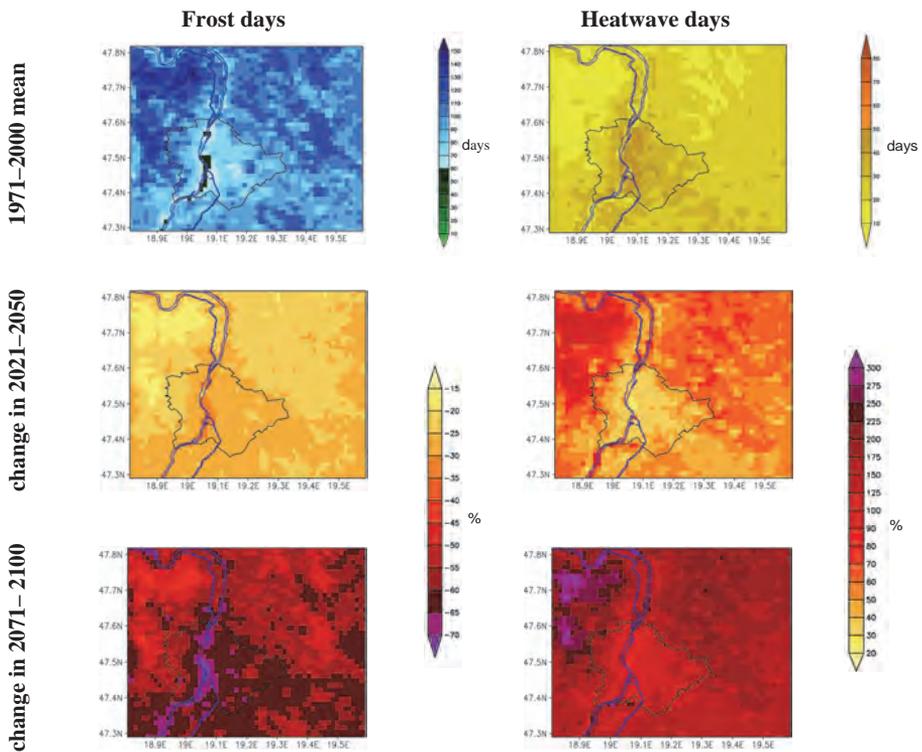
Fig. 4. Average number of frost days and heatwave days in SURFEX in 1971–2000 and their relative changes (%) in 2021–2050 and 2071–2100, with respect to 1971–2000.

Table 3. Average number of climate indices in 1971–2000 (first row) and their mean and relative changes (days and %, respectively) in 2021–2050 and 2071–2100 (second and third rows) over Budapest simulated by ALADIN and SURFEX, with respect to 1971–2000

	unit	Heat wave days		Tropical nights		Frost days		Very cold days	
		ALADIN	SURFEX	ALADIN	SURFEX	ALADIN	SURFEX	ALADIN	SURFEX
1971–2000 means	days	28	33	13	33	118	84	15	6
change in 2021–2050	%	59	43	126	60	-21	-27	-73	-82
	days	(17)	(14)	(16)	(17)	(-25)	(-22)	(-11)	(-5)
change in 2071–2100	%	148	127	374	167	-51	-62	-98	-100
	days	(42)	(40)	(48)	(47)	(-61)	(-51)	(-15)	(-6)

3.2. Change of UHI

The decrease of UHI intensity at 0 UTC is projected by SURFEX in each season for both future periods (*Fig. 5* and *Table 4*). Spring and summer may reckon with the largest change, i.e., -0.27 and -0.22 °C in 2021–2050 and -0.35 and -0.32 °C in 2071–2100, respectively. Note that these seasons are characterized by the largest UHI in the past (2.0 in spring and 2.1 °C in summer). In contrast, in autumn and winter, the UHI intensity drop does not exceed 0.2 °C in each future period, and there is no substantial difference between the urban and rural gridpoints. The projected negative tendencies seem to significantly reduce in the second half of the century, since the decrease between 2021–2050 and 1971–2000 is much larger than between the two future periods. Note that ALADIN (the driving model of SURFEX) projects 10-30% wetter future conditions for Hungary throughout the year for the entire 21st century in conjunction with a strong temperature increase (*Bán et al.*, 2021). However, this does not have straightforward impact on the soil conditions. In summer, the soil moisture (of the middle layer) is reduced by up to 5% at the end of the century over the SURFEX domain (*Fig. 6*). In spring and autumn, after a few % of increase in the first half of the century, the soil moisture returns to the conditions of the reference period, while it increases heavily in winter. A continuous increase is seen in the soil temperature (also of the middle layer) in every seasons, most intensively in spring, although, the largest 2 m temperature was obtained in winter. All this suggests that the more precipitation in ALADIN cannot prevent the summer soil moisture loss in the future, and the strong soil temperature increase in spring and summer (while the surface properties of the paved and built-up areas in the city remain invariant) may explain

the larger nocturnal UHI reduction in these seasons. *Hamdi et al.* (2014) and *Chapman et al.* (2019) found similar results in terms of future reduction of the nocturnal UHI intensity for Brussels, Paris, and Brisbane, and also explained the stronger drying of natural land surfaces around the city by soil moisture reduction.

Table 4. Seasonal mean nocturnal UHI intensity (at 0 UTC; °C) in Budapest simulated by SURFEX in 1971–2000 (first row), and its mean changes (°C) in 2021–2050 and 2071–2100, with respect to 1971–2000 (second and third rows)

	MAM	JJA	SON	DJF
1971–2000 means	2.0	2.1	1.8	1.4
change in 2021–2050	-0.27	-0.22	-0.14	-0.13
change in 2071–2100	-0.35	-0.32	-0.16	-0.14
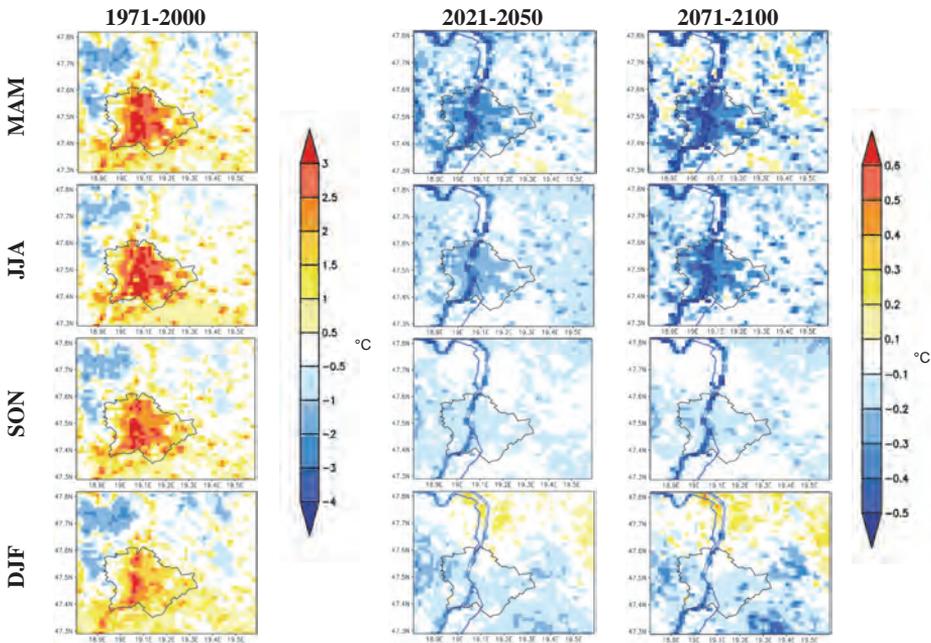
Fig. 5. First column: seasonal mean nocturnal UHI intensity (at 0 UTC; °C) simulated by SURFEX in 1971–2000. Second and third column: change (°C) of mean nocturnal UHI intensity in 2021–2050 and 2071–2100, respectively; reference: 1971–2000.
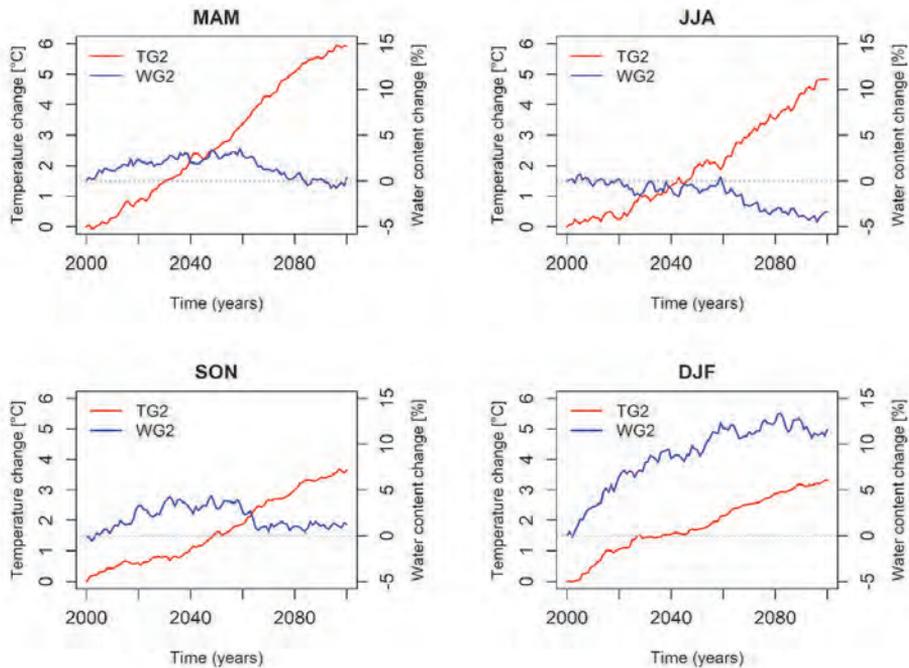
Fig. 6. Seasonal mean soil moisture (WG2) and soil temperature (TG2) change (in % and in °C, respectively) between 2000 and 2100 in the middle soil layer of SURFEX averaged over the model domain. The year-to-year variability is smoothed with 30-year running average (in each year the precedent 30-year mean is indicated). Reference: 1971–2000.

3.3. Bias adjustment of mean temperature of SURFEX

In the previous sections it was shown, that the high temperature extremes may change at a smaller rate inside the city than in the outskirt regions, and the UHI intensity may reduce in the future. Despite these results indicate the modification of the urban-rural contrast in terms of temperature and temperature indices, this change is much smaller than the contrast itself. Therefore, the fact that the urbanized areas are especially exposed to certain aspects of climate change is partly hidden in the results presented by the classical way developed in the climate model community, i.e., considering mean changes. All these suggest that the (bias adjusted) future means provided by the model may provide more actionable and visionable information for the users interested in urban climate.

All bias adjustment methods require long, quality observations, suitable for the target needs. From urban climate perspectives, to correct a km-scale land surface model, a km-scale gridded reference dataset based on station

687

measurements, that comprises urban signature is needed. In Budapest, from the beginning of the 2000s, four urban stations are operating, although most of them are not included in the 10 km resolution CARPATCLIM-HU. Therefore, even if it is interpolated to 1 km resolution, the detailed urban effect would be missing due to the lack of long urban measurements. Therefore, using this reference to directly bias-correct the SURFEX outputs would eliminate the urban pattern from the model. In the following, a simple method is given to provide future means of SURFEX that are cleaned from systematic biases.

Since the benefit of SURFEX is that it can simulate the urban effect compared to ALADIN, the idea is to bias adjust the 10 km resolution area means of ALADIN using the CARPATCLIM-HU and adding the "urban effect" field to this value. E.g., in the case of temperature, this urban effect is the UHI, since it shows how different the temperature is over the city compared to the environment (that can be simulated by ALADIN). *Fig. 7* shows the mean seasonal temperature of SURFEX in 2021–2050 and 2071–2100. Based on this method, the mean temperature in Budapest can be 22–23 and 25 °C in summer, and 5–6 and 6–7 °C in winter, in 2021–2050 and 2071–2100, respectively, which are approximately 2 °C warmer than the natural surfaces in the outskirts.

It must be mentioned, that this method should be considered as a first approximation to bias-adjust SURFEX and can be improved several ways. First, Budapest is situated in a complex orography area, surrounded by mountains, and for the mean rural temperature computation, we considered all rural gridpoints regardless of their elevation. However, especially the Buda Hills have a cooling effect on the rural temperature, that may result exaggerated UHI intensity. The UHI intensity must be especially well defined, when it may affect the outcome of the impact studies.

Moreover, in this method only the RCM is corrected, but the inaccuracies of urban pattern (i.e., the intensity and spatial distribution of UHI) were kept unchanged due to the lack of a high-resolution urban station network.

Finally, it must be also bear in mind, that no urban development scenario (i.e., land cover change) was taken into account in this century-long simulation, therefore, only the impact of altered climate conditions was assessed on the present conditions of Budapest. However, *Chapman et al.* (2019) showed that considering urban growth and climate change hand in hand, the negative effects of climate change (e.g., number of hot nights, dangerous heat stress) were amplified compared to ignoring the change of city structure. *Lemonsu et al.* (2015) studied several urban expansion and structural change scenarios and found that urban densification increases UHI especially at night, while implementing green areas in the city center led to reduced nocturnal UHI, but amplified daytime values.
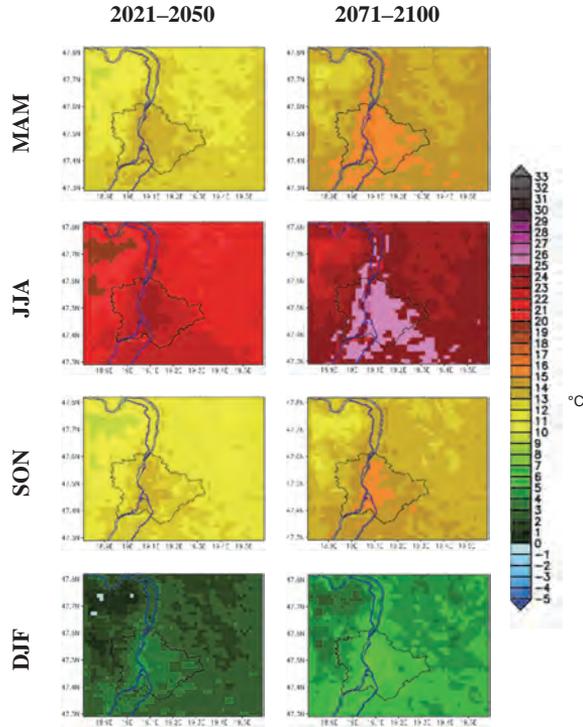
Fig. 7. Seasonal mean bias-adjusted 2m temperature (°C) in 2021–2050 and 2071–2100 according to the SURFEX.

4. Conclusions

In this paper, the first results of future temperature and UHI changes of Budapest achieved by the ALADIN driven SURFEX land surface model are presented. Besides the analysis of the 1 km resolution SURFEX, the scope of the paper was to investigate how different the simulated urban climate is from the 10 km resolution RCM results, that considers urban processes with a simple bulk scheme (i.e., the urbanized surfaces are represented by rocks).

The largest temperature change over Budapest is expected in winter (1.9 °C and 4.3 °C in 2021–2050 and 2071–2100), that is in line with the ALADIN results for Hungary (*Bán et al.*, 2021). Except for autumn, SURFEX clearly projects more moderate temperature change compared to its driving model, especially in spring and summer. This discrepancy may be explained by that the set-up of SURFEX slightly differs to the one built-in ALADIN, and that the LSM does not model the full atmosphere.

Heatwave days and tropical nights may increase in the city with 43% and 60% in 2021–2050, while they may at least double at the end of the century. Only low temperature indices are projected to larger decrease in SURFEX compared to ALADIN and in the downtown compared to the suburbs and rural areas.

According to SURFEX, the nocturnal UHI in Budapest may be less intense in the future, to the most in spring and summer, when the model gave the strongest UHI in the past. This natural UHI mitigation may be explained by that the soil in the rural areas dry out in the future, therefore, these areas warm at a higher rate compared to the city. These findings reassure, that the relationship between the urban and rural areas may change in the future due to altered physical processes, which can properly be simulated only with dynamical models.

Finally, an attempt to bias-adjust the SURFEX temperature fields were given using the delta method on ALADIN mean temperature, superimposed by the UHI field derived from SURFEX. The bias-adjusted future results of SURFEX reveal that more extreme conditions are expected in the city, this information may be hidden by considering mean changes.

However, it must be emphasized, that in order to adequately estimate the future climate change in cities, more simulations are needed, driven by different scenarios and models. This need drives our future plans, to conduct century-long simulations with SURFEX with the RCP4.5 scenario and to couple SURFEX to the REMO regional climate model, also adapted at the HMS.

References

Avissar, R. and *Pielke, R.A.*, 1989: A Parameterization of Heterogeneous Land Surfaces for Atmospheric Numerical Models and Its Impact on Regional Meteorology. *Month. Weather Rev. 117*, 2113– https://doi.org/10.1175/1520-0493(1989)117<2113:APOHLS>2.0.CO;2

Bassett, R., Young, P.J., Blair, G.S., Cai, X.-M., and *Chapman, L.*, 2020: Urbanisation's contribution to climate warming in Great Britain. *Environ. Res. Lett. 15*, 114014. https://doi.org/10.1088/1748-9326/abbb51

Bán, B., Szépszó, G., Allaga-Zsebeházi, G., and *Somot, S.,* 2021: ALADIN-Climate at the Hungarian Meteorological Service: from the beginnings to the present day's results, *Időjárás 125*, 647–673. https://doi.org/10.28974/idojaras.2021.4.6

Bihari, Z., Lakatos, M., and *Szentimrey, T.,* 2017: Felszíni megfigyelésekből készített rácsponti adatbázisok az Országos Meteorológiai Szolgálatnál. *Légkör 62*, 148–151. (in Hungarian)

Boone, A., Calvet, J.-C., and *Noilhan, J.*, 1999: Inclusion of a Third Soil Layer in a Land Surface Scheme Using the Force–Restore Method. *J. Appl. Meteorol. 38*, 1611–1630. https://doi.org/10.1175/1520-0450(1999)038<1611:IOATSL>2.0.CO;2

Bougeault, P., 1985: A simple parameterization of the large-scale effects of cumulus convection. *Month. Weather Rev. 113*, 2108–2121. https://doi.org/10.1175/1520-0493(1985)113<2108:ASPOTL>2.0.CO;2

Chapman, S., Thatcher, M., Salazar, A., Watson, J.E.M., and *McAlpine, C.A.*, 2019: The impact of climate change and urban growth on urban climate and heat stress in a subtropical city. *Int. J. Climatol. 39*, 3013–3030. https://doi.org/10.1002/joc.5998

Dian, Cs., Pongrácz, R., Dezső, Zs., and *Bartholy, J.*, 2020: Annual and monthly analysis of surface urban heat island intensity with respect to the local climate zones in Budapest. *Urban Climate*, *31*, 100573. https://doi.org/10.1016/j.uclim.2019.100573

Ehret, U., Zehe, E., Wulfmeyer, V., Warrach-Sagi, K., and *Liebert, J.*, 2012: HESS Opinions 'Should we apply bias correction to global and regional climate model data?' *Hydrol. Earth Syst. Sci. 16*, 3391–3404. https://doi.org/10.5194/hess-16-3391-2012

Fouquart, Y. and *Bonnel, B.*, 1980: Computation of solar heating of the Earth's atmosphere: A new parameteizatio. *Beitr. Phys. Atmos. 53*, 35–62.

Geleyn, J.-F., 1988: Interpolation of wind, temperature and humidity values from model levels to the height of measurement. *Tellus A 40*, 347–351. https://doi.org/10.1111/j.1600-0870.1988.tb00352.x

Hamdi, R. and *Masson, V.*, 2008: Inclusion of a Drag Approach in the Town Energy Balance (TEB) Scheme: Offline 1D Evaluation in a Street Canyon. *J. Appl. Meteorol. Climatol. 47*, 2627–2644. https://doi.org/10.1175/2008JAMC1865.1

Hamdi, R., Van de Vyver, H., De Troch, R., and *Termonia, P.*, 2014: Assessment of three dynamical urban climate downscaling methods: Brussels's future urban heat island under an A1B emission scenario: BRUSSELS'S FUTURE URBAN HEAT ISLAND. *Int. J. Climatol. 34*, 978–999. https://doi.org/10.1002/joc.3734

Lakatos, M. and *Bihari, Z.*, 2011: A közelmúlt megfigyelt hőmérsékleti- és csapadéktendenciái. In (eds.: *Bartholy, J., Bozó, L., Haszpra, L.*: Klímaváltozás – 2011: Klímaszcenáriók a Kárpát-medence térségére Hungarian Academy of Sciences and Meteorological Department of ELU, Budapest, 146–169.

Langendijk, G.S., Rechid, D., and *Jacob, D.*, 2019: Urban Areas and Urban–Rural Contrasts under Climate Change: What Does the EURO-CORDEX Ensemble Tell Us?—Investigating near Surface Humidity in Berlin and Its Surroundings. *Atmosphere 10*, 730. https://doi.org/10.3390/atmos10120730

Lauwaet, D., De Ridder, K., Saeed, S., Brisson, E., Chatterjee, F., van Lipzig, N.P.M., Maiheu, B., and *Hooyberghs, H.*, 2016: Assessing the current and future urban heat island of Brussels. *Urban Climate 15*, 1–15. https://doi.org/10.1016/j.uclim.2015.11.008

Lemonsu, A., Viguié, V., Daniel, M., and *Masson, V.*, 2015: Vulnerability to heat waves: Impact of urban expansion scenarios on urban heat island and heat stress in Paris (France). *Urban Climate 14, Part 4*, 586–605. https://doi.org/10.1016/j.uclim.2015.10.007

Lo, Y.T.E., Mitchell, D.M., Bohnenstengel, S.I., Collins, M., Hawkins, E., Hegerl, G.C., Joshi, M., and *Stott, P.A.*, 2020: U.K. Climate Projections: Summer Daytime and Nighttime Urban Heat Island Changes in England's Major Cities. *J. Climate 33*, 9015–9030. https://doi.org/10.1175/JCLI-D-19-0961.1

Masson, V., Champeaux, J.-L., Chauvin, F., Meriguet, C., and *Lacaze, R.*, 2003: A Global Database of Land Surface Parameters at 1-km Resolution in Meteorological and Climate Models. *J. Climate 16*, 1261–1282. https://doi.org/10.1175/1520-0442(2003)16<1261:AGDOLS>2.0.CO;2

Masson, V. and *Seity, Y.*, 2009: Including Atmospheric Layers in Vegetation and Urban Offline Surface Schemes. *J. Appl. Meteorol. Climatol. 48*, 1377–1397. https://doi.org/10.1175/2009JAMC1866.1

Masson, V., Le Moigne, P., Martin, E., Faroux, S., Alias, A., Alkama, R., Belamari, S., Barbu, A., Boone, A., Bouyssel, F., Brousseau, P., Brun, E., Calvet, J.-C., Carrer, D., Decharme, B., Delire, C., Donier, S., Essaouini, K., Gibelin, A.-L., Giordani, H., Habets, F., Jidane, M., Kerdraon, G., Kourzeneva, E., Lafaysse, M., Lafont, S., Lebeaupin Brossier, C., Lemonsu, A., Mahfouf, J.-F., Marguinaud, P., Mokhtari, M., Morin, S., Pigeon, G., Salgado, R., Seity, Y., Taillefer, F., Tanguy, G., Tulet, P., Vincendon, B., Vionnet, V., and *Voldoire, A.*, 2013: The SURFEXv7.2 land and ocean surface platform for coupled or offline simulation of earth surface variables and fluxes. *Geosci. Model Develop. 6*, 929–960. https://doi.org/10.5194/gmd-6-929-2013

Masson, V., 2000: A Physically-Based Scheme For The Urban Energy Budget In Atmospheric Models. *Bound.-Lay. Meteorol. 94*, 357–397. https://doi.org/10.1023/A:1002463829265

Meinshausen, M., Smith, S.J., Calvin, K., Daniel, J.S., Kainuma, M.L.T., Lamarque, J.-F., Matsumoto, K., Montzka, S.A., Raper, S.C.B., Riahi, K., Thomson, A., Velders, G.J.M., and *van Vuuren, D.P.P.*, 2011: The RCP greenhouse gas concentrations and their extensions from 1765 to 2300. *Climatic Change 109*, 213. https://doi.org/10.1007/s10584-011-0156-z

Mlawer, E.J., Taubman, S.J., Brown, P.D., Iacono, M.J., and *Clough, S.A.*, 1997: Radiative transfer for inhomogeneous atmospheres: RRTM, a validated correlated-k model for the longwave. *J. Geophys. Res.: Atmosph. 102*, 16663–16682. https://doi.org/10.1029/97JD00237

Noilhan, J. and *Planton, S.*, 1989: A Simple Parameterization of Land Surface Processes for Meteorological Models. *Month. Weather Rev. 117*, 536–549.
https://doi.org/10.1175/1520-0493(1989)117<0536:ASPOLS>2.0.CO;2

Oke, T.R., 1982: The energetic basis of the urban heat island. *Quart. J. Roy. Meteorol. Soc. 108*, 1–24. https://doi.org/10.1002/qj.49710845502

Revi, A., Satterthwaite, D.E., Aragón-Durand,F., Corfee-Morlot, J., Kiunsi,R.B.R., Pelling,M., Roberts, D.C., and *Solecki, W.*, 2014: Urban areas. In (eds.: *Field, C.B., Barros, V.R., Dokken, D.J., Mach, K.J., Mastrandrea, M.D., Bilir, T.E., Chatterjee, M., Ebi, K.L., Estrada, Y.O., Genova, R.C., Girma, B., Kissel, E.S., Levy, A.N., MacCracken, S., Mastrandrea, P.R., White, L.L*) Climate Change 2014: Impacts, Adaptation, and Vulnerability. Part A: Global and Sectoral Aspects. Contribution of Working Group II to the Fifth Assessment Report of the Intergovernmental Panel on Climate Change Cambridge University Press, Cambridge, United Kingdom and New York, NY, USA, 535–612.

Riahi, K., Rao, S., Krey, V., Cho, C., Chirkov, V., Fischer, G., Kindermann, G., Nakicenovic, N., and *Rafaj, P.*, 2011: RCP 8.5–A scenario of comparatively high greenhouse gas emissions. *Climatic Change 109*, 33. https://doi.org/10.1007/s10584-011-0149-y

Smith, R.N.B., 1990: A scheme for predicting layer clouds and their water content in a general circulation model. *Quart. J. Roy. Meteorol. Soc. 116*, 435–460. https://doi.org/10.1002/qj.49711649210

Szentimrey, T. and *Bihari, Z.*, 2007: Mathematical background of the spatial interpolation methods and the software MISH (Meteorological Interpolation based on Surface Homogenized Data Basis). In: *Proceedings from the Conference on Spatial Interpolation in Climatology and Meteorology*, Budapest, Hungary, 2004, COST Action 719, COST Office, 17–27.

Szentimrey, T., 2008: Development of MASH homogenization procedure for daily data. In: Proceedings of the Fifth Seminar for Homogenization and Quality Control in Climatological Databases, Budapest, Hungary, 2006. WCDMP-No.71, WMO/TD-No. 1493, 123–130.

Tatai, Zs., Bódi-Nagy, A., Frits, B., Pogány, A., Orosz, I., Szőke, B., and *Bedőcs, B.*, 2018: Budapest klímastratégiája. (in Hungarian)

Tatai, Zs., Bódi-Nagy, A., Orosz, I., Becsák, P., Pető, Z., and *Szabó, K.*, 2021: Budapest fenntartható energia- és klíma akcióterve (in Hungarian, under consultation).
https://budapest.hu/Documents/klimastrategia/BP_klimastrategia_SECAP_egyeztetesi_anyag.pdf

UN, 2014: Concise Report on the World Population Situation in 2014. Department of Economic and Social Affairs, United Nations, New York, USA. ISBN 978-92-1-151518-3

Voldoire, A., Sanchez-Gomez, E., Salas y Mélia, D., Decharme, B., Cassou, C., Sénési, S., Valcke, S., Beau, I., Alias, A., Chevallier, M., Déqué, M., Deshayes, J., Douville, H., Fernandez, E., Madec, G., Maisonnave, E., Moine, M.-P., Planton, S., Saint-Martin, D., Szopa, S., Tyteca, S., Alkama, R., Belamari, S., Braun, A., Coquart, L., and *Chauvin, F.*, 2013: The CNRM-CM5.1 global climate model: description and basic evaluation. *Climate Dynam. 40*, 2091–2121.
https://doi.org/10.1007/s00382-011-1259-y

Wilby, R.L., 2008: Constructing Climate Change Scenarios of Urban Heat Island Intensity and Air Quality. *Environ. Plan. B: Plan. Design 35*, 902–919. https://doi.org/10.1068/b33066t

Zsebeházi, G. and *Mahó, S.I.*, 2021: Assessment of the Urban Impact on Surface and Screen-Level Temperature in the ALADIN-Climate Driven SURFEX Land Surface Model for Budapest. *Atmosphere 12*, 709. https://doi.org/10.3390/atmos12060709

Zsebeházi, G. and *Szépszó, G.*, 2020: Modeling the urban climate of Budapest using the SURFEX land surface model driven by the ALADIN-Climate regional climate model results. *Időjárás 124*, 191–207. https://doi.org/10.28974/idojaras.2020.2.3

IDŐJÁRÁS

AUTHOR INDEX

TABLE OF CONTENTS

I. Papers

SUBJECT INDEX

W

Y

Z

INSTRUCTIONS TO AUTHORS OF *IDŐJÁRÁS*

The purpose of the journal is to publish papers in any field of meteorology and atmosphere related scientific areas. These may be

- research papers on new results of scientific investigations,
- critical review articles summarizing the current state of art of a certain topic,
- short contributions dealing with a particular question.

Some issues contain "News" and "Book review", therefore, such contributions are also welcome. The papers must be in American English and should be checked by a native speaker if necessary.

Authors are requested to send their manuscripts to

Editor-in Chief of IDŐJÁRÁS
P.O. Box 38, H-1525 Budapest, Hungary
E-mail: journal.idojaras@met.hu

including all illustrations. MS Word format is preferred in electronic submission. Papers will then be reviewed normally by two independent referees, who remain unidentified for the author(s). The Editor-in-Chief will inform the author(s) whether or not the paper is acceptable for publication, and what modifications, if any, are necessary.

Please, follow the order given below when typing manuscripts.

Title page should consist of the title, the name(s) of the author(s), their affiliation(s) including full postal and e-mail address(es). In case of more than one author, the corresponding author must be identified.

Abstract: should contain the purpose, the applied data and methods as well as the basic conclusion(s) of the paper.

Key-words: must be included (from 5 to 10) to help to classify the topic.

Text: has to be typed in single spacing on an A4 size paper using 14 pt Times New Roman font if possible. Use of S.I.

units are expected, and the use of negative exponent is preferred to fractional sign. Mathematical formulae are expected to be as simple as possible and numbered in parentheses at the right margin.

All publications cited in the text should be presented in the *list of references*, arranged in alphabetical order. For an article: name(s) of author(s) in Italics, year, title of article, name of journal, volume, number (the latter two in Italics) and pages. E.g., *Nathan, K.K.,* 1986: A note on the relationship between photo-synthetically active radiation and cloud amount. *Időjárás 90,* 10–13. For a book: name(s) of author(s), year, title of the book (all in Italics except the year), publisher and place of publication. E.g., *Junge, C.E.,* 1963: *Air Chemistry and Radioactivity.* Academic Press, New York and London. Reference in the text should contain the name(s) of the author(s) in Italics and year of publication. E.g., in the case of one author: *Miller* (1989); in the case of two authors: *Gamov* and *Cleveland* (1973); and if there are more than two authors: *Smith et al.* (1990). If the name of the author cannot be fitted into the text: *(Miller,* 1989); etc. When referring papers published in the same year by the same author, letters a, b, c, etc. should follow the year of publication. DOI numbers of references should be provided if applicable.

Tables should be marked by Arabic numbers and printed in separate sheets with their numbers and legends given below them. Avoid too lengthy or complicated tables, or tables duplicating results given in other form in the manuscript (e.g., graphs). *Figures* should also be marked with Arabic numbers and printed in black and white or color (under special arrangement) in separate sheets with their numbers and captions given below them. JPG, TIF, GIF, BMP or PNG formats should be used for electronic artwork submission.

More information for authors is available: journal.idojaras@met.hu